

5-1-2016

Effects of Vertical Ground Motion on Seismic Performance of Reinforced Concrete Flat-Plate Buildings

Sara Jean George
University of Nevada, Las Vegas

Follow this and additional works at: <https://digitalscholarship.unlv.edu/thesesdissertations>



Part of the [Civil Engineering Commons](#)

Repository Citation

George, Sara Jean, "Effects of Vertical Ground Motion on Seismic Performance of Reinforced Concrete Flat-Plate Buildings" (2016). *UNLV Theses, Dissertations, Professional Papers, and Capstones*. 2671.
<http://dx.doi.org/10.34917/9112068>

This Dissertation is protected by copyright and/or related rights. It has been brought to you by Digital Scholarship@UNLV with permission from the rights-holder(s). You are free to use this Dissertation in any way that is permitted by the copyright and related rights legislation that applies to your use. For other uses you need to obtain permission from the rights-holder(s) directly, unless additional rights are indicated by a Creative Commons license in the record and/or on the work itself.

This Dissertation has been accepted for inclusion in UNLV Theses, Dissertations, Professional Papers, and Capstones by an authorized administrator of Digital Scholarship@UNLV. For more information, please contact digitalscholarship@unlv.edu.

EFFECTS OF VERTICAL GROUND MOTION ON SEISMIC
PERFORMANCE OF REINFORCED CONCRETE
FLAT-PLATE BUILDINGS

By

Sara George

Bachelor of Science - Architectural Engineering
University of Wyoming
2007

Master of Science in Engineering - Civil Engineering
University of Nevada, Las Vegas
2012

A dissertation submitted in partial fulfillment
of the requirements for the

Doctor of Philosophy – Civil and Environmental Engineering

Department of Civil and Environmental Engineering and Construction
Howard R. Hughes College of Engineering
The Graduate College

University of Nevada, Las Vegas
May 2016

Dissertation Approval

The Graduate College
The University of Nevada, Las Vegas

April 14, 2016

This dissertation prepared by

Sara George

entitled

Effects of Vertical Ground Motion on Seismic Performance of Reinforced Concrete Flat-Plate Buildings

is approved in partial fulfillment of the requirements for the degree of

Doctor of Philosophy – Civil and Environmental Engineering
Department of Civil and Environmental Engineering and Construction

Ying Tian, Ph.D.
Examination Committee Chair

Kathryn Hausbeck Korgan, Ph.D.
Graduate College Interim Dean

Moses Karakouzian, Ph.D.
Examination Committee Member

Samaan G. Ladkany, Ph.D.
Examination Committee Member

Sarah Orton, Ph.d.
Examination Committee Member

Brendan O'Toole, Ph.D.
Graduate College Faculty Representative

ABSTRACT

Effects of Vertical Ground Motion on Seismic Performance of Reinforced Concrete Flat-Plate Buildings

By

Sara Jean George

Dr. Ying Tian, Examination Committee Chair
Associate Professor of Civil and Environmental Engineering and Construction
University of Nevada, Las Vegas

Reinforced concrete flat plate is a type of structural system widely used for office and residential buildings in many areas including those with high seismic risk. In the regions of high seismicity, moment frames or shear walls are employed to resist lateral loading while the flat-plate system is designed to primarily resist gravity loading. Flat-plate structures must maintain lateral deformation capacity as well as resist gravity loading under seismic loads. The deformation capacity of a slab-column connection is a function of vertical shear transferred from slab to column. The effects of vertical loading become even more exaggerated when the flat-plate structure is located near a fault. Near-source seismic events can cause large vertical-to-horizontal peak ground acceleration (V/H) ratios greater than unity with high velocity and frequencies which can have disastrous effects due to significant vertical accelerations.

Flat-plate structure is prone to punching shear failure at slab-column connections which may lead to a catastrophic progressive collapse. Slabs of flat-plates functioning only as gravity system generally have a reinforcement ratio less than 1% for the tensile bars resisting negative bending moment. Large vertical accelerations combined with low percentage of steel reinforcement may increase the risk of punching failure in flat plates. To date little is known

about the structural performance of flat plates subjected to strong vertical accelerations during a near source event.

In this study a flat-plate structure taken as a prototype is subjected to eight seismic ground motions recorded in stations with a distance less than approximately 35km to the seismic epicenter and fault line. The ground motions were scaled to reflect the seismic risk corresponding to the maximum considered earthquake for design purposes. It is found from the numerical simulation that the addition of vertical ground motion increases lateral drift of the building by less than 3% when compared with applying ground motions in the horizontal directions. However, the vertical ground motion can significantly increase the slab deformation localized at the columns on average by as much as 30% and create an average slab rotation near 0.05 radians. The deflection at slab panel centers is also enhanced due to the addition of vertical ground motion by an average of 39%. Finally, vertical ground motion amplifies the total vertical shear transferred between the slab and columns; as compared with bi-directional ground motion, an average of 29% change in the axial force in the columns is identified.

The potential of punching shear failure of flat-plate structures under combined effects of vertical and horizontal ground motion is examined based on the three design criteria given in ACI 318-14: eccentric shear stress model, story design drift limit for slab-column connections without shear reinforcement, and two-way shear strength for one side of a slab-column connection. The failure criterion suggested by Muttoni et al. (2008) is also used to evaluate punching failure potential. Results signify ACI 318 eccentric shear stress model and two-way shear strength approach may not be able to adequately predict the potential of punching shear failure in flat plates. Conversely ACI 318 drift limit approach and Muttoni's punching failure

criterion model predict similar risk of punching failure and a greater possibility of punching failure when vertical ground motion is incorporated.

Finally, soil-structure interaction is incorporated into the prototype structure model for dynamic tri-axial loading considering stiff soil. Translational and rotational soil springs are included with spring stiffness based upon the suggestions by Gazetas (1991). The incorporation of soil-structure interaction produces little change in the dynamic response of a flat-plate structure if the soil is stiff. Insights gained from this study will create knowledge needed to improve design of flat-plate buildings subjected to vertical ground motions.

TABLE OF CONTENTS

ABSTRACT.....	III
LIST OF TABLES.....	VIII
LIST OF FIGURES	IX
1. INTRODUCTION	1
1.1 INTRODUCTION TO REINFORCED CONCRETE FLAT-PLATE STRUCTURES	1
1.2 BEHAVIOR OF SLAB-COLUMN CONNECTIONS	3
1.2.1 Behavior of Slab-Column Connections under Gravity Loading.....	3
1.2.2 Behavior of Slab-Column Connections under Cyclic Lateral Loading	7
1.3 PROPERTIES OF VERTICAL GROUND MOTIONS	13
1.3.1 Frequency Content	14
1.3.2 Ratio of Peak Vertical Acceleration to Peak Horizontal Acceleration	15
1.3.3 Time Interval of Vertical and Horizontal Peak Ground Accelerations.....	16
1.4 DESIGN CODE REQUIREMENTS FOR VERTICAL GROUND MOTION.....	18
1.5 PREVIOUS STUDIES ON REINFORCED CONCRETE STRUCTURES	20
1.5.1 Vertical Ground Motion Effects on Bridges.....	20
1.5.2 Vertical Ground Motion Effects on Buildings.....	22
1.6 FIELD EVIDENCE OF FLAT SLAB STRUCTURE DAMAGE DUE TO VERTICAL MOTION.....	24
1.7 MOTIVATION OF RESEARCH	26
1.8 RESEARCH OBJECTIVES, SCOPE AND METHODOLOGY	27
1.9 OUTLINE OF DISSERTATION	29
2. MODELING OF PROTOTYPE FLAT-PLATE BUILDING.....	30
2.1 PROTOTYPE STRUCTURE	30
2.1.1 Overview.....	30
2.1.2 Slab-Column Frames	33
2.1.3 Perimeter Moment Frames.....	34
2.2 MODELING OF PROTOTYPE STRUCTURE	37
2.2.1 Overview.....	37
2.2.2 Modeling of Beams and Columns in Perimeter Moment Frames.....	37
2.2.3 Material Modeling for Perimeter Frames	39
2.3 MODELING OF SLAB	42
2.3.1 Grid Beam Model	42

2.3.2 Modeling of Principle Bending Moment	44
2.3.3 Modeling of Torsion	46
2.3.4 Hysteretic Model for Flexure and Torsion.....	47
2.4 LOADING.....	51
2.4.2 Scaling Selected Ground Motion Records.....	58
2.4.3 Analysis Procedure	68
3. DYNAMIC FORCE AND DEFORMATION DEMANDS OF PROTOTYPE STRUCTURE	70
3.1 OVERVIEW	70
3.2 RESULTS OF PUSHOVER ANALYSIS.....	72
3.3 DYNAMIC LATERAL DISPLACEMENT RESPONSE.....	73
3.3.1 Lateral Displacement under Uni-directional Ground Motion.....	73
3.3.2 Lateral Displacement under Bi-directional Ground Motion	76
3.3.3 Lateral Displacement under Tri-directional Ground Motion.....	77
3.4 DYNAMIC RESPONSE OF SLAB ROTATION	78
3.4.1 Slab Rotation under Uni-directional Ground Motion	79
3.4.2 Slab Rotation under Bi-directional Ground Motion	82
3.4.3 Slab Rotation under Tri-directional Ground Motion	85
3.4.4 Effects of Vertical Ground Motion Properties on Slab Rotation.....	87
3.5 DYNAMIC RESPONSE OF AXIAL FORCE IN INTERIOR COLUMNS	90
3.5.1 Column Axial Force under Uni-directional Ground Motion	90
3.5.2 Column Axial Force under Bi-directional Ground Motion	92
3.5.3 Column Axial Force under Tri-directional Ground Motion	93
3.6 DYNAMIC RESPONSE OF SLAB CENTER DEFLECTION	95
3.6.1 Slab Deflection Due to Uni-directional Ground Motion	95
3.6.2 Slab Deflection Due to Bi- and Tri-Directional Ground Motions	97
3.7 DEFINING VERTICAL GROUND MOTION EFFECTS	99
4. EFFECTS OF VERTICAL GROUND MOTION ON PUNCHING FAILURE.....	103
4.1 OVERVIEW	103
4.2 APPLICATION OF ECCENTRIC SHEAR STRESS MODEL.....	104
4.2.1 Using Eccentric Shear Stress Model for Uni-directional Ground Motion.....	105
4.2.2 Using Eccentric Shear Stress Model for Bi-directional Ground Motion.....	107
4.2.3 Using Eccentric Shear Stress Model for Tri-directional Ground Motion.....	108

4.3 APPLICATION OF DRIFT LIMIT APPROACH.....	110
4.3.1 Using Drift Capacity for Uni-directional Ground Motion.....	111
4.3.2 Using Drift Capacity for Bi-directional Ground Motion	113
4.3.3 Using Drift Capacity for Tri-directional Ground Motion	115
4.4 USING TWO-WAY SHEAR STRENGTH DEFINED BY ACI.....	117
4.5 USING PUNCHING RESISTANCE MODEL SUGGESTED BY MUTTONI (2008)	119
4.5.1 Using Slab Rotation Capacity for Uni-directional Ground Motion.....	120
4.5.2 Using Slab Rotation Capacity for Bi-directional Ground Motion	123
4.5.3 Using Slab Rotation Capacity for Tri-directional Ground Motion	124
4.6 SUMMARY OF PUNCHING FAILURE RISK USING DIFFERENT CRITERIA.....	125
5. EFFECTS OF SOIL-STRUCTURE INTERACTION	128
5.1 INTRODUCTION.....	128
5.2 FOOTING DESIGN OF PROTOTYPE BUILDING	128
5.3 MODELING SOIL-STRUCTURE INTERACTION	130
5.3.1 Overall Modeling Considerations	130
5.3.2 Modeling Spring Stiffness for SSI.....	133
5.4 SOIL-STRUCTURE INTERACTION RESULTS.....	137
5.4.1 Lateral Displacement Response Considering SSI.....	138
5.4.2 Dynamic Response of Slab Rotation considering SSI.....	140
5.4.1 Dynamic Response of Axial Force in Interior Columns Considering SSI	143
6. SUMMARY AND CONCLUSIONS	146
6.1 RESEARCH SUMMARY	146
6.2 CONCLUSIONS	147
6.3 RECOMMENDATIONS FOR FUTURE WORK	149
REFERENCES	151
CURRICULUM VITAE.....	163

LIST OF TABLES

Table 1-1 Vertical Coefficient C_v Values	19
Table 1-2 Column axial forces due to vertical motion (Koukleri 1992)	23
Table 2-1 Seismic Design Parameters	33
Table 2-2 Beam and Column Sections	37
Table 2-3 Comparison of IBC and USGS Site Classification	53
Table 2-4 Properties of Selected Ground Motion Records	53
Table 2-5 Scaled spectral accelerations for 1994 Northridge earthquake	62
Table 2-6 Scale Factors for Selected Ground motions	63
Table 3-1 Maximum displacement per seismic record	75
Table 3-2 Maximum Slab Rotation per Seismic Record	82
Table 3-3 Arrival time of peak rotation, vertical PGA and peak lateral drift for tri-axial loading	89
Table 3-4 Maximum compressive axial force per seismic record	92
Table 3-5 Maximum center slab deflection per seismic record	97
Table 3-6 Scale Factor (q) for S_{DS}	100
Table 4-1 Maximum normalized shear stress per seismic record for eccentric shear stress	110
Table 4-2 Maximum normalized lateral drift per seismic record	113
Table 4-3 Maximum normalized shear stress per seismic record	118
Table 4-4 Maximum normalized slab rotation angle per seismic record	122
Table 5-1 Soil properties used to design column footings	129
Table 5-2 Spread footing sections of prototype building	129
Table 5-3 Soil spring stiffness for translational directions	135
Table 5-4 Maximum displacement response due to tri-directional ground motion with and without considering soil-structure interaction	139
Table 5-5 Maximum Rotation per Seismic Record	142
Table 5-6 Maximum compressive axial force per seismic record	143

LIST OF FIGURES

Figure 1-1	Classification of flat slab construction (Park and Gamble, 2000).....	1
Figure 1-2	Flat-plate apartment building with shear walls as lateral load-resisting system (Delray Engineering Inc., 2015).....	2
Figure 1-3	Punching failure and typically used slab shear reinforcement.(Park and Gamble, 2000).....	3
Figure 1-4	Load-center deflection response of slab-column connections under concentric gravity loading (Eltner and Hognestad, 1956).....	4
Figure 1-5	Deflection of slab-column connection (Guandalini et al., 2009)	5
Figure 1-6	Comparison between a punching failure criterion and the results of 99 tests (Muttoni, 2008).....	7
Figure 1-7	Typical test setup for slab-column connection under cyclic lateral loading (Tian et al. 2008).....	8
Figure 1-8	Lateral load-displacement response envelope (Pan and Moehle, 1992)	9
Figure 1-9	Effect of gravity load on lateral drift capacity (Pan and Moehle, 1992).....	10
Figure 1-10	Effect of gravity shear on lateral drift capacity (Robertson and Johnson, 2006).....	11
Figure 1-11	Experimental results (Tian et al., 2008): (a) Vertical load-deflection response under gravity loading, (b) lateral load-drift response envelope	12
Figure 1-12	Horizontal and vertical ground motion accelerations recorded in the 1994 Northridge earthquake	15
Figure 1-13	Distance from source verse V/H ratio: (a) data collected by Elnashai and Collier (2001), (b) V/H-ratio as a function of source distance and magnitude proposed by Elnashai and Papazoglou (1997)	16
Figure 1-14	Comparison of arrival times of peak vertical and peak horizontal ground accelerations: (a) 1994 Northridge earthquake, (b) 1992 Erzincan (Turkey) earthquake	17
Figure 1-15	Distance of source verse PGA time interval (Elnashai and Collier, 2001).....	18
Figure 1-16	Design spectra for horizontal and vertical seismic loading	20
Figure 1-17	Punching shear failure at Bullocks store (photograph courtesy of Earthquake Engineering Research Institute)	25
Figure 1-18	Collapse due to punching failure in a 4 story, flat-plate parking garage during the 2011 Christchurch earthquake (Kam, 2011; Swanson, 2011).....	26
Figure 2-1	Prototype building layout	32
Figure 2-2	Slab reinforcing of prototype building	35
Figure 2-3	Reinforcement design results for perimeter moment frames	36
Figure 2-4	Arrangement of different types of elements.....	38
Figure 2-5	Typical beam and column cross section.....	39
Figure 2-6	Constitutive model of concrete: (a) uniaxial stress-strain relationship, (b) hysteretic stress-strain relationship	41
Figure 2-7	Constitutive model for reinforcing steel.....	42
Figure 2-8	Grid beam model (Tian et al. 2012)	43
Figure 2-9	Nonlinear flexure model for grid beam	45
Figure 2-10	Nonlinear model for torsion in grid beams	47
Figure 2-11	Hysteretic model for primary bending and torsion in grid beams.....	48

Figure 2-12 Calibration of parameters in hysteretic model from a cyclic loading test: (a) simulation result, (b) experimental result.....	50
Figure 2-13 Slab vertical deflection verses lateral drift.....	51
Figure 2-14 Ground motion accelerations: 1999 Chi-Chi, Taiwan.....	54
Figure 2-15 Ground motion accelerations: 1999 Duzce, Turkey.....	54
Figure 2-16 Ground motion accelerations: 1992 Erzincan, Turkey.....	55
Figure 2-17 Ground motion accelerations: 1979 Imperial Valley, California.....	55
Figure 2-18 Ground motion accelerations: 1989 Loma Prieta, California.....	56
Figure 2-19 Ground motion accelerations: 1994 Northridge, California.....	56
Figure 2-20 Ground motion accelerations: 1966 Parkfield, California.....	57
Figure 2-21 Ground motion accelerations: 1981 Westmorland, California.....	57
Figure 2-22 Comparison of response spectra obtained in this study and by PEER for 1994 Northridge earthquake.....	59
Figure 2-23 Response spectra for scaled motion record using SRSS method.....	60
Figure 2-24 Geomean for each scaled seismic records.....	61
Figure 2-25 Average SRSS and geomean for scaled seismic records.....	61
Figure 2-26 Vertical design spectrum verse scaled vertical response spectrum.....	64
Figure 2-27 Scaled ground motion accelerations: 1999 Chi-Chi, Taiwan.....	64
Figure 2-28 Scaled ground motion accelerations: 1999 Duzce, Turkey.....	65
Figure 2-29 Scaled ground motion accelerations: 1992 Erzincan, Turkey.....	65
Figure 2-30 Scaled ground motion accelerations: 1979 Imperial Valley, California.....	66
Figure 2-31 Scaled ground motion accelerations: 1989 Loma Prieta, California.....	66
Figure 2-32 Scaled ground motion accelerations: 1994 Northridge, California.....	67
Figure 2-33 Scaled ground motion accelerations: 1966 Parkfield, California.....	67
Figure 2-34 Scaled ground motion accelerations: 1981 Westmorland, California.....	68
Figure 3-1 Reference diagram for prototype building.....	71
Figure 3-2 Node layout at slab-column connections.....	71
Figure 3-3 Lateral load vs. lateral displacement response obtained from pushover analyses of the prototype structure.....	72
Figure 3-4 Time-history of lateral displacement due to scaled ground motions applied only in x-direction.....	74
Figure 3-5 Time-history of lateral displacement due to scaled ground motions applied only in y-direction.....	75
Figure 3-6 Time-history of lateral displacement due to scaled ground motions applied in both x- and y-directions.....	76
Figure 3-7 Time-history of lateral displacement due to scaled ground motions applied in all three directions.....	78
Figure 3-8 Slab rotation about y-axis at two nodes neighboring column 5007 due to scaled ground motions applied only in x-direction.....	80
Figure 3-9 Time history of slab rotation about x-axis at two nodes neighboring column 4012 due to scaled ground motions applied only in y-direction.....	81
Figure 3-10 Time history of slab rotation due to scaled ground motions applied in both x- and y-directions.....	84
Figure 3-11 Time history of slab rotation due to scaled ground motions applied all three directions.....	86

Figure 3-12 Effects of V/H-ratio on peak response of slab relative rotation.....	87
Figure 3-13 Effects of vertical spectral acceleration on peak response of slab relative rotation..	88
Figure 3-14 Time-history of column axial force under ground motion applied in x-direction.....	91
Figure 3-15 Time-history of column axial force under ground motion applied in y-direction.....	91
Figure 3-16 Time-history of column axial force under ground motions applied in both x- and y- directions	93
Figure 3-17 Time-history of column axial force under ground motions applied in all three directions	94
Figure 3-18 Slab deflection due to ground motion applied only in x-direction.....	96
Figure 3-19 Slab deflection due to ground motion applied only in y-direction.....	96
Figure 3-20 Slab deflection due to ground motions applied in both x- and y-directions	98
Figure 3-21 Slab deflection due to ground motions applied in all three directions.....	98
Figure 3-22 Effects of different vertical ground motion properties on q -factor for S_{DS}	102
Figure 4-1 Eccentric shear stress model.....	104
Figure 4-2 Normalized eccentric shear stress due to ground motion applied in x-direction	106
Figure 4-3 Normalized eccentric shear stress due to ground motion applied in y-direction	107
Figure 4-4 Normalized eccentric shear stress due to bi-directional ground motion	108
Figure 4-5 Normalized eccentric shear stress due to tri-directional ground motion.....	109
Figure 4-6 Normalize lateral drift due to ground motion applied in x-direction	111
Figure 4-7 Normalized lateral drift due to ground motion applied in y-direction	112
Figure 4-8 Normalized lateral drift in x-direction due to bi-directional ground motion.....	114
Figure 4-9 Normalized lateral drift in y-direction due to bi-directional ground motion.....	115
Figure 4-10 Normalized lateral drift in x-direction due to tri-directional ground motion.....	116
Figure 4-11 Normalized lateral drift in y-direction due to tri-directional ground motion.....	117
Figure 4-12 Normalized shear stress due to bi-directional ground motion	119
Figure 4-13 Normalized shear stress due to tri-directional ground motion.....	119
Figure 4-14 Normalized slab rotation due to ground motion applied in x-direction.....	121
Figure 4-15 Normalized slab rotation due to ground motion applied in y-direction.....	122
Figure 4-16 Normalized slab rotation due to 2-directional ground motion.....	123
Figure 4-17 Normalized slab rotation due to 3-directional ground motion.....	125
Figure 4-18 Summary of results of punching failure prediction.....	126
Figure 5-1 SSI modeling	130
Figure 5-2 Translation and rotational springs for soil-interaction	131
Figure 5-3 Frequency factor for translational spring stiffness	132
Figure 5-4 Foundational footing dimensions	132
Figure 5-5 Soil spring model at end of column.....	136
Figure 5-6 OpenSees elastic material definition	137
Figure 5-7 Lateral displacement due to ground motions applied tri-directionally for SSI	139
Figure 5-8 Slab rotation about the x- and y-axes for tri-directional ground motion with SSI..	141
Figure 5-9 Column axial force due to tri-directional ground motion with SSI.....	144

CHAPTER 1

INTRODUCTION

1.1 INTRODUCTION TO REINFORCED CONCRETE FLAT-PLATE STRUCTURES

One of the most common structural elements is reinforced concrete (RC) floor slabs. Concrete floor slab systems have taken many forms since their introduction, but one of the most economical is a beamless floor system supported directly by columns, generically referred to as flat slab or flat plate. There are three types of flat slabs used for RC buildings: flat slab with drop panels (Figure 1-1a), flat slab with both drop panels and column capitals (Figure 1-1b), and flat slab of uniform thickness (Figure 1-1c), more commonly referred to as flat plate. Flat-plate construction is frequently used in residential and office buildings where gravity loads are low and relatively short spans are utilized. Regions with high seismicity require the flat-plate system to be designed as a gravity load-carrying system while lateral loads are resisted by conjunctionally used shear walls (Figure 1-2) or perimeter moment frames (Park and Gamble, 2000).

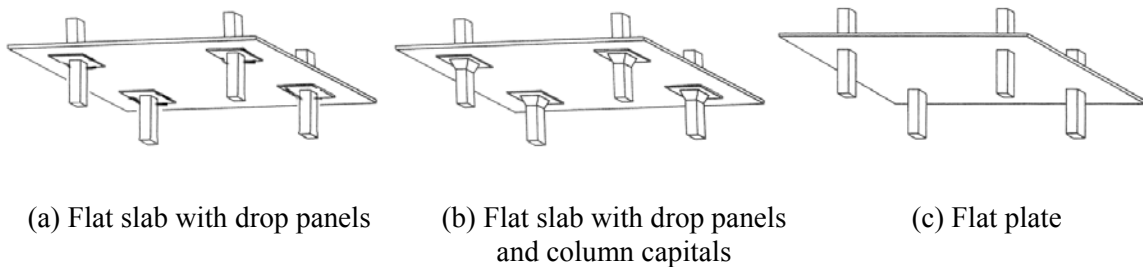


Figure 1-1 Classification of flat slab construction (Park and Gamble, 2000)

Without the use of beams, a flat plate inherently has low vertical stiffness; consequently, the clear span for a flat plate building is generally limited to 20 feet, roughly corresponding to a span-to-depth ratio of 30. Post-tensioning can be used to increase this ratio to approximately 45

(Xia, 2008). The slab thickness of flat plates is generally controlled by design code provisions regarding two-way shear resistance or deflection serviceability. Commonly a reinforcement ratio less than 1.0% is used for slab resisting negative bending moment at a slab-column connection (Sherif and Dilger, 1996). Slab bottom reinforcement, resisting positive moment, is often governed by the minimum reinforcement requirements with an even lower reinforcement ratio.



Figure 1-2 Flat-plate apartment building with shear walls as lateral load-resisting system (Delray Engineering Inc., 2015)

The failure of flat plates is most generally controlled by punching failure of slab at columns. Punching shear, as shown in Figure 1-3a, is defined as an event where the highly concentrated slab bending moment and shear localized at a column creates a shear failure cone that breaks through the slab. Punching shear can be brittle and, although it is local failure, the surrounding connections will need to carry additional gravity loads initially held by the failed slab-column connection. If the surrounding connections are unable to bear the redistributed loads, a chain reaction of punching failure over the entire floor will be triggered, resulting in a large-scale or even complete collapse of the building. A solution to avoiding punching failure is through the use of shear reinforcement such as shear studs (Figure 1-3b). Shear studs can be used in a flat-plate structure under the following situations: (1) a large unbalanced moment caused by

pattern or lateral loads needs to be transferred by slab-column connections; (2) the slab carries heavy gravity loads; or (3) the span length is relatively large. However, for slabs that have low reinforcement ratios as is common in a flat plate, flexural capacity can govern the design even with large amounts of shear reinforcement (Lips et al., 2012).

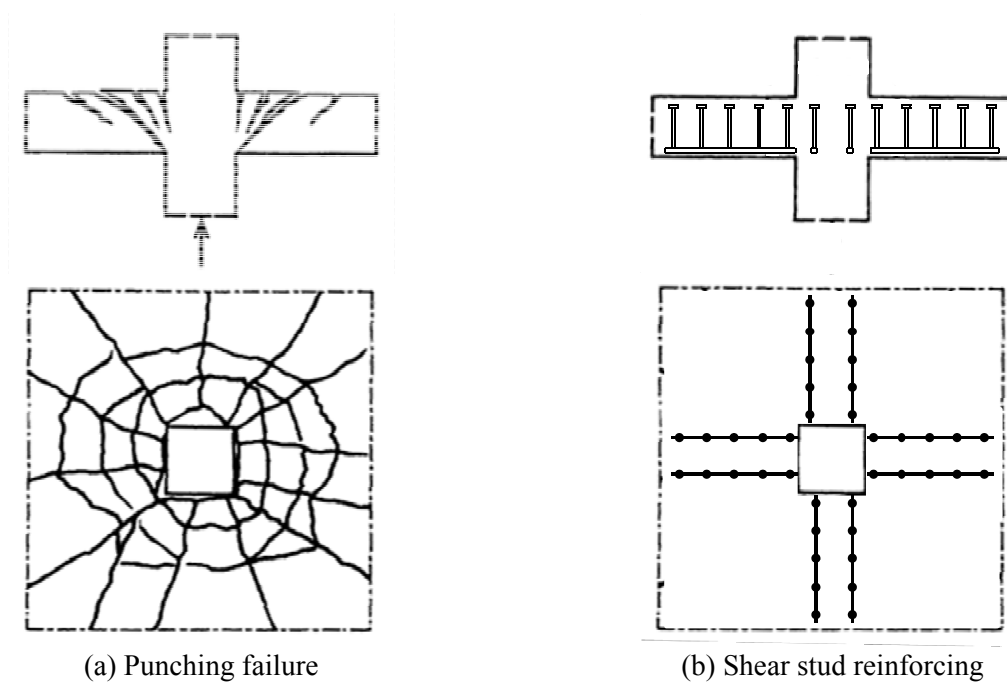


Figure 1-3 Punching failure and typically used slab shear reinforcement.(Park and Gamble, 2000)

1.2 BEHAVIOR OF SLAB-COLUMN CONNECTIONS

1.2.1 Behavior of Slab-Column Connections under Gravity Loading

Numerous experimental studies have been conducted to investigate the shearing capacity of flat plates. The tests generally involved isolated slab-column connections with a square slab and centrally located column stub. The edges of the slab approximately represented the location of inflection points in a slab subjected to concentric gravity loading. Vertical loading was applied

at either the center column or slab edges to introduce both bending moment and shear into the slab. The following outlines the relevant studies.

A classic series of tests were conducted on 39 isolated slab-column connections by Elstner and Hognestad (1956). These tests examined the effects of concrete strength, slab tensile reinforcement ratio, column size, loading approach (concentric vs. eccentric), and supporting conditions on punching resistance. Concentric gravity loading was applied to a group of specimens with varying tensile reinforcement ratios. The recorded load-deformation response organized by slab tensile reinforcement ratio is shown in Figure 1-4, where specimen B-14 had the highest reinforcement ratio of $\rho = 3.0\%$ and specimens B-2 and B-1 had the lowest tensile reinforcement ratio of $\rho = 0.5\%$.

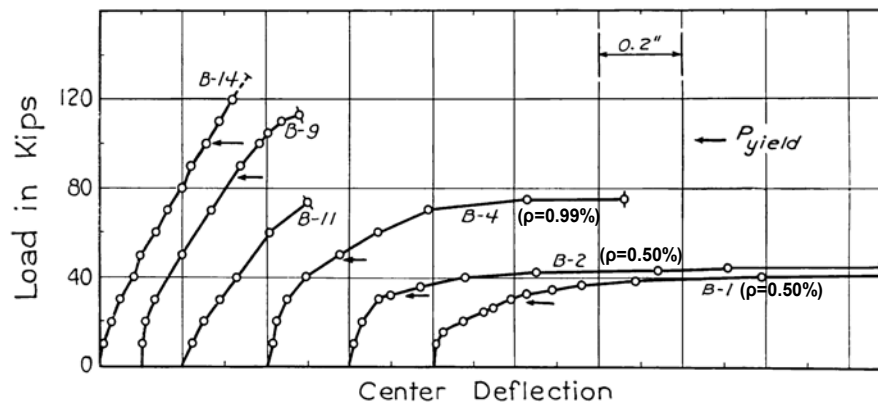


Figure 1-4 Load-center deflection response of slab-column connections under concentric gravity loading (Elstner and Hognestad, 1956)

From Figure 1-4 it is clear that slab tensile reinforcement ratio plays a significant role in the overall behavior of a slab-column connection. Nearly all the specimens experienced yielding of tensile reinforcement near the column as indicated by P_{yield} prior to reaching the ultimate punching failure. In fact, for slabs with low-to-moderate reinforcement ratios ($\rho < 1.0\%$),

punching failure was produced by excessive deformation rather than reaching a critical value of shear. Even though each specimen ultimately failed in punching due to the inclined shear cracking, their failure was defined as a flexural failure and the final punching failure was treated as secondary since the loading capacity of each specimen reached that evaluated from the yield line theory.

Eleven isolated slab-column specimens were tested by Guandalini et al. (2009). The slab tensile reinforcement ratio was less than 1.5% and shear reinforcement was not used. Gravity load effects were simulated by a vertical load applied upward through the center column. The main focus of the research was to investigate the effects of the specimen scale size on punching resistance; however, pertinent information was obtained regarding deformation characteristics of the slab prior to its final punching failure. Deflections were measured at the top and bottom slab surfaces in nine locations as a function of load level (Figure 1-5). The study revealed that for a lightly reinforced flat plate, slab deflection can be attributed primarily to rigid body rotation similar to that of plastic hinges in beams or columns. This rotation is caused by concrete cracking and flexural reinforcement yielding due to highly localized slab deformation near the column.

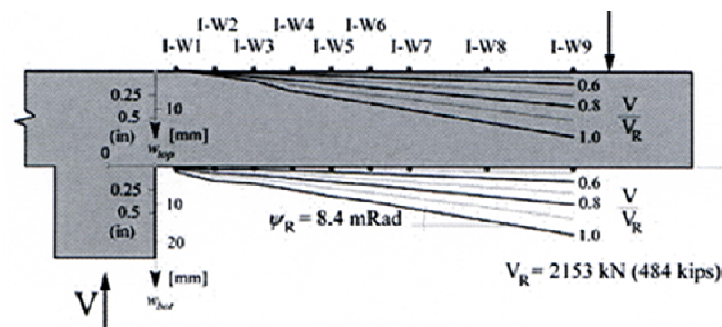


Figure 1-5 Deflection of slab-column connection (Guandalini et al., 2009)

Muttoni (2008) provided a mechanical model defining punching resistance of flat slabs without shear reinforcement based on test observations and a critical shear crack width theory. This theory assumed that a critical shear crack propagates through the slab within the theoretical compression strut that transfers shear forces to the column. Concrete is able to resist a fraction of shear while the critical crack remains narrow and the friction along the crack due to rough concrete surface exists. As the slab rotates and the crack widens, punching shear capacity is further reduced. Therefore, it was assumed that punching strength is a function of the critical shear crack opening in the slab. Using this model, a failure criterion that considered the size effects of slab was derived per Equation 1-1 where ψ is the rotation of slab outside the critical shear crack, d_g is the maximum aggregate size, and d_{g0} is a reference aggregate size equal to 0.63 in. (16 mm).

$$\frac{V_R}{b_o d \sqrt{f'_c}} = \frac{9}{1 + 15 \frac{\psi d}{d_{g0} + d_g}} \quad (psi, in.)$$

$$\frac{V_R}{b_o d \sqrt{f'_c}} = \frac{3/4}{1 + 15 \frac{\psi d}{d_{g0} + d_g}} \quad (N, mm)$$

Equation 1-1

The failure criterion was compared with results from previous slab-column tests with varied parameters such as: reinforcement ratio, column location, slab size, concrete strength, and steel yield strength. In all, 99 tests were analyzed and plotted with the failure criterion given in Equation 1-1, as shown in Figure 1-6, where punching strength and slab rotation were normalized to provide a direct correlation. It should be noted that for slabs where flexural capacity (V_{flex}) was reached before punching failure (V_R) (denoted by empty squares) the ACI 318-05 (2005) formulation for punching shear, which is identical to that in the ACI 318-14 (2014), overestimates the shear capacity of slab-column connections without a high tensile reinforcement ratio. As shown previously, the punching failures of slabs with low tensile

reinforcement ratios, which are commonly found in flat-plate construction, are prominently deformation-controlled and are more likely to reach flexural capacity before the final punching shear. Therefore it is reasonable to assume that punching strength may be overestimated by the ACI code formulations for commonly used flat-plate structures.

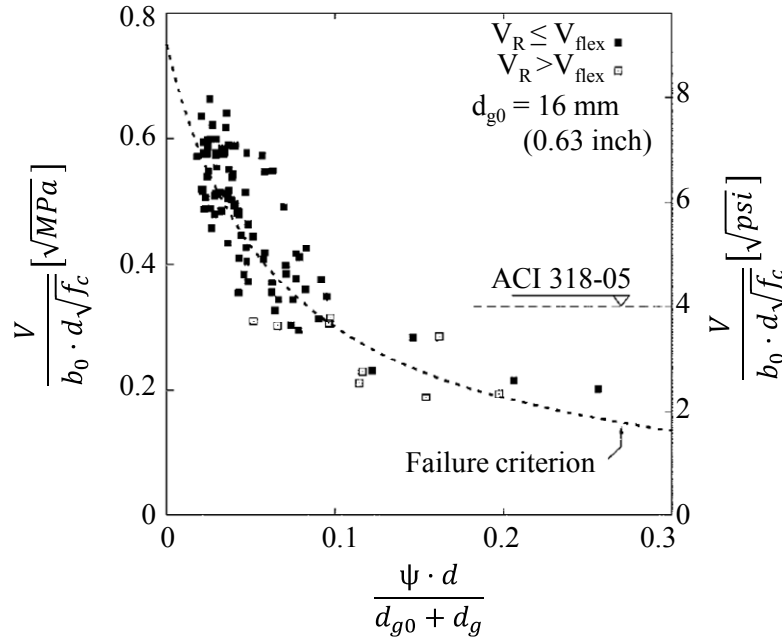


Figure 1-6 Comparison between a punching failure criterion and the results of 99 tests (Muttoni, 2008)

1.2.2 Behavior of Slab-Column Connections under Cyclic Lateral Loading

Flat-plate structures located in regions of high to moderate seismicity usually include shear walls or moment frames as a lateral system to resist seismic loads. However, the flat plate, normally taken as a gravity system, must be able to sustain gravity loading capacity, transfer moments between slab and column, and maintain deformation compatibility with the lateral system by achieving sufficient deformation capacity. The following experimental studies investigated lightly reinforced (1.0% or less), slab-column connections of flat plates. Load combinations in the tests included cyclic lateral and gravity loading using a test set up similar to

that shown in Figure 1-7. A heavily reinforced column was used in each test to reduce the effects of column deformations on the behavior of the connection.

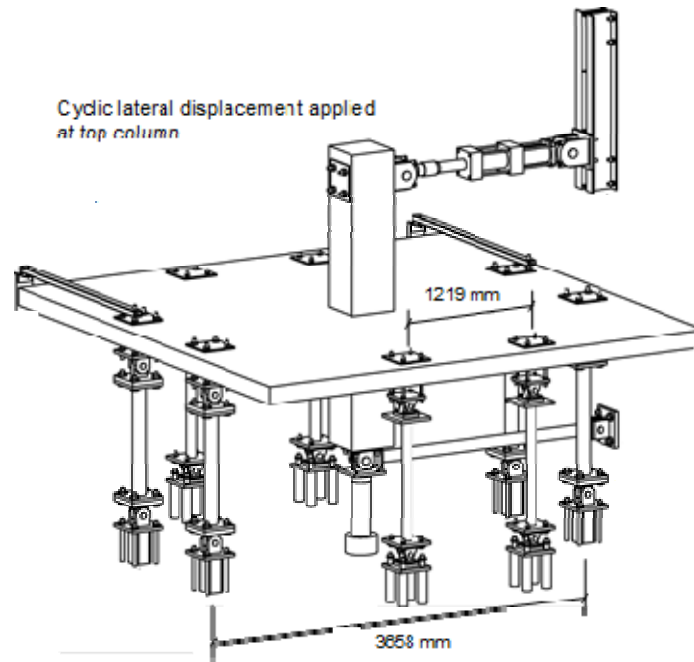


Figure 1-7 Typical test setup for slab-column connection under cyclic lateral loading (Tian et al. 2008)

Four interior slab-column connections modeled after a typically reinforced flat-plate building in a high seismic region were tested by Pan and Moehle (1992). Slabs were nominally identical with continuous bottom reinforcement at the column. The test variables included gravity load level and loading history. The testing consisted of either a “high” gravity loading which caused an average gravity shear at the code-specified critical section of $v_g = 1.4\sqrt{f'_c}$ (psi) or a “low” gravity loading of $v_g = 0.88\sqrt{f'_c}$ (psi) in conjunction with lateral loading applied uniaxially or biaxially. An identical displacement history was used for lateral loading in each direction. All specimens were noted to have failed in punching. Figure 1-8 illustrates lateral load-displacement response envelope for each test specimen. This figure clearly indicates that

ductility, drift capacity and stiffness were significantly higher for slab-column connection subjected to lower gravity loads. Biaxial loading also had a similar effect by reducing strength, ductility, drift capacity, and stiffness. Damage was also found to be much more extensive around the slab-column connections under biaxial loading. These effects were found to be more significant when drifts are above 0.5%. However, Pan and Moehle (1992) pointed out that biaxial loading effect may be dependent upon lateral load pattern and the rate it is applied.

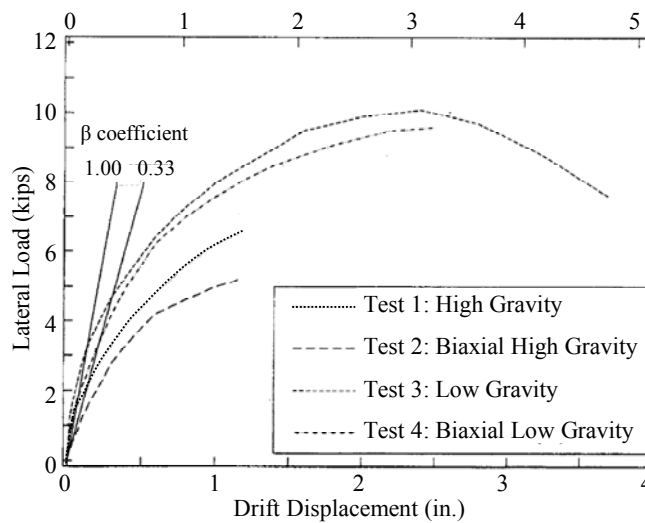


Figure 1-8 Lateral load-displacement response envelope (Pan and Moehle, 1992)

The experimental studies demonstrated that the level of gravity load is one of the most critical factors in determining the lateral deformation capacity of slab-column connection. An increase in gravity loading reduces the available drift capacity. In turn there is less shear capacity to resist moment transfer due to lateral loading. Figure 1-9 demonstrates this trend of decreasing drift capacity with increasing shear. Data from the tests were supplemented with data from other slab-column connection experiments and the gravity shear (V_g) was normalized by the nominal punching resistance (V_0) given in Equation 1-2, where d is slab average effective depth and b_0 is

the perimeter of code-defined shear critical section located at a distance of d away from column faces.

$$V_0 = 4\sqrt{f'_c}b_0d \quad (\text{psi}) \quad \text{Equation 1-2}$$

Figure 1-9 indicates that, if the gravity shear ratio V_g/V_0 is less than 0.4, a drift capacity of at least 1.5% is obtainable for a flat-plate building. However, slab-column connections having higher gravity shear ratios are susceptible to a premature punching shear failure at lower lateral drift ratios.

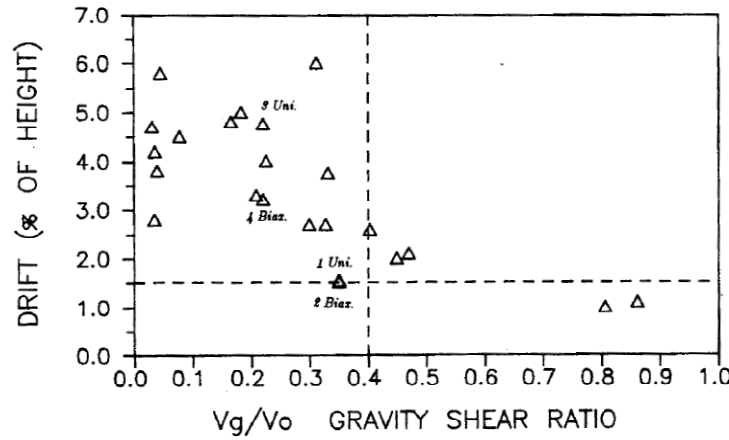


Figure 1-9 Effect of gravity load on lateral drift capacity (Pan and Moehle, 1992)

Robertson and Johnson (2006) further summarized test data obtained from past studies regarding the relationship between lateral drift capacity and gravity shear ratio for slab-column framing, as shown in Figure 1-10. It is obvious that, as gravity shear level increases, the lateral drift capacity consistently decreases. In this figure, the solid line shows the current ACI code provision formulating drift capacity as a function of gravity shear ratio, which often governs the design of a flat-plate building in high seismic regions.

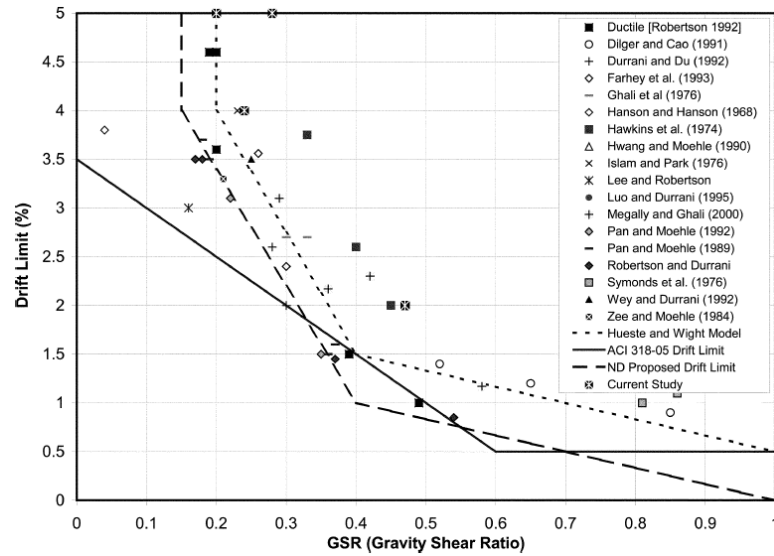
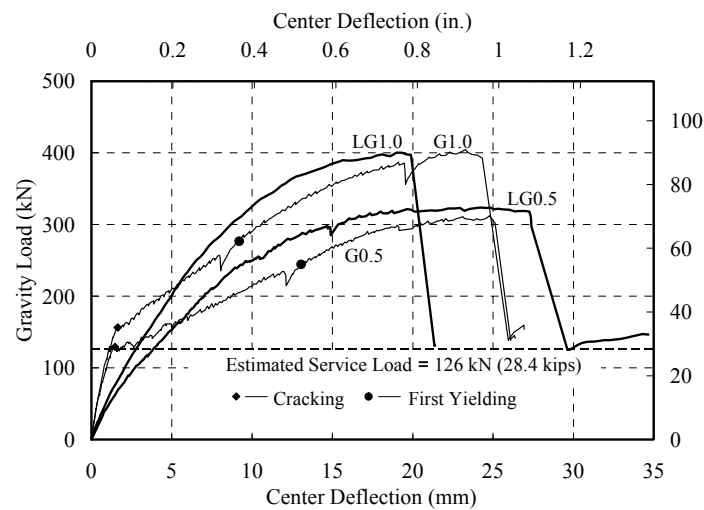


Figure 1-10 Effect of gravity shear on lateral drift capacity (Robertson and Johnson, 2006)

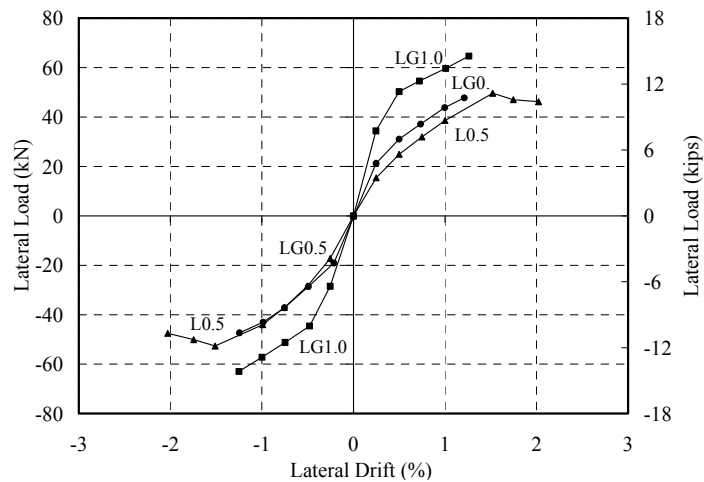
Tian et al. (2008) conducted experiments on five isolated slab-column specimens. The slabs were representative of existing flat-plate systems designed following pre-1980's design codes that did not require continuous bottom reinforcement at the column. Slab top reinforcement ratio of 0.5 and 1.0% were used as well as three loading combinations: (1) gravity loading to failure (G), (2) combined gravity and cyclic lateral loading to failure (L), and (3) combined gravity and cyclic lateral loading to degrade slab-column connection followed by gravity loading to failure (LG). Each test specimen is designated by a letter indicating load combination and a number representing percentage top reinforcement ratio. Under lateral loading specimen L0.5 was tested to punching failure, whereas lateral loading for LG0.5 and LG1.0 was used to introduce earthquake-induced damage without punching failure.

Figure 1-11a shows the vertical load-deflection response in addition to the envelope curve for lateral load-drift response in Figure 1-12b. From the figure it can be seen that all specimens experienced general yielding prior to punching failure even though they were

subjected to different loading histories. Therefore the failure is more accurately described as a deformation-driven shear failure because failure was a result of large flexural deformations rather than critical shear stresses. By comparison of the behaviors of G0.5 to LG0.5 and G1.0 to LG1.0, it can be seen that gravity load-carrying capacity was not reduced by cyclic loading. However, the stiffness of the connection was greatly diminished due to concrete cracking and reinforcement yielding.



(a)



(b)

Figure 1-11 Experimental results (Tian et al., 2008): (a) Vertical load-deflection response under gravity loading, (b) lateral load-drift response envelope

It was found from the tests that the two-way shear strength of the slab-column connections with low tensile reinforcement ratios under concentric gravity loading was overestimated by ACI 318-08 (2008), while the ACI eccentric shear stress model underestimated the lateral strength of the specimens subjected to combined gravity and lateral cyclic loading. Moreover, the lateral deformation capacity of Specimen L0.5 was well predicted by the ACI 318-08 (2008) code provisions regarding lateral drift capacity as a function of gravity shear level.

1.3 PROPERTIES OF VERTICAL GROUND MOTIONS

The effects of horizontal components of a seismic ground motion on structural performance have been studied extensively. Conversely, the influence of the vertical component of a ground motion has been given very little attention due to beliefs that: (1) vertical acceleration is usually significantly lower than horizontal acceleration and (2) a large safety factor is utilized for static vertical loads in properly engineered buildings creating a low probability of failure from vertical seismic forces (Elnashai and Papazoglou, 1997). However, several seismic events, such as the 1994 Northridge and 2011 Christchurch earthquakes, have produced a high level of structural damage. In each event, large vertical accelerations were recorded at near-source stations. Field evidence also suggested that structural damage could be attributed to strong vertical ground motions (Papazoglou and Elnashai, 1996; Bradley and Cubrinovski, 2011). The following outlines the typical characteristics associated with vertical ground motions.

1.3.1 Frequency Content

Seismic ground motion consists of two types of body waves known as P-waves and S-waves. Vertical ground motion is associated with vertical propagating P-waves in the epicentral

region while S-waves are the main cause of horizontal ground motion. P-waves travel faster than S-waves with shorter wavelength. Consequently, the shortened wavelength of P-waves translates into a higher frequency recorded by the vertical ground motion. This is additionally demonstrated by elastic theory of wave propagation which indicates that the P-wave velocity will always be higher than that of an S-wave for earth materials (Elnashai and Papazoglou, 1997). As an example, Figure 1-12 graphs the horizontal and vertical ground motion accelerations recorded during the 1994 Northridge earthquake. The figure demonstrates the high frequency associated with vertical ground motion. The frequency of the vertical component is much larger than that of the horizontal component. For a RC frame structure, the rate of vertical movement may cause premature failure as the axial forces in the columns fluctuate between compression and tension. Papazoglou and Elnashai (1996) noted from numerical simulations the reduced moment capacity and rotational ductility in RC columns experiencing vertical seismic motions. Of other significance is that the high frequency of vertical ground motion could cause the floor slabs to oscillate compounding upon gravitational forces and possibly causing early collapse of the structure.

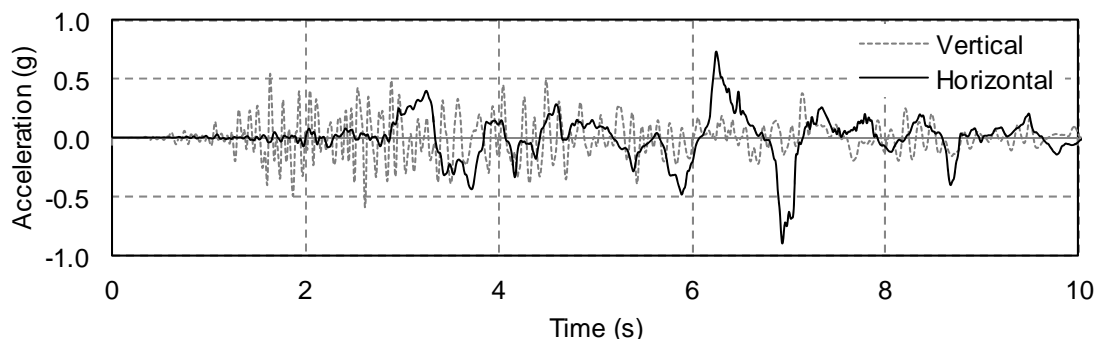


Figure 1-12 Horizontal and vertical ground motion accelerations recorded in the 1994 Northridge earthquake

1.3.2 Ratio of Peak Vertical Acceleration to Peak Horizontal Acceleration

One significant parameter of a vertical ground motion is its peak acceleration. It has been historically assumed vertical-to-horizontal peak ground acceleration (V/H) ratio as $2/3$ to uniformly scale the horizontal acceleration spectrum for the vertical component of ground motion. This method was originally proposed by Newmark et al. (1973). The procedure implies that all components of motion have the same frequency content. However, the frequency content is demonstratively different as shown in the previous section. Furthermore, the $2/3$ rule can largely underestimate the effects of vertical ground motion on a near-source structure. The opposite is true for a structure at a large epicentral distance. This trend has long been the case. Even the earliest records of near-source seismic events have recorded a V/H-ratio greater than $2/3$, but these data were often excluded and considered outliers. An example is the Long Beach earthquake of 1933. The earthquake was recorded approximately 4 miles from the source and had a V/H-ratio exceeding 1.0 (Elnashai and Papazoglou, 1997).

Since P-waves degrade quicker than S-waves, the magnitude of a vertical ground motion is affected by source distance. Figure 1-13(a) correlates V/H-ratio to source distance based on an investigation completed by Collier and Elnashai (2001). The study analyzed the records obtained at various source distances during the 1979 Imperial Valley earthquake and the 1984 Morgan Hill earthquake having a magnitude of 6.5 and 6.3, respectively. It is seen from the figure that the average V/H-ratio is larger than 1 at near-source distances but diminishes with greater distance. Furthermore, higher magnitudes of an earthquake cause a larger V/H-ratio for near-source events. Elnashai and Papazoglou (1997) proposed V/H ratio as a function of both source distance and magnitude, as shown in Figure 1-13(b). The formulation was suggested based on the data collected from the Imperial College data bank for near-field earthquakes with a

magnitude greater than 5.0 as well as the data from Borzognia and Niazi (1993). Both Figures 1-13(a) and 1-13(b) confirm V/H ratios can be greater than 2/3 for a seismic event that occurs near-source.

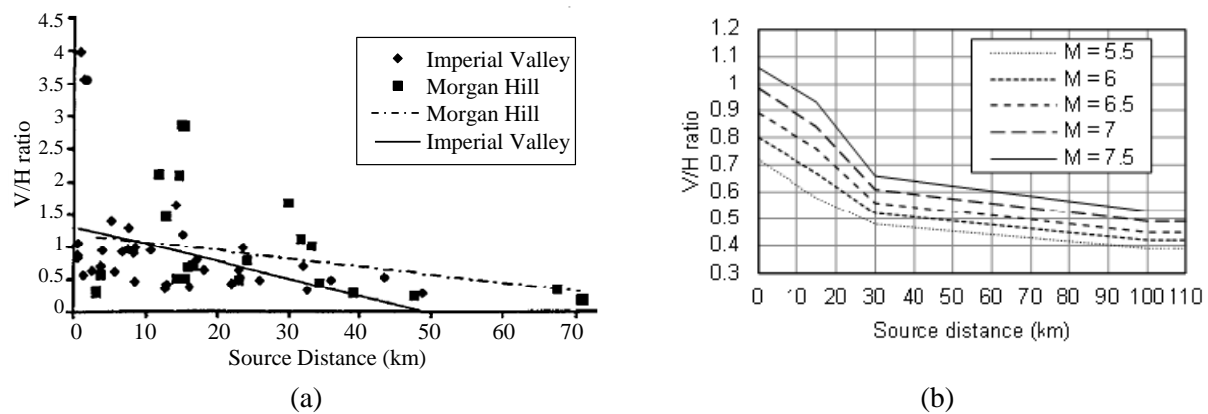


Figure 1-13 Distance from source verse V/H ratio: (a) data collected by Collier and Elnashai (2001), (b) V/H-ratio as a function of source distance and magnitude proposed by Elnashai and Papazoglou (1997)

1.3.3 Time Interval of Vertical and Horizontal Peak Ground Accelerations

The time interval between the arrival of the peak horizontal acceleration and that of the peak vertical acceleration can significantly affect a structure. Available seismic records indicate two possibilities. First, vertical peak ground acceleration (PGA) is achieved well before horizontal PGA, as shown in Figure 1-14(a) for the 1994 Northridge earthquake. Second, the vertical PGA may occur almost coincidentally with the horizontal PGA, as shown in Figure 1-14(b) for the 1992 Erzincan (Turkey) earthquake.

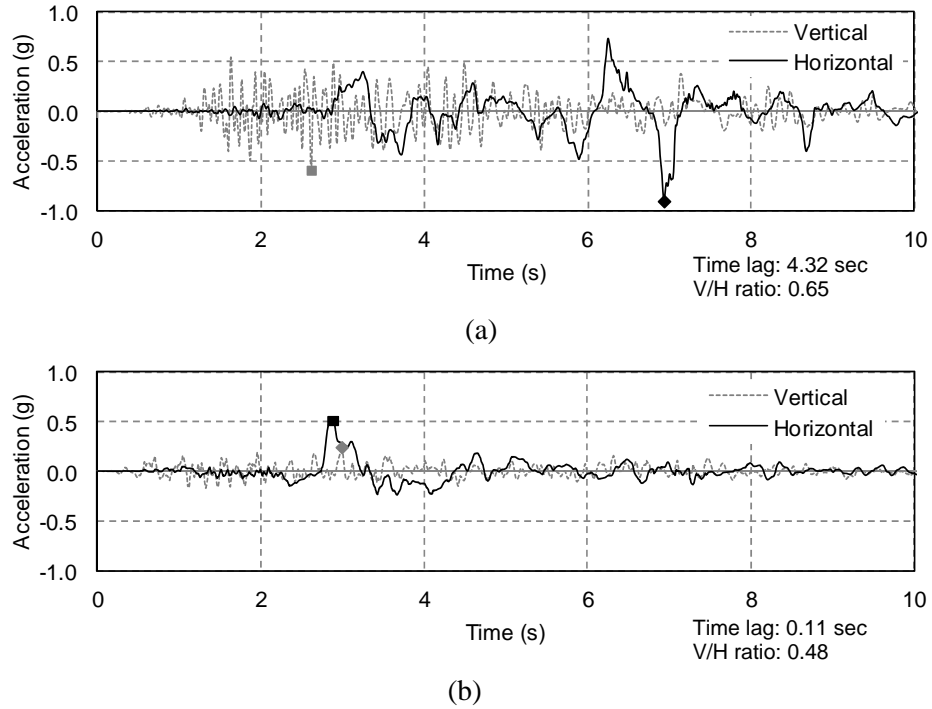


Figure 1-14 Comparison of arrival times of peak vertical and peak horizontal ground accelerations: (a) 1994 Northridge earthquake, (b) 1992 Erzincan (Turkey) earthquake

In the case where the vertical PGA occurs earlier, significant damage may be incurred on a structure before the arrival of horizontal motion, which may have considerable effects on the structure's overall response and ability to withstand additional loading. In the event that the vertical and horizontal peaks arrive simultaneously the structure would experience high levels of distress. Collier and Elnashai (2001) investigated 32 seismic records with a PGA greater than 0.10 g obtained at various source distances (Figure 1-15). It was determined that the time interval increased with distance from the source, but sources less than 5 kilometers should be considered to have identical arrival time.

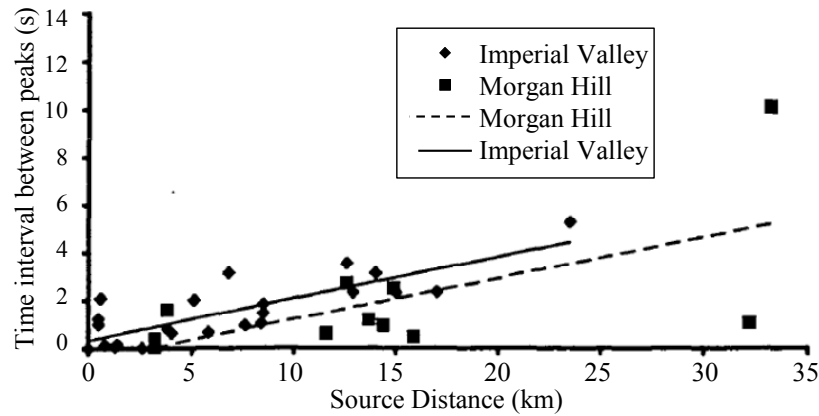


Figure 1-15 Distance of source verse PGA time interval (Collier and Elnashai, 2001)

1.4 DESIGN CODE REQUIREMENTS FOR VERTICAL GROUND MOTION

Historically earthquake codes accounted for the effects of vertical motion by deriving the vertical spectrum from the horizontal spectrum. As discussed previously, a V/H-ratio of 2/3 proposed by Newmark et al. (1973) was used uniformly for all applications. This ratio was found to either underestimate or overestimate expected vertical ground motions, depending on the distance from the fault, natural period of the structure, or local site conditions. The current ASCE/SEI 7-10 standard (2010) defines vertical loading effects by the use of a constant fraction of the design spectral acceleration at short periods (S_{DS}) for horizontal seismic loading. The load accounting for vertical ground motion (E_v) is determined by Equation 1-3 where D is the design dead load.

$$E_v = 0.2S_{DS}D \quad \text{Equation 1-3}$$

Special circumstances allow E_v to be taken as zero. This includes when S_{DS} is less than or equal to 0.125g or the demand on the soil-structure interface of foundations can be determined.

In 2009 the National Earthquake Hazards Reduction Program (NEHRP) made further recommendations to determine a vertical design response spectrum (S_{av}). The provision has been adopted by ASCE/SEI 7-10 (2010) for cases where a more explicit consideration of vertical

ground motion effects is advised. This includes some types of tanks, material storage facilities, and electric power generation facilities. The spectrum is divided into four regions outlined in Equation 1-4, where T_v is the vertical vibration period (in seconds) of the structure and is dependent upon S_{DS} and a vertical coefficient C_v . C_v is determined by site class and mapped design spectral acceleration at short periods for 5% damping ratio (S_s) given in Table 2-1.

$$S_{av} = \begin{cases} 0.3C_vS_{DS} & 0 \leq T_v \leq 0.025 \\ 20C_vS_{DS}(T_v - 0.025) + 0.3C_vS_{DS} & 0.025 < T_v \leq 0.05 \\ 0.8C_vS_{DS} & 0.05 < T_v \leq 0.15 \\ 0.8C_vS_{DS} \left(\frac{0.15}{T_v} \right)^{0.75} & 0.15 < T_v \leq 2.0 \end{cases} \quad \text{Equation 1-4}$$

Table 1-1 Vertical Coefficient C_v Values

MCE _R spectral response parameter at short periods ^a	Site Class A, B	Site Class C	Site Class D, E, F
$S_s \geq 2.0$	0.9	1.3	1.5
$S_s = 1.0$	0.9	1.1	1.3
$S_s = 0.6$	0.9	1.0	1.1
$S_s = 0.3$	0.8	0.8	0.9
$S_s \leq 0.2$	0.7	0.7	0.7
^a Use straight-line interpolation for intermediate values of S_s			

Figure 1-16 graphs the horizontal design spectrum specified by ASCE/SEI 7-10 (2010), the vertical response spectrum assuming a V/H-ratio of 2/3, and ASCE/SEI 7-10 (2010) vertical response spectrum for site class D. It is seen from this figure that, for the ASCE/SEI 7-10 vertical design spectrum, short periods are shown to have a V/H ratio greater than 1.0 while mid-to-long periods have a V/H-ratio less than or equal to the 2/3 ratio. This is consistent with the observations discussed previously.

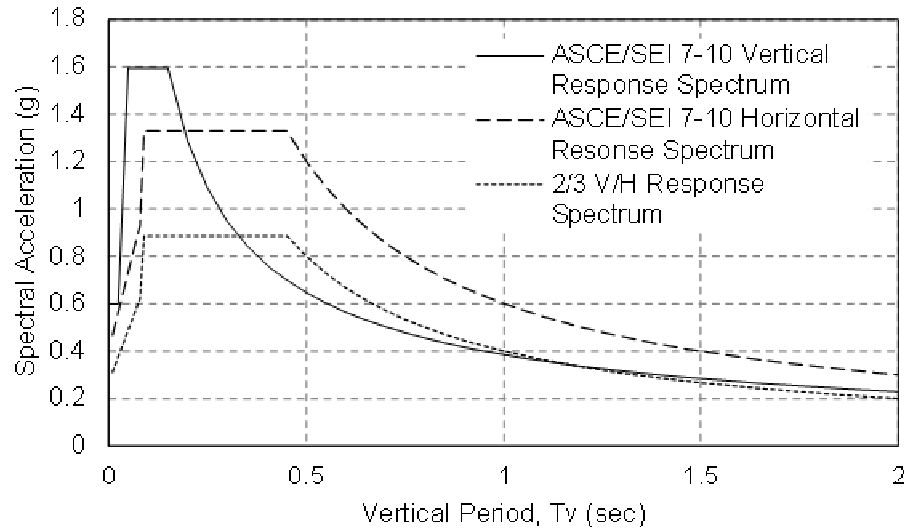


Figure 1-16 Design spectra for horizontal and vertical seismic loading

1.5 PREVIOUS STUDIES ON REINFORCED CONCRETE STRUCTURES

The field evidence of the potentially damaging effect of vertical ground motion has become more available in recent years as investigations in near-source seismic events are conducted. Several analytical studies have been published concerning the effect of vertical ground motion on RC bridges and buildings. In this section, several of these studies are briefly reviewed.

1.5.1 Vertical Ground Motion Effects on Bridges

Saadeghaziri and Foutch (1991) conducted a 3-D finite element analysis on 6 hypothetical RC bridges using a grid model. Each bridge consisted of 2 spans with either a single or double-column bent at the center. Each bridge was subjected to two nonlinear time history analyses, horizontal motion only and vertical combined with horizontal motion. The study concluded that the addition of vertical motion aggravated sustained damage and had the potential to cause failure. Furthermore, axial forces were quite varied within the column causing unstable hysteresis loops that resulted in larger horizontal displacements and fluctuation in the shear

capacity of the column. When horizontal motion alone was considered, columns remained mostly elastic, but the addition of vertical motion created greater inelastic behavior, which in turn caused greater damage and higher possibility of shear failure. The study also found that the additional damage was minimal for seismic events with an effective peak acceleration of 0.4g or lower while considerably more damage occurred with an effective peak acceleration of 0.7g or higher.

In a parametric study conducted by Button et al. (2002), 6 bridges with varying geometry and material type representative of typical highway bridges were analyzed. Varying magnitudes, soil type, and fault distances were used to perform response spectrum analysis on each bridge for all ground motion parameters. Response results including and excluding vertical ground motion were compared. Additionally, 3 bridges were analyzed using linear time-history analysis and 1 bridge was used to conduct a nonlinear analysis. The study concluded that the 2/3 rule for determining vertical spectral acceleration should be discontinued as V/H-ratios were significantly higher or lower depending upon the natural period of a bridge. It was also found that vertical ground motion affected axial forces within columns considerably, especially when fault distances were less than 10 to 20 km. However, the vertical motions had little influence on values of horizontal response quantities. Finally, it was concluded that beyond a distance of 60 km from a fault, vertical ground motion could be safely ignored.

Kunnath et al. (2008) analyzed 6 different structural configurations of a 2-span highway bridge with double-column bent subjected to combined vertical and horizontal loading. The study found that vertical ground motion did not influence the horizontal displacements of the bridge deck. However, the axial force demand in the columns was significantly influenced by vertical ground motion. Furthermore, positive and negative moment demand at the face of the

bent cap and the mid-span of the girder were considerably impacted by vertical motion. In some cases the girder moment due to vertical motion caused demand to exceed the capacity and subsequently cause failure.

1.5.2 Vertical Ground Motion Effects on Buildings

A large variation in compressive or tensile load in the column can diminish the capacity of concrete columns resisting flexure or shear thereby causing premature failure (Paulay and Priestley, 1992). The study by Papazoglou and Elnashai (1996) indicated that vertical ground motion can accentuate axial forces in RC columns for both compression and tension. Tension forces usually occur in upper stories of multi-story buildings.

Koukleri (1992) conducted a nonlinear dynamic analysis of an 8-story, 3-bay RC moment-resisting frame. The frame was designed according to the Uniform Building Code (UBC) (1991) and subjected to Imperial Valley Centro-6 ground motion. The result of the inclusion of vertical ground motion is summarized in Table 2-2. As shown in this table, tensile forces were recorded at each level with ground level and mid-stories experiencing the largest effects from the vertical ground accelerations. The tensile forces in interior columns were slightly higher than those in exterior columns. Given that horizontal loading alone did not cause any tensile force in the columns, the tensile force must be the result of vertical motions. Compressive forces were shown to increase with the addition of vertical loading and were more significant in the upper story where compressive force was increase by as much as 64%, as shown in Table 2-2. Compressive forces in interior column due to vertical ground motion were much higher than those in exterior columns. Amplified compressive forces can reduce rotational ductility of a column (Koukleri, 1992).

Table 1-2 Column axial forces due to vertical motion (Koukleri 1992)

Column Story and Location	Tensile Force (kN) H+V	Tensile Displ. (mm) H+V	Compressive Force (kN) H	Compressive Force (kN) H+V	Contribution of vertical motion to total compressive force (%)
1 st - exterior	475	1.90	1500	1750	14
4 th - exterior	350	1.30	750	1250	40
8 th - exterior	150	0.60	125	350	64
1 st - interior	500	1.95	1450	2500	42
4 th - interior	750	3.75	800	2525	68
8 th - interior	210	0.70	215	1200	82

An analytical study was conducted by Mwafy and Elnashai (2006) on mid-rise RC buildings utilizing 3 structural systems: 8-story irregular frame, 12-story regular frame, and 8-story frame-wall dual system. RC buildings were designed for a combination of two ductility classes (High & Medium and Medium & Low) and two peak ground accelerations (0.15g and 0.30g) leading to four investigated cases within each structural system. Each structure was analyzed under actual ground motions with medium to high V/H-ratios. It was concluded for the numerical simulations that vertical ground motion had a significant effect at both the member and system level. The V/H-ratio, however, did not cause the anticipated effect of vertical ground motion. Instead, it was more dependent upon ground motion characteristics, horizontal and vertical periods of the structure, and earthquake intensity. Vertical motion had a larger effect when horizontal motion was relatively small, as was the case for columns in low-rise buildings and interior columns at higher stories of tall structures. It was also pointed out that top displacement, inter-story drift, or base shear may increase by more than 20% when RC buildings were design to a PGA of 0.30g and the inter-story drift collapse limit state was frequently reached at lower earthquake intensities when vertical ground motion was included. Compressive axial forces in the columns were also observed to increase by up to 45%. Tensile forces were

detected only when vertical ground motion was included. Finally, the curvature ductility demand increased by nearly 60% with the addition of vertical ground shaking.

Kadid et al. (2010) investigated the behavior of low, medium, and high-rise RC buildings under simultaneous horizontal and vertical ground motions. 2-D structures of two, five, and eight stories were designed according to the Algerian code and analyzed using both lumped mass and distributed mass approaches. The results demonstrated that the vertical component of motion had significant effects on axial loading of columns; however, the lumped mass model may overestimate those effects. Vertical accelerations could also create column tensile forces which in turn could enhance overturning moment. More importantly, large vertical accelerations within flexible floor systems can be amplified creating larger vertical displacements. Finally, the vertical ground motion component was found to have little effect on story drifts and base shears.

1.6 FIELD EVIDENCE OF FLAT SLAB STRUCTURE DAMAGE DUE TO VERTICAL MOTION

The 1994 Northridge earthquake and the 2011 Christchurch earthquake are two examples that demonstrated the damaging effect of vertical ground motion on RC flat-plate structures. The damage could be associated with peak vertical accelerations that were near or larger than that of the horizontal components.

The Northridge earthquake that occurred January 17, 1994 is considered one of the most destructive earthquakes in the western United States. It is of particular interest because it was one of the first seismic events to record high vertical accelerations by numerous instruments. The magnitude of 1994 Northridge earthquake was 6.7 and significant structural damage was observed in modern buildings. Vertical accelerations and V/H-ratios reached as high as 1.18g and 1.79, respectively. Of significance is that a large amount of RC buildings experienced

intermediate damage or even collapse. Some of these failures can be attributed to the participation of higher modes, significant changes in stiffness and strength at higher elevations, or poor design in higher stories; however, there is surmountable evidence that many structural failures were caused from the direct action of vertical motion.

The collapse of the Bullocks store in Fashion Island Mall provides an example of failure caused by vertical motion (Figure 1-17). The failure mode of the waffle slab, a variation of flat slab, was punching shear in the upper two floors. The failure could be the result of strong vertical oscillations of the slabs (Papazoglou and Elnashai, 1996) because high vertical accelerations and minimal column damage suggested that the horizontal effect was limited.



Figure 1-17 Punching shear failure at Bullocks store (photograph courtesy of Earthquake Engineering Research Institute, 2015)

In February 22, 2011 an earthquake of magnitude 6.3 occurred in Christchurch, New Zealand. The level of damage due to this earthquake unparalleled the damage caused by any other earthquakes in the country's history including a 7.1 magnitude earthquake that took place the previous September, 30 km to the west. The Christchurch earthquake was centered 10 km southeast of the city center at a shallow depth of 5 km. 16% of the RC buildings in the central

business district were severely damaged and two mid-rise RC buildings completely collapsed. Vertical accelerations and V/H ratios reached as high as 2.21g and 4.68 respectively (Bradley and Cubrinovski, 2011). It was likely that the nature of near-source ground motion caused much of the damage. One example of failure most likely caused by vertical ground motion was a post-tensioned RC flat-plate garage (Figure 1-18). The structure experienced a progressive collapse initiated by punching failures at slab-column connections. Forensic inspection discovered that the post-tensioning in the slab did not pass through the columns and could provide collapse resistance following punching failures. No other failure in post-tensioned structures was recorded; however, post-tensioning was not widely used in Christchurch (Kam et al., 2011).



Figure 1-18 Collapse due to punching failure in a 4 story, flat-plate parking garage during the 2011 Christchurch earthquake (Kam, 2011; Swanson, 2011)

1.7 MOTIVATION OF RESEARCH

The research presented in this dissertation is motivated by both the high consequence of progressive collapse caused by punching shear failure in flat-plate buildings and the gap in existing knowledge regarding the structural performance of flat plates during a near source event. To date, there is extremely limited information regarding the effects of strong vertical ground motion on the local force and deformation demands on slab-column connections, which are vulnerable to a punching failure that can lead to a large-scale structural failure.

In high seismic regions, even though the primary use for flat-plate system is as a gravity load-carrying system with moment frames or shear walls to resist lateral loads, the flat-plate system must be able to sustain the earthquake-induced nonlinear deformation localized at slab-column connections to avoid punching failure and thus maintain gravity load-carrying capacity. The vertical component of a near-source seismic event causes slabs to oscillate and may create large fluctuations in vertical loads acting on the slabs. Consequently, larger shear transferred between slab and columns and greater nonlinear slab deformation exist in slab near columns. This in turn leads to higher vulnerability of flat-plate structures to punching failure during a near source event. The reduced lateral deformation capacity at the initiation of a punching failure due to greater vertical loads on slabs has been clearly demonstrated in the many experimental studies. The current design codes have also embodied such an effect to ensure structural safety of flat-plate buildings subjected to seismic loads. However, extremely limited study has specifically addressed the vertical ground motion effects on flat-plate structures.

1.8 RESEARCH OBJECTIVES, SCOPE AND METHODOLOGY

The overall goal of this research is to understand the structural response and punching failure potential of RC flat-plate buildings subjected to near source ground motions. The research is limited to flat plates where the design of slabs is governed by gravity loads, the slabs are supported on square columns without using any shear reinforcement, and moment frames are used to resist seismic loading. Specific objectives are to answering the following prominent and pertinent questions:

- Given that the peak vertical ground acceleration may not happen simultaneously with the peak horizontal acceleration, how does the vertical excitation affect the local deformation and force demands on slab-column connections?
- Is the current design approach, which translates a fraction of horizontal spectral acceleration into an equivalent gravity load, able to equivalently define the vertically ground motion effects on flat plates?
- To what degree does the vertical ground motion component lead to greater punching failure potential in a flat-plate building?
- The vertical vibration frequency of slabs is generally greater than that of the horizontal vibrations; meanwhile, the vertical ground motion frequency is also greater compared with horizontal excitations. This may lead to large dynamic response. In such a situation, will considering soil-structure interaction lead to reduced force and deformation demands?
- Even though flat-plate is taken only as a gravity load-carrying system, it has inherent lateral strength provided by slab-column connections. Given that there can be a large number of slab-column connections in a flat-plate structure, how much contribution can the flat-plate system provide to resist lateral loads?

To achieve the aforementioned goal and objectives, nonlinear finite element analyses are performed on a prototype flat-plate structure subjected to service level gravity loads as well as seismic events recorded near the seismic epicenters. Comparisons between seismic ground motion applied in a single lateral direction, perpendicular bi-lateral direction, and in three directions including two perpendicular lateral directions and vertically are included. The analyses determine the slab local force and deformation demands at columns, which are then compared

with the strength and deformation capacity of slab-column connections subjected to near-source seismic ground motion to identify the likelihood of punching failure of flat slabs.

1.9 OUTLINE OF DISSERTATION

Chapter 2 first presents the design of a RC flat-plate structure in accordance with current building codes. The details of nonlinear finite element modeling of columns, beams, and slab of the structure prototype are then described. Finally, the selection and scaling of seismic ground motion selection used to perform time-history analyses of the building are discussed.

Chapter 3 provides the results obtained from the nonlinear static and dynamic analyses. The dynamic analyses considers uni-axial, bi-axial, and tri-axial seismic loading. The results of dynamic demands in terms of lateral drift, slab rotation and deflection, and slab-column shear transfer are compiled. Based on the simulation results, the effects of vertical ground motion on these performance indexes are discussed, and the effectiveness of current design approach addressing vertical ground motion effects is examined.

Chapter 4 examines the risk of punching failure in a flat-plate structure due to vertical seismic ground motion. Punching failure potential is evaluated based on four criteria which consider either shear stress, or lateral drift, or localized slab rotation at the slab-column connections.

Chapter 5 examines the effects of soil-structure interaction (SSI) on the seismic performance of the prototype building. For this purpose, modeling approach for SSI is described and the analyses results incorporating SSI are presented and compared with those neglecting SSI.

Finally, Chapter 6 summarizes the findings from this research and the suggestions for further studies.

CHAPTER 2

MODELING OF PROTOTYPE FLAT-PLATE BUILDING

2.1 PROTOTYPE STRUCTURE

2.1.1 Overview

To study the effects of vertical ground motion on the seismic performance of RC flat-plate structures, a series of nonlinear time-history analyses are conducted on a prototype building. For a flat plate, vertical ground motions affect not only the primary lateral resisting systems, such as shear walls or moment-resisting frames, but also the slab-column frames where disastrous punching failure may occur even though they are designed only as a gravity system. For a dynamic analysis of a RC building under horizontal ground motion alone, a single lumped mass with horizontal degrees of freedom is conventionally assigned at the mass center of each floor because of the high in-plane rigidity of slabs. However, this approach cannot realistically simulate the actual distribution of the inertia forces acting on the floor slabs due to vertical accelerations and thus the internal forces in the slabs. In order to accurately capture the forces transferred between slabs and columns and the nonlinear deformations in the slabs near the columns, the masses associated with the vertical degree of freedom shall be distributed over the slabs. This, however, leads to a dramatically increased number of degrees of freedom in an analysis. Therefore, to reduce computational cost, a single story flat-plate building is taken as the prototype in this study to investigate the effects of vertical ground motions.

It is noted that the observations made from the analyses of a single story building can be extended to the behavior of multistory flat plates for two reasons. First, punching failure occurs in floor slab near the columns. Thus, the nonlinear response of slab at a story, especially caused by vertical excitations, does not affect the behavior of slabs at other stories. Moreover,

experiments conducted on slab-column subassemblies have repeatedly indicated that the unbalanced moment due to lateral loading caused no damage to the columns due to their much higher stiffness and strength as compared with the slabs. It is expected that, for a multi-story flat-plate building, only the bottom end of a column in the first story of slab-column framing experiences flexural yielding. After this yielding, the column of slab-column frames in all other places behaves nearly as a rigid body and the slab-column connections along this column at different stories respond in a similar manner.

The single story prototype flat-plate structure, shown in Figure 2-1, has a 10 ft. story height and four bays in each direction spanning 20 ft. between column centers. Perimeter moment-resisting frames are used for the lateral system and the interior slab-column frames are employed as gravity system. The design of the prototype structure follows the building design codes ASCE 07-10 (2010), and ACI 318-14 (2014).

The site is assumed to be stiff soil with a shear wave velocity of 600-1200 ft/s corresponding to a site class of D per ASCE 7-10 (2010) classifications. The mapped maximum considered earthquake (MCE) spectral acceleration at a period of 1-sec (S_1) and at short periods (S_s) are 0.6g and 2.0g, respectively. These values are commonly found near fault lines in southern California. The building is designed as occupancy category II with corresponding seismic use group of I based on ASCE 07-10 (2010). Table 3-1 summarizes seismic design parameters.

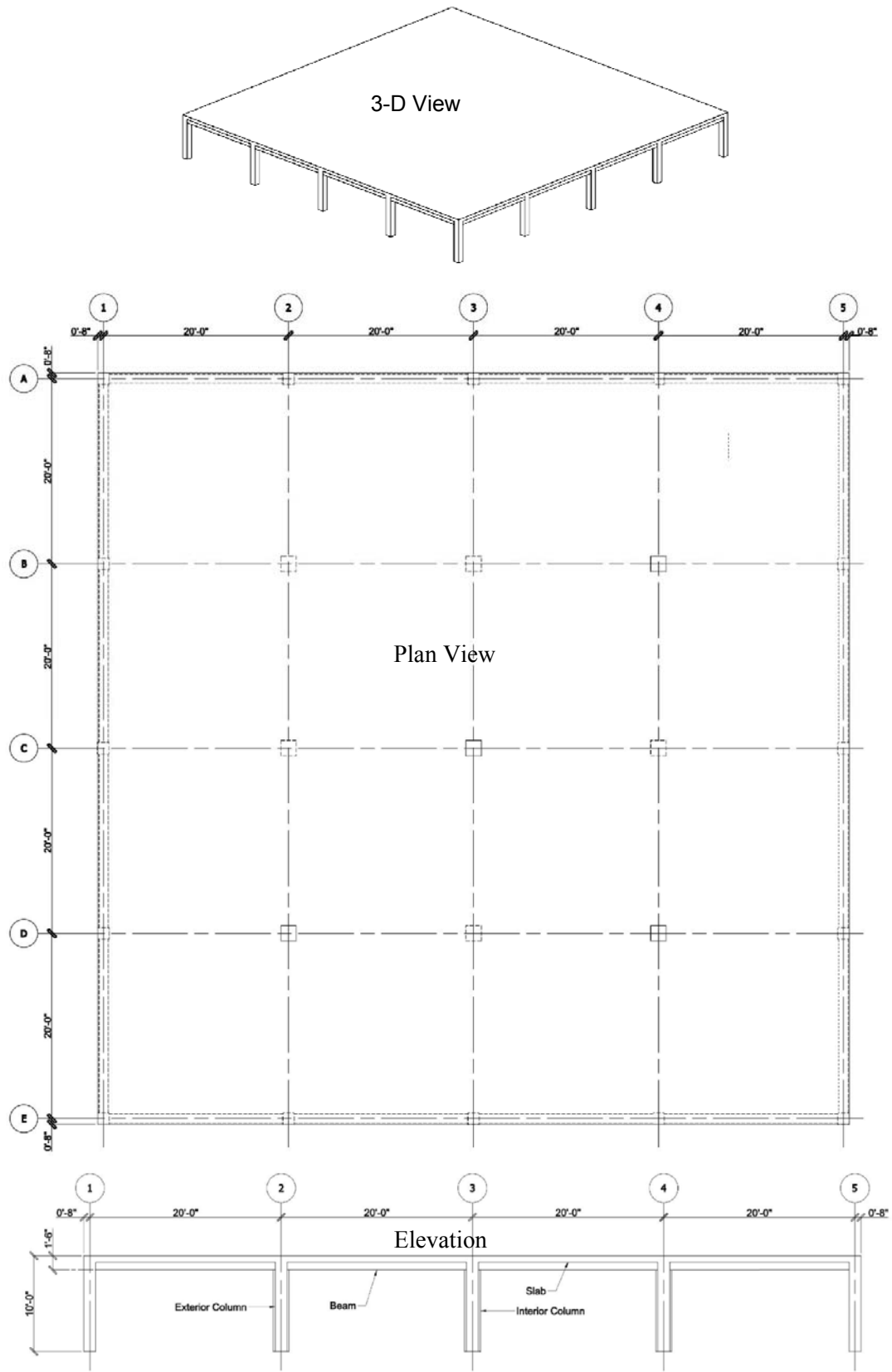


Figure 2-1 Prototype building layout

Table 2-1 Seismic Design Parameters

Occupancy Category	II
Seismic Use Group	I
S_1	0.6g
S_s	2.0g
S_{D1}	0.6g
S_{DS}	1.33g
Site class	D
Seismic Design Category	D

The design gravity loads consist of slab self-weight plus superimposed dead load for a total dead load of 120 psf and 40 psf live load. Grade 60 hot-rolled reinforcement $f_y = 60$ ksi and normal weight concrete with a cylinder compressive strength of 5000 psi are used to construct the slabs and columns.

2.1.2 Slab-Column Frames

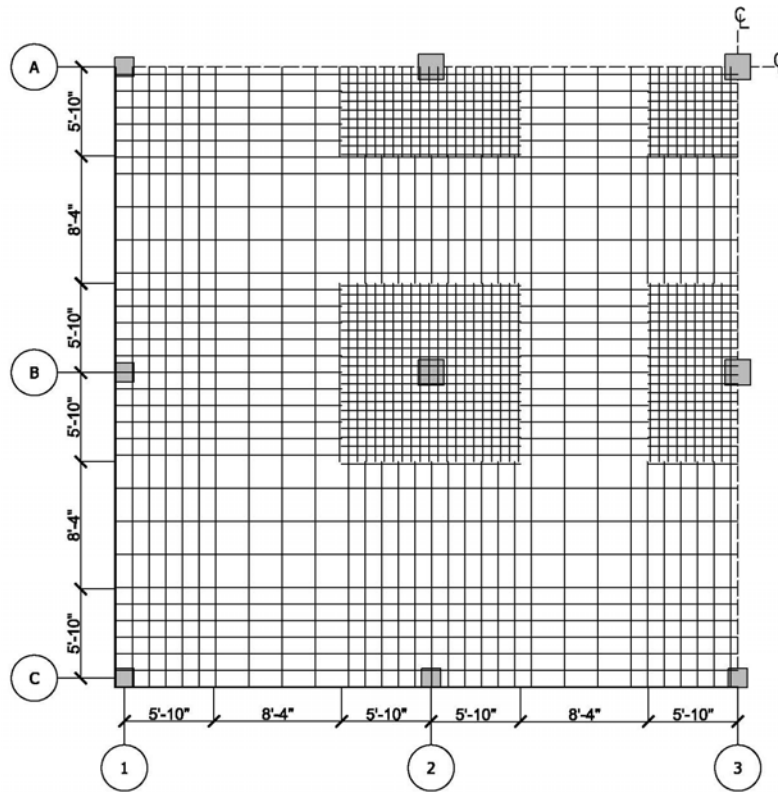
Although only a single story building is considered, this study intends to investigate the performance of typical flat-plate buildings. Thus, the size of column is chosen as 20 in. square to reflect the typical column size in multistory flat-plate buildings. The slabs are supported directly on the columns without using shear capitals or drop panels. Because the building has a regular floor plan and more than three bays in each direction, the *Direct Design Method* provided in ACI 318-14 (2014) is used to design the floor slabs. Two types of load combinations are considered for the vertical loads acting on the floor: (1) $1.2DL$ (dead load) + $1.6LL$ (live load) and (2) $(1.2 + 0.2S_{DS})DL + 0.5LL$, where S_{DS} is the design spectral acceleration at short periods and the use of parameter $0.25S_{DS}$ considers the effects of vertical ground motion per ASCE 7-10 (2010).

Even though slab-column frames are designed as a gravity system, ACI 318-14 (2014) requires sufficient two-way shear strength must be provided to slab-column connections so they can deform compatibly with the lateral load-resisting system. The slab thickness is chosen as 8

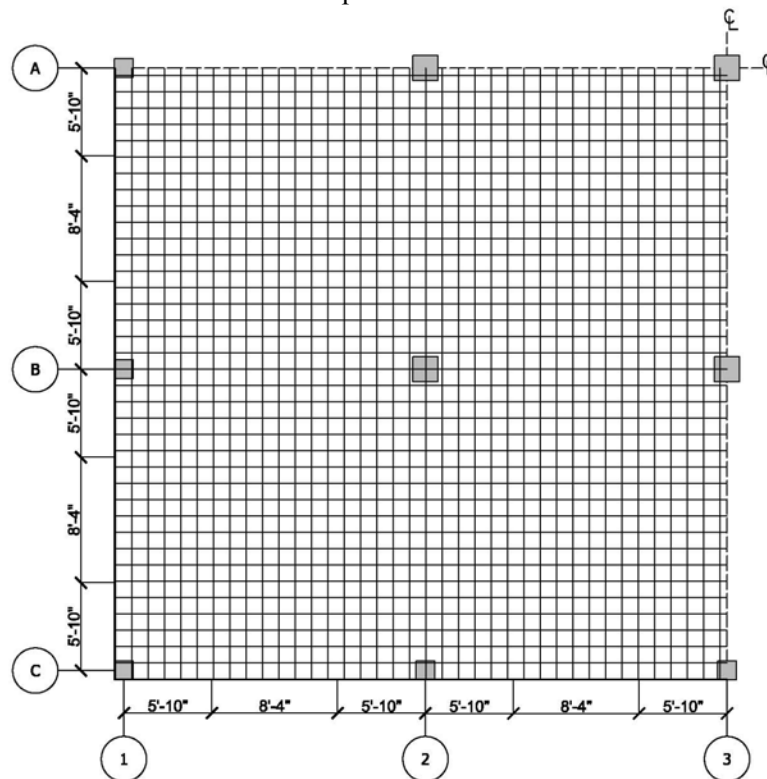
in. and no slab shear reinforcement is used. This slab thickness satisfies the code requirements regarding both deflection serviceability and two-way shear strength under an expected seismic lateral drift of 1.65 in. No. 4 bars are used for all slab reinforcement. The clear cover of slab flexural reinforcement is 3/4 in. The slab top reinforcement ratio is 0.53% at the interior slab-column connections and 0.27% at the exterior connections. The design of slab top and bottom reinforcement at the middle strips is governed by the code minimum reinforcement requirements to control cracking due to shrinkage and normal temperature changes. The design layout of slab reinforcement is shown in Figure 2-2 for a quarter of the floor based on symmetry.

2.1.3 Perimeter Moment Frames

Special moment frames are employed as the seismic force-resisting system at the perimeter of the prototype building. Because of the adequate ductility for surviving large inelastic deformation demands, special moment frames are essential for buildings designed in more severe seismic design categories. According to ASCE 7-10 (2010), the story drift under MCE shall be controlled within 2.4 in. (2% drift ratio). The perimeter moment frames consists of 15 in. square columns and 12 in. wide by 18 in. high beams, which allow the drift limit to be met.



Slab top reinforcement



Slab bottom reinforcement

Figure 2-2 Slab reinforcing of prototype building

From the mapped spectral accelerations at long and short periods, the design spectral acceleration at 1-sec period (S_{D1}) and at short periods (S_{DS}) are calculated as 0.6g and 1.33g corresponding to a seismic design category D (Table 2-1), respectively. The seismic lateral load for design is determined based on S_{D1} , S_{DS} , seismic mass, lateral stiffness, assumed site condition, and a strength reduction factor of $R = 8$ for special RC moment frames. The seismic design loads are then combined with the gravity loads to determine the internal force demands on the moment frames. The strong-column/weak-beam design approach is implemented in designing and detailing the beams and columns of the perimeter frames. The detailing of beams and columns follows the seismic design provisions in ACI 318-14 (2014). The design results are shown in Figure 2-3 and summarized in Table 2-2.

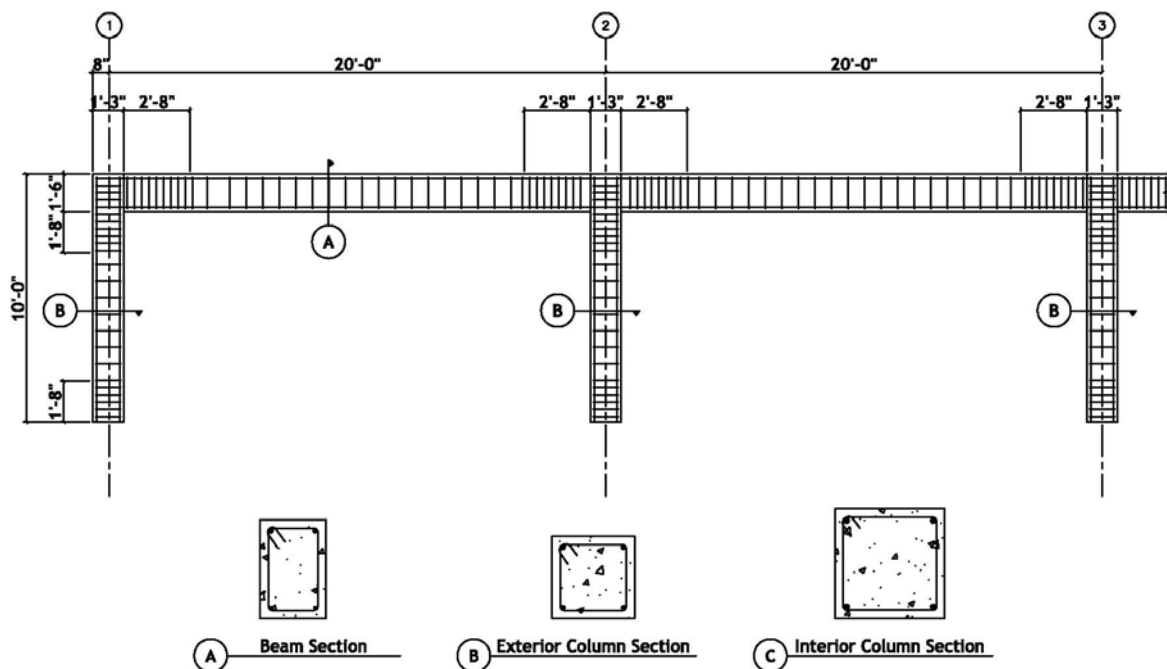


Figure 2-3 Reinforcement design results for perimeter moment frames

Table 2-2 Beam and Column Sections

Component	Width (in.)	Height (in.)	Steel Reinforcement	Reinforcing Ties		Concrete cover (in.)
				Size	Spacing (in.)	
Beam	12	18	Top: 2 #7 Bottom: 2 #5	#3	Hinge: 3.5 Center: 8	1.5
Interior column	20	20	4 #9	#4	Hinge: 4 Center: 12	1.5
Exterior column	15	15	4 #7	#4	Hinge: 3.5 Center: 6	1.5

2.2 MODELING OF PROTOTYPE STRUCTURE

2.2.1 Overview

The finite element analysis package Open System for Earthquake Engineering simulation (OpenSees 2011), an open-source software developed by the Pacific Earthquake Engineering Research Center (PEER), is adopted in this study as a simulation platform to analyze the seismic performance of the prototype structure. OpenSees offers a variety of elements and materials suitable for simulating the nonlinear behavior of RC structural components including beams, columns, and walls subjected to loading reversals. Thus, OpenSees have been widely employed in the earthquake engineering research community. The following discussion describes model creation of beams, columns, and slab and material properties for concrete and reinforcing steel.

2.2.2 Modeling of Beams and Columns in Perimeter Moment Frames

Elastic elements are used for the beam-column joints. Stiffness properties are defined so that the joints act rigidly. In the remaining regions of beams and columns of the perimeter frames, nonlinear displacement-based elements are utilized. A displacement-based element allows plasticity to be distributed along the length of the element. For each displacement-based element, five integration points are defined as shown in Figure 2-4a. Figure 2-4b shows the location of each type of element used for beams and columns. Columns are separated into 4

elements, 3 of which are displacement-based and 1 elastic element at the beam-column joint. Beams are divided into 11 displacement-based elements and 2 elastic elements at the joints, one at each joint.

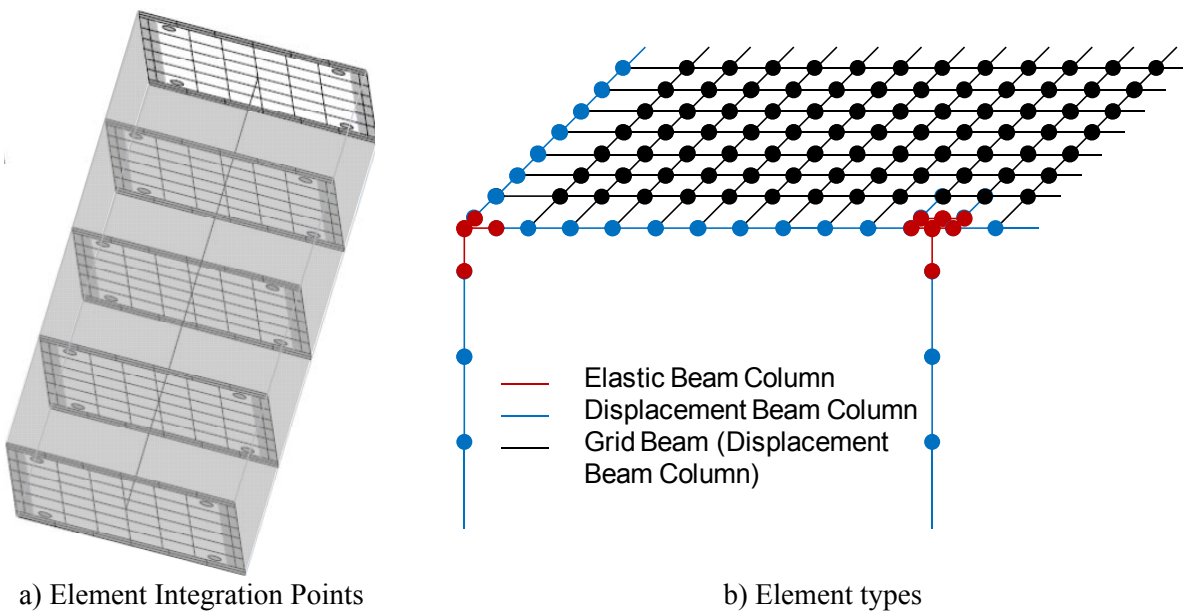


Figure 2-4 Arrangement of different types of elements

Fiber sections are assigned to the displacement-based beam-column elements to simulate the axial and flexural behaviors of beams and columns. A fiber section controls the hysteretic behavior through non-linear material models of individual fibers within the system. Fiber section is advantageous for simulating RC sections subjected to hysteretic behavior because it (1) can avoid defining an assumed plastic hinge length at beam and column ends, which is a function of many parameters varying along loading, (2) has proven to be accurate in capturing seismic behavior of RC beams and columns (Spacone et al., 1996), (3) compared with solid elements for system level simulation of nonlinear response, involves significantly lower computational costs, and (4) automatically considers both axial and bi-directional flexural loading effects and their interactions. Fiber sections can only simulate flexure and axial loading. Models for shear and

torsion need to be combined with the use of fiber section to define all actions associated with 6 degrees of freedom.

The use of a fiber section allows creation of section layout at specified integration points. The model is then able to predict the moment-curvature relationship at integration points over the length of a member. The capability of fiber models to calculate elastic or inelastic response enables the use of one element to model components. Cross-sections can then be separated into a collection of fibers using *patch* command. Each fiber patch is assigned a uniaxial constitutive material model. Finally, reinforcing steel can be incorporated into the section with the use of *layer* command, which defines the number of bars, area, and location.

For this study, column and beam cross sections are separated into unconfined (cover) concrete, confined (core) concrete and reinforcing steel. A typical section can be seen in Figure 2-5. Uniaxial material models and cross section details can be found in Section 2.2.3 and Table 2-2, respectively.

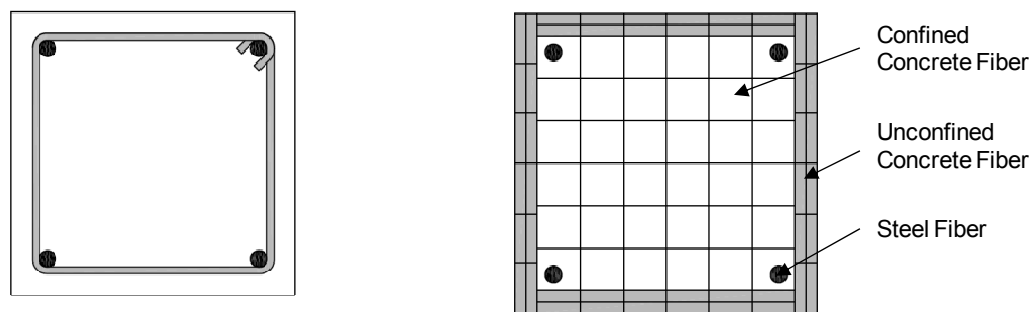


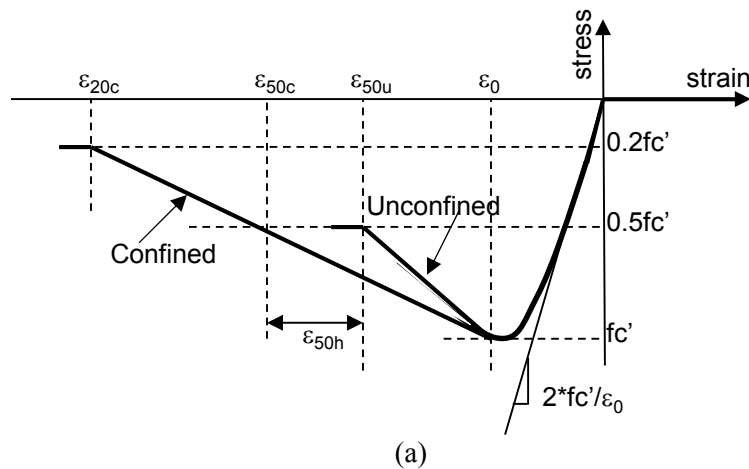
Figure 2-5 Typical beam and column cross section

2.2.3 Material Modeling for Perimeter Frames

Several types of stress-strain relations have been proposed (Hillerborg et al. 1976; Gilbert and Warner 1978; Damjanic and Owen 1984; Cope 1986; Guo and Zhang 1987; Mander 1988)

for concrete in tension, but no consensus has been reached and considering concrete tensile strength often leads to significantly reduced convergence in a nonlinear structural analysis. Additionally, concrete tensile strength is very low when compared to its compressive strength, providing little assistance to enhance flexural strength. Once cracks form in concrete under cyclic loading reversals, its tensile strength is lost relatively quickly and cannot contribute during the subsequent loading cycles. Therefore, the concrete tensile strength is neglected in this study and *Concrete01* in OpenSees is used to model concrete.

The uniaxial Kent-Scott-Park model for concrete material under cyclic compressive stresses proposed by Kent and Park (1971) and modified later by Scott et al. (1980) is used with degraded linear unloading/reloading stiffness according to the work of Karsan and Jirsa (1969) for unconfined (cover) concrete. Confined (core) concrete in compression is defined using Kent-Park model (1971). The fundamental model and parameters are shown in Figure 2-6 for monotonic and cyclic loading. For the prototype building investigated in this study, concrete compressive strength (f'_c) is defined as 5000 psi for all members with a strain at peak stress (ϵ_0) of 0.002. Crushing strength and strain are defined differently for the confined concrete cover and unconfined concrete core in the beams and columns.



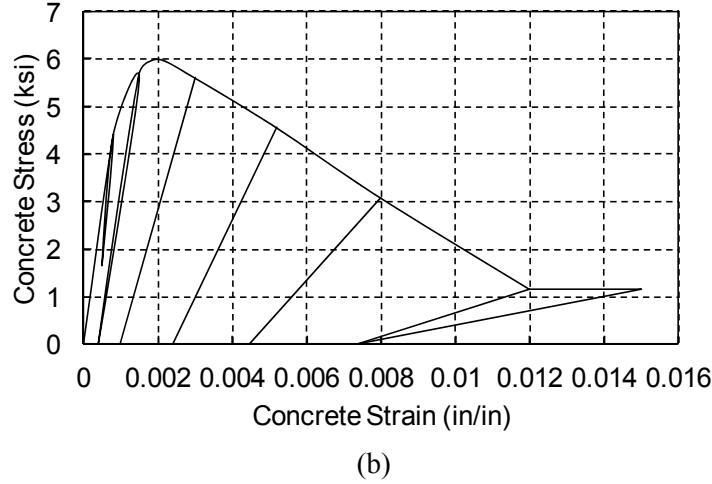


Figure 2-6 Constitutive model of concrete: (a) uniaxial stress-strain relationship, (b) hysteretic stress-strain relationship

For unconfined concrete, the crushing strength is defined at $0.5f_c'$ with a corresponding crushing strain (ϵ_{50u}) per Equation 2-1. Confined concrete crushing strain (ϵ_{20c}) is defined at a concrete compressive strength of $0.2f_c'$ according to the size and spacing of transverse reinforcement used in the beams or columns. ϵ_{20c} can be determined based on the linear function of concrete strength degradation and the two strain parameters ϵ_{50h} and ϵ_{50c} formulated in Equations 2-2 and 2-3.

$$\epsilon_{50u} = \frac{3 + 0.002f_c'}{f_c' - 1000} \quad \text{Equation 2-1}$$

$$\epsilon_{50h} = 0.75\rho_s \sqrt{\frac{b''}{s_h}} \quad \text{Equation 2-2}$$

$$\epsilon_{50c} = \epsilon_{50u} + \epsilon_{50h} \quad \text{Equation 2-3}$$

where ρ_s is the volumetric transverse reinforcement ratio evaluated using the volume of confined core, b'' is the width of confined core and s_h is the hoop spacing.

The reinforcing steel is modeled using *Steel01*, a uniaxial bilinear stress-strain relation with kinematic hardening. Figure 2-7 illustrates the material behavior of *Steel01* under monotonic and cyclic loading. The initial elastic tangent (E_0) is defined as 29,000 ksi and the

strain-hardening ratio is assumed as 0.01. Isotropic hardening is neglected for the reinforcing steel.

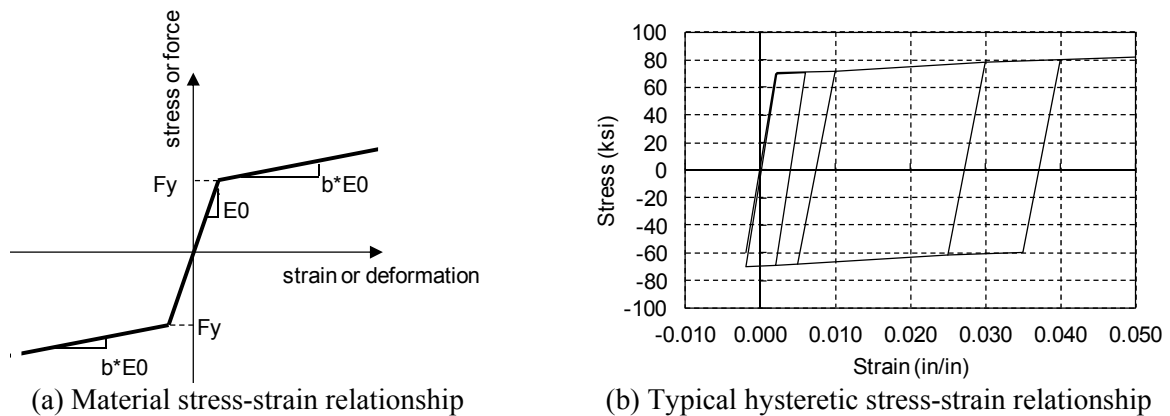


Figure 2-7 Constitutive model for reinforcing steel.

2.3 MODELING OF SLAB

2.3.1 Grid Beam Model

Simulating the nonlinear response of the slab in a flat-plate structure is challenging mainly due to the complex state of stresses in the slab near the supporting columns. For a system level analysis, shell elements as reduced finite element modeling approach can potentially be used to simulate slabs; however, the study performed by Liu et al. (2015) indicated that the use of shell elements tends to overestimate the torsional resistance of slab-column connections subjected to unbalanced moment transfer.

As more simplified modeling approaches, equivalent frame and equivalent beam methods (Morrison et al. 1983; Akiyama and Hawkins 1984; Luo et al. 1995; Robertson 1997; Tian et al., 2009; Kang et al. 2009) have been proposed to simulate the nonlinear behavior of slab-column framing under seismic type of loading. These models, however, were developed for flat plates dominated by seismic lateral loading and are two dimensional in nature because a spatially

continuous flat-plate system needs to be idealized into planar frames. Therefore, the equivalent frame and equivalent beam methods may be unsuitable for simulating the nonlinear behavior of flat plates under both horizontal and vertical ground motions. This study considers the grid beam approach suggested by Tian et al. (2012) to model the slab in the prototype building. This macromodel, defining constitutive relationships at force-deformation rather than stress-strain level, was developed and validated using the experiments conducted on slab-column connections subjected to three types of loading conditions: (1) concentric gravity loading, (2) unevenly distribution gravity loads causing unbalanced moment transfer, and (3) combined gravity and cyclic lateral loading.

In the grid beam model, as shown in Figure 2-8, the slab-column joint is represented by rigid beam elements (the thicker lines) where two beam elements frame with the column. Outside the joint regions, orthogonally deployed nonlinear beam elements are used to simulate the slabs. Two beam elements are connected to each side of a joint. The length of beam elements near the column is identical to column size, creating a square grid. Each grid beam is defined with a depth equal to slab thickness and a width equivalent to half of the beam spacing. Each node contains six degrees of freedom and transfers bending moment, shear, axial force and torsion.

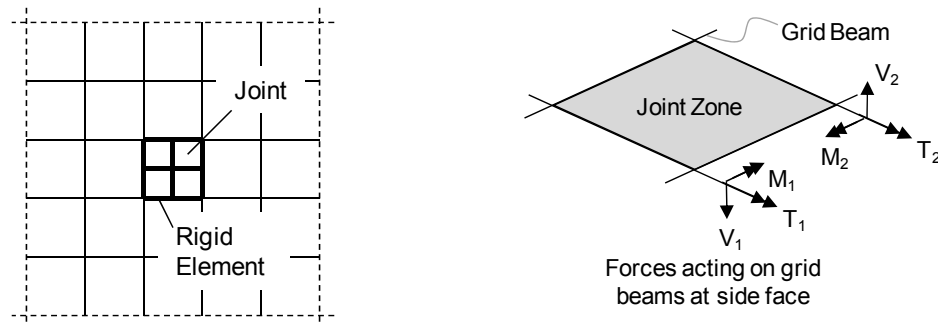


Figure 2-8 Grid beam model (Tian et al. 2012)

The use of two grid beams, rather than only one beam, connected to each side of slab-column joint allows the torsion to be carried by both the torque in the members and the bending moment produced by vertical shears in the beam elements (V_1 and V_2 in Figure 2-8) about the joint centroid. Slab torsion is much more complicated than other types of actions and there exists extremely limited experimental data. Thus, such a grid pattern is advantageous because it reduces the portion of unbalanced moment that must be carried by torsion in the beam elements and thus reduces modeling uncertainty. The principal bending moment and torsion for grid beams are modeled with nonlinear behavior. All other actions are assumed to be linear elastic. This simplification is reasonable based on the testing of slabs (Guandalini et al. 2009; Elstner and Hognestad 1956; Tian et al. 2008) which have demonstrated that deformation of slab-column connection at failure is caused primarily by excessive slab rotation due to flexural yielding at the column face.

The columns in the slab-column framing are modeled by elastic line elements. It is noted that only a single-story building is simulated in this study; however, the behavior of slab-column framing in this structure is expected to be representative of that in a multi-story flat plate, where the column in the upper stories behave elastically without any cracking and yielding. In order to reflect such a behavior and the actual lateral stiffness contributed from the slab-column framing, the rotational degrees of freedom at the bottom ends of the interior columns are not restrained in the simulations.

2.3.2 Modeling of Principle Bending Moment

Figure 2-9 shows the tri-linear model for principle bending moment (M) versus curvature (ϕ) response in the grid beams under monotonic loading, which is also used as the envelope of

M - ϕ behavior under cyclic loading. Three loading stages are used to construct the model including concrete cracking, tensile yielding of reinforcement, and concrete crushing. Concrete cracking is calculated based on the initial flexural stiffness (K_F) of the grid beam. K_F is defined based on suggestions from Coronelli (2010) and shown in Equation 2-4 where E_c is Young's modulus of concrete evaluated per ACI 318-2014 (2014) and I is the beam moment of inertia determined according to assumed grid beam width and depth.

$$K_F = \frac{1}{2} E_c I \quad \text{Equation 2-4}$$

The cracking moment (M_{cr}) is defined by reducing the concrete modulus of rupture by half. This reduction is made mainly because of the effects of restrained concrete shrinkage, two-way bending, and coarse aggregate settlement above slab top bars.

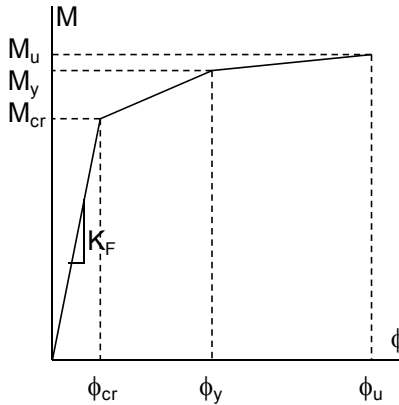


Figure 2-9 Nonlinear flexure model for grid beam

The yield moment (M_y) and ultimate moment (M_u) are determined using the conventional approach for an actual RC beam. However, Tian et al. (2012) recommended using a correction factor of $\gamma = 2.5$ to account for two-way bending effects on slab deformation. Therefore, yield curvature is calculated per Equation 2-5 where $\phi_{y,0}$ is the yield curvature evaluated

conventionally. Furthermore, because the yield moment is close to ultimate moment for beams with typical reinforcement ratios, $M_y = 0.95M_u$ is generally a good estimation. Lastly, the ultimate curvature (ϕ_u) is primarily used to control the post-yielding flexural stiffness of grid beams because concrete crushing in slab can seldom be observed in the tests of slab-column connections. A concrete crushing strain of 0.004 is used to determine ϕ_u .

$$\phi_y = \gamma\phi_{y,0} \quad \text{Equation 2-5}$$

2.3.3 Modeling of Torsion

Torsion is assumed to have a bilinear relationship as shown in Figure 2-10 for monotonic loading, which also serves as the response envelop under cyclic loading. Torsion (T) is defined as a function of twist angle (θ). The elastic torsional stiffness (K_T) is evaluated using Equation 2-6, which was developed by Yettram and Husain (1965) for elastic grid beam model assuming that the Poisson's ratio of concrete is equal to zero.

$$K_T = E_c I \quad \text{Equation 2-6}$$

The torsional strength of a grid beam is limited to $T_u = \lambda T_{cr}$ where T_{cr} is the pure torsional resistance at cracking of the grid beam and λ is a strength reduction factor calibrated as $\lambda = 0.8$ per Tian et al. (2012). T_{cr} per Equation 2-7 was developed by Hsu (1968) for RC beams without shear reinforcement

$$T_{cr} = 0.217y(x^2 + 6450)\left(\sqrt[3]{f'_c}\right) \text{ (units in: mm and MPa)} \quad \text{Equation 2-7}$$

where x and y are the smaller and larger dimension of the grid beam cross-section, respectively. The experiments conducted on slab-column connections subjected purely to torsion (Kanoh and Yoshizaki, 1979) demonstrated that torsional cracking did not lead to an immediate reduction of torsional strength due to the existence of slab flexural reinforcement. Therefore, no strength

degradation is assumed once T_u has been reached. Finally, to ensure analysis convergence, the post-cracking torsional stiffness is assumed to be $0.01K_T$.

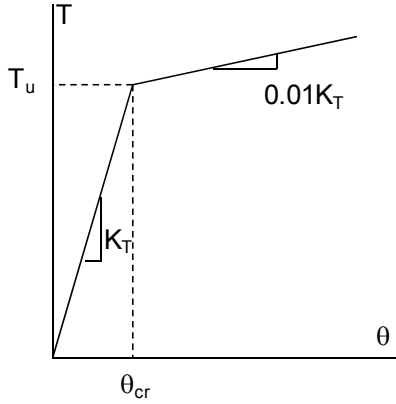


Figure 2-10 Nonlinear model for torsion in grid beams

2.3.4 Hysteretic Model for Flexure and Torsion

When using grid beams to simulate the seismic behavior of flat-plate structures, the hysteretic property of flexure and torsion needs to be defined. Reversal of lateral loading as found in a seismic event causes the slab-column connection to be subject to pinching of load-deformation loops due to cracks in slab opening and closing. In this study, the hysteretic model for general RC components proposed by Elwood and Moehle (2003) and shown in Figure 2-11 is adopted to define the hysteresis of flexure and torsion in grid beams. Due to the lack of experimental data, identical parameters for the hysteretic response are defined for flexure and torsion. It is noted that the monotonic responses described in Sections 2.3.2 and 2.3.2 defines the response envelop for flexure and torsion.

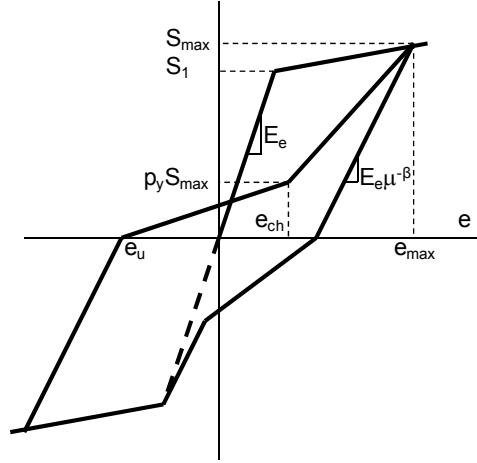


Figure 2-11 Hysteretic model for primary bending and torsion in grid beams

In Figure 2-11, e and S represent deformation (curvature or twist angle) and force (bending moment or torque), respectively. In order to apply this model, four factors need to be defined, including the pinching factors (p_x and p_y), unloading stiffness degradation factor (β) and stiffness degradation factor (γ_1), which will be discussed subsequently. For flexure, the elastic limit (S_1) is defined at cracking due to slab stiffness degradation that occurs early in slab-column connections subjected to lateral loading. The following equations define some characteristic points in the hysteretic model shown in Figure 2-11.

$$e_{ch} = e_1 + p_x(e_2 - e_1) \quad \text{Equation 2-14}$$

$$e_1 = e_u + p_y(e_{max} - e_u) \quad \text{Equation 2-15}$$

$$e_2 = e_{max} - (1 - p_y)(S_{max}/E) \quad \text{Equation 2-16}$$

$$E = E_e \mu^{-\beta} \quad \text{Equation 2-17}$$

$$\mu = \frac{e_{max}}{S_1} \quad \text{Equation 2-18}$$

Many combinations of the values for the pinching factor (p_x, p_y), unloading stiffness degradation factor (β) and flexural stiffness degradation factor (γ_1) can be used. The experiment conducted on Specimen L0.5 by Tian et al. (2008) is simulated using the grid beam model to

determine the values of these parameters. The experiment setup has been described previously. This test is chosen for calibration purpose because the specimen had a large size (6 in. thick slab and 16 in. square column). Additionally, the ratio of column size to slab effective depth and the slab tensile reinforcement ratio of 0.5%, two parameters affecting slab punching resistance, are similar to those in the prototype building.

In the simulation using grid beam model, the average top reinforcement ratio in the slab column strip of 0.49% and 0.25% everywhere else are used to define the flexural behavior of slab. The column is restrained from lateral displacement at the bottom end while vertical displacement is allowed. Slab self-weight is applied in the simulation as well as a vertical load of 23.6 kip at the slab center to replicate service level gravity loads transferred between slab and column. Cyclic lateral displacement is then applied until three loading cycles at 2.0% drift are completed since punching failure occurred in experimental tests soon after this drift was achieved. From the simulation it was determined that $p_x = 0.6$, $p_y = 0.2$, $\beta = 0.45$ and $\gamma_1 = 0.03$. These values will then be used for simulating the prototype building. The simulation result is shown in Figure 2-12(a) and is compared with the experimental results shown in Figure 2-12(b). The figure demonstrates that the slab-column connection lateral stiffness and strength have been well simulated. The hysteretic model leads to less pinching than that observed in the experiments, which would overestimate the energy dissipation capacity of slab-column connections. However, because of the much lower flexural strength of slab compared with the perimeter frames, it is expected that such an underestimated pinching effect from the model will lead to only slightly overestimated energy dissipation capacity of the entire structural system of the prototype building.

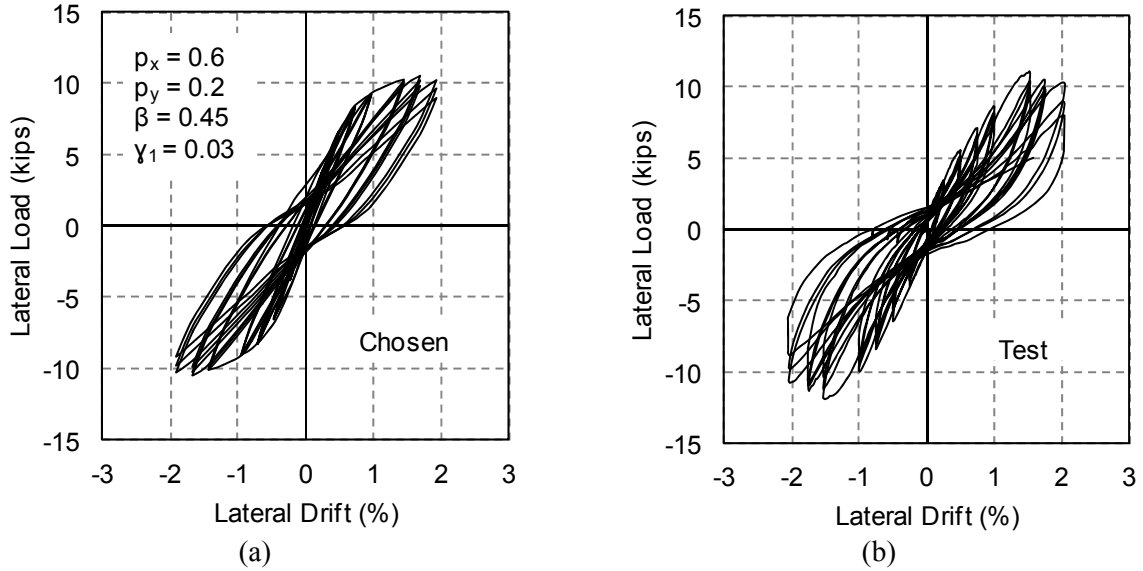


Figure 2-12 Calibration of parameters in hysteretic model from a cyclic loading test: (a) simulation result, (b) experimental result.

Under combined gravity and cyclic lateral loading and because of slab stiffness degradation due to slab cracking and yielding, the slab vertical deflection increases. In order to further examine the suitability of the chosen parameters defining the hysteretic properties. The simulation results regarding the slab vertical deflection are compared with test data, as shown in Figure 2-13. The slab center deflection in this figure refers to that determined when the specimen has been unloaded after the three loading cycles at a drift level have been completed. It is seen that good agreement is achieved between the test and simulation results with a largest difference of about 20%.

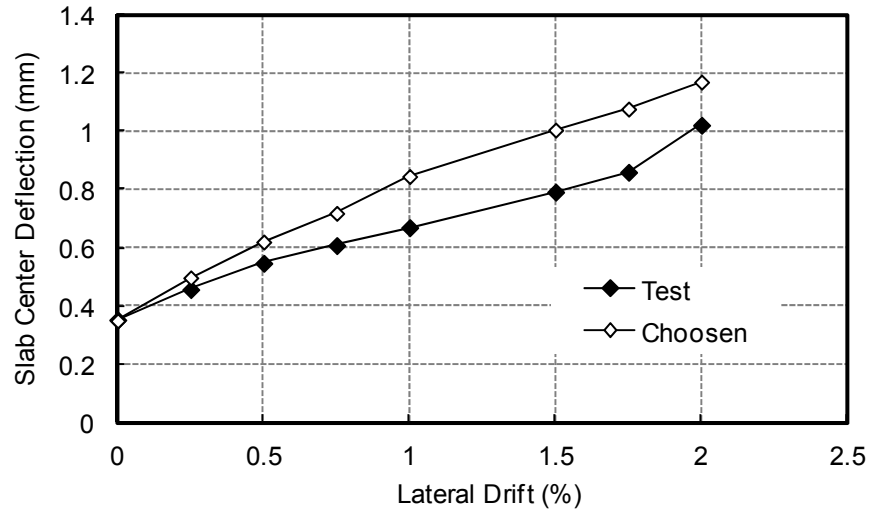


Figure 2-13 Slab vertical deflection verses lateral drift

2.4 LOADING

2.4.1 Gravity Loading

In the simulations, gravity loading is first applied statically on the nodes connecting the elements for slab, beams and columns in the prototype building. Gravity loads consist of 120 psf superimposed dead load (DL) and 40 psf live load (LL). A load combination of $1.2DL + 0.5LL$ is used for the prototype structure during its analyses under ground shaking. Mass is also assigned for the structure at these nodes in both the horizontal and vertical directions. The horizontal component of mass is based on dead load only while the vertical component of mass considers some participation of live loads and determined based on $DL + 0.25LL$.

A Newton solution algorithm is made use of in the gravity load analysis. The algorithm command determines the sequence of steps that must be taken to solve the non-linear equation. In this case, the Newton algorithm uses Newton-Raphson method to advance to the next time step. For each iteration the tangent stiffness is updated on the load verse displacement response.

2.4.2 Selection of Ground Motions

To design a building using time-history analysis approach, ASCE 7-10 (2010) requires a minimum of three separate seismic events each containing two horizontal components and, if relevant, a vertical component. If three events are used, the maximum response should be used as design basis. In the case seven or more events are considered, the average response may be used. In this study, eight ground motion records are selected from separate seismic events provided by the PEER Strong Motion Database. Two criteria are used for ground motion sections: (1) the ground motions shall be recorded in the stations having a site classification identical to that of the prototype building, and (2) the distance to the seismic epicenter and fault line shall be less than approximately 35 km in order to insure a close source distance where vertical ground motions are prominent.

The IBC (2015) site class D identifies a stiff soil with an average shear velocity of 600-1200 ft/s in the top 100 ft of soil (v_{100}). However, the PEER database utilizes the USGS site classification to define ground motions. Table 2-3 compares the two site classification systems. It is seen that the USGS site class C corresponds to IBC (2015) site class D. Therefore, the ground motions are selected from the PEER database corresponding to USGS site class C. Table 2-4 summarizes the distance to epicenter, the distance to fault rupture, and the peak ground accelerations in three directions for each recorded ground motion. Figures 2-14 through 2-21 display the time histories of the eight seismic ground motions in terms of accelerations in the vertical (z) and two horizontal (x and y) directions. To reflect the uncertainties involved in seismic ground motions, the selected ground motion records contain different characteristics in terms of the V/H-ratios, different time internals between reaching peak vertical acceleration and

peak horizontal acceleration, different frequency properties of horizontal accelerations, and different durations.

Table 2-3 Comparison of IBC and USGS Site Classification

Site Class	v_{100} in IBC (ft/s)	IBC soil type	v_{100} in USGS (ft/s)	USGS soil type
A	> 5000	Hard rock	> 2500	Rock
B	2500-5000	Rock	1200-2500	Soft rock
C	1200-2500	Very dense soil and soft rock	600-1200	Stiff soil
D	600-1200	Stiff soil	< 600	Soft soil
E	< 600	Soft clay soil	-	-
F	-	Soils requiring site response analysis	-	-

Table 2-4 Properties of Selected Ground Motion Records

Earthquake	Station	USGS Site class	Distance (km) ^a		PGA (g)		
			ED	CD	Long.	Trans.	Vert.
Chi-Chi, Taiwan (1999)	CHY024	C	24.1	9.64	0.278	0.175	0.152
Duzce, Turkey (1999)	Duzce	C	1.61	6.58	0.358	0.519	0.357
Erzincan, Turkey (1992)	95 Erzincan	C	8.97	4.38	0.486	0.420	0.248
Imperial Valley, California (1979)	Chihuahua	C	18.9	28.7	0.284	0.266	0.218
Loma Prieta, California (1989)	Halls Valley	C	36.3	31.6	0.099	0.129	0.056
Northridge, California (1994)	Sylmar-Converter	C	13.1	5.4	0.594	0.795	0.586
Parkfield, California (1966)	Cholame	C	34.0	12.9	0.247	0.270	0.116
Westmorland, California (1981)	Westmorland Fire Sta.	C	7.02	6.50	0.412	0.399	0.838
^a ED = epicentral distance and CD = closest distance to fault rupture							

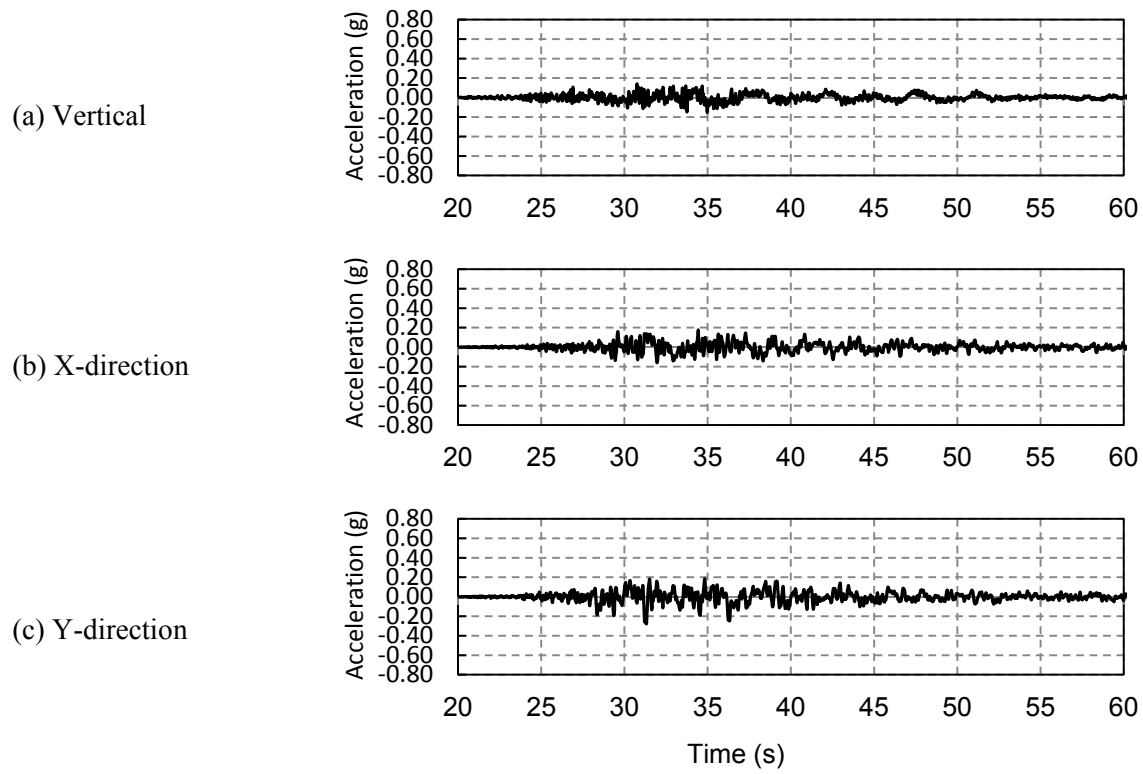


Figure 2-14 Ground motion accelerations: 1999 Chi-Chi, Taiwan

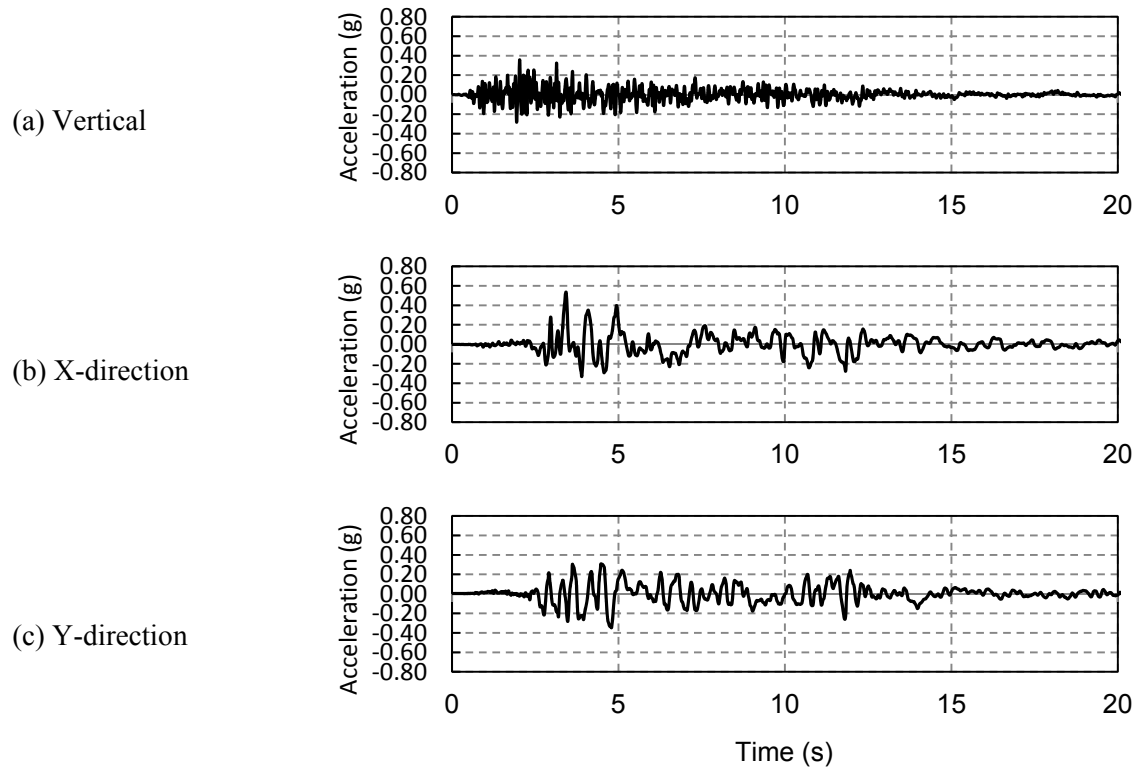


Figure 2-15 Ground motion accelerations: 1999 Duzce, Turkey

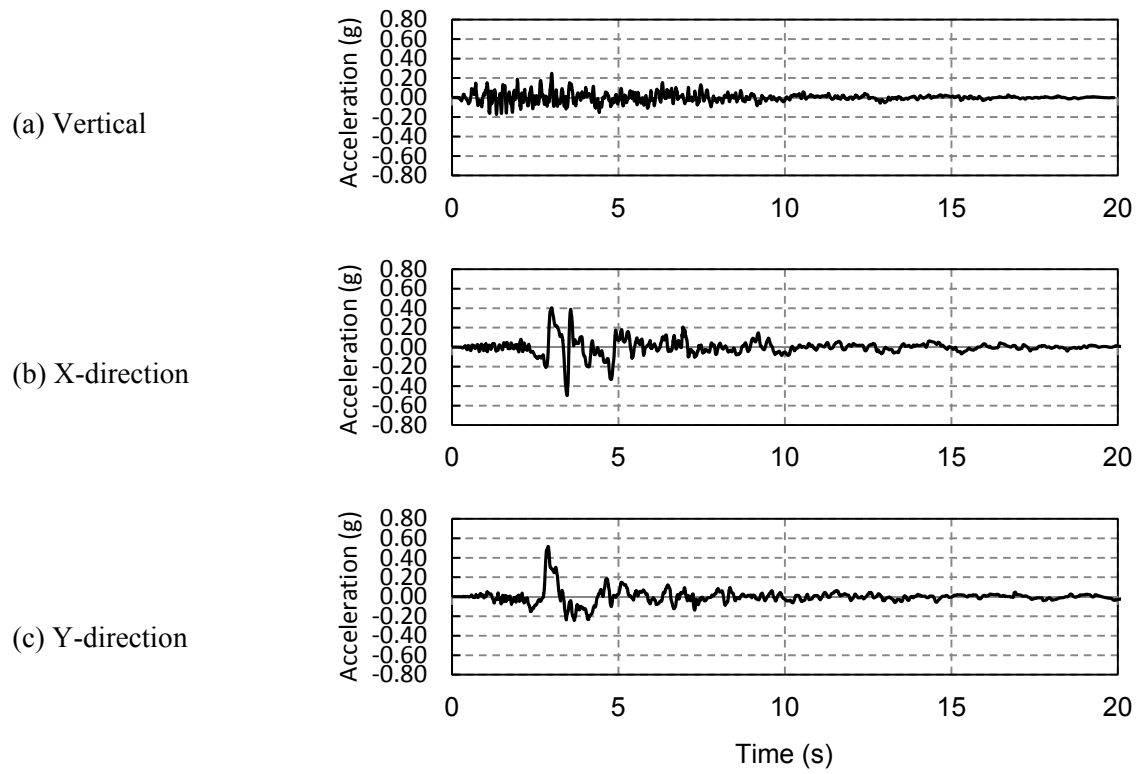


Figure 2-16 Ground motion accelerations: 1992 Erzincan, Turkey

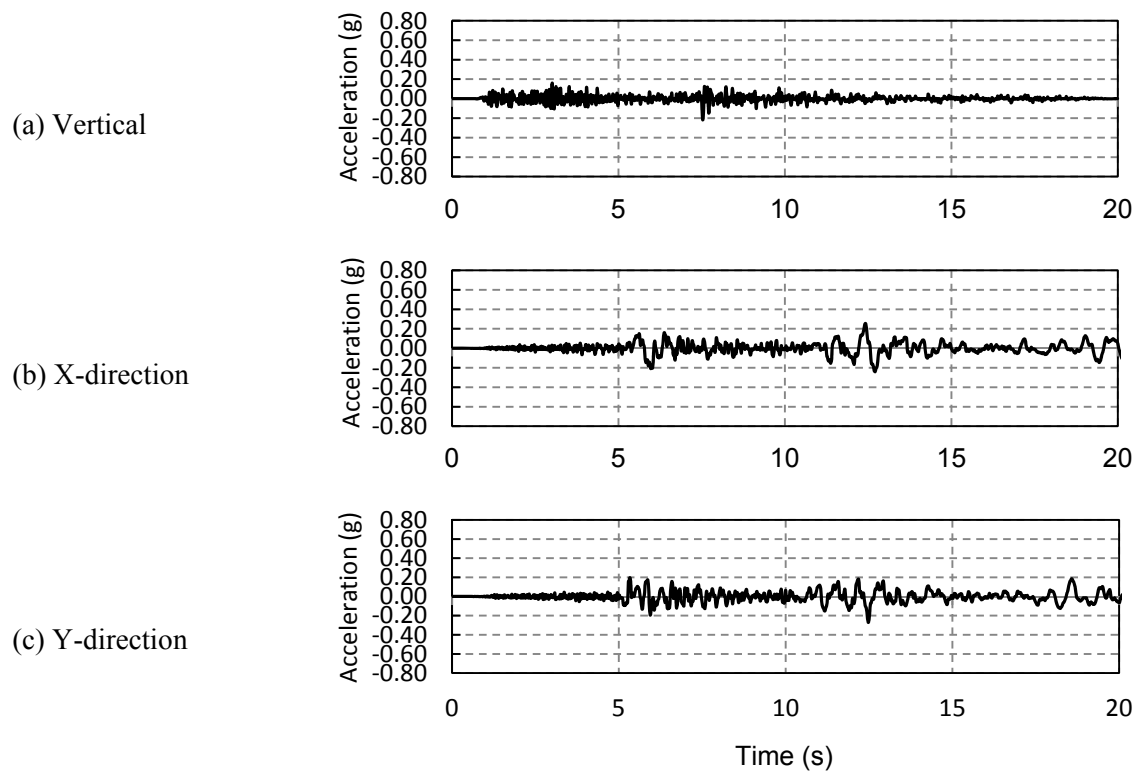


Figure 2-17 Ground motion accelerations: 1979 Imperial Valley, California

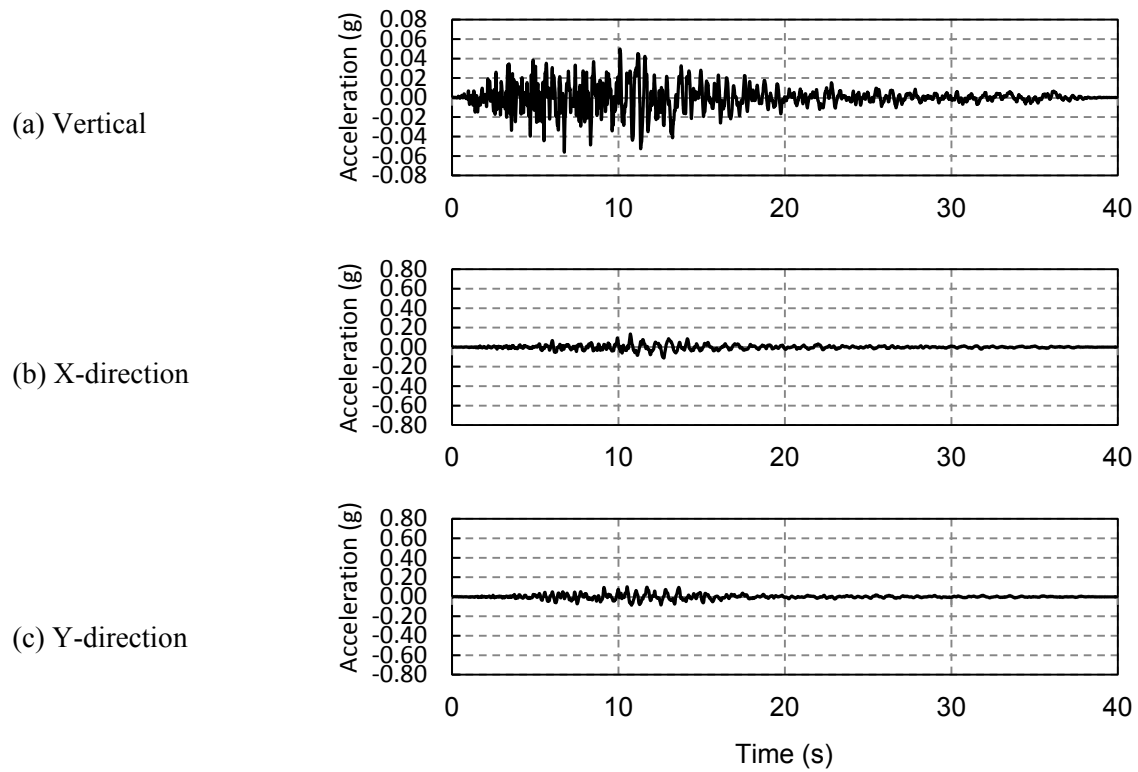


Figure 2-18 Ground motion accelerations: 1989 Loma Prieta, California

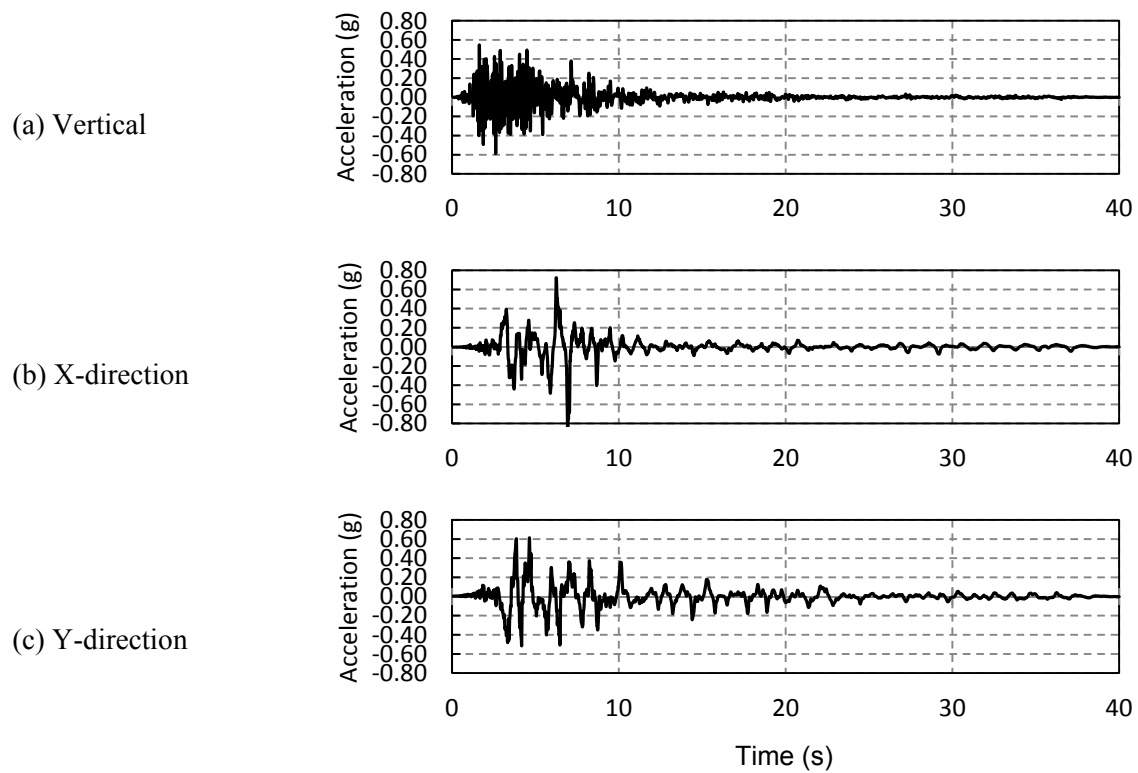


Figure 2-19 Ground motion accelerations: 1994 Northridge, California

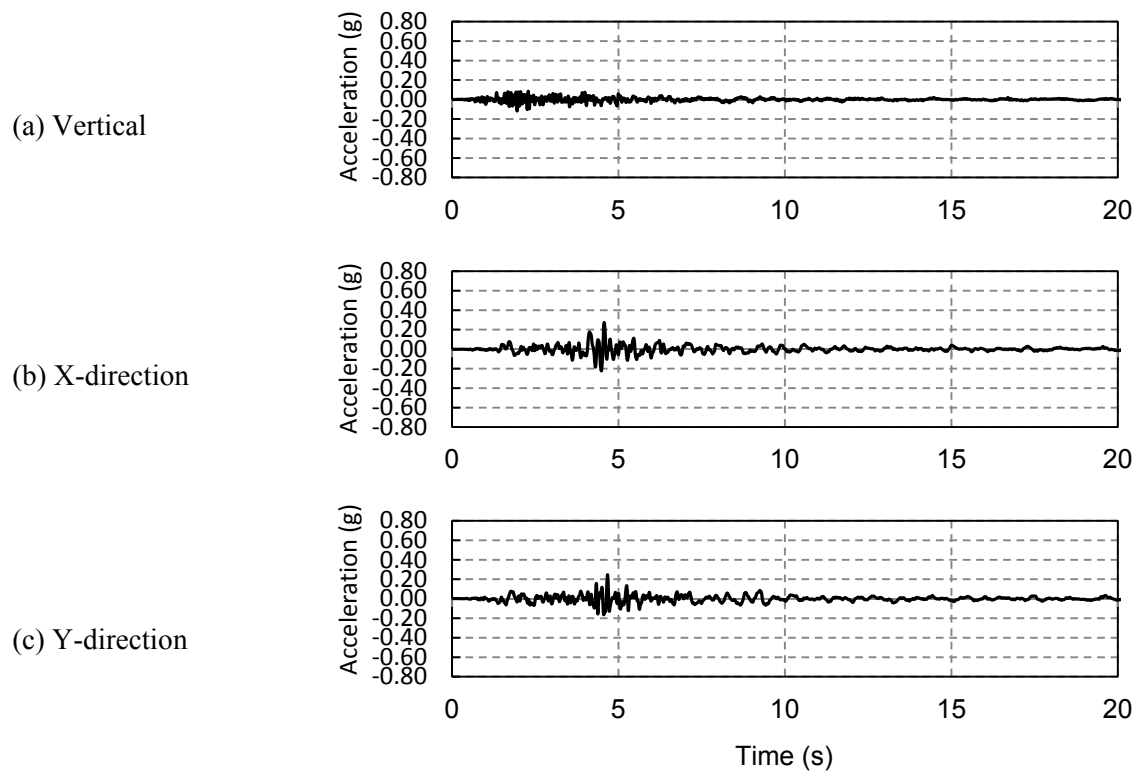


Figure 2-20 Ground motion accelerations: 1966 Parkfield, California

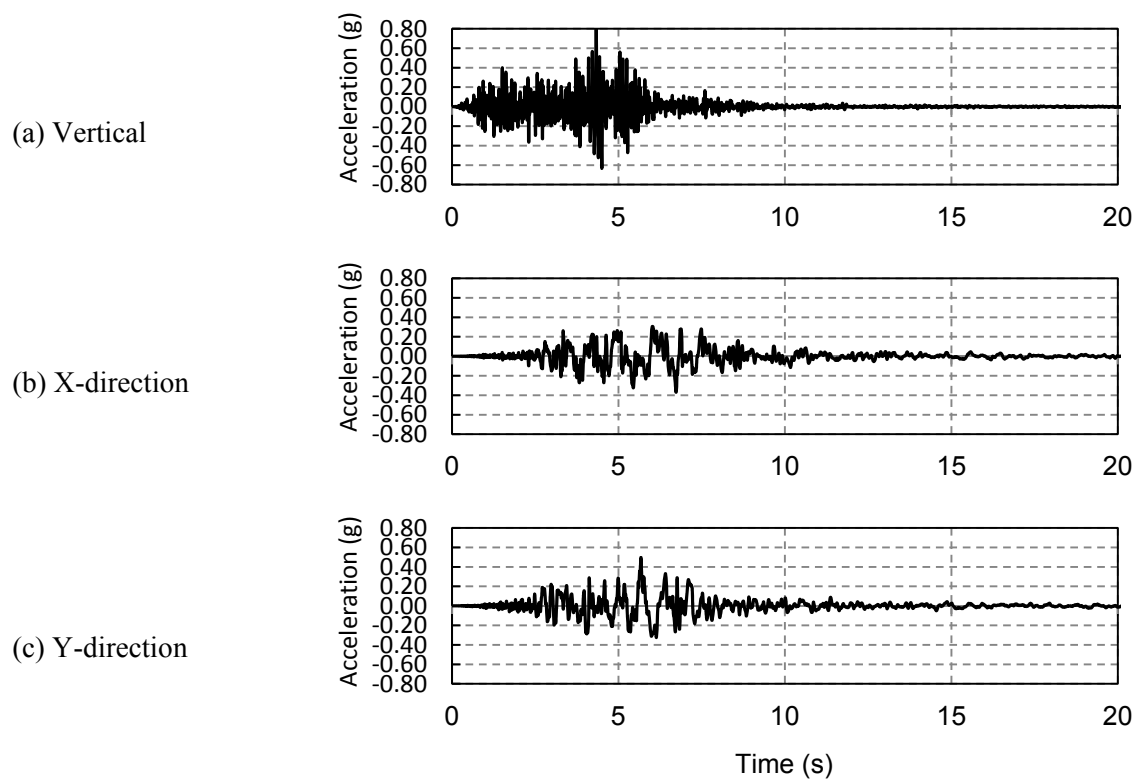


Figure 2-21 Ground motion accelerations: 1981 Westmorland, California

2.4.2 Scaling Selected Ground Motion Records

To reflect the seismic risk for which the prototype building is designed, the selected ground motion records are scaled with the criterion that the response spectral accelerations of these ground motions can match the target design spectrum at the natural period close to that of the structure. For the prototype structure, a design spectral acceleration is determined as $S_{DS} = 1.33g$. Eigenvalue analysis conducted by OpenSees (2011) produces a natural period (T_n) of 0.32 seconds. However, this natural period has not considered the lateral stiffness reduction due to cracking of the structural components. A pushover analysis is conducted to consider the effects of concrete cracking. Based on the elastic drift limit of 0.3 in. and a design base shear of 156 kips, a natural period of 0.41 second is found for the prototype structure and used to scale the selected ground motion records. Duhamel's Integration with the use of Simpson Method was employed to generate response spectrum for the motion records and to determine the appropriate scale factors for transverse (X) and longitudinal (Y) ground motion components. An example using the 1994 Northridge earthquake is given subsequently.

In order to assure the numerical analysis is providing reliable results, unscaled ground motion records are used in the numerical analysis and the resulting spectral response accelerations are compared with those given by PEER for various periods. Mathcad (2015), engineering calculation software, is used to implement Duhamel's Integrations. A damping ratio of 5% is assumed and Simpson's Method is applied to evaluate the numerical integration. Figure 2-22 presents the response spectral acceleration verse natural period for the ground motions in longitudinal and transverse directions for the 1994 Northridge earthquake. It is seen that a good correlation exists. The minor differences likely result from unknown assumptions and procedures used by PEER to develop the response spectrum.

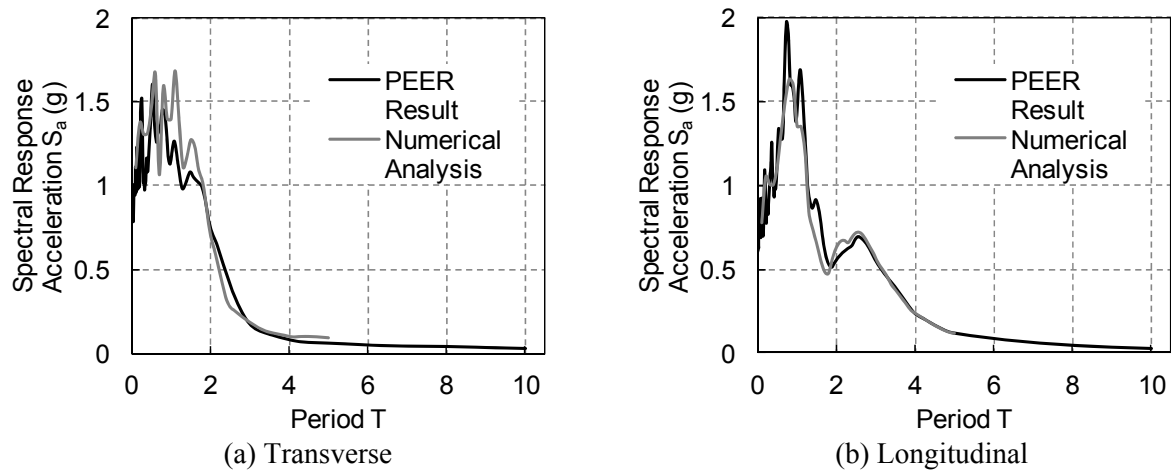


Figure 2-22 Comparison of response spectra obtained in this study and by PEER for 1994 Northridge earthquake

When ground motion is applied in two directions for three dimensional analyses, ASCE 7-10 (2010) requires the ground motions be scaled so that the average of the square root of the sum of squares (SRSS) response spectra from each horizontal component does not fall below the design spectrum over the period range of $0.2T_1$ to $1.5T_1$, where T_1 is the fundamental period of the structure. FEMA P-58 (2012) also gives scaling recommendations for intensity-based assessments by constructing a geometric mean or geomean (S_{gm}) represented by

$$S_{gm}(T) = \sqrt{S_x(T) \cdot S_y(T)} \quad \text{Equation 2-19}$$

where $S_x(T)$ and $S_y(T)$ are two orthogonal components of spectral acceleration at a natural period of T for a ground motion. The geomean spectrum for each ground motion is then compared with the design spectrum over the period range of $0.2T_1$ and $2.0T_1$ for an adequate fit.

The two horizontal motion records of each selected earthquake are individually scaled using the aforementioned scaling approaches. The results are shown comparatively with the design spectrum in Figure 2-23 and 2-24. A summary of the average scaled response spectrum determined based on the SRSS and average geomean methods for all the eight earthquakes are

shown in Figure 2-25. It is seen from the figures that the spectral accelerations scaled using the SRSS method recommended in ASCE 7-10 (2010) for each ground motion are above or near the design spectrum in the period range of interest. This also results in an average spectrum using the ASCE 7-10 approach greater than the design spectrum by a factor varying between 1.35 and 1.43. This is consistent with the statement in FEMA P-752 (2012): the use of SRSS of two spectra will always be larger than its average response spectra by a factor of 1.4 to 1.5. However, as shown in Figure 2-26, the geomean spectrum for each ground motion displays a relatively good fit with the design spectrum in the required period range and thus is used in this study to scale the selected ground motion records for the time-history analyses of the prototype building.

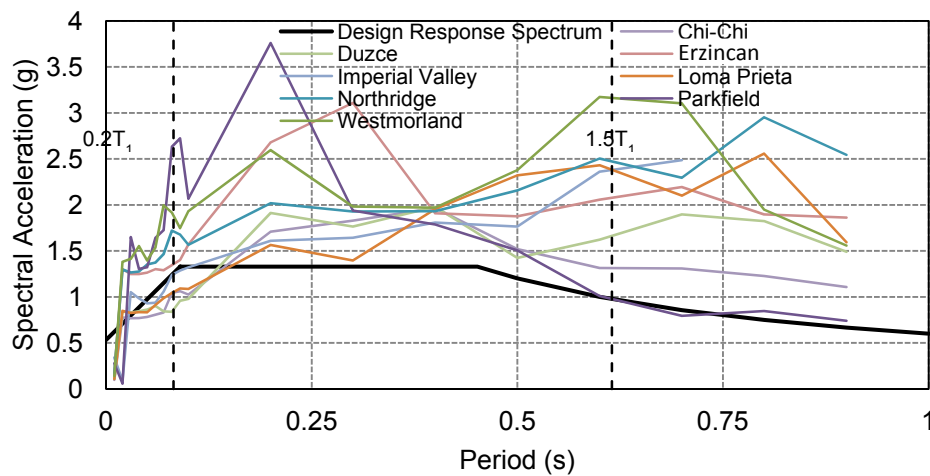


Figure 2-23 Response spectra for scaled motion record using SRSS method

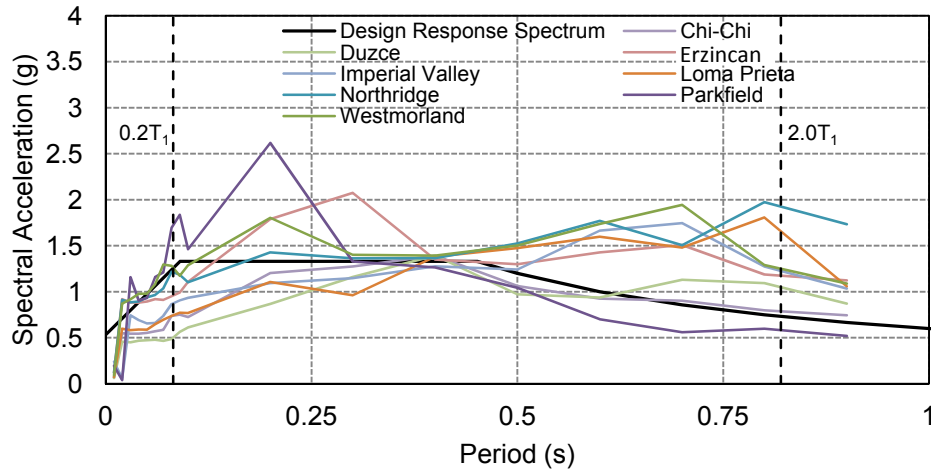


Figure 2-24 Geomean for each scaled seismic records

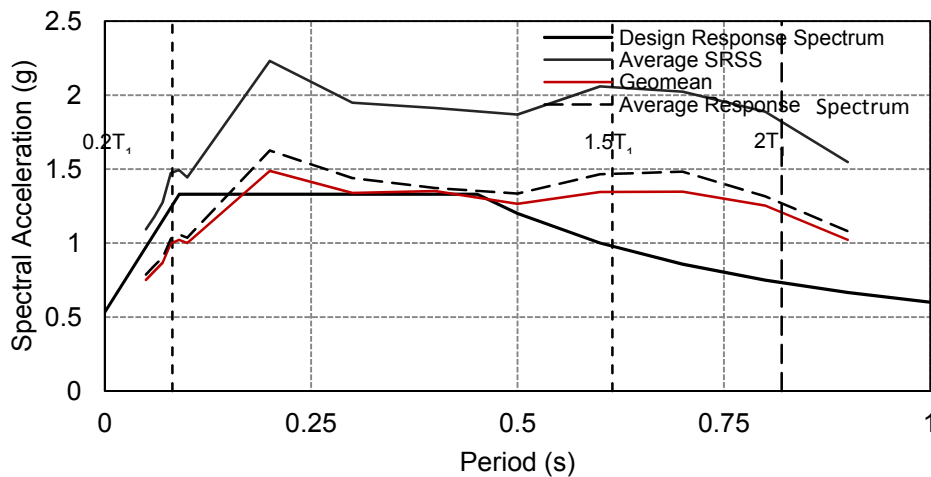


Figure 2-25 Average SRSS and geomean for scaled seismic records

The scaling process uses trial and error until desired results shown in Figures 2-23 and 2-24 are achieved. The scaling considers varying natural periods of a structure in the range of interest. A sample of the scaling results is shown in Table 2-5 for the 1994 Northridge earthquake for a natural period of $T = 0.41$ s for the prototype building and a target spectral acceleration of 1.33g. For comparison purpose, Table 2-5 also shows the spectral accelerations for the two horizontal components for some other natural periods ranging from 0.39 s to 0.43 s. Once the horizontal ground motions have been scaled, the vertical ground motion record of a selected earthquake is then scaled.

Table 2-5 Scaled spectral accelerations for 1994 Northridge earthquake

	Transverse	Longitudinal
Period (s)	Spectral Acceleration (g)	Spectral Acceleration (g)
0.39	1.422	1.358
0.40	1.403	1.329
0.41	1.33	1.33
0.42	1.285	1.331
0.43	1.309	1.33

Currently, various approaches for scaling ground motion exist. The national earthquake hazards reduction program (NEHRP), compiled code recommendations for selecting and scaling earthquake ground motion (NIST, 2011) and identified that scaling of vertical ground motions is a key concern facing design professionals. Several codes were evaluated including ASCE/SEI 7-05 (2006), ASCE/SEI 7-10 (2010), ASCE/SEI 41-06 (2007), AASHTO LRFD Bridge Design Specifications (2010), ASCE/SEI 43-05 (2005), FERC (2007), FEMA 65 (2005), EC1110-2-6000 (2009), and UFC 3-310-04 (2004). However, only the EC1110-2-6000 (2009) by the Civil Works, U.S. Army Corps of Engineers mentions any recommendations regarding the scaling of vertical ground motion and states that *“The vertical component is usually scaled by the same factor used for the horizontal components. If the vertical component is important to the response of the structure, the response spectra of the vertical components of the records should be evaluated for reasonableness by comparing the spectra with a design vertical spectrum.”*

Therefore, the vertical ground motion is scaled using the same factor for scaling the horizontal ground motions. For a specific selected earthquake, the larger of the two horizontal scale factors considered in the previous scaling process is used. The scale factors finally chosen are summarized in Table 3-6 for each ground motion. Figure 2-23 shows the vertical response

spectrum for each vertical ground motion compared with the design spectrum of vertical ground motion determined based on ASCE/SEI 7-10 (2010). The average spectral acceleration is also shown in this figure by the dashed line. It is seen that the average vertical response spectrum for the vertical ground motions is close to the design spectrum. In addition, the natural period of the prototype building for vertical vibration is determined as 0.16 s, which is also shown in Figure 2-26. Corresponding to this vibration period, the spectral acceleration of 1.52g is defined by ASCE/SEI 7-10 (2010), which is about 19% greater than that defined by the average response spectrum. Figures 2-27 through 2-34 show the scaled ground motion acceleration histories for all the three components that are ultimately applied to the prototype structure in the nonlinear dynamic analyses.

Table 2-6 Scale Factors for Selected Ground motions

Earthquake	Station	Scale Factor for PGA (g)		
		Long.	Trans.	Vert.
Chi-Chi, Taiwan	CHY024	1.92	2.91	2.91
Duzce, Turkey	Duzce	0.72	1.44	1.44
Erzincan, Turkey	95 Erzincan	1.72	1.74	1.74
Imperial Valley, California	Chihuahua	2.32	2.30	2.32
Loma Prieta, California	Halls Valley	5.28	4.45	5.28
Northridge, California	Sylmar-Converter	1.32	1.07	1.32
Parkfield, California	Cholame	3.84	3.27	3.84
Westmorland, California	Westmorland Fire Sta.	2.19	1.62	2.19

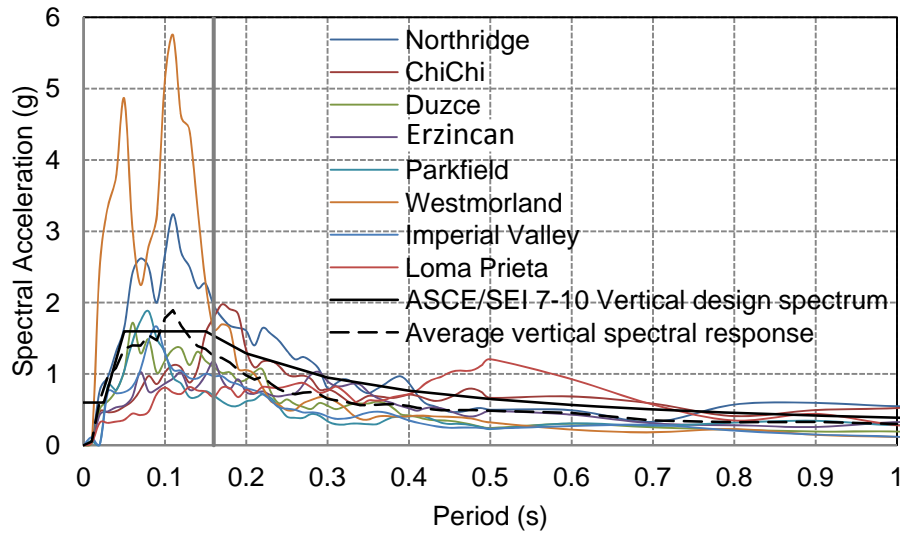


Figure 2-26 Vertical design spectrum verse scaled vertical response spectrum

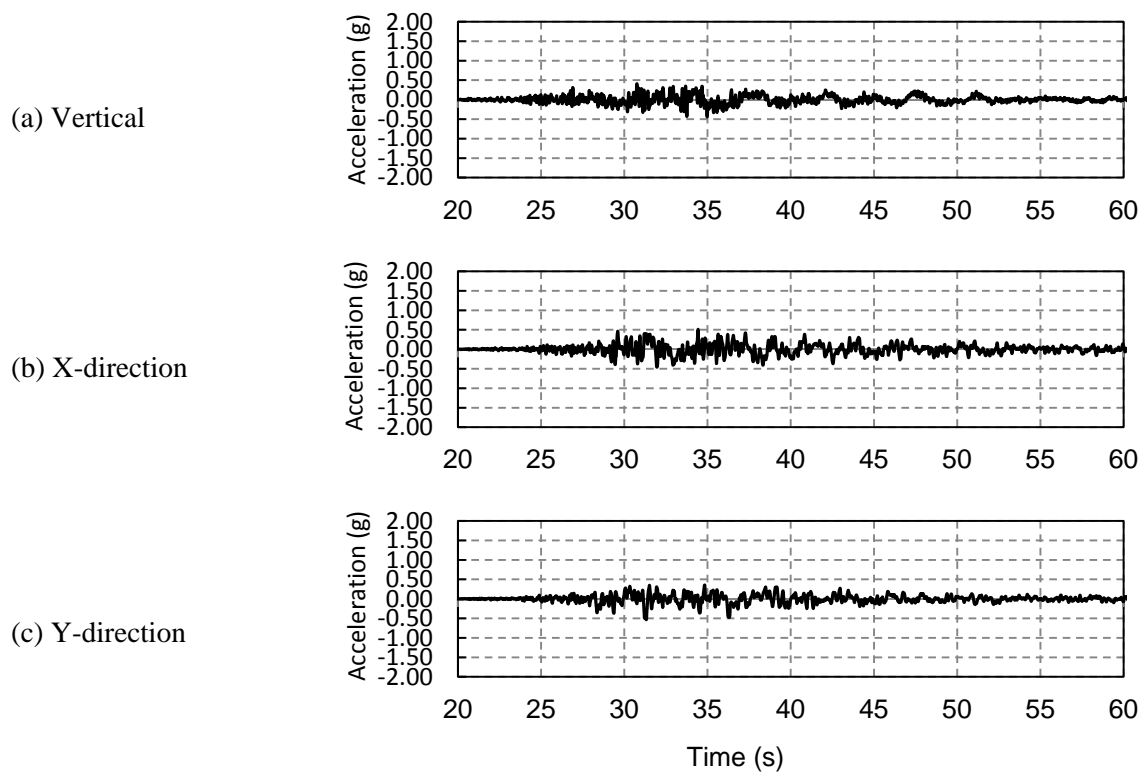


Figure 2-27 Scaled ground motion accelerations: 1999 Chi-Chi, Taiwan

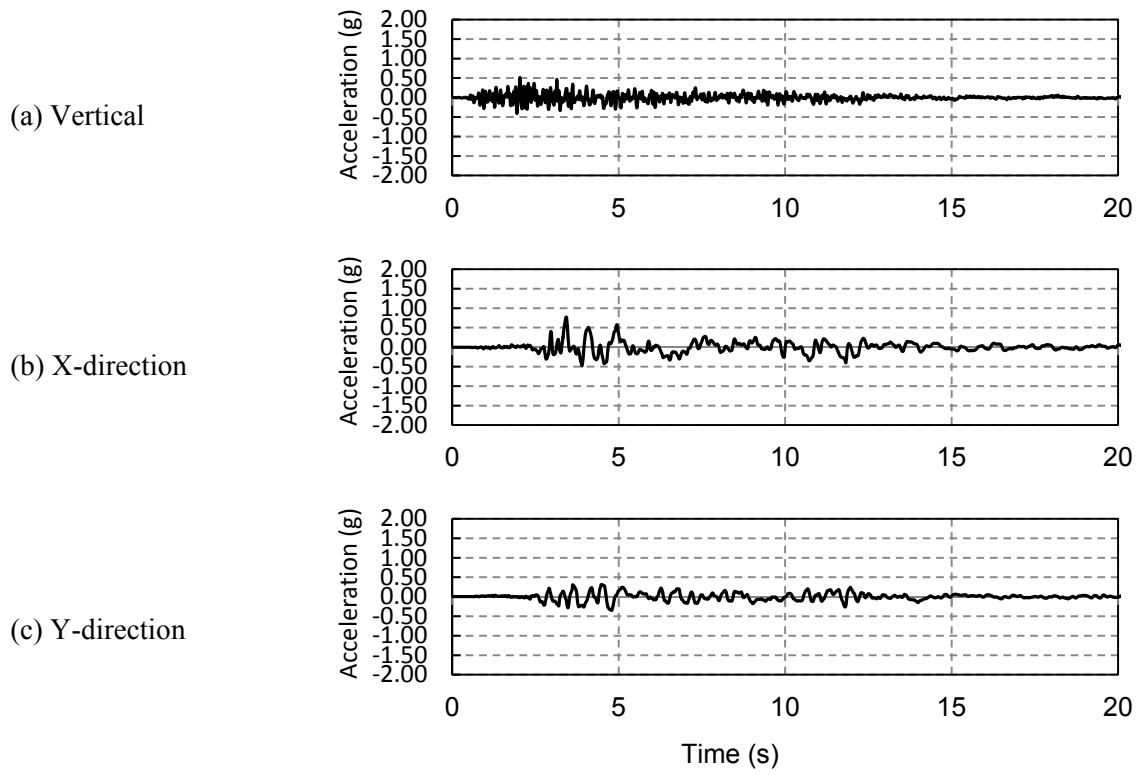


Figure 2-28 Scaled ground motion accelerations: 1999 Duzce, Turkey

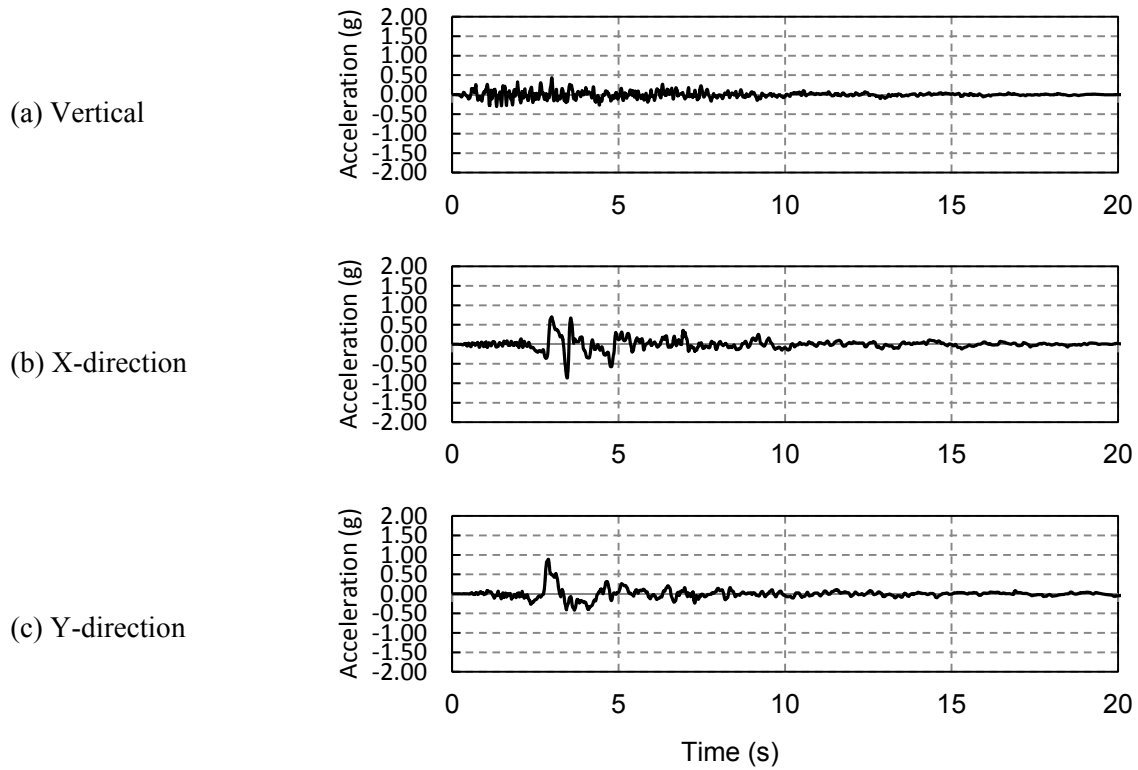


Figure 2-29 Scaled ground motion accelerations: 1992 Erzincan, Turkey

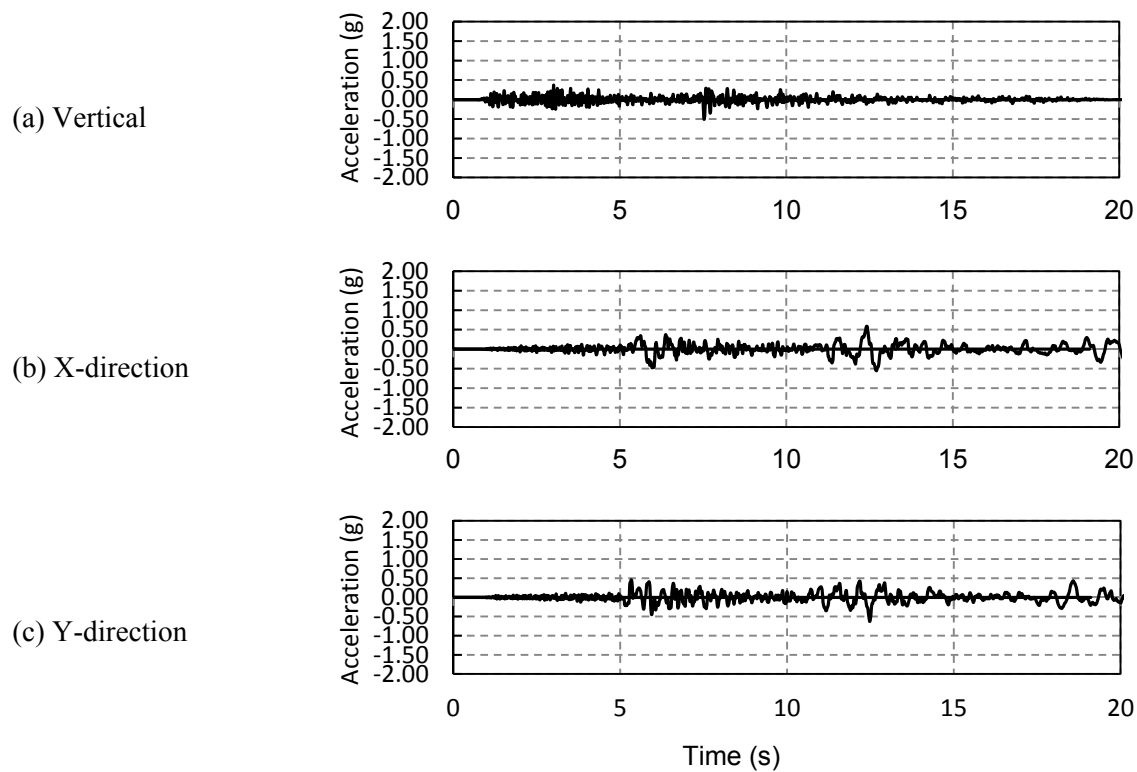


Figure 2-30 Scaled ground motion accelerations: 1979 Imperial Valley, California

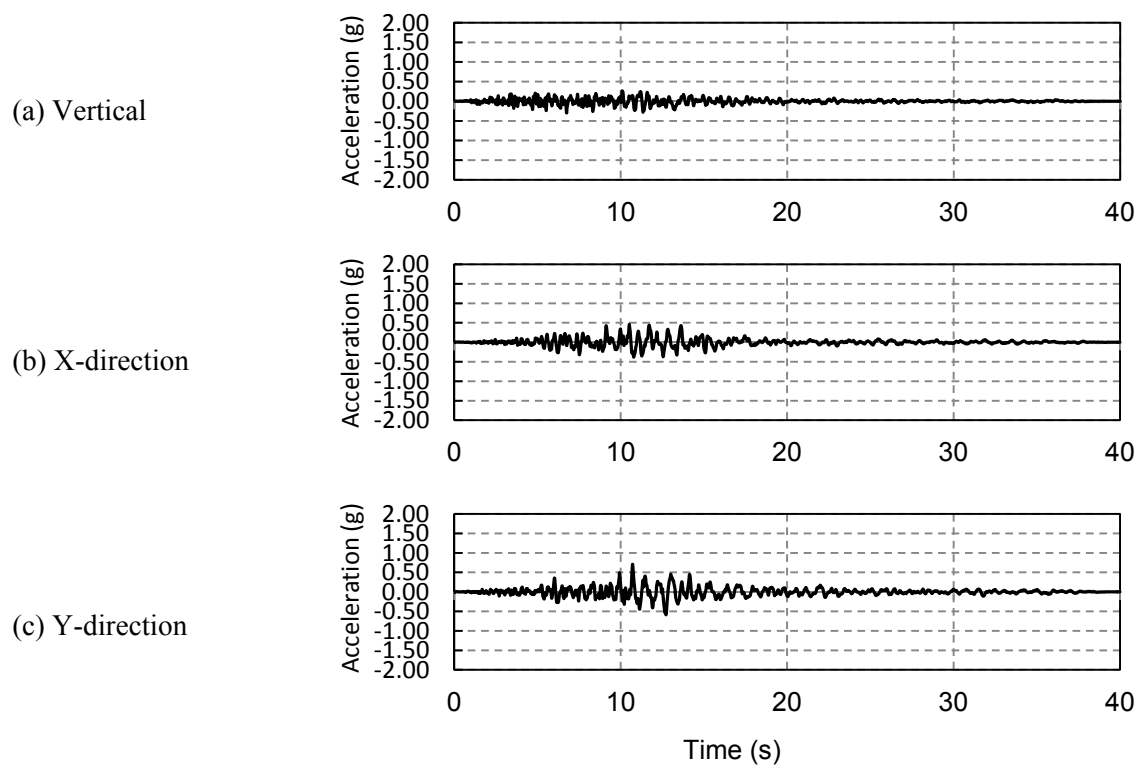


Figure 2-31 Scaled ground motion accelerations: 1989 Loma Prieta, California

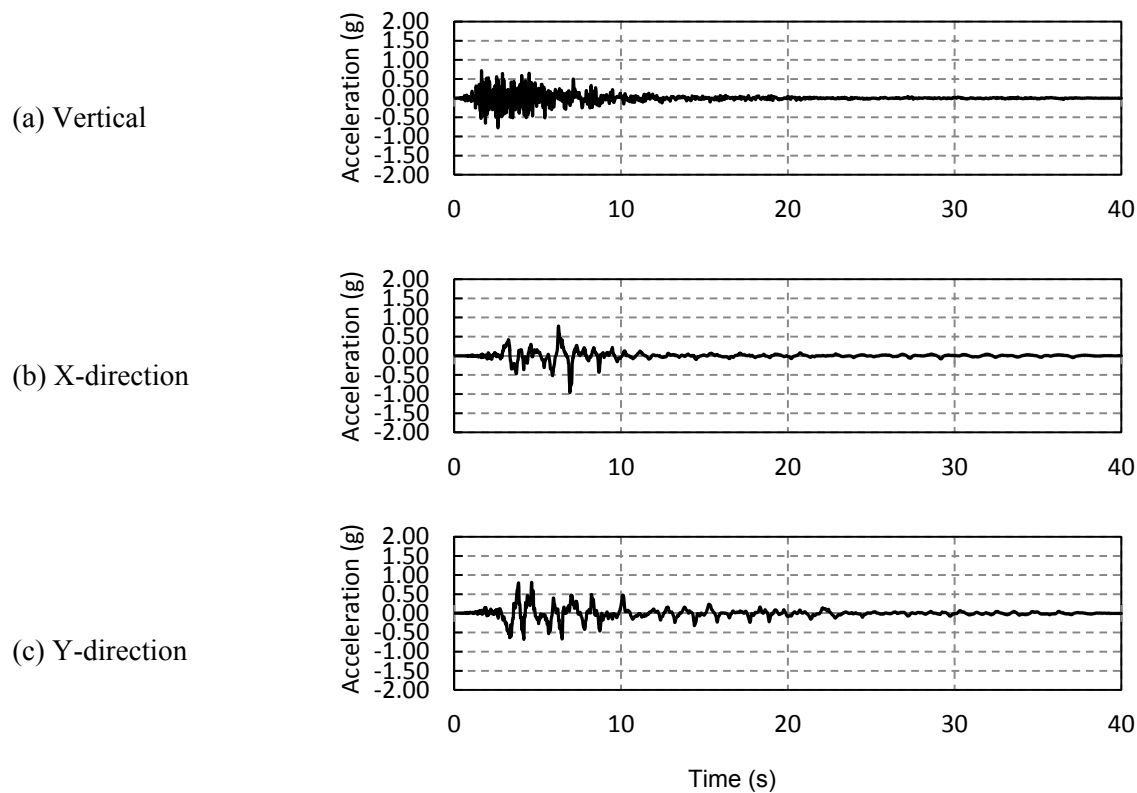


Figure 2-32 Scaled ground motion accelerations: 1994 Northridge, California

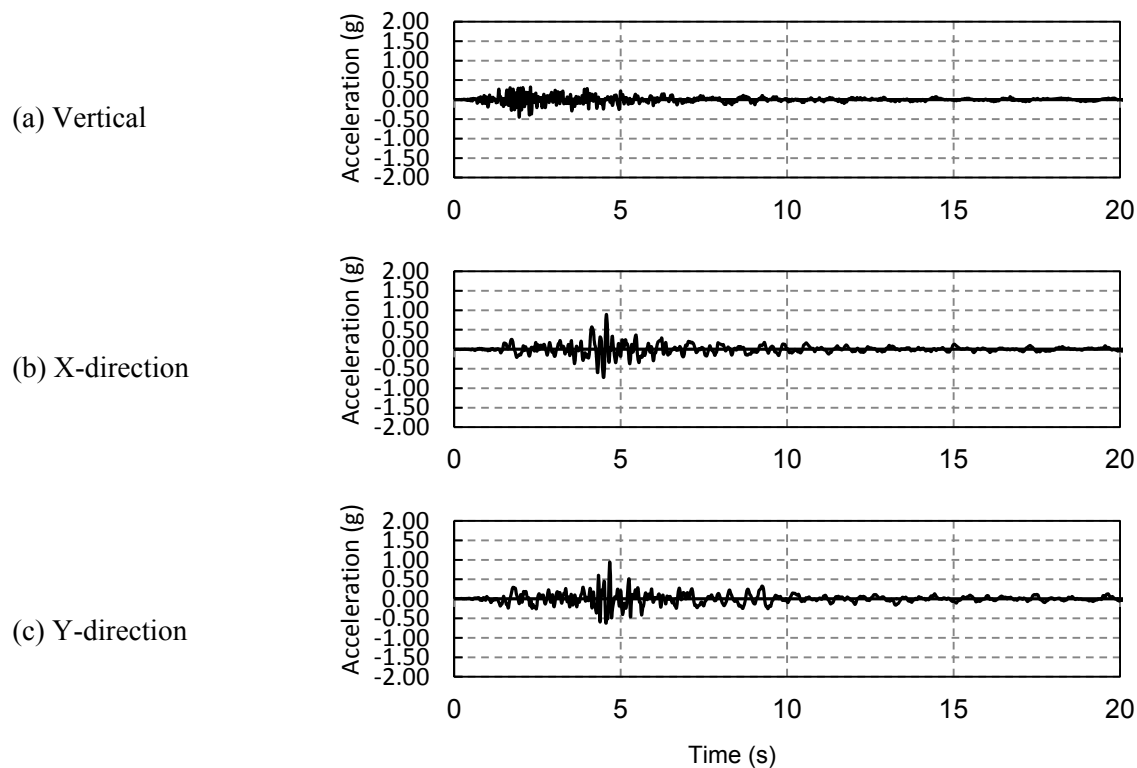


Figure 2-33 Scaled ground motion accelerations: 1966 Parkfield, California

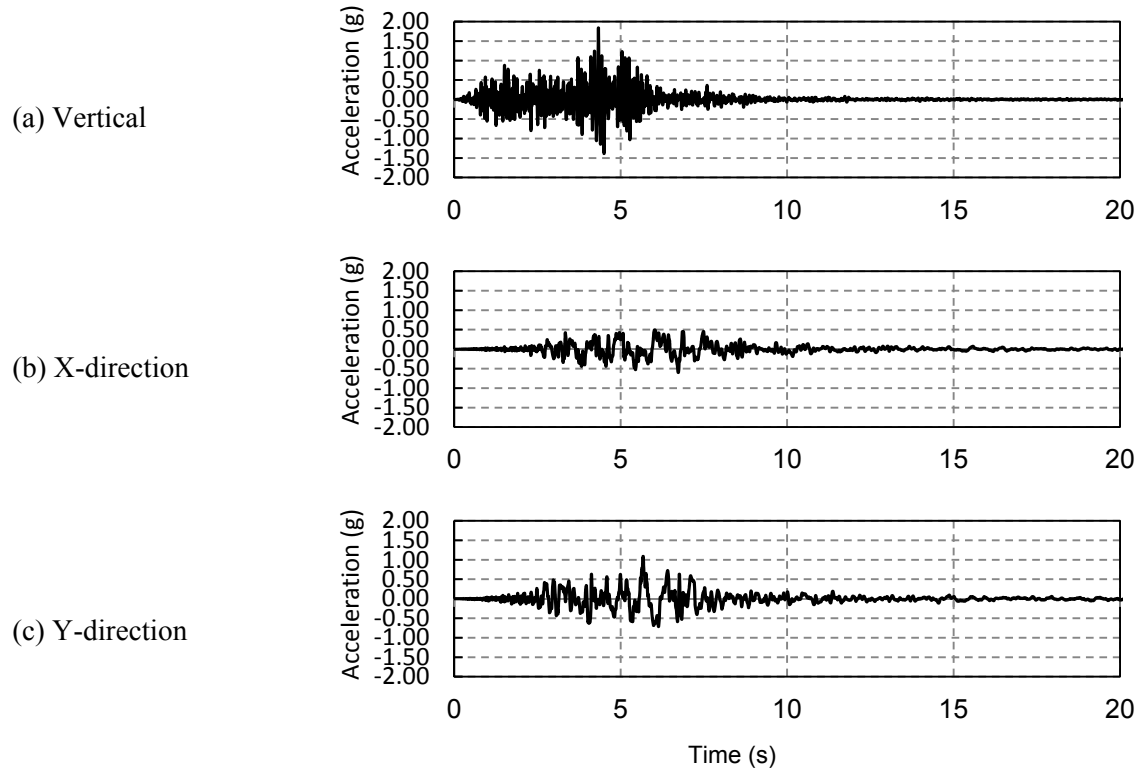


Figure 2-34 Scaled ground motion accelerations: 1981 Westmorland, California

2.4.3 Analysis Procedure

Gravity loads, as described earlier, are applied first in an analysis and followed by lateral loading. Two types of lateral loading analysis are conducted: (1) nonlinear static analysis (pushover analysis) and (2) nonlinear dynamic analysis. For the pushover analysis, a displacement-driven analysis is conducted to identify the stiffness and strength contribution for the slab-column framing. The structure is initially analyzed with gravity load alone. The structure is then pushed at an increment of 0.01 in. until a specified displacement is achieved or convergence is no longer obtained.

Nonlinear dynamic analyses constitute the primary body of this research. During a dynamic analysis, ground motions are uniformly applied at the supports. Newmark integrator is used with a gamma value of 0.5 and beta of 0.25 which is equal to the average acceleration

method. Because a small time step (< 0.1 sec.) is employed for most ground motions, the Newmark method with aforementioned parameters will be stable. A damping matrix must also be defined for the Newmark method. The damping matrix may be specified as a combination of stiffness and mass damping matrices. In this study, a damping ratio of 5% is used as recommended by Newmark and Hall (1982) for reinforced concrete structures with considerable cracking and specified by code for earthquake forces and design spectrum (Chopra, 2007). The Rayleigh damping matrix is specified as a combination of a mass matrix determined at initial loading state and a tangent stiffness matrix determined at the last analysis step.

CHAPTER 3

DYNAMIC FORCE AND DEFORMATION DEMANDS OF PROTOTYPE STRUCTURE

3.1 OVERVIEW

Finite element analyses using the modeling approach described in the previous chapter are to estimate the performance of the prototype building under seismic loading. Two types of analysis are conducted: nonlinear static (pushover) analysis and nonlinear time-history analysis. The purpose of pushover analyses is to identify the lateral stiffness and strength contributed by the slab-column framing.

For the dynamic analyses, because seismic event consists of motion in three directions, four combinations of scaled ground motions were applied to the prototype structure separately: transverse x-direction, longitudinal y-direction, x and y directions simultaneously (bi-directional), and x, y and vertical z-direction simultaneously (tri-directional). This procedure is repeated for all eight scaled seismic ground motions. Five of the seismic records were truncated due to a peak ground acceleration of nearly zero at the beginning or end of the time history. The ground motion records for the 1999 Chi Chi, 1992 Erzincan, 1989 Loma Prieta, 1994 Northridge, and 1966 Parkfield earthquakes, were adopted only during the following time intervals: 20 to 60 seconds, 0 to 10 seconds, 0 to 20 seconds, 0 to 20 seconds, and 0 to 10 seconds respectively. It should be noted for the subsequent results that a time of zero seconds corresponds to the beginning of a truncated ground motion. The dynamic responses to be identified from the simulations include both global and local responses. The roof lateral displacement is taken as a global dynamic response index; the rotation of slab relative to the columns, the vertical deflection at slab panel center, the axial force in the interior columns of flat plates, and the shear forces at slab-column connections are used as local response parameters. For convenience of

presenting analysis results regarding the aforementioned response parameters, relevant nodes for column and slab are given in Figures 3-1 and 3-2. Nodes 4012, 5007, and 5012 are positioned at the center of the column at the slab level (slab-column joint center). Nodes 328, 867, and 878 are situated at the center of three slab panels. All other nodes shown in Figure 3-2 connect elements with slab-column joint and are located a distance of 20 inches from face of column, where the slab rotations relative to the column are identified.

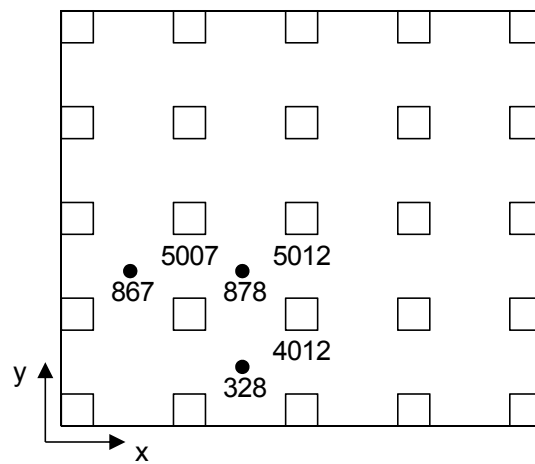


Figure 3-1 Reference diagram for prototype building

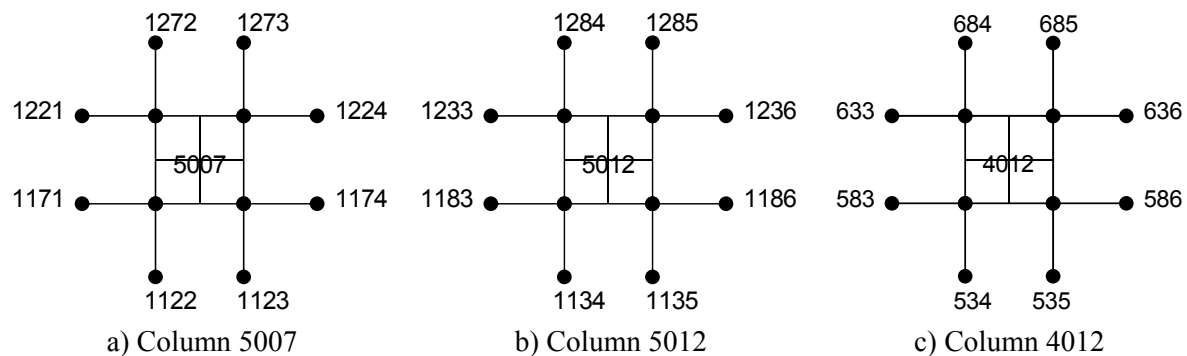


Figure 3-2 Node layout at slab-column connections

3.2 RESULTS OF PUSHOVER ANALYSIS

Two pushover analyses are conducted, one on the perimeter moment frames without slab-column framing and another one on the entire structure. Figure 3-3 shows the lateral force vs. lateral roof displacement response. It is seen that the moment frames are the main lateral force-resisting system contributing a majority of the lateral resistance. However, even though the slab-column framing are inherently weaker than the moment frames, it can still provide more than 20% extra strength and stiffness due mainly to the larger number of slab-column connections existing in the building. At a lateral displacement of 1 in., corresponding to 0.8% drift ratio, a force difference of 100 kips between the two pushover analyses is calculated.

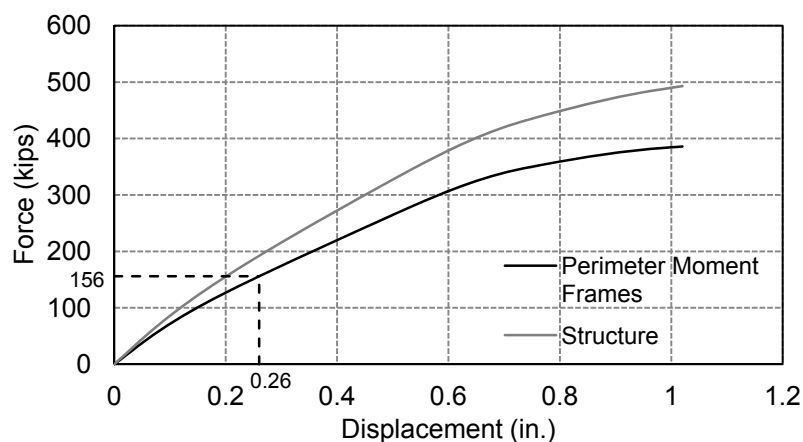


Figure 3-3 Lateral load vs. lateral displacement response obtained from pushover analyses of the prototype structure

Furthermore, the pushover analysis of the primary lateral load-resisting system predicts a 0.26 in. lateral displacement at the design base shear of 156 kips. This lateral drift is within the elastic drift limit set by ASCE 7-10 (2010). It is noted that the actual lateral strength, as shown in Figure 3-3, is far greater than the 156 kips design base shear. This is due to the use of load

increase factors, the strength reduction factors, and the inherent overstrength properties of a RC structure.

3.3 DYNAMIC LATERAL DISPLACEMENT RESPONSE

Lateral drift is considered one of the indicators of seismic response of a building structure. To understand the effect of vertical ground motion on the lateral displacement response of the prototype structure, the time-history of lateral drift at roof is recorded for the four separate combinations of ground motion mentioned previously. Due to the high in-plane rigidity of slab and beams, the columns displace similarly. Therefore, only the displacement time-history at the top of the center column of the building (node 5012 per Figure 3-1) is presented.

3.3.1 Lateral Displacement under Uni-directional Ground Motion

Figures 3-4 and 3-5 demonstrate the lateral displacement response for seismic ground motion applied only in the x-direction and y-direction, respectively. All these uni-directional ground motions caused relatively large lateral deformations. Under x-direction ground motion, the scaled 1994 Northridge ground motion produces the largest lateral displacement of 3.73 in. corresponding to a 3.1% drift ratio, whereas the scaled 1966 Parkfield ground motion results in the lowest peak lateral displacement of 1.76 in. The average peak horizontal displacement from all eight seismic events was 2.78 in. with an average drift ratio of 2.32%. Under x-direction ground motion, the largest peak lateral displacement of 5.52 in. is produced by the scaled 1981 Westmorland ground motion, while the smallest peak lateral displacement of 1.62 in. is created by the 1999 Chi Chi ground motion. An average lateral drift of 2.94 in. corresponding to a story drift ratio of 2.45% is found for all the eight scaled seismic records.

Note that, according to the structural type (RC structure) and the assumed risk category of the prototype building, the design story drift limit is 2% per ASCE 7-10 (2010). Thus, the

average story drift of the prototype structure under uni-directional ground motions slightly exceeds the drift limit by about 20%. Table 3-1 summaries the peak lateral displacement and story drift ratio obtained from the uni-directional time-history analyses together with those from the response of prototype structure subjected to the bi-directional and tri-directional ground excitations.

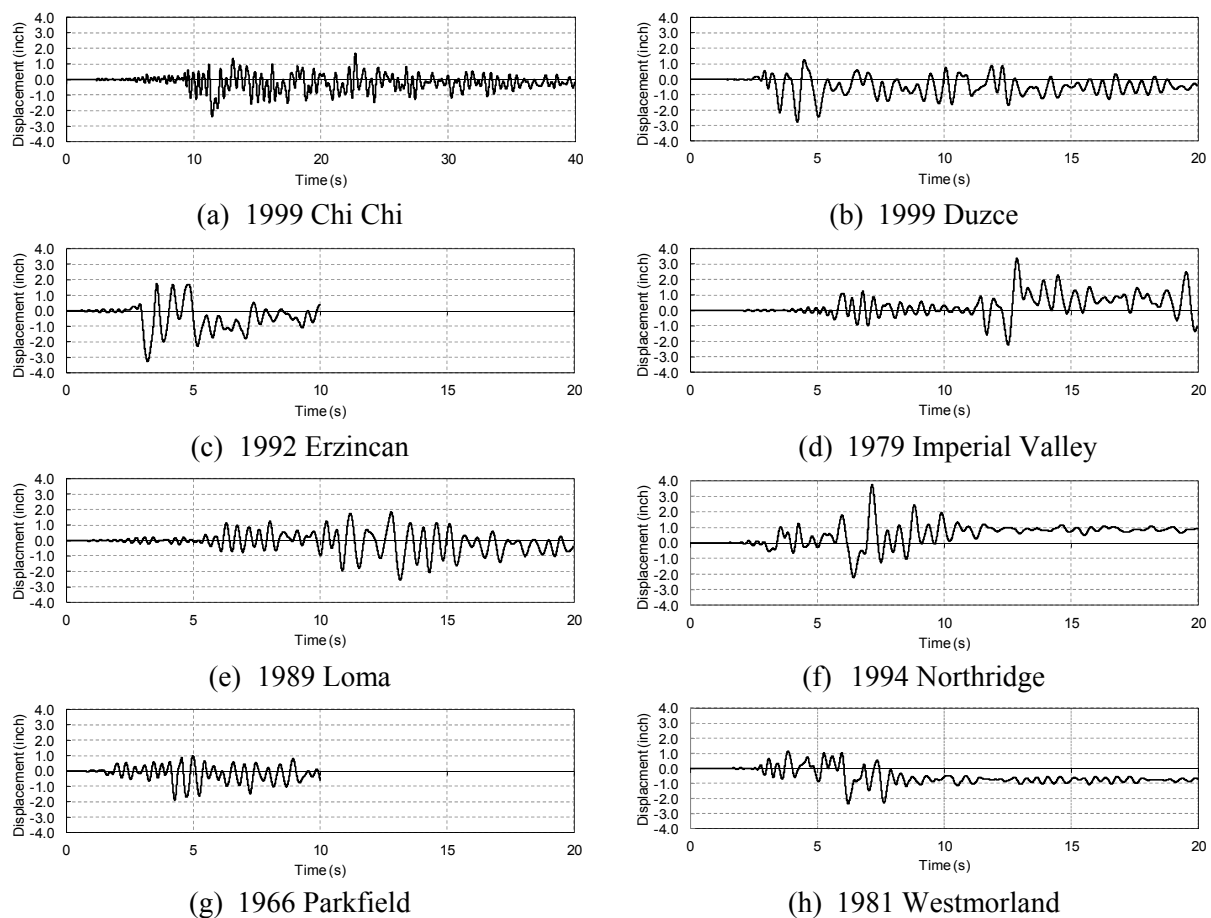


Figure 3-4 Time-history of lateral displacement due to scaled ground motions applied only in x-direction

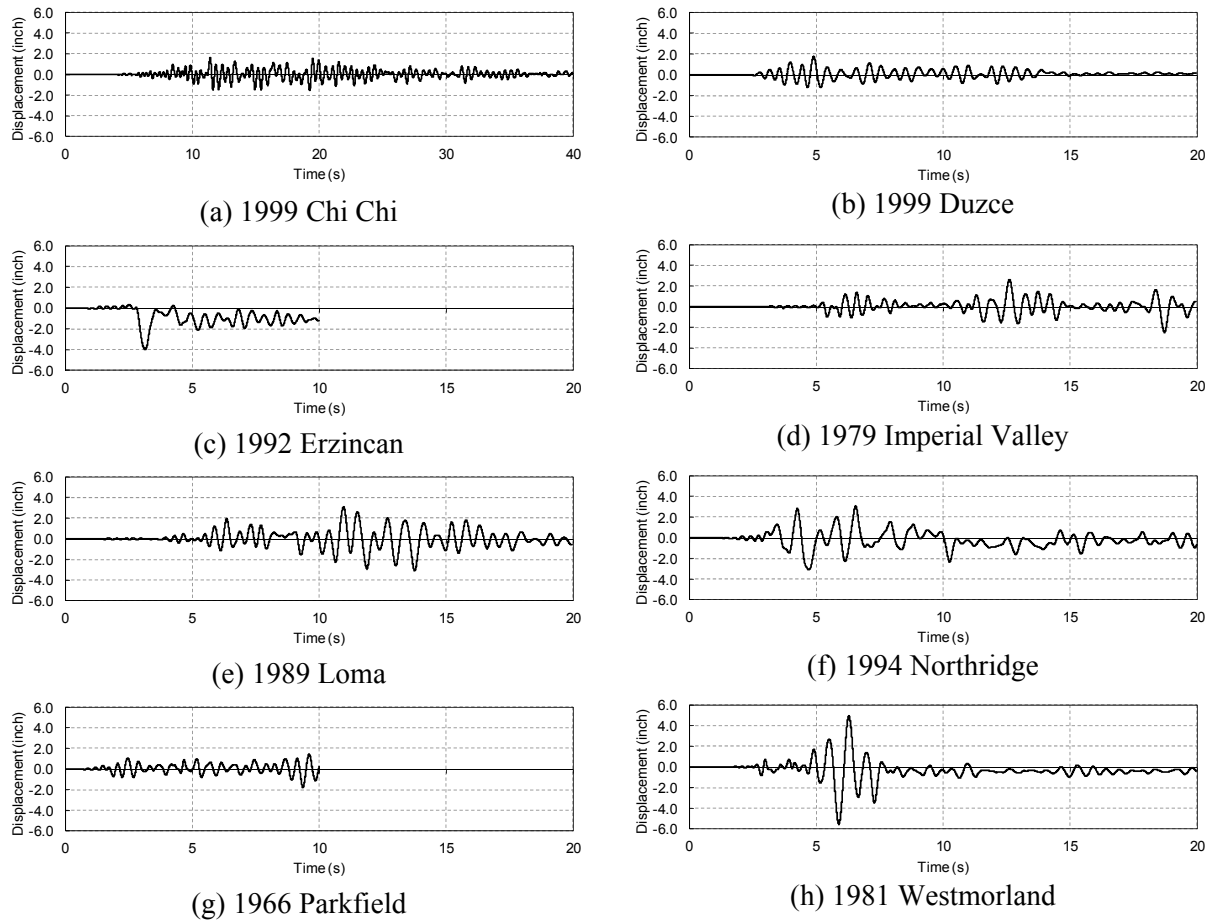


Figure 3-5 Time-history of lateral displacement due to scaled ground motions applied only in y-direction

Table 3-1 Maximum displacement per seismic record

Seismic Record	Displacement (in.)								% Change between bi- and tri-directional motion
	x	y	bi-directional			tri-directional			
			x	y	Resultant	x	y	Resultant	
Chi Chi	2.37	1.62	2.50	1.90	3.00	2.48	1.94	3.03	1.00
Duzce	2.76	1.76	2.88	1.33	3.00	3.26	1.28	3.27	8.61
Erzincan	3.25	3.97	4.74	4.49	6.39	4.85	4.68	6.62	3.54
Imperial Valley	3.36	2.63	3.30	3.19	3.92	3.35	3.23	3.96	1.02
Loma	2.54	3.12	3.66	3.47	3.91	3.65	3.46	3.92	0.26
Northridge	3.73	3.11	5.48	4.38	6.61	5.60	4.76	7.19	8.41
Parkfield	1.88	1.77	1.90	1.45	1.94	1.90	1.44	1.92	-
Westmorland	2.36	5.52	3.54	5.54	6.21	3.6	5.46	6.27	0.96
Average	2.78	2.94	3.50	3.22	4.37	3.59	3.28	4.52	2.84
Ave. Drift Ratio %	2.32	2.45	2.92	2.68	3.64	2.99	2.73	3.77	2.37

3.3.2 Lateral Displacement under Bi-directional Ground Motion

Figure 4-5 shows the lateral displacement response for seismic ground motion applied in the x- and y-direction simultaneously. Because ground motions are applied bi-directionally, the resultant horizontal displacement obtained from the two orthogonal components is provided in this figure. The largest peak lateral displacement for bi-directional loading is 6.61 in. created by the scaled 1994 Northridge ground motion record; the 1966 Parkfield ground motion recorded the lowest peak lateral displacement of 1.94 in. On average a peak lateral displacement of 4.37 in. with an average drift ratio of 3.64% was obtained.

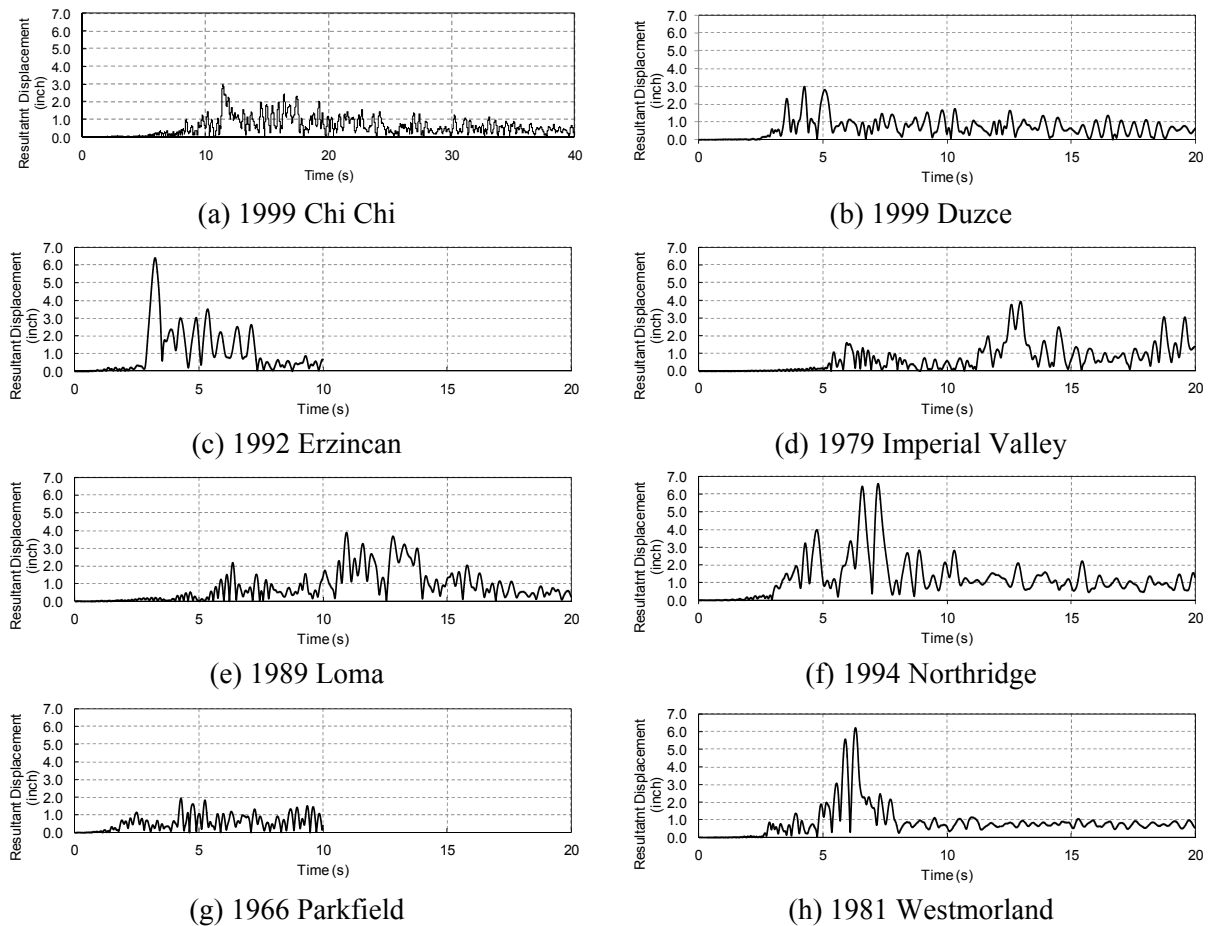


Figure 3-6 Time-history of lateral displacement due to scaled ground motions applied in both x- and y-directions

The analysis results including the peak resultant horizontal displacement, the corresponding two components in the x- and y-directions, story drift ratio, and the average peak response are summarized in Table 3-1. It is seen from the values of two orthogonal components given in this table that, compared with uni-axial loading, the bi-axial loading increased the peak lateral displacement for almost all eight scaled ground motions.

3.3.3 Lateral Displacement under Tri-directional Ground Motion

Figure 3-7 shows the lateral displacement response for seismic ground motion applied in the x-, y- and z- (vertical) directions simultaneously. The lateral displacement shown in this figure is the resultant displacement obtained from its horizontal two orthogonal components. The peak dynamic response is given in Table 3-1 using a similar manner for the uni-axial and bi-axial loading.

Under tri-directional loading, the scaled 1994 Northridge ground motion produces the largest peak lateral displacement of 7.19 in. with an average lateral displacement of 4.52 in. Compared with bi-axial loading, the scaled 1999 Duzce, 1992 Erzincan, and 1994 Northridge ground motions increase the lateral drift by 9%, 4%, and 8%, respectively. However, in general, the incorporation of vertical ground motion does not increase the lateral drift significantly. As shown in Table 3-1, the average drift ratio under tri-directional loading is 3.77 in, which is only 2.4% greater than that under bi-axial loading. Such a result can be expected, because the overall lateral deformation of the entire structural system is governed by the perimeter moment frame, which may not be affected much by the vertical ground motion (Kadid et al. 2010).

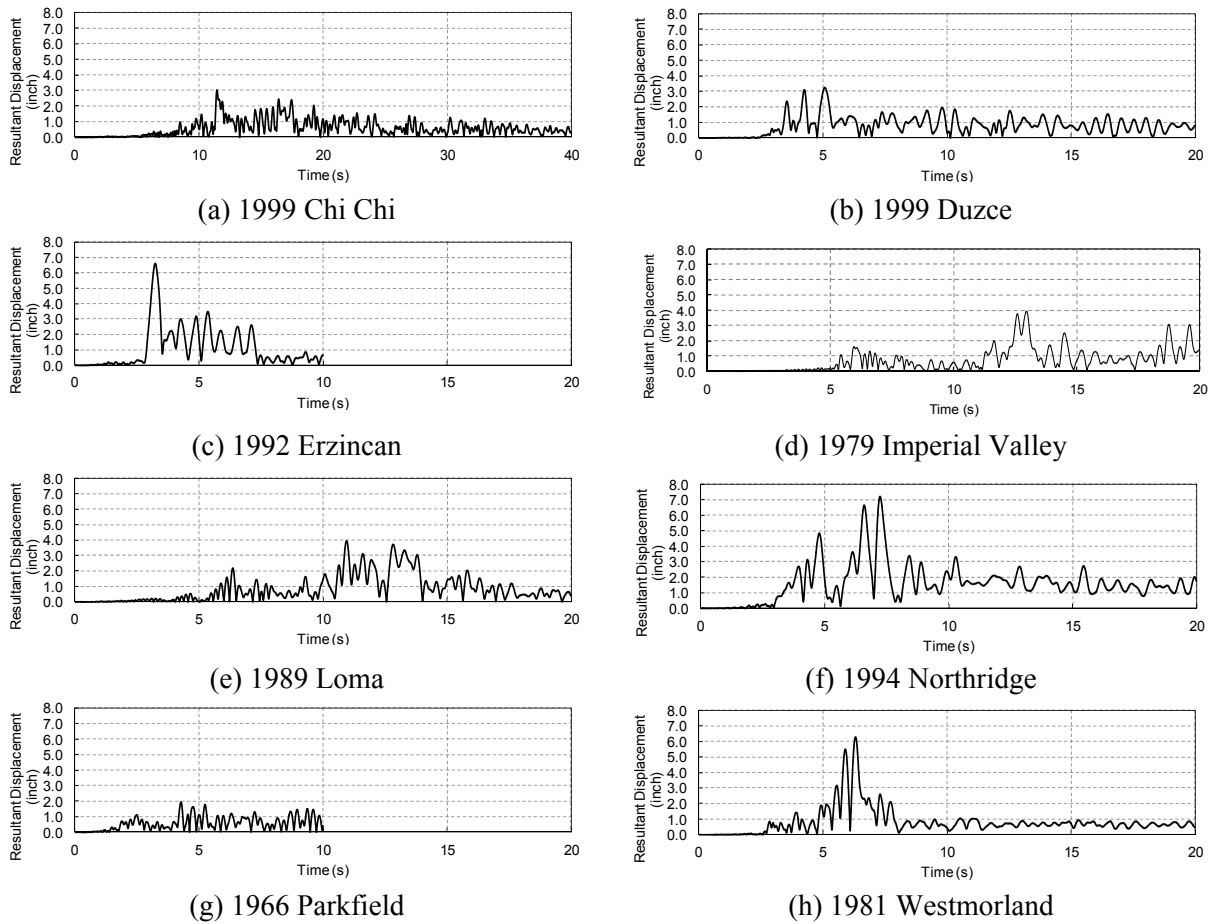


Figure 3-7 Time-history of lateral displacement due to scaled ground motions applied in all three directions

3.4 DYNAMIC RESPONSE OF SLAB ROTATION

For the seismic performance of a flat-plate structure, its resistance to punching failure has long been correlated empirically with gravity load level and lateral drift demand based on experimental data. Such a correlation essentially reflects the influence of slab local deformation near the columns. Even though the effects of this deformation property were generally not measured in the seismic loading experiments, they have been recognized in the tests of slab-column connections under gravity loading. It was found that the rotational response of the slab

near interior columns is a critical indicator of premature punching shear failure in a flat-plate structure (Guandalini et al., 2009).

To identify slab local response of the prototype structure, the time-history of slab rotation relative to column at the far end node of an element connected to the slab-column joint region is obtained from the simulation output data. Slab relative rotation is recorded at each face of the column. However, only the slab rotations at two column faces perpendicular to the line of motion are of interest. Furthermore, there are two elements at each column face. Because they behave almost identically, only the slab rotation at one of the two elements is reported. For instance, under x-direction ground motion, even though there are eight nodes surrounding column 5007 (Figure 3-1), only the relative rotations at nodes 1171 and 1174 are examined.

3.4.1 Slab Rotation under Uni-directional Ground Motion

Slab relative rotation about the y-axis near the column due to the ground motion applied only in the x-direction is recorded for the eight seismic records. The largest slab relative rotations are consistently found near column 5007; therefore the rotational response is reported at the two nodes 1171 and 1174 located on either side of this column per Figure 3-8. It is observed that the reach of the peak slab rotation response coincides with that of the peak roof lateral displacement response, indicating that slab rotation relative to column is caused primarily by lateral drift in the uni-axial loading condition.

Same as for the lateral displacement response, the scaled 1994 Northridge ground motion causes the greatest slab rotation. As shown in Figure 3-8, the slab rotation reaches a peak value as high as almost 0.05 rad. and leads to a high unrecoverable residual rotational deformation of about 0.025 rad. It is noteworthy that such a large slab rotational deformation capacity can seldom be observed from the test data of slab-column connections. The large slab rotation can

lead to wide inclined shear crack and significantly undermined aggregate interlocking force that contributes to connection shear strength (Guandalini et al., 2009). Thus, it is likely that, even without considering ground motions applied in the two other directions, the scaled 1994 Northridge ground motion in the x-direction can cause punching failure in the prototype structure. The 1966 Parkfield ground motion causes the smallest peak slab relative rotation of approximately 0.02 rad.

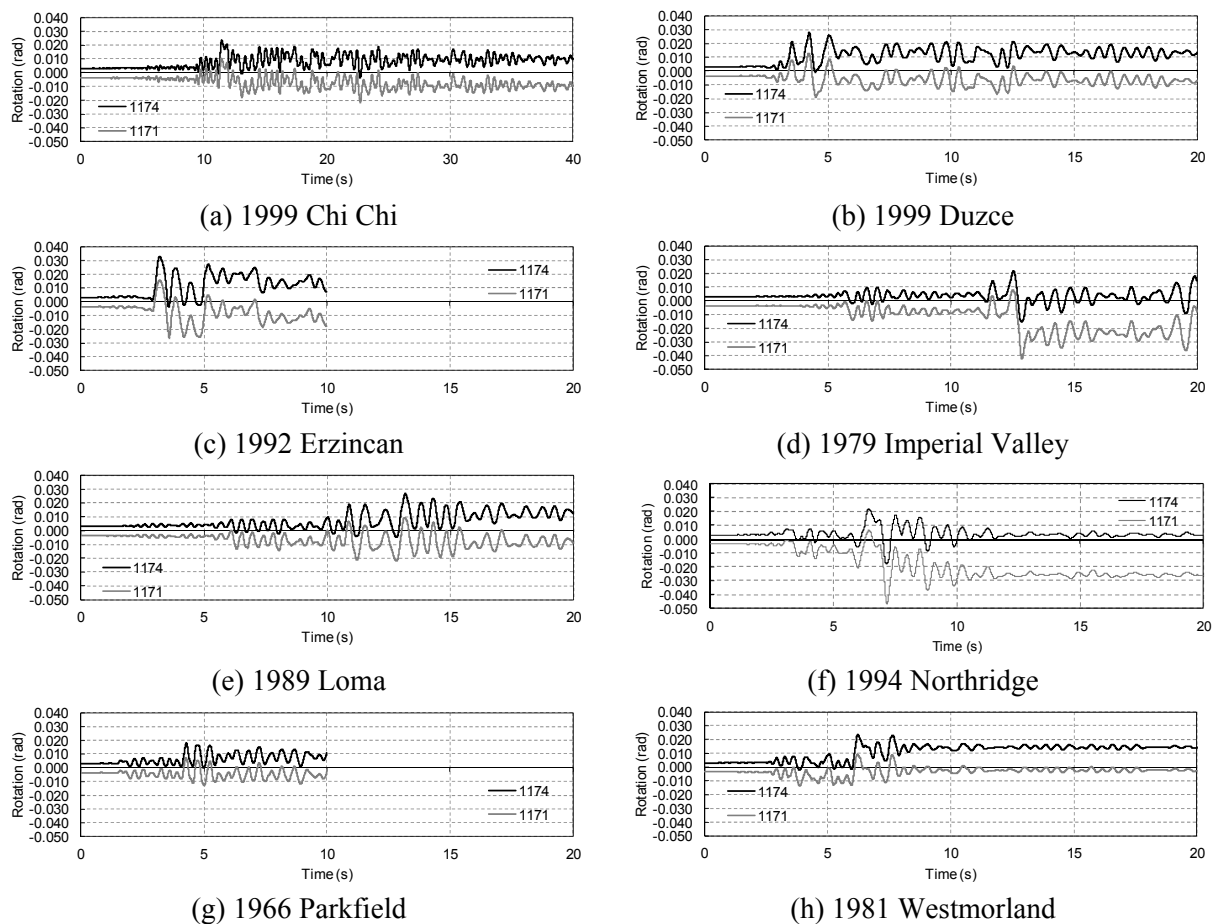


Figure 3-8 Slab rotation about y-axis at two nodes neighboring column 5007 due to scaled ground motions applied only in x-direction

Under the scaled ground motions applied only in the y-direction, the peak slab rotation response also happens along with the peak lateral drift response and the largest slab relative

rotation is found near column 4012. The slab rotational response about x-axis is reported at the two nodes 684 and 534 located on either side of this column (see Figure 4-1). Figure 4-8 shows the slab relative rotation time-history for the eight scaled seismic records. Same as for lateral displacement response, the scaled 1981 Westmorland ground motion produces the greatest slab local response with a maximum peak response of nearly 0.06 rad., which is significantly larger than the response due to any other ground motion record.

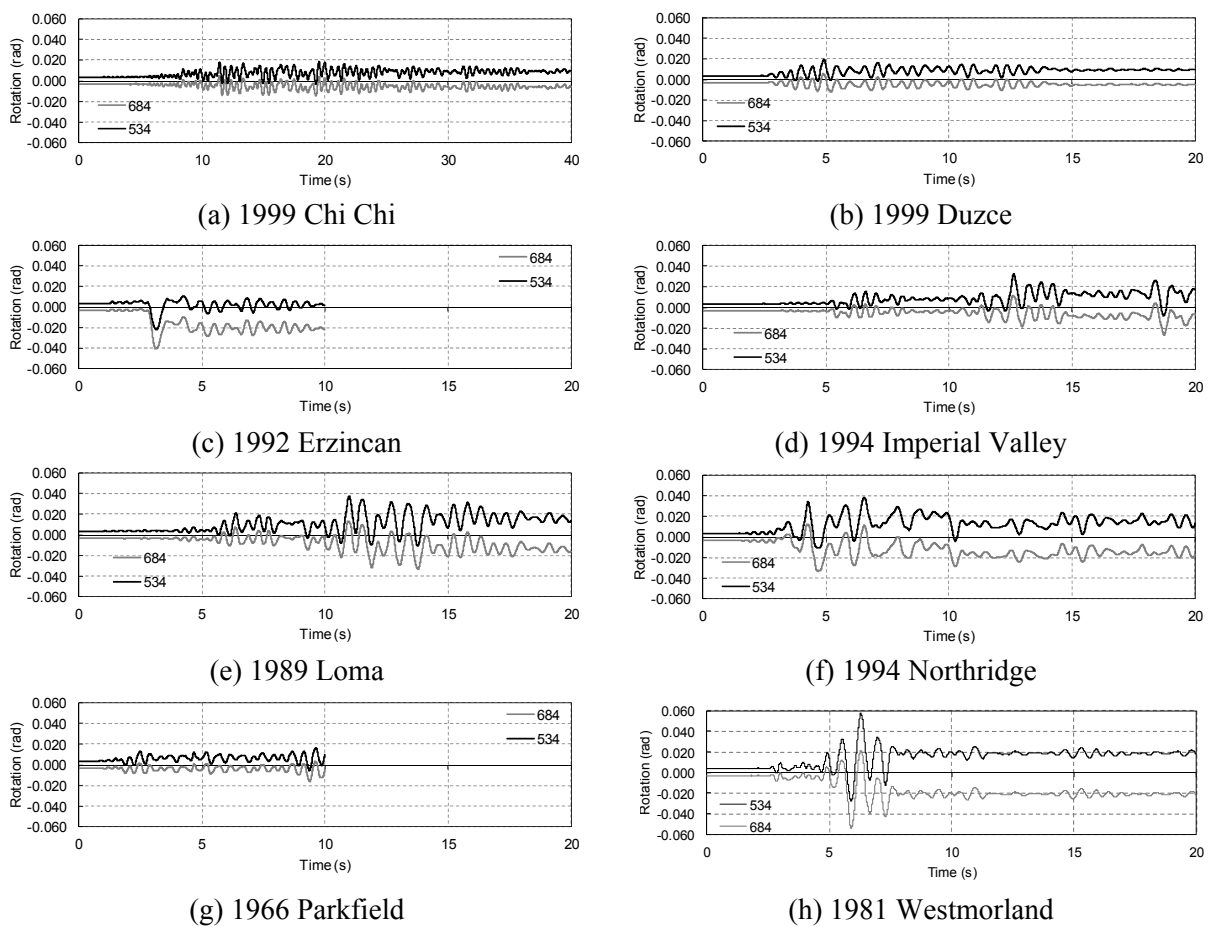


Figure 3-9 Time history of slab rotation about x-axis at two nodes neighboring column 4012 due to scaled ground motions applied only in y-direction

The lowest peak slab rotation due to ground excitations applied in the y-direction alone is 0.017 rad., which is caused by the scaled 1966 Parkfield motion. On average a slab rotation of 0.029 rad. is reported for all eight scaled ground motions. Table 3-2 summaries the peak

response of slab relative rotation under the different ground motions applied uni-directionally. Note that the slab rotation relative to column can be considered as the additive results from lateral drift and gravity loads acting on the slab. Thus, as shown in Tables 3-1 and 3-2, the average peak response of slab rotation is about 25% greater than that of story drift.

Table 3-2 Maximum Slab Rotation per Seismic Record

Seismic Record	Rotation (rad)						% Change between bi and tri-directional motion	
	θ_x	θ_y	bi-directional		tri-directional			
			θ_x	θ_y	θ_x	θ_y	θ_x	θ_y
Chi Chi	0.024	0.018	0.027	0.009	0.040	0.044	38.8	132
Duzce	0.028	0.019	0.031	0.019	0.042	0.025	30.1	27.3
Erzincan	0.033	0.040	0.049	0.047	0.050	0.049	2.02	4.17
Imperial Valley	0.042	0.033	0.043	0.040	0.048	0.042	10.7	4.88
Loma	0.027	0.038	0.040	0.041	0.054	0.043	29.8	4.76
Northridge	0.047	0.038	0.072	0.055	0.094	0.071	26.5	25.4
Parkfield	0.018	0.017	0.019	0.019	0.020	0.022	5.13	14.6
Westmorland	0.024	0.058	0.040	0.061	0.047	0.068	16.1	10.9
Average	0.031	0.029	0.040	0.033	0.050	0.042	19.9	28.0

3.4.2 Slab Rotation under Bi-directional Ground Motion

Under uniaxial lateral loading, slab bending moment is significant only about the column face perpendicular to lateral loading direction, whereas the bending moment about the column face oriented in another direction is caused mainly due to gravity loading. However, bi-directional ground motions can cause significant slab bending moment and thus rotation relative to the column about each principle direction. The slab rotational response is reported at the columns where the largest rotational response for motion applied in the x- or y-direction alone. For clarity one node on either side of the column will be reported for all the eight scaled ground

motion records: slab rotation about the y-axis, θ_x , is reported at nodes 1171 and 1174 near column 4012; slab rotation about the x-axis, θ_y , is reported at nodes 534 and 684 at column 5007.

Figure 4-9 shows the slab rotational time-history.

The combination of lateral loading in two directions produces a peak slab rotation response of 0.072 rad. about the y-axis under the scaled 1994 Northridge ground motion and 0.06 rad. about the x-axis under the scaled 1981 Westmorland ground motion. The scaled 1966 Parkfield ground motion produces the smallest peak rotation about the x-axis of 0.019 rad. For rotation about the y-axis, the scaled 1999 Chi Chi ground motion causes the smallest peak rotational response of approximately 0.01 rad. On average, the eight records produce a peak slab rotation of 0.040 rad. and 0.033 rad. about the x- and y-axis, respectively. Table 3-2 summarizes the key simulation results regarding slab rotation responses.

The peak rotation response about x- and y-direction increases by 23% and 14%, respectively when compared with the uniaxial loading condition. Such a degree of increase in slab rotation is comparable to that in lateral drift response. Therefore, the increase in slab local deformation response in bi-directional loading is caused mainly by the effects of bi-axial loading on the perimeter moment frames as the primary lateral load-resisting system.

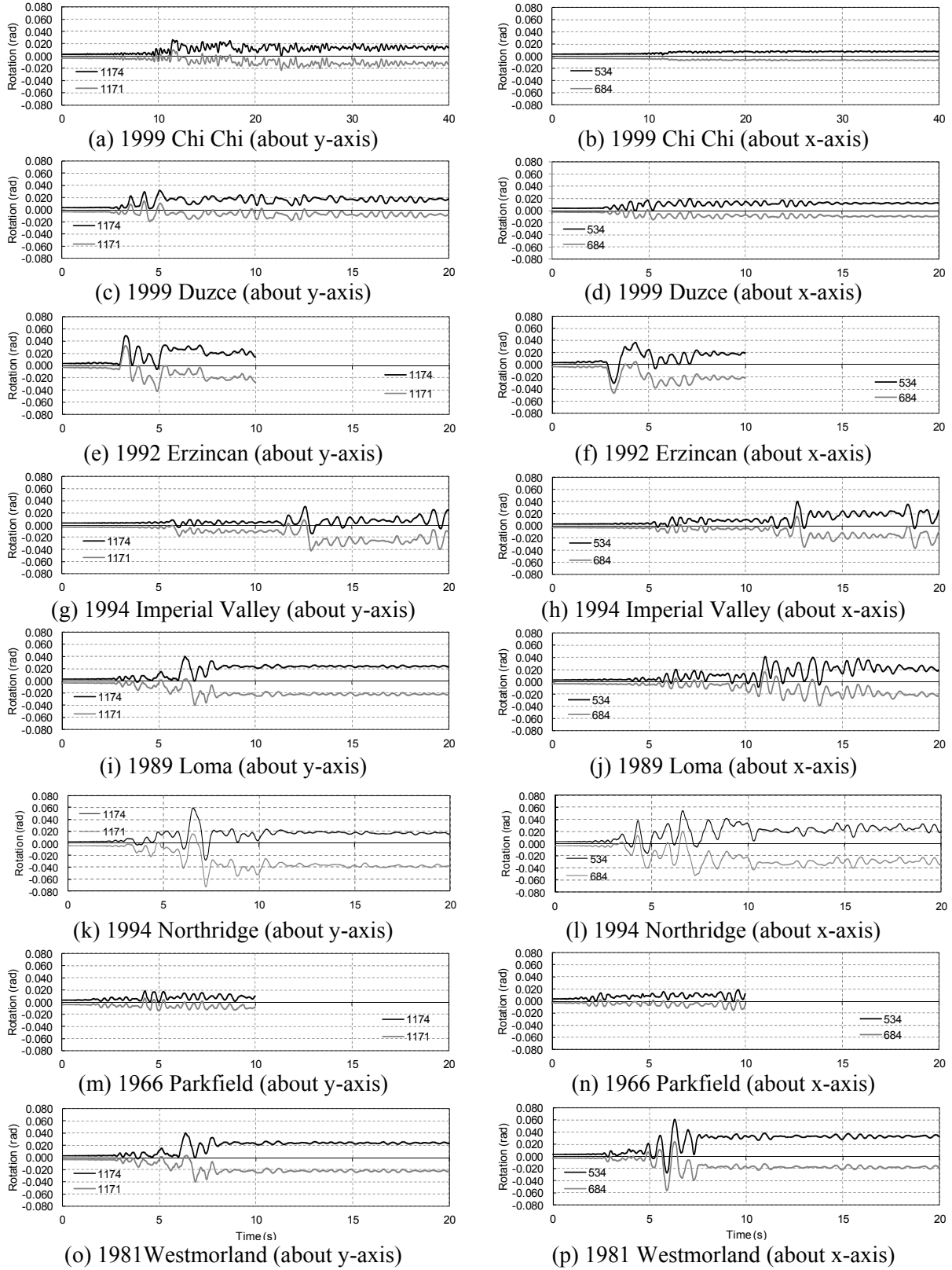


Figure 3-10 Time history of slab rotation due to scaled ground motions applied in both x- and y-directions

3.4.3 Slab Rotation under Tri-directional Ground Motion

The slab rotational response under tri-directional ground motion is examined at the same nodes as those used to report the slab rotations due to bi-axial loading condition: for rotation about the y-axis, nodes 1171 and 1174 near column 4012 are considered; nodes 534 and 684 near column 5007 are considered for slab rotation about the x-axis. Figure 4-10 shows time-history of slab relative rotation under ground motions applied in all three directions.

The scaled 1994 Northridge ground motion record produced the maximum peak slab rotation response with a value of 0.094 rad. and 0.071 rad. about the x- and y-axis, respectively. The scaled 1966 Parkfield ground motion record results in the lowest peak slab rotation about the x- and y-axis of 0.02 rad. On average, a peak slab rotation of 0.050 rad. is achieved about the x-axis and 0.042 rad. about the y-axis. It is noted that, except for the scaled 1966 Parkfield ground motion, all other motion records have caused a relative rotation exceeding 0.040 rad. It is clear that the addition of ground motion in the vertical z-direction significantly magnifies slab rotation near the columns. As shown in Table 3-2, an average 20% and 28% increase in peak slab relative rotation is calculated for all ground motions in the x- and y-direction, respectively. However, because the peak acceleration for vertical ground motion often occurs earlier than that of the horizontal motion, there is no clear correlation between the V/H-ratio and the degree of increase in slab relative rotation response (Figure 3-12). For instance, the scaled 1981 Westmorland ground motion has the highest V/H-ratio of 2.03; however, only 16% of slab rotation increase is found. On the other hand, the scaled 1999 Chi Chi ground motion has a V/H-ratio of 0.83 but created an increase of slab rotation about x-axial as high as 39%.

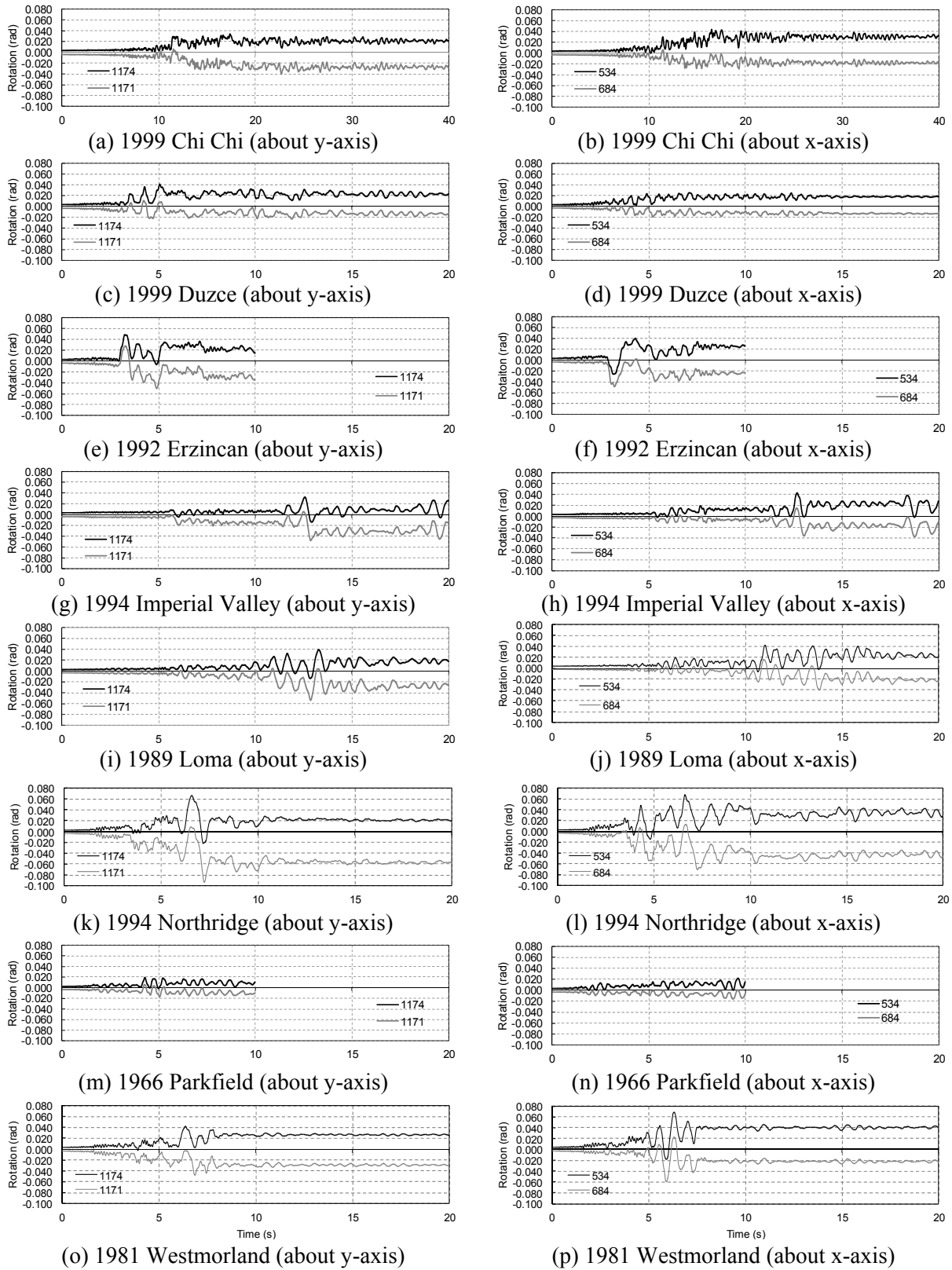


Figure 3-11 Time history of slab rotation due to scaled ground motions applied all three directions

3.4.4 Effects of Vertical Ground Motion Properties on Slab Rotation

It is likely that vertical ground motion affects slab local deformation demand by means of both creating vertical inertia force and cumulating slab damage thus degrading slab stiffness during loading reversals. However, the effects of vertical ground motion on slab local deformation demand represented by slab local rotation are directly impacted by neither the V/H-ratio nor the spectral acceleration for vertical motion. This can be illustrated by Figures 3-12 and 3-13, which show the change in slab rotation between the cases of bi-axial loading and tri-axial loading versus V/H-ratio and the spectral acceleration for vertical motion. It is seen that, even if the vertical ground motion of the scaled 1999 Chi Chi ground motion has a significant influence, there is no clear trend of the effects of these two parameters on the peak slab local deformation response.

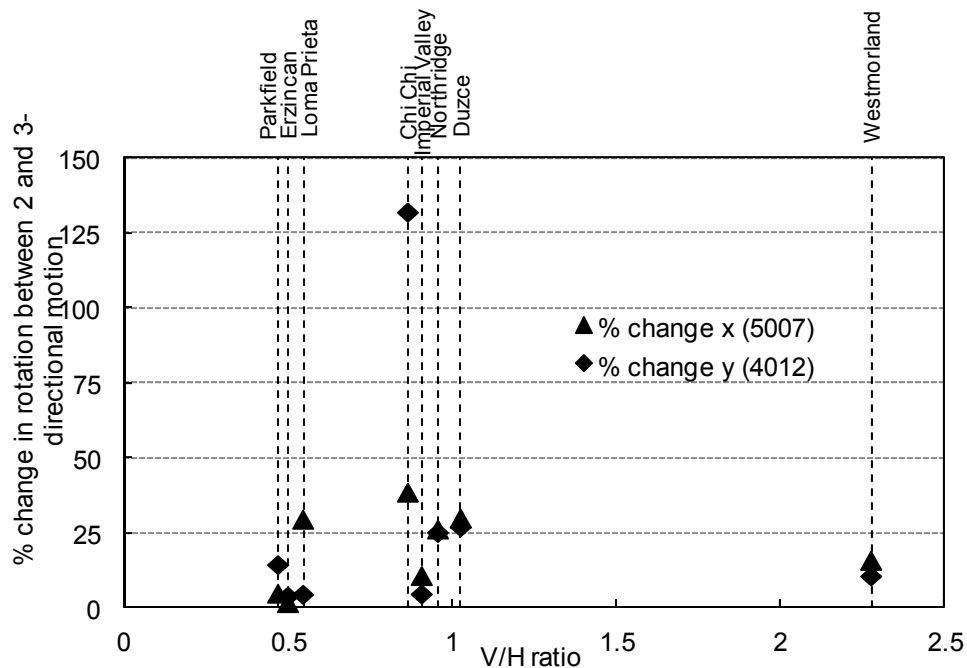


Figure 3-12 Effects of V/H-ratio on peak response of slab relative rotation

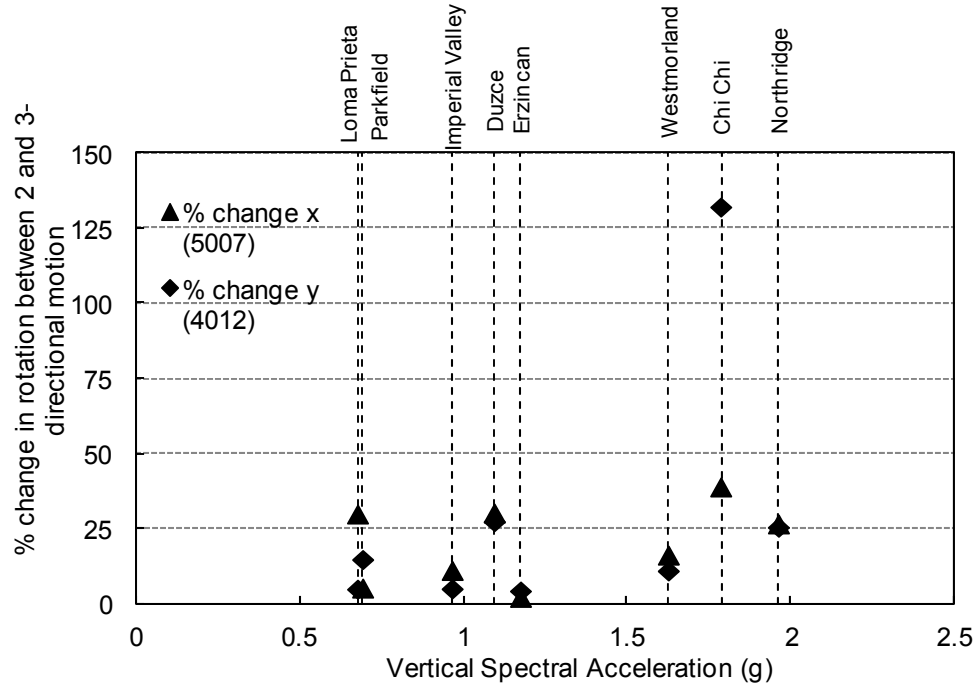


Figure 3-13 Effects of vertical spectral acceleration on peak response of slab relative rotation

As described in Chapter 1, another parameter that may be related to the vertical ground motion effects is the time interval between reaching the vertical PGA and horizontal PGA that dominates the lateral drift responses. Table 3-3 examines the time-history of the peak slab rotation θ_{\max} (Figure 3-11), peak lateral drift Δ_{\max} (Figure 3-7) and the peak vertical ground motion acceleration PGA_v for the prototype building under tri-axial loading. On average the peak lateral drift happens within 1.53 sec. of the occurrence of peak slab rotation. Only three scaled ground motion records, 1999 Chi Chi, 1966 Parkfield, 1989 Loma, experience a time difference of more than 1 sec. between reaching the peak lateral drift and the peak relative slab rotation with the 1966 Parkfield ground motion recording the largest time difference of 5.36 sec. The scaled 1999 Duzce, 1992 Erzincan, 1994 Imperial Valley, 1994 Northridge and 1981 Westmorland ground motions experience peak rotations within 0.11 sec. of peak lateral drift. The result suggests a strong association between relative slab rotation and lateral drift.

When peak slab relative rotation is compared with the peak vertical ground motion acceleration the average time difference is 3.82 sec. It is worth noting that the peak vertical ground motion acceleration always occurs before the peak slab rotation. The largest time difference of 7.68 sec. is recorded by scaled 1966 Parkfield ground motion. Scaled 1992 Erzincan ground motion has a 0.35 sec. time gap between peak slab rotation and peak vertical ground acceleration. The scaled 1999 Chi Chi ground motion leads to the greatest effects of vertical acceleration of slab rotation, as shown in Table 3-2, Figure 3-12, and Figure 3-13. The peak rotation occurs only 1.5 sec. later than achieving PGA_V but 11.4 sec. earlier than reaching the peak lateral drift. This likely explains the significant vertical ground motion effects of this seismic record.

Table 3-3 Arrival time of peak rotation, vertical PGA and peak lateral drift for tri-axial loading

Seismic Record	Time (s)				
	Peak Rotation (θ_{max})	PGA_V	Peak Lateral Drift (Δ_{max})	Δt between reaching θ_{max} and PGA_V	Δt between reaching θ_{max} and Δ_{max}
Chi Chi	16.48	14.98	11.44	1.50	5.04
Duzce	5.05	2.03	5.07	3.02	-0.02
Erzincan	3.34	3.00	3.24	0.35	0.11
Imperial Valley	12.87	7.53	12.97	5.34	-0.10
Loma	12.83	6.75	10.95	6.09	1.88
Northridge	7.22	2.62	7.23	4.61	-0.01
Parkfield	9.63	1.95	4.28	7.68	5.36
Westmorland	6.31	4.33	6.31	1.98	-0.002
Average				3.82	1.53

3.5 DYNAMIC RESPONSE OF AXIAL FORCE IN INTERIOR COLUMNS

As indicated by experimental evidence, slab punching failure is related to both slab local rotation relative to column and the vertical shear force at a slab-column connection. Axial force recorded at a supporting column of a flat plate identifies the shear forces transferred from the surrounding slab to this column. In order to examine the effects of vertical ground motion on shear force transfer, the time-history of axial loading is recorded for the interior columns of the prototype building for the four seismic loading combinations. Due to symmetry, data for axial force in columns 4012, 5007, and 5012 shown in Figure 3-2 are compiled. The initial compressive forces in these columns due to gravity loads prior to applying seismic loading are similar and equal to 75.6, 75.5 and 72.9 kips, respectively.

3.5.1 Column Axial Force under Uni-directional Ground Motion

Figures 3-14 and 3-15 show the recorded shear force transferred from slab to the interior columns for ground motion applied only in the x-direction and only in the y-direction. It is seen that the axial force slightly fluctuates for each ground motion record. An almost identical average maximum axial force of about 88 kips was recorded for all eight seismic events applied individually in the two horizontal directions. For x-direction loading, the scaled 1992 Erzincan ground motion produced the largest maximum axial force of 91.3 kips, while for y-direction loading, the maximum axial force of 93.0 kips is found during the scaled 1981 Westmorland ground motion. Additionally, all columns are consistently subjected to compression. Table 3-4 lists the peak axial force response under different seismic loading conditions.

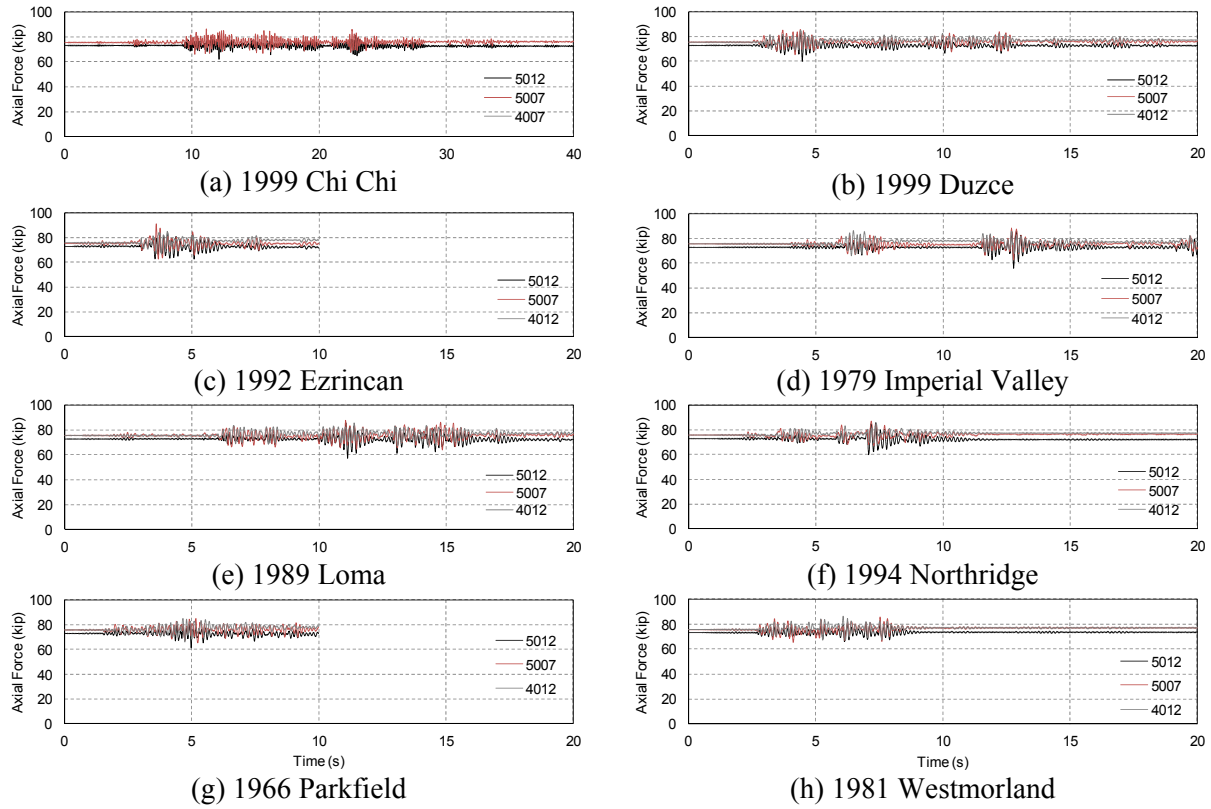


Figure 3-14 Time-history of column axial force under ground motion applied in x-direction

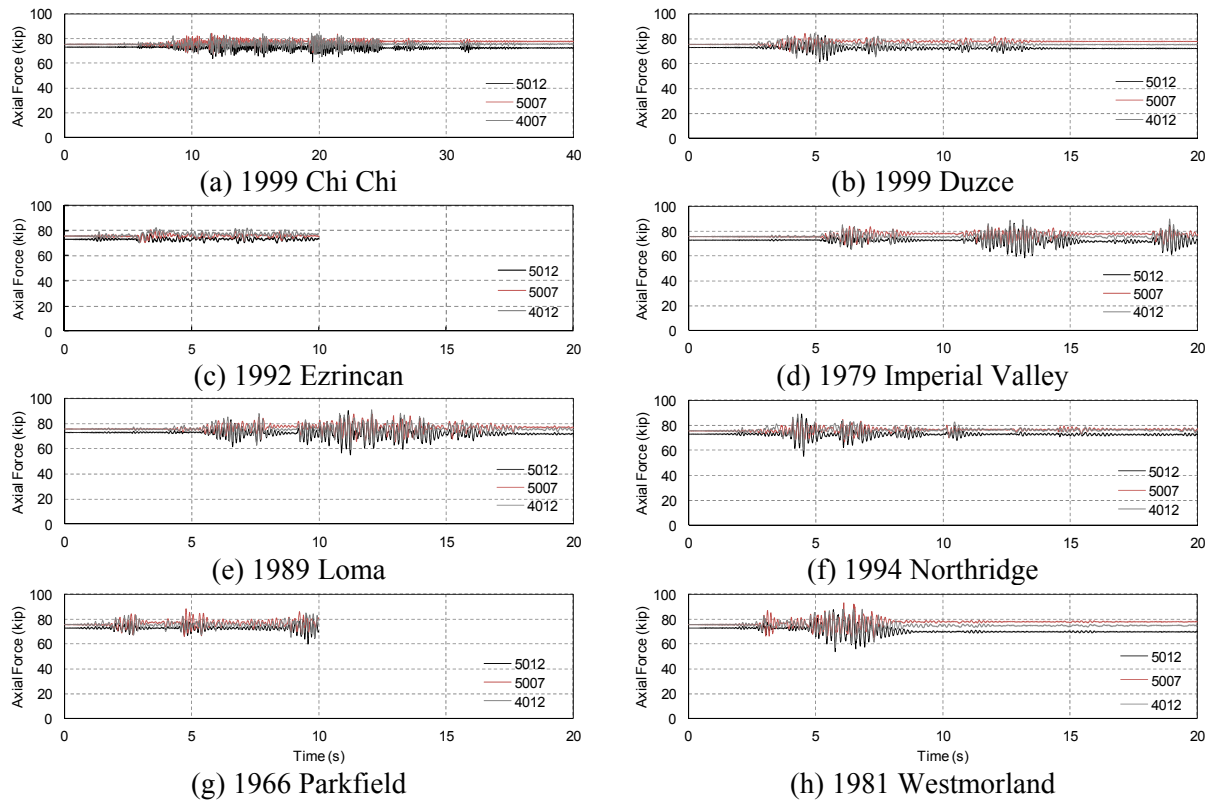


Figure 3-15 Time-history of column axial force under ground motion applied in y-direction

Table 3-4 Maximum compressive axial force per seismic record

Seismic Record	Axial Force (kip)				% Change between bi- and tri-directional motion
	x	y	bi-directional	tri-directional	
Chi Chi	86.8	84.6	86.8	135.1	43.6
Duzce	85.7	84.6	90.0	117.4	26.5
Erzincan	91.3	82.3	84.4	111.9	28.1
Imperial Valley	88.5	89.4	87.3	114.3	26.8
Loma	87.7	91.1	88.5	106.9	18.8
Northridge	86.8	88.9	90.0	126.5	33.8
Parkfield	85.1	88.5	85.6	101.7	17.1
Westmorland	86.5	93.0	91.7	130.0	34.6
Average	87.3	87.8	88.0	118.0	28.6

3.5.2 Column Axial Force under Bi-directional Ground Motion

The effect of ground motion applied in two directions simultaneously shows no heightened effect on column axial force per Figure 3-16. The average maximum axial force is 88.0 kips for all eight seismic records and is nearly identical to the maximum column axial force when the ground motions are applied in a single direction. This is also true for the peak force reported for individual seismic record as shown in Table 3-4. Hence, the combination of seismic motion in two horizontal directions concurrently has little effect on column axial force variation within the interior columns.

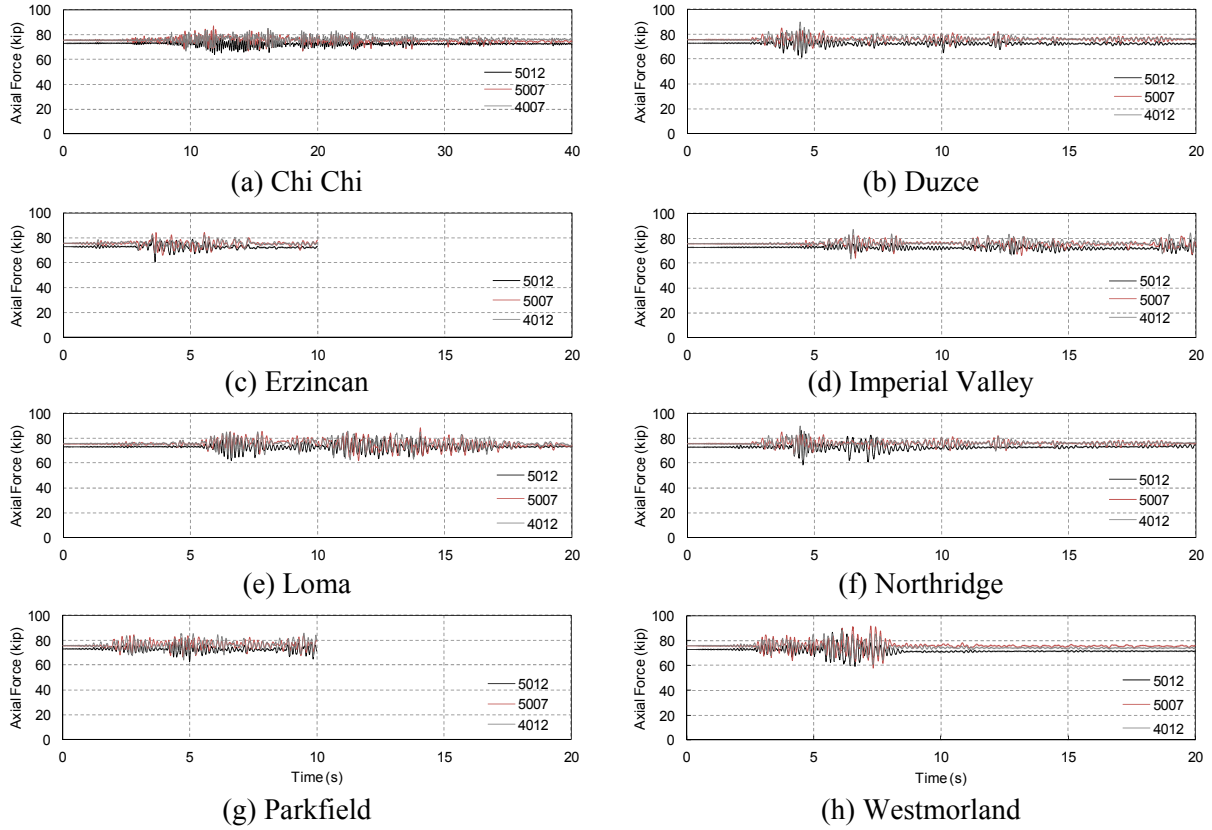


Figure 3-16 Time-history of column axial force under ground motions applied in both x- and y-directions

3.5.3 Column Axial Force under Tri-directional Ground Motion

Figure 3-17 shows the time-history of column axial force for the prototype building subjected simultaneously to vertical and two horizontal ground excitations. Comparing the data shown in this figure and those in Figures 3-14 through 3-16, it can be seen that, for each seismic record, the addition of vertical ground motion leads to a significant column axial force increase. This increase corresponds to the increase of shear transferred from slab to column, which can significantly increase the risk of punching failure at slab-column connections of the prototype building.

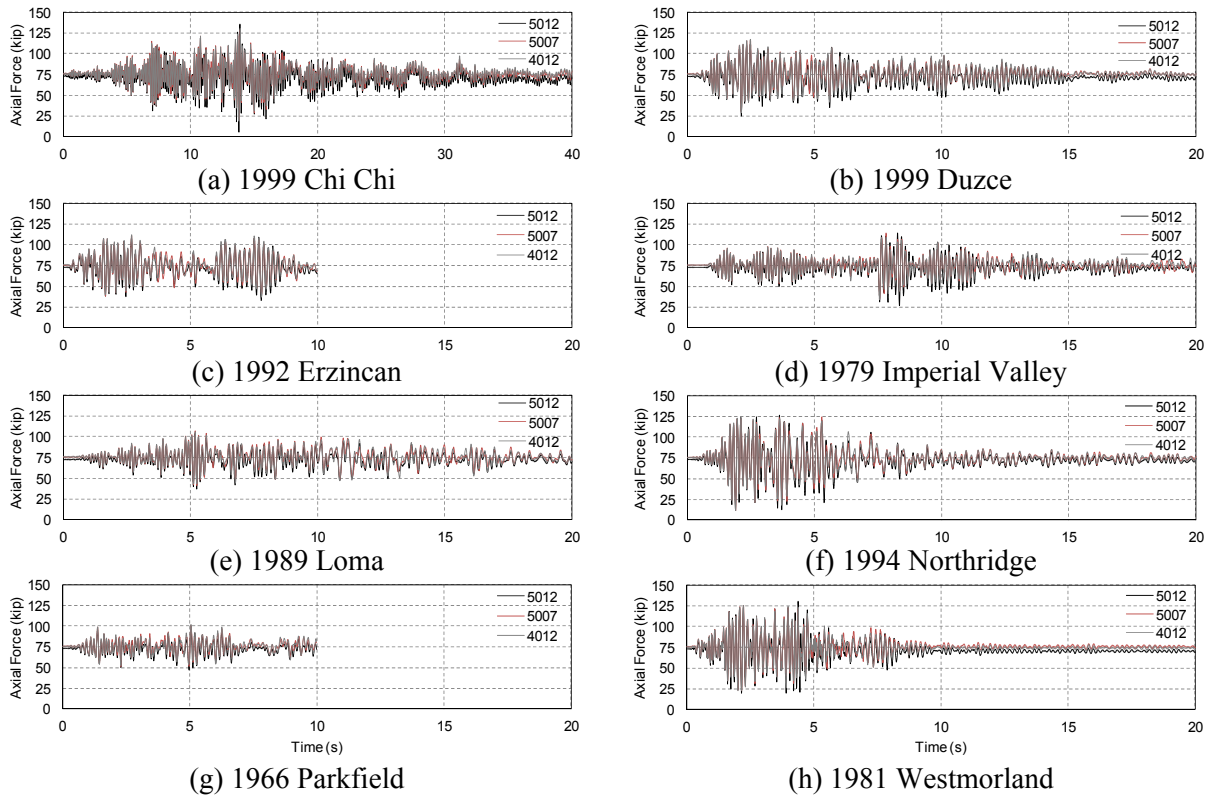


Figure 3-17 Time-history of column axial force under ground motions applied in all three directions

The average maximum axial force produced by the eight scaled seismic ground motions is 118 kips, corresponding to about 55% increase from the axial force caused by gravity loading alone and nearly a 29% increase from the axial force due to bi-directional loading (shown in Table 3-4). The scaled 1999 Chi Chi seismic motion produces the largest axial force of 135 kips. It is obvious that vertical ground motion plays a critical role in the shear force transferred to columns. Based on the ground motion acceleration time-history presented in Figures 2-27 through 2-34, it is found that the peak axial force in the columns is caused by reaching the peak vertical acceleration for a ground motion. In addition, none of the ground motions produces tensile forces (negative axial force) in the column. However, a few ground motions, such as the scaled 1999 Chi Chi, 1994 Northridge, and 1981 Westmorland, come close to obtaining an axial force of zero with the inclusion of vertical ground acceleration.

3.6 DYNAMIC RESPONSE OF SLAB CENTER DEFLECTION

Slab deflection is a secondary indicator of seismic damage of a flat-plate structure. Under cyclic loading, the slab near the columns is subjected to stiffness degradation, which increases slab rotation relative the column. Slab deformation is recorded for the prototype building at nodes 328, 867 and 878 located in the center of three slab panels per Figure 3-1.

3.6.1 Slab Deflection Due to Uni-directional Ground Motion

Figures 3-18 and 3-19 show slab deflection response for the prototype structure under ground motion applied only in the x- and y-direction, respectively. Table 3-5 summarizes the primary analysis results in terms of slab deflection. For each of the seismic records considered in this study, Node 867 has the largest vertical deflection under x-direction motion and Node 328 has the maximum deflection under y-direction motion. The average peak vertical deflection is 0.92 in. and 0.96 in. for x-direction and y-direction ground motion, respectively. The scaled 1994 Northridge seismic record produces the largest deflection of 1.19 in. for x-direction loading while the Westmorland records the largest deflection of 1.49 in. during the y-direction loading.

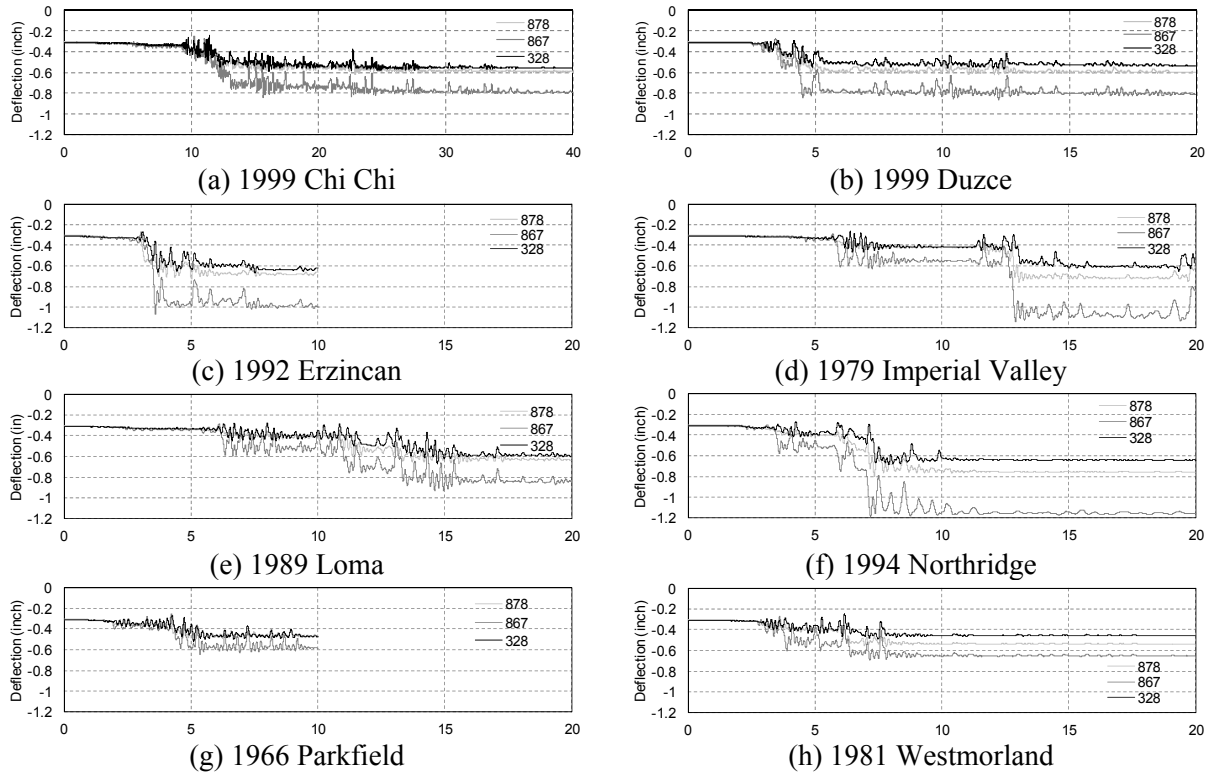


Figure 3-18 Slab deflection due to ground motion applied only in x-direction

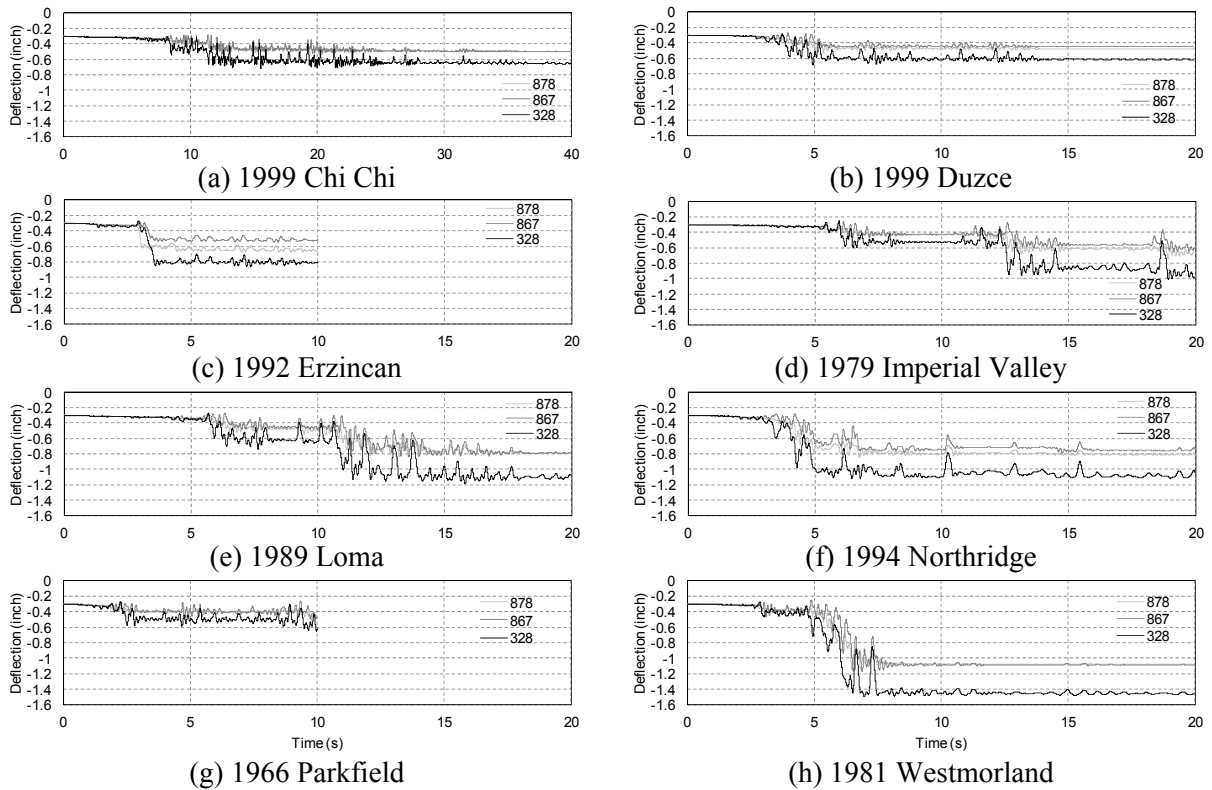


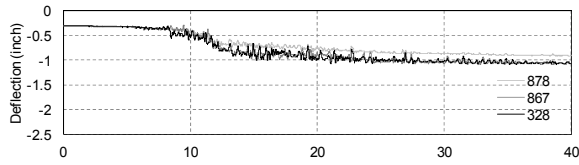
Figure 3-19 Slab deflection due to ground motion applied only in y-direction

Table 3-5 Maximum center slab deflection per seismic record

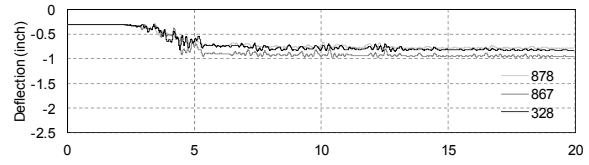
Seismic Record	Deflection (in.)				% Change between bi- and tri-directional motion
	x	y	bi-directional	tri-directional	
Chi Chi	0.85	0.71	1.09	2.65	83.4
Duzce	0.86	0.68	0.98	1.63	49.8
Erzincan	1.06	0.86	1.50	2.26	40.4
Imperial Valley	1.14	1.01	1.52	1.96	25.3
Loma	0.93	1.19	1.93	2.03	5.05
Northridge	1.19	1.12	2.35	4.16	55.6
Parkfield	0.65	0.65	0.81	0.96	17.0
Westmorland	0.69	1.49	1.93	2.73	34.3
Average	0.92	0.96	1.51	2.30	38.9

3.6.2 Slab Deflection Due to Bi- and Tri-Directional Ground Motions

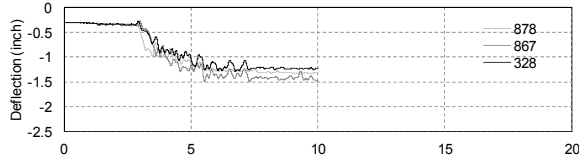
As shown in Figure 3-20, when seismic ground motions are applied in two horizontal directions simultaneously, slab center deflection increased significantly. An average maximum center slab deflection of 1.51 in. was recorded for all records. This average slab deflection is more than 55% greater than that during uniaxial loading. The scaled 1994 Northridge ground motion results in the largest slab center deflection of 2.35 in., whereas the scale 1966 Parkfield motion leads to the smallest slab deflection of 0.81 in. With the addition of vertical ground motion, slab center deflection is further increases as seen in Figure 3-21. On average a maximum center slab deflection of 2.30 in. is achieved for all ground motions. This is approximately a 40% change from two-directional loading and an average deflection of $L/100$ (where L is the clear span between columns). Again, the scaled 1994 Northridge ground motion produces the largest center slab deflection of 4.16 in.



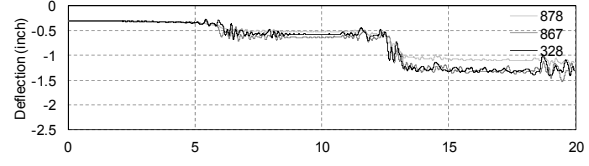
(a) 1999 Chi Chi



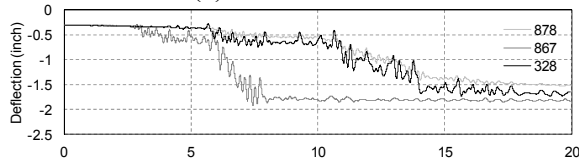
(b) 1999 Duzce



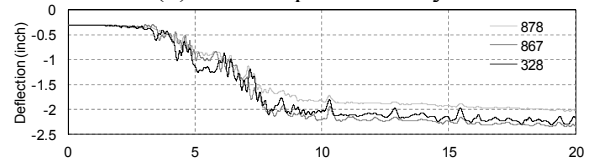
(c) 1992 Erzincan



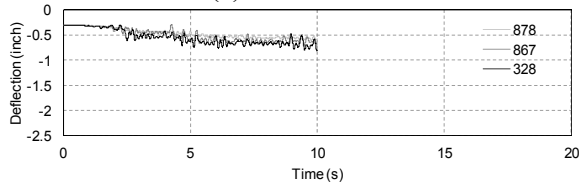
(d) 1979 Imperial Valley



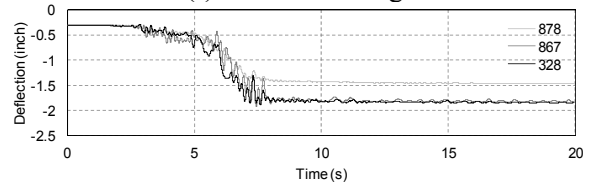
(e) 1989 Loma



(f) 1994 Northridge

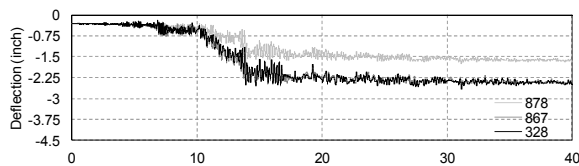


(g) 1966 Parkfield

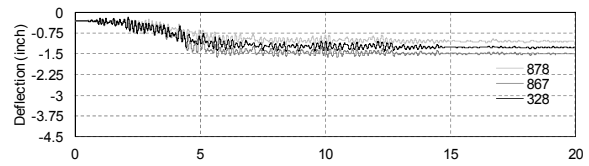


(h) 1981 Westmorland

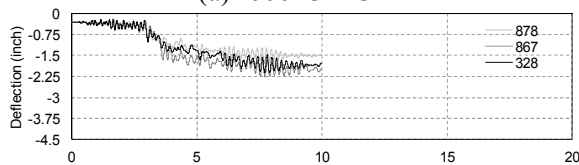
Figure 3-20 Slab deflection due to ground motions applied in both x- and y-directions



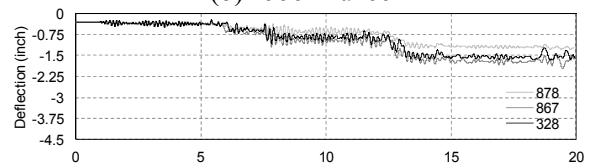
(a) 1999 Chi Chi



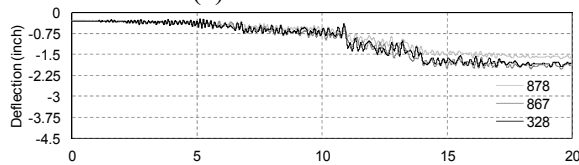
(b) 1999 Duzce



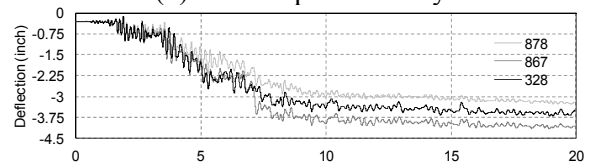
(c) 1992 Erzincan



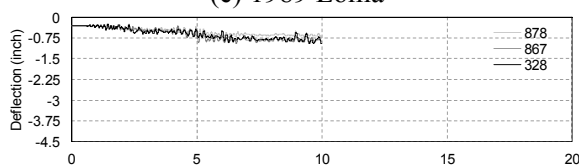
(d) 1979 Imperial Valley



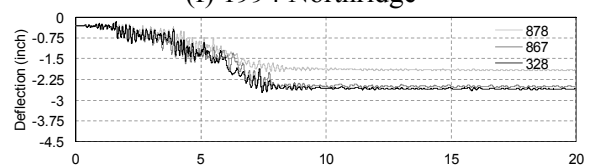
(e) 1989 Loma



(f) 1994 Northridge



(g) 1966 Parkfield



(h) 1981 Westmorland

Figure 3-21 Slab deflection due to ground motions applied in all three directions

The vertical acceleration of the scaled 1989 Loma ground motion causes the least increase in slab deflection; however this ground motion also has the lowest vertical peak ground acceleration of any of the records, which occurs nearly 4 seconds before the peak ground acceleration in either horizontal direction. It is also interesting to note that the scaled 1999 Chi Chi ground motion has the greatest percent change (83%) of slab deflection as compared with the case of bi-axial loading even though this ground motion record has the lowest vertical peak ground acceleration. Examining the analysis results indicate that the large slab deflection occurs because horizontal and vertical peak ground accelerations occur nearly simultaneously.

3.7 DEFINING VERTICAL GROUND MOTION EFFECTS

As discussed previously, the current design approach of ASCE/SEI 7-10 standard (2010) requires vertical seismic loading effects be considered by using a fraction of the horizontal spectral acceleration $0.2S_{DS}$ to define a gravity load as $E_v = 0.2S_{DS}DL$ (Equation 1-3). As discussed in Section 3.4.4, this study cannot find a direct correlation of the slab local deformation demand with either V/H-ratio or PGA_v . Thus, this study still considers defining the vertical ground motion effects equivalently based on the horizontal spectral acceleration S_{DS} as $E_v = qS_{DS}D$. Slab rotation relative to the column is used to evaluate the q -factor because punching shear is an inherent problem associated with flat-plate structures and slab rotation is one of the most important effects in determining the potential for punching failure as presented by Muttoni et al. (2008).

A series of comparison analyses of the prototype structure subjected to dynamic tri-directional loading and bi-directional loading are conducted with a focus on the slab rotational demand. The tri-directional loading analyses are those that have already been shown in the previous sections. Different from the time-history analyses described previous, the bi-directional

analyses presented herein consider different gravity loads $((1.2 + qS_{DS})DL + 0.5LL)$ acting on the slab. Taking the maximum slab rotation due to tri-axial loading as the target response, these gravity loads are adjusted by changing the value of q until the peak slab rotation demand at the column is less than 5% different from that produced by the tri-axial seismic loading. Trial-and-error is used in this process and a value of q is determined for each ground motion record.

Table 3-6 presents the calibrated q -factor factor S_{DS} for each of the eight seismic ground motions. The largest factor of $q = 0.37$ is produced by the scaled 1999 Chi Chi ground motion and followed closely by the scaled 1999 Duzce ground motion with $q = 0.34$. Four of the seismic records produced an identical factor of $q = 0.11$. For the scaled 1992 Erzincan ground motion, there is no need to consider any scale factor ($q = 0$) due to negligible rotational demand increase for tri-axial loading. Overall an average scale factor of 0.17 is found. This value compares well with the current code requirements ($q = 0.2$) in ASCE/SEI 7-10 (2010).

Table 3-6 Scale Factor (q) for S_{DS}

Earthquake Record	q	% error
Chi-Chi, Taiwan (1999)	0.37	2.09
Duzce, Turkey (1999)	0.34	3.17
Erzincan, Turkey (1992)	0	2.02
Imperial Valley, California (1979)	0.11	0.36
Loma Prieta, California (1989)	0.11	3.76
Northridge, California (1994)	0.25	3.66
Parkfield, California (1966)	0.11	2.67
Westmorland, California (1981)	0.11	4.21
Average	0.17	2.68

Further investigation of the q -factor for S_{DS} is conducted in order to better understand the influence of various vertical ground motion characteristics. Previous research has shown trends to exist regarding higher V/H ratios and lower time intervals between peak vertical and horizontal ground acceleration at closer source distances. Consequently it is reasonable to assume that similar trends may exist between the q -factor and similar variables.

Figure 3-22 graphs the calibrated q -factors versus six different variables including the vertical peak ground acceleration, epicentral source distance, time interval between peak vertical and horizontal ground acceleration, V/H ratio, vertical response spectral acceleration at the natural period of the prototype structure for vertical vibration, and time interval between peak vertical acceleration and peak rotation. It is seen from Figure 3-22 that there is significant scatter in each of the six graphs. No obvious trends regarding the effects of different variables on the q -factor can be reported by the figures. When the S_{DS} scale factor is plotted against the vertical response spectrum there is some but unobvious tendency for the scale factor to increase as the vertical response spectrum increases.

From the data it is concluded that the scale factor of $0.2S_{DS}$ for current ASCE/SEI 7-10 (2010) code is reasonable for design of vertical seismic effects. The data for eight seismic motions show no clear trend for determining a higher or lower q -factor. This may be because of the many variables accounting for vertical acceleration effects. Due to the complex nature of vertical loading, a more accurate representation may be obtained through the use of more data points. The eight seismic records considered in this study also have highly varied characteristics such as peak ground accelerations vertically and horizontally, source distance, V/H-ratio, and arrival time of peak ground acceleration. Thus, eight ground motions may not be enough to

identify a convincing trend for the effects of various parameters related to vertical ground motions.

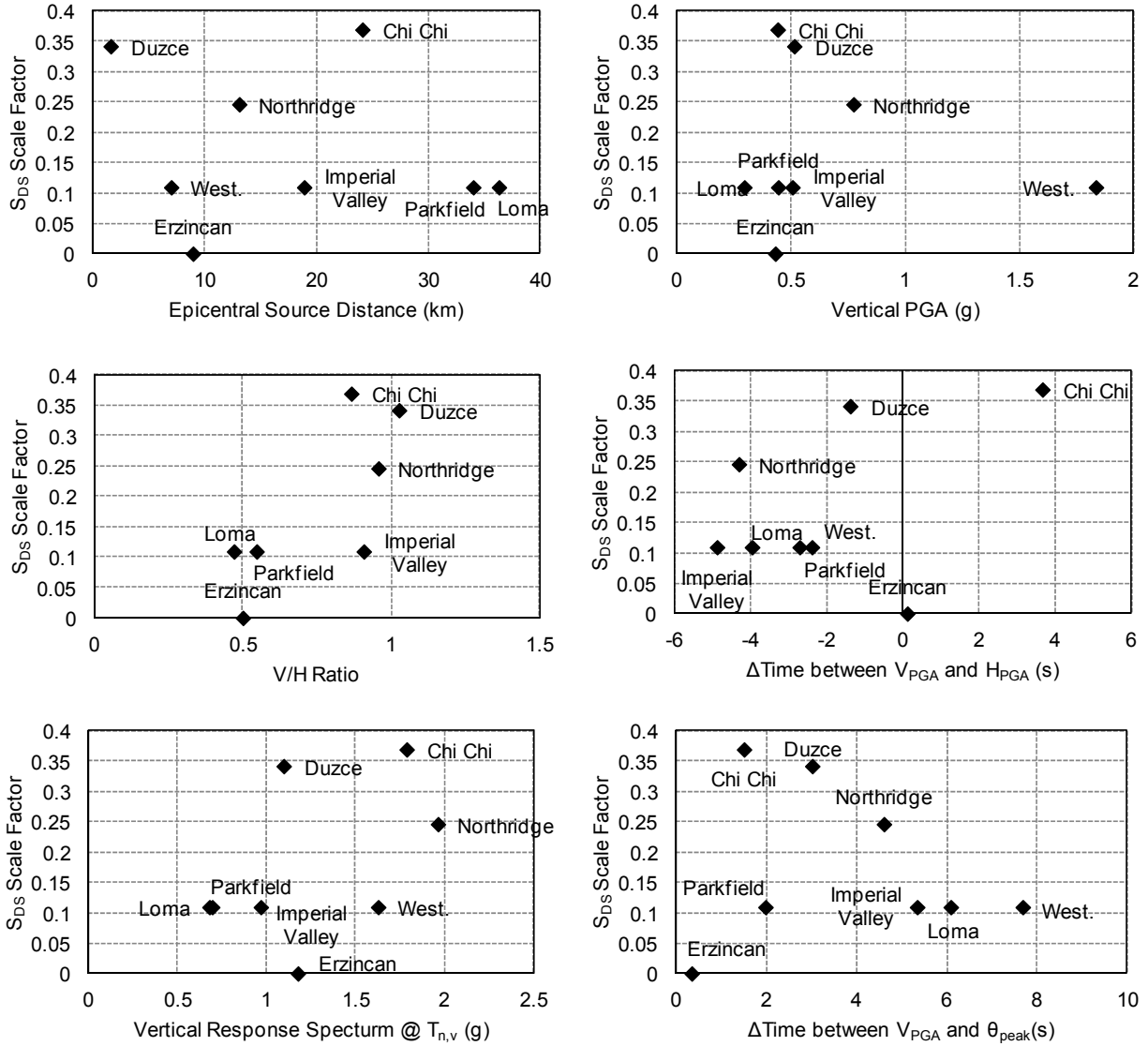


Figure 3-22 Effects of different vertical ground motion properties on q -factor for S_{DS}

CHAPTER 4

EFFECTS OF VERTICAL GROUND MOTION ON PUNCHING FAILURE

4.1 OVERVIEW

The resistance of slab-column connections to punching failure is critical for a flat-plate building to avoid disastrous progressive collapse. The study presented in the previous chapter examined force and deformation demands caused by vertical ground motions. It has been found that the existence of vertical ground acceleration during a near source event can significantly increase both the vertical shear carried by a slab-column connection and slab local deformation measured by relative rotation. Given that both effects are directly related to slab punching failure but they do not occur simultaneously, these effects cannot be simply superimposed. Thus, the slab punching failure potential of the prototype building is evaluated based on four existing failure criteria using the data obtained from the series of nonlinear time-history analysis. Three of the failure criteria are available in ACI 318-14 (2014) including the eccentric shear stress model, two-way shear design using a target story design drift limit, and two-way shear stress limit. The last punching failure criterion considered in this study is the model suggested by Muttoni et al. (2008).

In order to implement the aforementioned approaches, the shear stresses in the nonlinear grid beam elements connected to the slab-column joints are evaluated based on the vertical shear forces obtained from analysis output data as well as beam dimensions. As indicated in Chapter 3, the peak dynamic response of slab local deformation occurs at either column 5007 or column 4012 shown in Figure 2-1, focus will be given to the punching failure potential at these locations.

4.2 APPLICATION OF ECCENTRIC SHEAR STRESS MODEL

ACI 318-14 (2014) provides eccentric shear stress model for determining the maximum shear stress due to the transfer of unbalanced moments between columns and slabs. It is assumed that a fraction (γ_f) of the factored unbalanced moment (M_u) is resisted by flexure in slab, whereas the remaining portion is carried by eccentric shear stress along the perimeter of assumed shear critical section. For slab-column connections with square columns, this method assumes that 60% of the moment is transferred by flexure while 40% of the moment is caused by eccentricity of shear about the centroid of the critical section. The analysis also assumes that shear stress will vary linearly with the distance from the centroid of the critical section. Figure 4-1 shows the eccentric shear stress distribution along the perimeter of critical section for a slab-column connection subjected to both gravity shear and unbalanced moment about one axis.

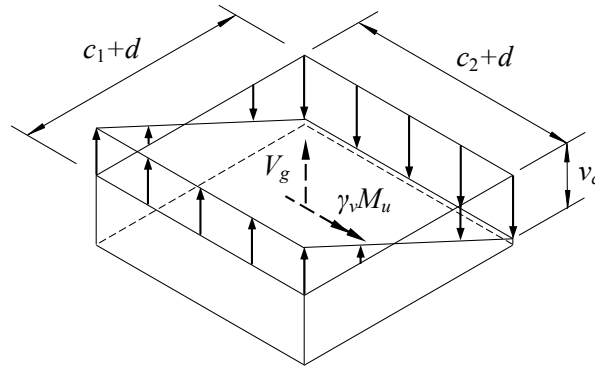


Figure 4-1 Eccentric shear stress model

Under unbalanced moments existing about two horizontal axes, the shear stress caused by unbalanced moment (v_u) is calculated per Equation 4-1 where V_u is the total vertical shear force transferred from slab to column, $M_{u,x}$ is the unbalanced moment about x -axis, $M_{u,y}$ is the unbalanced moment about y -axis, A_c is area of concrete at the critical section, γ_v equals 0.6 for interior square columns, c is the distance from centroidal axis of the column to a distance of d

(slab average effective depth) away from the column face, and J_c is polar moment of inertia for the critical section.

$$v_u = \frac{V_u}{A_c} + \frac{\gamma_v M_{u,x} c}{J_c} + \frac{\gamma_v M_{u,y} c}{J_c} \quad \text{Equation 4-1}$$

If v_u exceeds the code-defined two-way shear capacity of $4\sqrt{f'_c}$, a punching failure is predicted. To use Equation 4-1, the unbalanced moments about two axes are determined from the bending moments at the top end of the interior columns calculated from the simulations; the vertical shear force V_u is determined from the axial force of the supporting interior column. Moreover, for convenience, the shear stress demand is normalized as $v_u/(4\sqrt{f'_c})$ so that if this ratio is greater than unity, a punching failure is identified based on the eccentric shear stress model. The following sections present the evaluation results corresponding to different loading conditions.

4.2.1 Using Eccentric Shear Stress Model for Uni-directional Ground Motion

Figures 4-2 and 4-3 show the normalized shear stress in slab at column 5007 for ground motion applied only in the x-direction and that at column 4012 for ground motion only in the y-direction, respectively. A few records cause the normalized shear stress close to unity: the scaled 1979 Imperial Valley and 1994 Northridge ground motions in the x-direction lead to a value of about 0.95 respectively, and the scaled 1981 Westmorland ground motion in y-direction results in a value of 0.98. However, as seen in Figures 4-2 and 4-3, for both loading conditions, none of the seismic records produce a normalized shear stress greater than a value of one, indicating that shear demand never reaches capacity and punching failure should not happen based on the eccentric shear stress model.

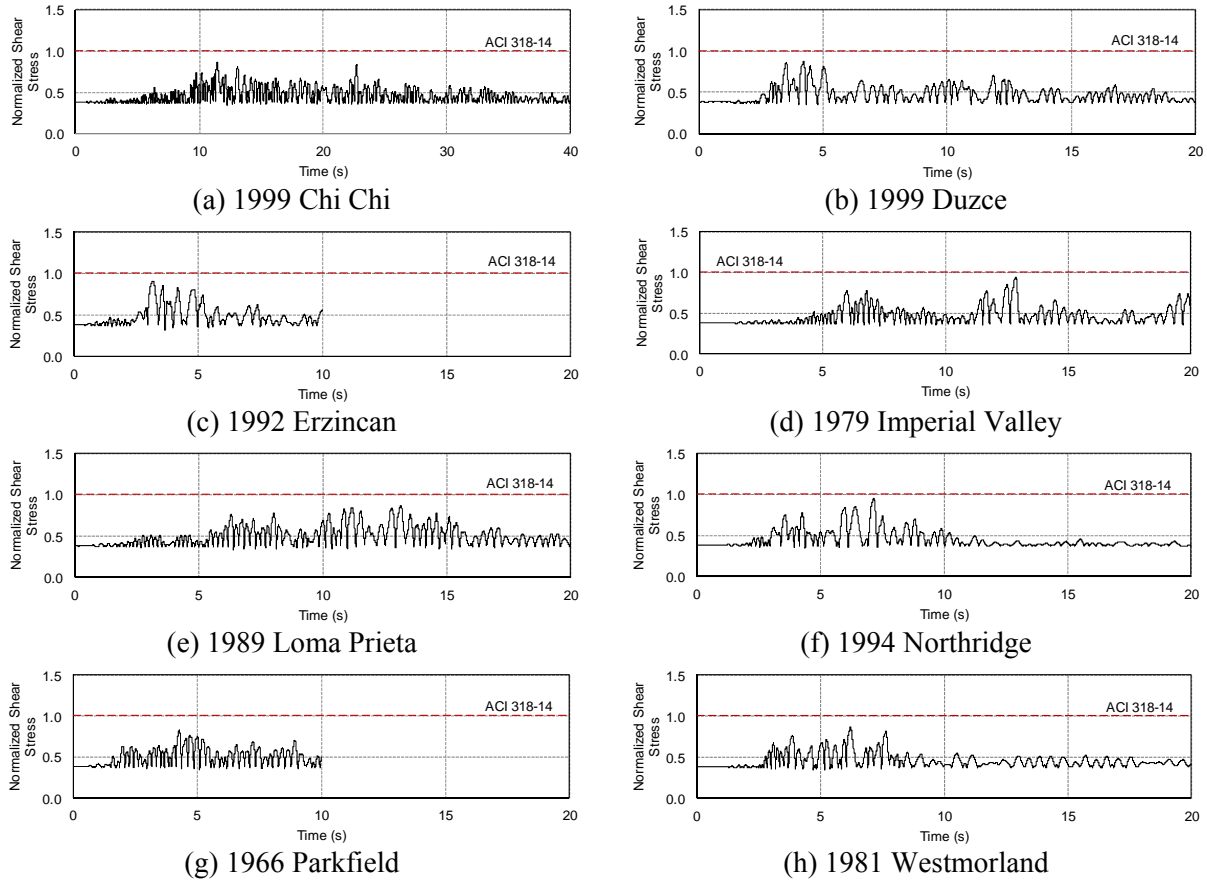


Figure 4-2 Normalized eccentric shear stress due to ground motion applied in x-direction

It is noted that the eccentric shear stress model was developed based primarily on the work by Hanson and Hanson (1968) who tested a limited number of small-scale isolated slab-column specimens. The model essentially considers only an elastic action of slab-column connections because it is assumed that punching failure occurs before flexural capacity of slab has been reached. Moreover, even though this model has been used for decades in the American concrete design codes without any changes, the appropriateness of the parameter γ_f has long been argued by some researchers such as Robertson and Durrani (1992) and Tian et al. (2009).

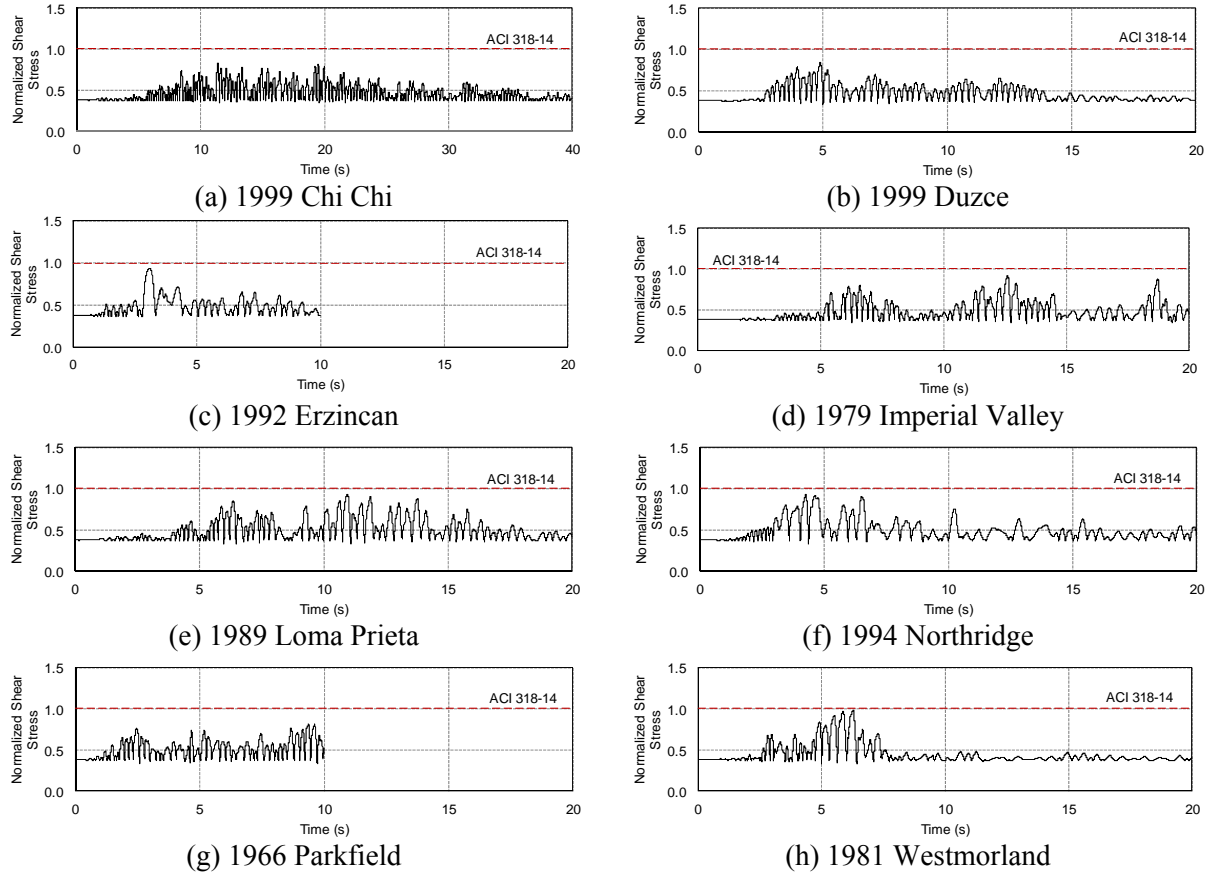


Figure 4-3 Normalized eccentric shear stress due to ground motion applied in y-direction

4.2.2 Using Eccentric Shear Stress Model for Bi-directional Ground Motion

Figure 4-4 displays the results for normalized shear stress when seismic ground motion is applied in two horizontal directions simultaneously. It is found that all seismic records lead to a shear demand exceeding the capacity except for the scaled 1966 Parkfield, which still causes a normalized shear stress of 0.96. The largest normalized shear stress is due to the 1992 Erzincan ground motion at 1.31, i.e. 31% greater shear demand than capacity.

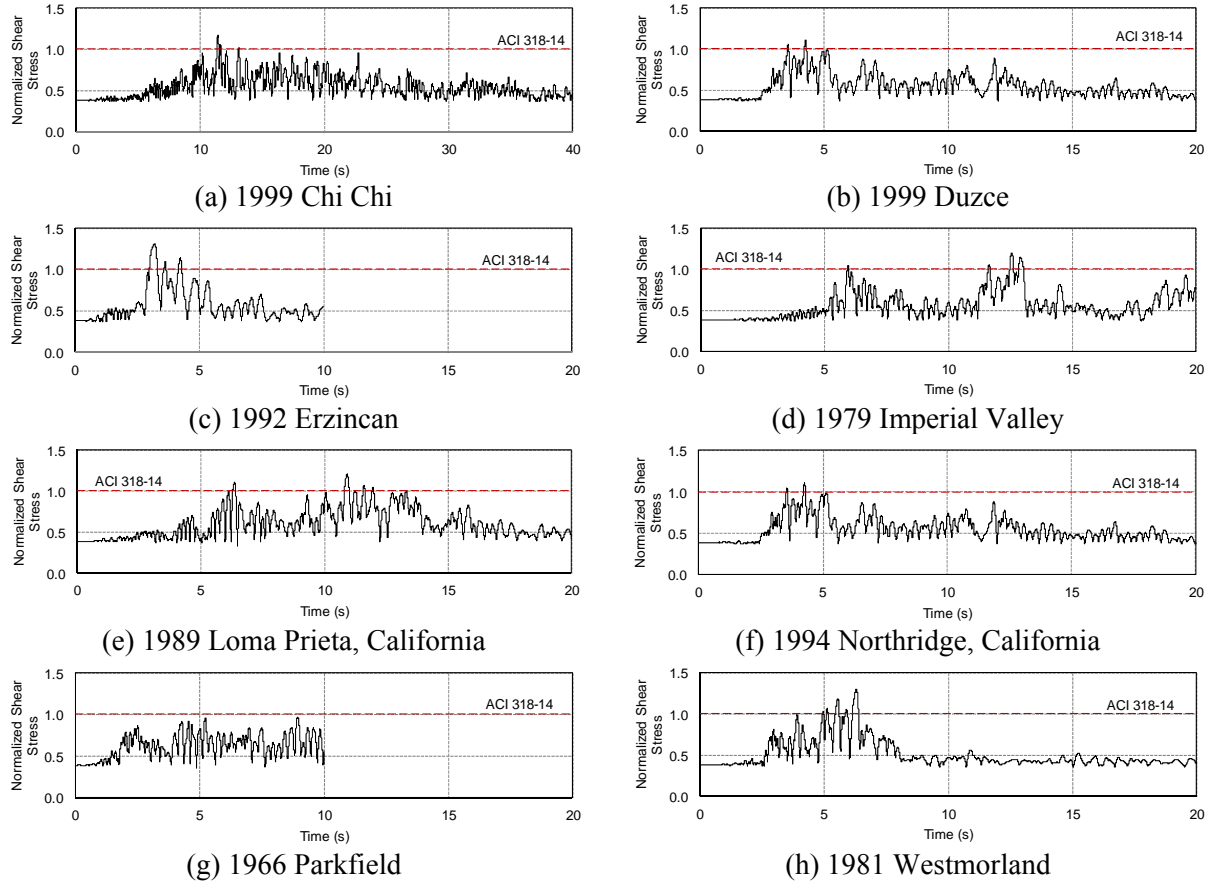


Figure 4-4 Normalized eccentric shear stress due to bi-directional ground motion

4.2.3 Using Eccentric Shear Stress Model for Tri-directional Ground Motion

Figure 4-5 records the normalized shear stress for seismic ground motion applied in the two horizontal directions and the vertical direction simultaneously. Comparing Figures 4-4 and 4-5, it is seen that high frequency shear stress components are added due to the incorporation of vertical ground excitations, leading to some increase of shear stress over certain time period. However, no significant change is seen in terms of the maximum shear stress. The largest normalized shear stress is recorded by the scaled 1994 Northridge ground motion, with a value of 1.34, while the smallest is recorded by the scaled 1966 Parkfield ground motion at 1.05. The very limited effects of vertical ground motion are likely due to the following facts: (1) The

unbalanced moment $M_{u,x}$ and $M_{u,y}$ in Equation 4.1 are associated mainly with story drift, which is affected little by the vertical ground motions, as described in Chapter 3. (2) The vertical inertia force at the reach of peak eccentric shear stress stops increasing due to the yielding of slabs; thus the increase of V_u in Equation 4-1 is limited.

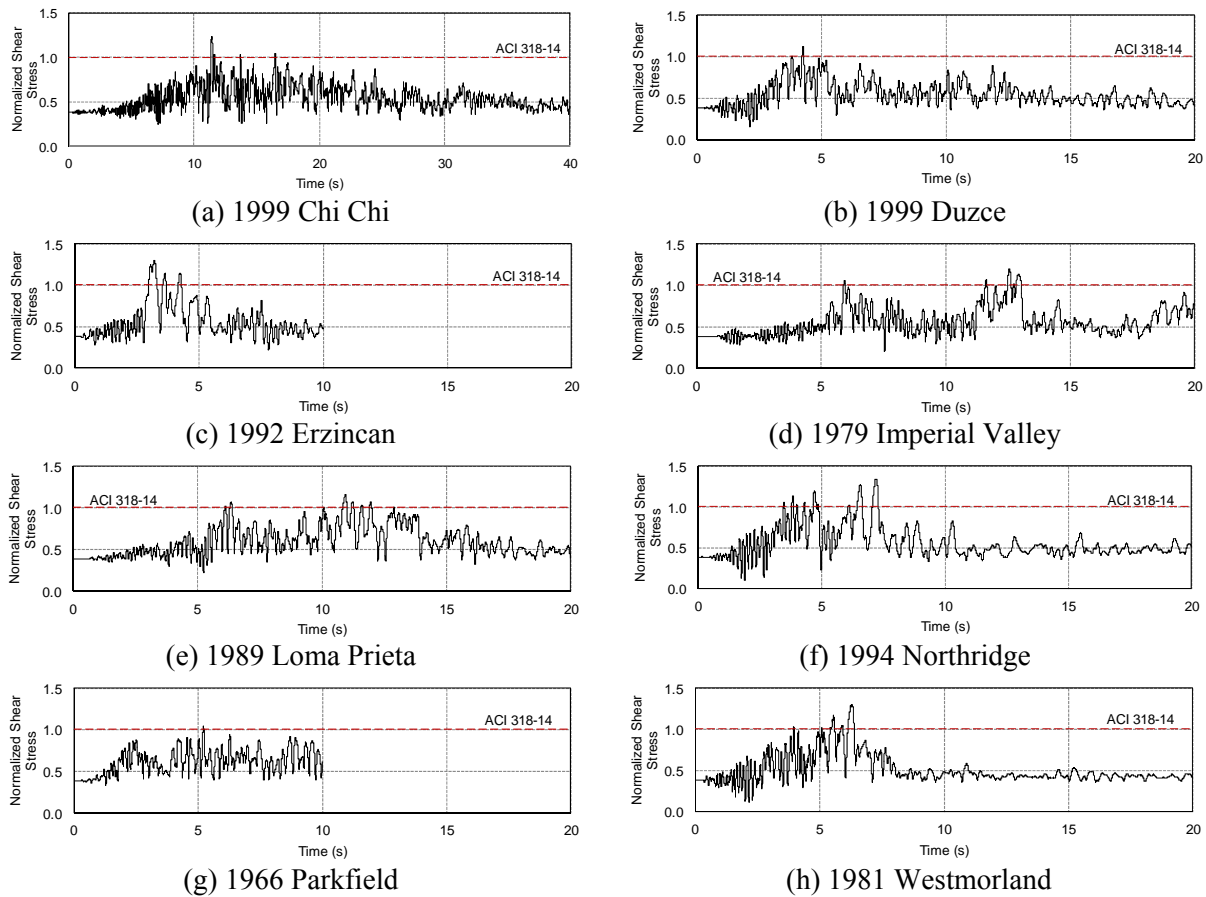


Figure 4-5 Normalized eccentric shear stress due to tri-directional ground motion

Table 4-1 summarizes the results for peak shear stress predicted from the eccentric shear stress model. The percent change between 2-directional and 3-directional is small and in most cases negligible.

Table 4-1 Maximum normalized shear stress per seismic record for eccentric shear stress

Seismic Record	Normalized shear stress				% Change between 2 and 3-directional motion
	x	y	2-directional	3-directional	
Chi Chi	0.86	0.83	1.18	1.23	4.15
Duzce	0.88	0.84	1.11	1.12	0.90
Erzincan	0.91	0.94	1.31	1.30	-
Imperial Valley	0.94	0.92	1.20	1.19	-
Loma	0.87	0.94	1.20	1.16	-
Northridge	0.95	0.93	1.11	1.34	18.8
Parkfield	0.82	0.81	0.96	1.05	8.96
Westmorland	0.86	0.98	1.30	1.30	-
Average	0.89	0.90	1.17	1.21	3.47

4.3 APPLICATION OF DRIFT LIMIT APPROACH

The punching capacity for a slab-column connection without using shear reinforcement is defined from ACI 318-05 (2005) to ACI 318-14 (2014) as a function of lateral drift, expressed in Equation 4-2, and shown in Figure 1-10.

$$Drift\ Ratio\ Capacity\ (\%) = \begin{cases} 3.5 - 5 \frac{V_{ug}}{V_c} & \frac{V_{ug}}{V_c} \leq 0.6 \\ 0.5 & \frac{V_{ug}}{V_c} > 0.6 \end{cases} \quad \text{Equation 4-2}$$

where V_c is the two-way shear strength defined as V_0 in Equation 1-2 for an interior slab column connection, V_{ug} is the total gravity shear transferred from slab to the column.

For the following calculations the lateral drift demand is normalized by dividing the drift ratio demand identified from the simulations using the lateral drift ratio capacity defined using Equation 4-2. Therefore, values larger than 1.0 or smaller than -1.0 would indicate a lateral drift demand greater than capacity and thus a possible punching failure. For ease of discussion and comparison, values will be reported as absolute values.

4.3.1 Using Drift Capacity for Uni-directional Ground Motion

Normalized lateral drift is recorded for seismic motion applied separately in the x-and y- directions. The results are shown in Figures 4-6 and 4-7. The scaled 1966 Parkfield ground motion applied in the x-direction and the 1999 Chi Chi, the 1999 Duzce, and 1966 Parkfield ground motions applied in the y-direction produce a normalized drift less than one; however, for all other ground motions, the drift capacity is exhausted. The largest normalized lateral drift in the x-direction is recorded by the scaled 1994 Northridge ground motion with a value of 2.26 and that in the y-direction is caused by the 1981 Westmorland ground motion with a value of 3.00.

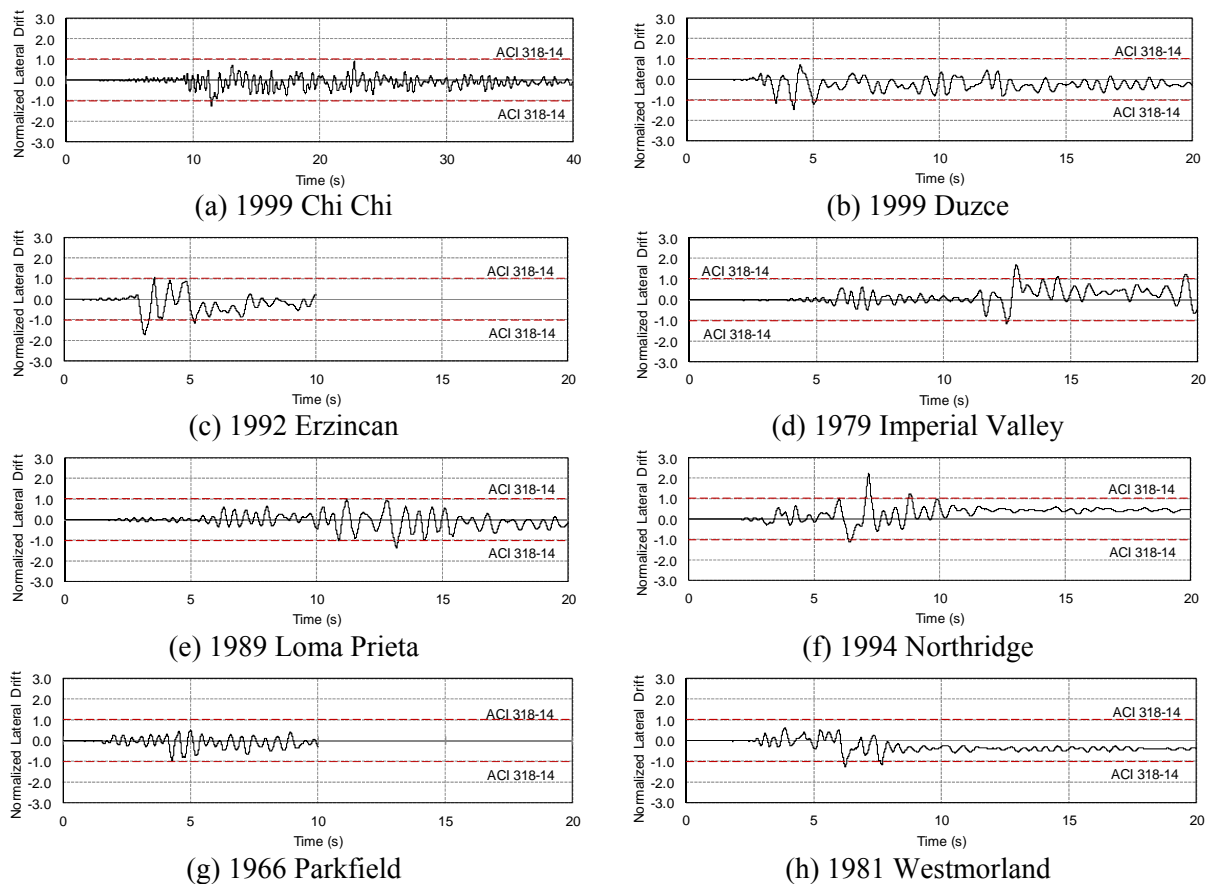


Figure 4-6 Normalize lateral drift due to ground motion applied in x-direction

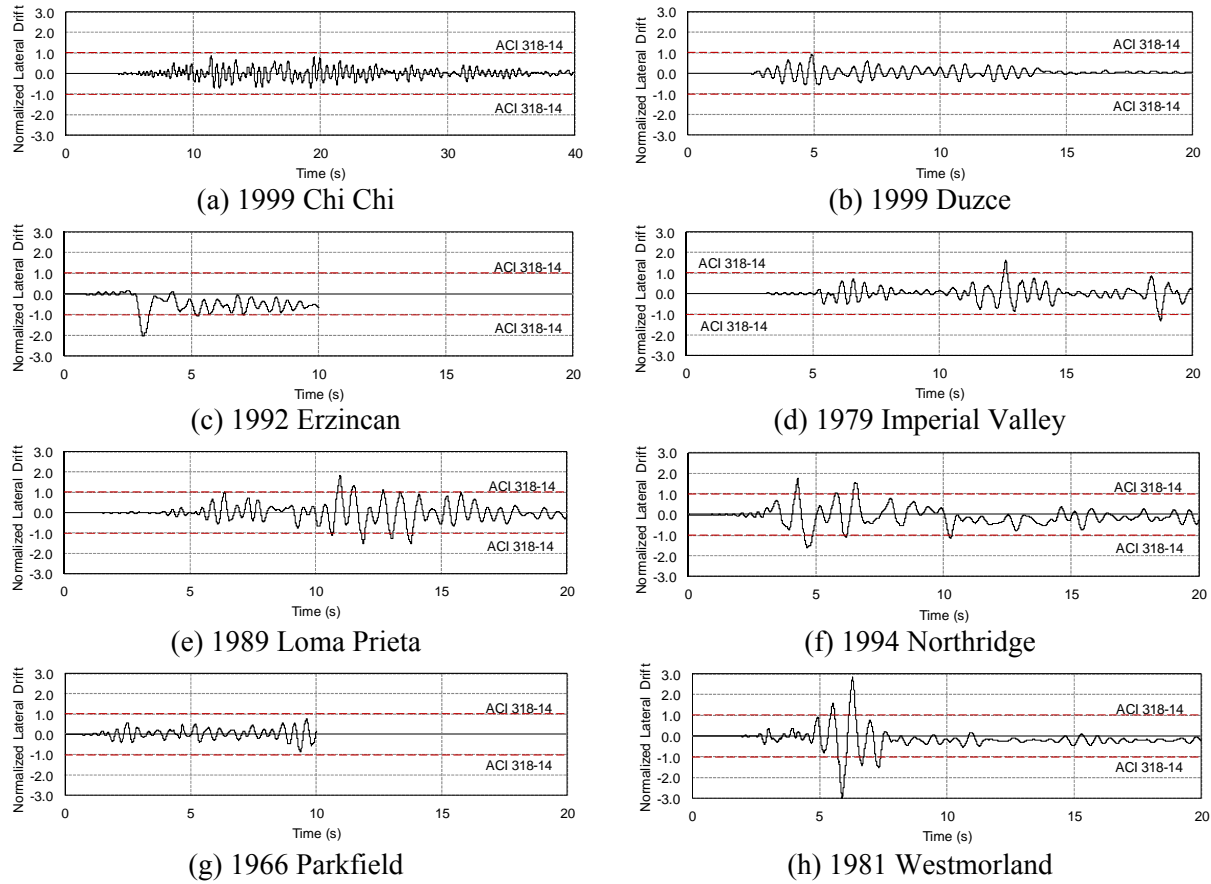


Figure 4-7 Normalized lateral drift due to ground motion applied in y-direction

The average normalized drift is 1.50 and 1.61 for x- and y-direction ground motion, respectively, indicating at least 50% of drift capacity has been exceeded. Such a degree of normalized drift demand is due to two reasons. First, the prototype building is expected in the design to have a maximum story drift ratio of 2%; however, the average drift due to ground motions applied individually in the x- and y-directions is 2.92% and 2.68%, as shown in Table 3-1. Moreover, as indicated in Section 3.5, lateral loading has caused total shear transferred at columns 5007 and 4012 to be about 12% greater than that under the initial gravity loading. The combined effects from the increased vertical shear at a slab-column connection and the increased lateral drift demand significantly increased the normalized drift ratio. Table 4-2 summarizes the peak normalized story drift under various loading conditions.

Table 4-2 Maximum normalized lateral drift per seismic record

Seismic Record	Lateral Drift				% Change between 2 and 3-directional motion
	x	y	2-directional	3-directional	
Chi Chi	1.26	0.87	1.36	2.08	41.9
Duzce	1.47	0.94	1.45	2.43	50.5
Erzincan	1.72	2.04	2.33	2.92	22.5
Imperial Valley	1.69	1.61	1.74	1.8	3.39
Loma	1.37	1.84	1.98	2.58	26.3
Northridge	2.26	1.74	2.83	4.81	51.8
Parkfield	0.97	0.85	0.93	0.94	1.07
Westmorland	1.27	3.00	2.97	3.16	6.20
Average	1.50	1.61	1.95	2.59	25.5

4.3.2 Using Drift Capacity for Bi-directional Ground Motion

Normalized lateral drift ratio for seismic ground motion applied in two directions simultaneously produced comparable results to those when motion was only applied in a singular direction. However, a majority of the seismic records logged a slightly higher normalized lateral drift with two-directional motion. Equation 4-2 defines drift capacity along a principle direction rather than a resultant drift obtained from two horizontal components. Thus, the normalized drift ratios for x- and y-directions are individually examined.

Figures 4-8 and 4-9 show the time history of normalized lateral drifts for each seismic record. The maximum value between the x- and y-direction drift for each event can be found in Table 4-2. The scaled 1966 Parkfield is the only record to record a value less than one. The 1981 Westmorland produces the largest normalized lateral drift of 2.97. The average maximum lateral drift for all seismic records was 95% greater than the drift capacity.

Compared with uniaxial loading condition, the bi-directional loading increased the normalized drift by about 20%. As shown in Table 3-3, bi-directional loading affects little the

total vertical shear carried by a slab-column connection. Therefore, the increase in the normalized story drift is primarily caused by the increased lateral drift demand during biaxial loading.

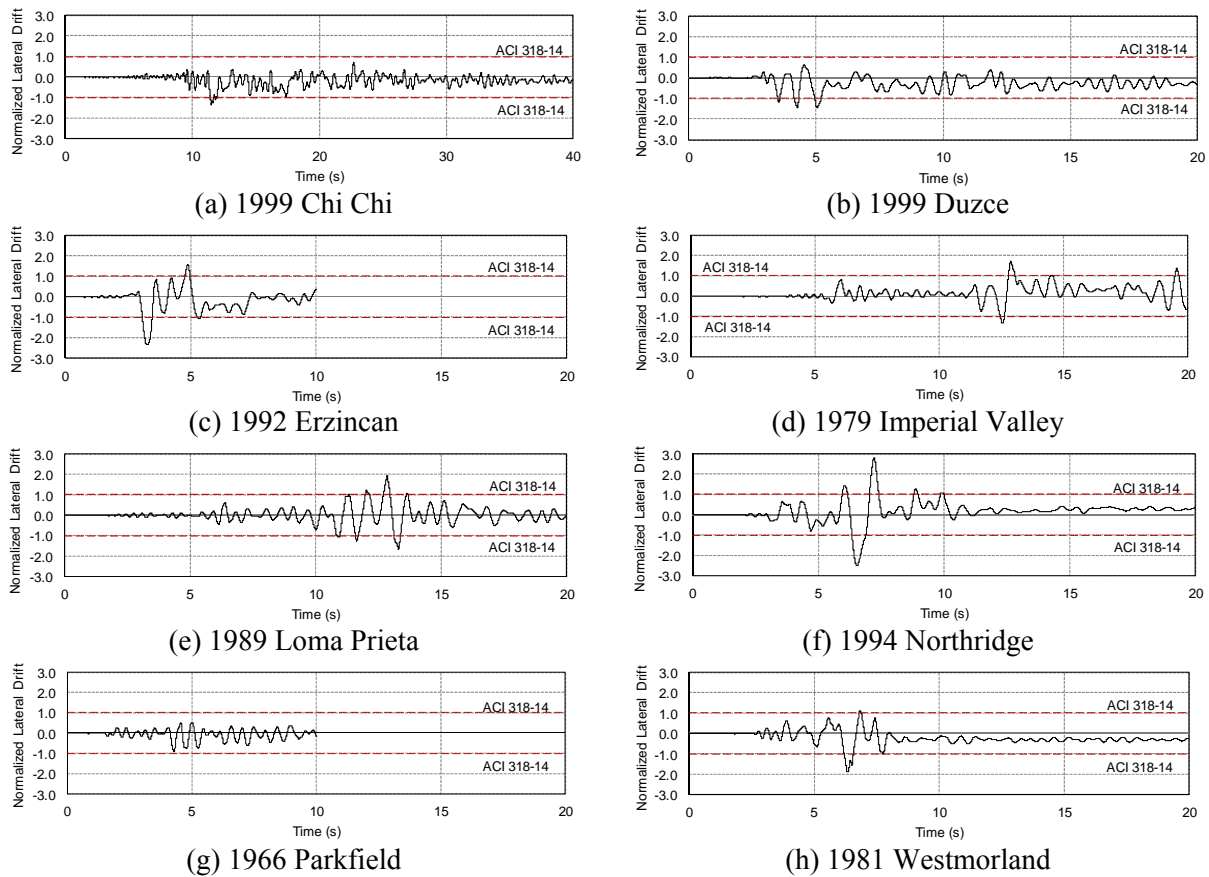


Figure 4-8 Normalized lateral drift in x-direction due to bi-directional ground motion

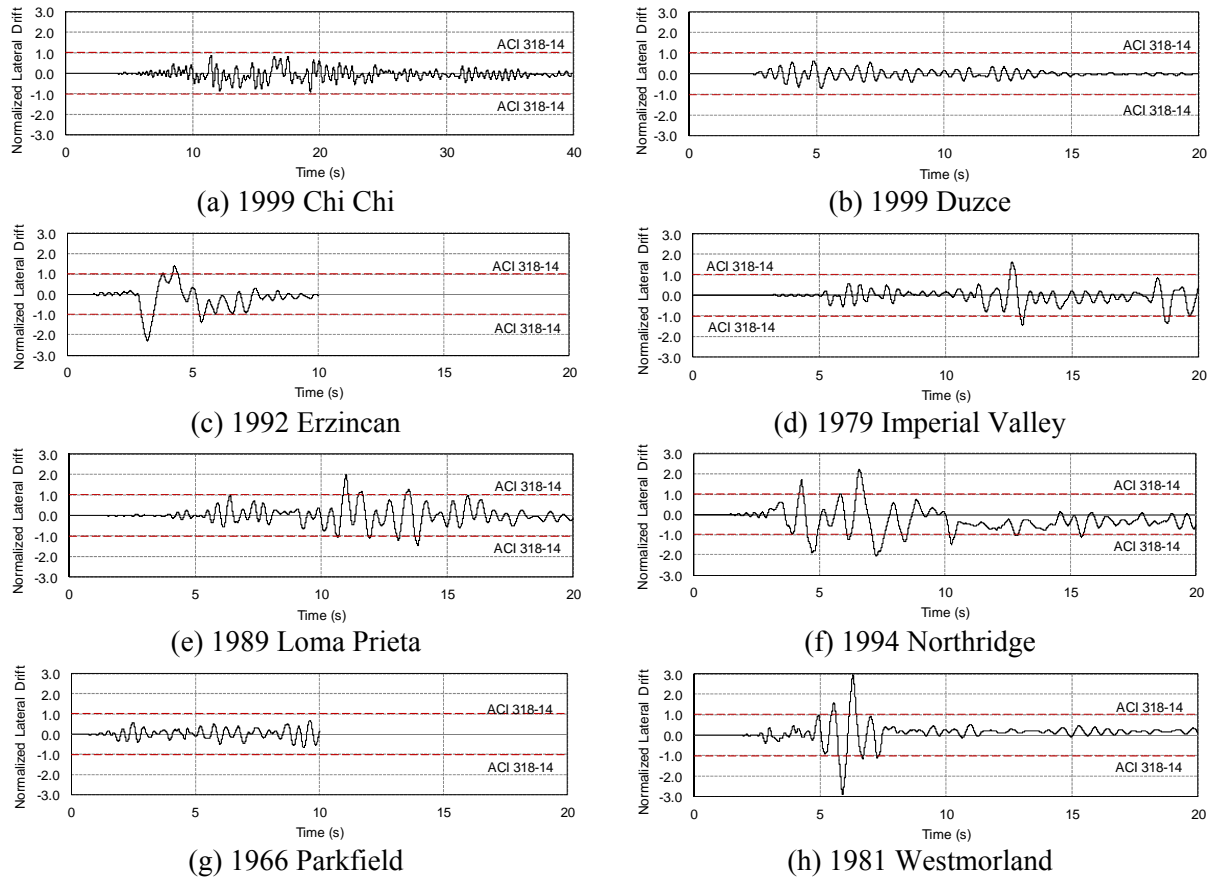


Figure 4-9 Normalized lateral drift in y-direction due to bi-directional ground motion

4.3.3 Using Drift Capacity for Tri-directional Ground Motion

Seismic ground motion is applied in three directions simultaneously: two horizontal directions perpendicular to one another and vertically. The results of normalized lateral drift in the x- and y- directions are shown Figures 4-10 and 4-11 and summarized in Table 4-2. Results for ground motion in three directions recorded a lateral drift demand larger than allowable drift for all seismic records except the scaled 1966 Parkfield which recorded a value of 0.94. The scaled 1994 Northridge ground motion results in the largest lateral drift of 380% over lateral drift capacity. The average maximum lateral drift for all seismic records is 2.59 or 159% over drift capacity.

The effect of vertical ground motion on the punching failure potential evaluated using drift capacity is more pronounced than the drift demand. As shown in Table 4-2, the vertical ground motion on average increases the normalized drift ratio by 25%. Examining the ground motion histories in the three directions (Figures 2-27 through 2-34), the lateral drift response due to ground motions applied in x- or y-direction alone (Figures 3-4 and 3-5), and the normalized drift (Figures 4-8 and 4-9), it is found that the vertical ground motions cause the drift capacity at punching failure to be reached well prior to the peak drift demand. This is obvious for the 1999 Chi Chi, the 1994 Northridge, and the 1981 Westmorland earthquakes. However, it is also found that reaching the drift capacity is still governed by the lateral deformation response.

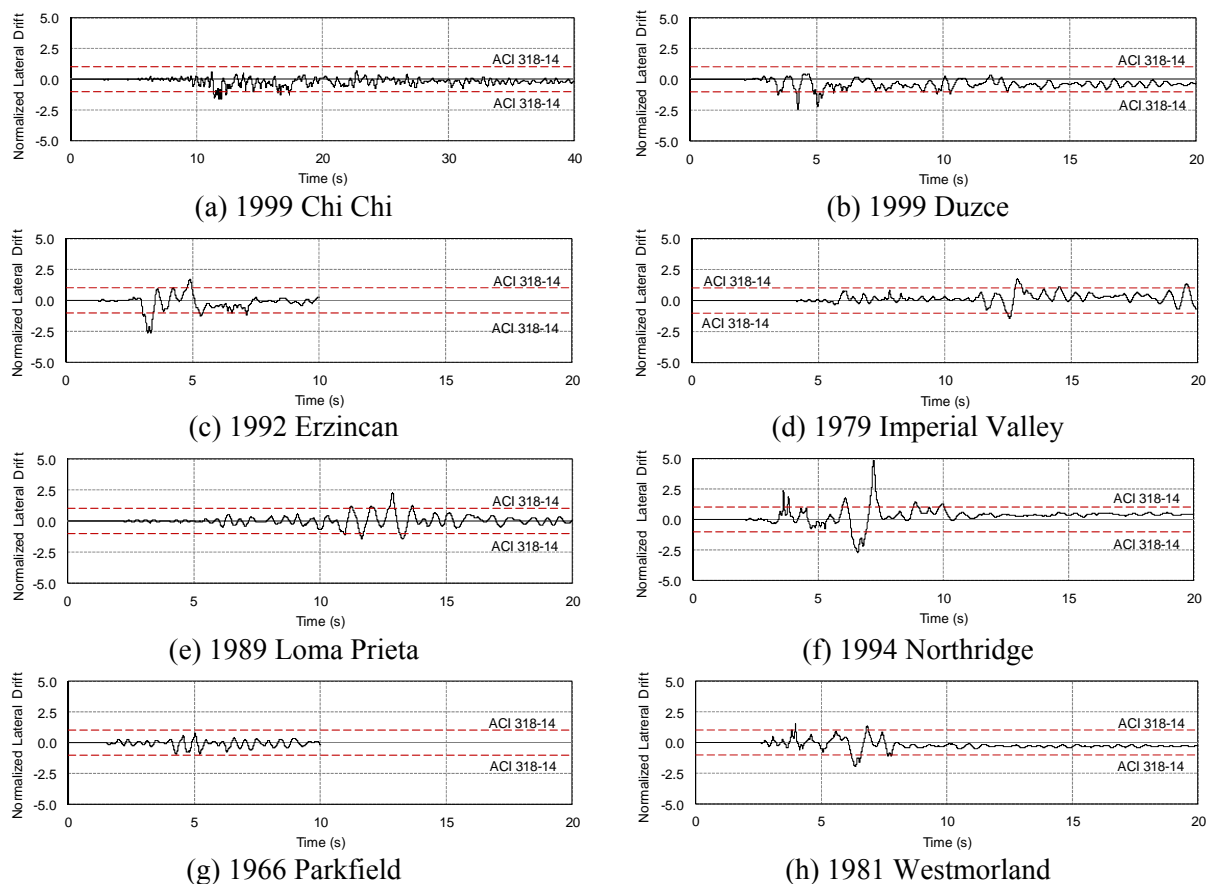


Figure 4-10 Normalized lateral drift in x-direction due to tri-directional ground motion

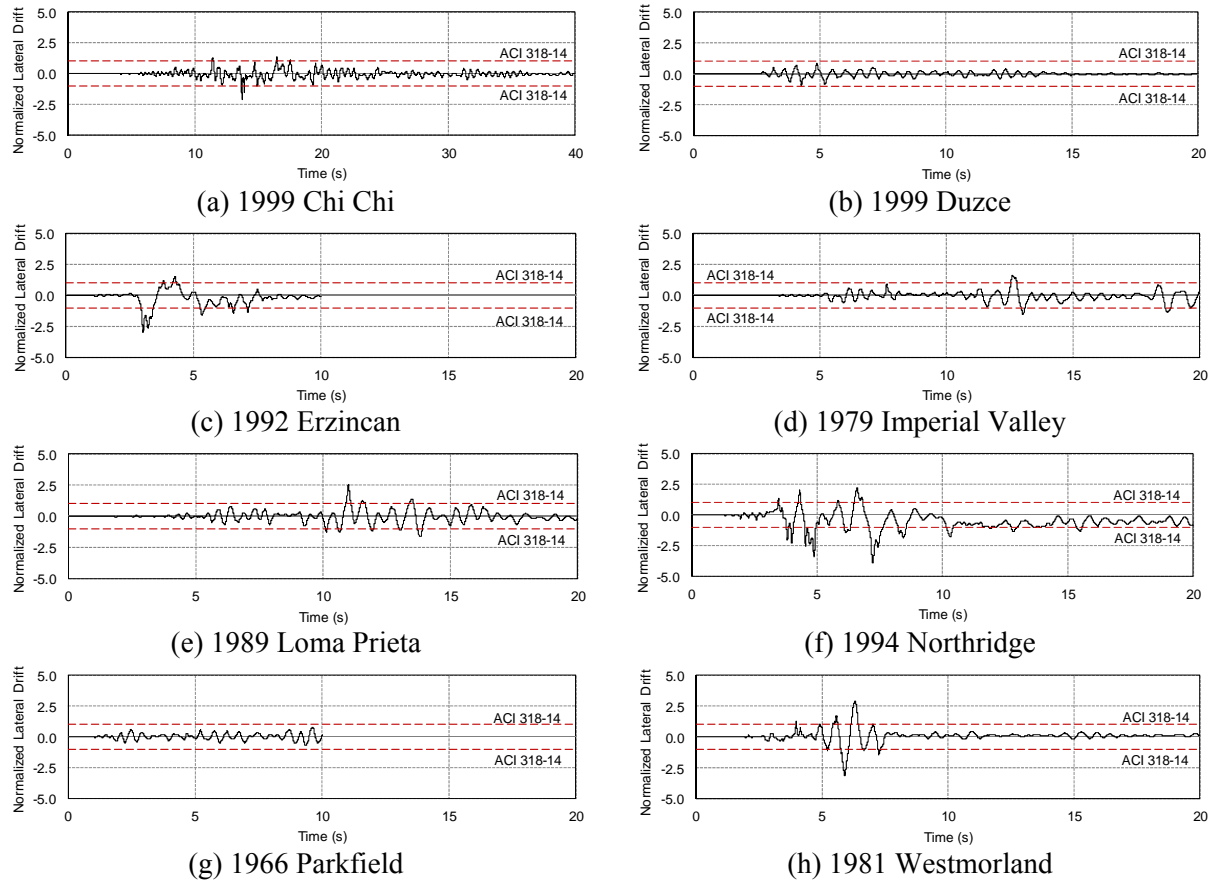


Figure 4-11 Normalized lateral drift in y-direction due to tri-directional ground motion

4.4 USING TWO-WAY SHEAR STRENGTH DEFINED BY ACI

ACI 318-14 (2014) considers a limiting vertical shear stress v_c at punching failure for slab supported at a square column as

$$v_c = 4\sqrt{f'_c} \quad \text{Equation 4-3}$$

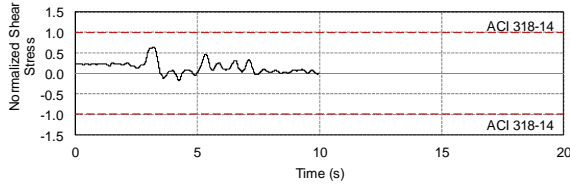
As described in Chapter 1, numerous experiments have clearly demonstrated that, for a slab-column connection with low-to-moderate slab tensile reinforcement ratio, the punching failure is more associated with excessive slab local deformation and the punching strength is overestimated by the code-defined two-way shear strength. However, Equation 4-3 is still commonly used by practicing engineers to estimate punching resistance of a slab-column

connection. Moreover, as claimed earlier, the eccentric shear stress model may not be able to reflect the actual stress condition due to assumption of the linear elastic response of slab-column connection prior to its punching failure. In this section, the shear stress in the elements connected to the slab-column joints are calculated based on the dimension of these elements and the shear force obtained from the output data. The shear stress is then normalized by dividing the shear capacity defined in Equation 4-3. Therefore, a result greater than 1.0 or less than -1.0 would indicate a shear failure.

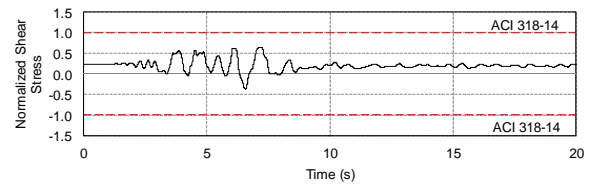
Table 4-3 summaries the results which indicate that none of the grid beam elements reach a value of one for the normalized shear stress. Figures 4-12 and 4-13 show, as examples, the normalized shear stress time history for two ground motions, the scaled 1994 Northridge and the 1992 Erzincan ground motions that cause the large peak responses for lateral drift and slab relative rotation. The results for bi-axial and tri-axial loading are shown in these figures.

Table 4-3 Maximum normalized shear stress per seismic record

Seismic Record	Normalized Shear stress				% Change between 2 and 3-directional motion
	x	y	2-directional	3-directional	
Chi Chi	0.58	0.53	0.61	0.62	1.63
Duzce	0.6	0.53	0.61	0.61	-
Erzincan	0.61	0.59	0.63	0.63	-
Imperial Valley	0.61	0.57	0.62	0.63	1.60
Loma	0.59	0.57	0.63	0.63	-
Northridge	0.61	0.57	0.64	0.65	1.55
Parkfield	0.55	0.52	0.56	0.56	-
Wesmorland	0.58	0.63	0.63	0.64	1.57
Average	0.59	0.56	0.62	0.62	0.79

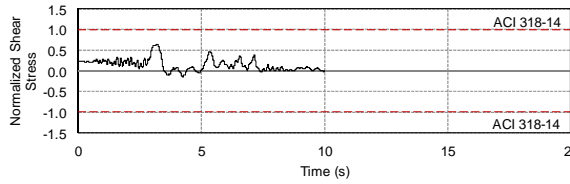


(a) 1999 Chi Chi

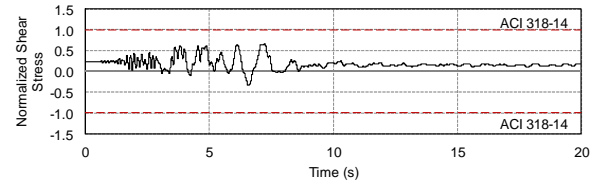


(b) 1994 Northridge

Figure 4-12 Normalized shear stress due to bi-directional ground motion



(a) 1999 Chi Chi



(b) 1994 Northridge

Figure 4-13 Normalized shear stress due to tri-directional ground motion

4.5 USING PUNCHING RESISTANCE MODEL SUGGESTED BY MUTTONI (2008)

The punching resistance model suggested by Muttoni (2008) has been described in Section 1.2.2 and given in Equation 1-1. The model correlates the punching strength of a slab-column connection as a function of slab rotation outside the shear critical area. The Swiss codes (2003) and the European Model Code (2010) have recently incorporated this model as the foundation for two-way shear design of flat-plate structures. Even though this model has not been examined for cyclic loading conditions, Liu et al. (2015) demonstrated that the model can accurately capture both strength and deformation capacity of slab-column connections resisting monotonically applied unbalanced moment. The model is believed to have best reflected the nature of a punching failure to date by the author of the present study and thus used to evaluate the punching failure risk of the prototype building.

For convenience of discussion, Equation 1-1 is repeated below as Equation 4-4 where ψ is slab rotation relative to the supporting column and V_R is the total shear resistance of slab-column connection under concentric gravity loading. The definition of other variables can be found in Section 1.2.1. Because the slab-column connections are subjected to unbalanced

moment, Equation 4-4 is applied individually to the grid beam elements shown in Figure 3-2. Because there are a total of eight grid beam elements connected to an interior column, the shear resistance of each beam is assumed as 1/8 of that defined by Equation 4-4. From Equation 4-4, the slab rotation capacity ψ_R corresponding to a punching failure is formulated using Equation 4-5, where V is shear force in a single grid beam element identified from the numerical simulations.

$$\frac{V_R}{b_o d \sqrt{f'_c}} = \frac{9}{1 + 15 \frac{\psi d}{d_{g0} + d_g}} \quad (\text{units: psi, in.}) \quad \text{Equation 4-4}$$

$$\psi_R = \frac{1}{15} \left(\frac{9 b_o d \sqrt{f'_c}}{8V} - 1 \right) \left(\frac{d_{g0} + d_g}{d} \right) \quad (\text{units: psi, in.}) \quad \text{Equation 4-5}$$

For the prototype structure, the maximum aggregate size has been assumed as $d_g = 0.75$ in. The slab rotation ψ predicted from the simulations is then normalized as the ratio of ψ/ψ_R . If the ratio is equal to or greater than unity, a punching failure at the grid beam element is predicted. The following sections present the results of punching failure evaluation using the Muttoni's model.

4.5.1 Using Slab Rotation Capacity for Uni-directional Ground Motion

Figures 4-14 and 4-15 show the normalized rotation angle of slab relative to column for the prototype building subjected to ground motions applied only in one direction. Under the ground motions in the x-direction alone, half of the records cause the slab at column 5007 to exceed the rotational capacity as can be seen in Figure 4-14. The scaled 1994 Northridge ground motion records the peak normalized slab rotation of 2.02, whereas the 1966 Parkfield record logs the lowest peak value of 0.58. The average normalized slab relative rotation is 1.16.

As shown in Figure 4-15, seismic ground motion applied in the y-direction alone produces similar results to ground motion applied in the x-direction only. Five of the seismic records produce a rotational demand larger than capacity. The scaled 1981 Westmorland motion causes the largest slab rotation three times the rotational capacity. The 1966 Parkfield motion logs the lowest normalized slab rotation of 0.54 or 54% of the rotational capacity. The average normalized slab rotation is 1.42 for all seismic records. Table 4-4 lists the evaluation results using the Muttoni's punching failure model for the prototype building under different seismic loading conditions.

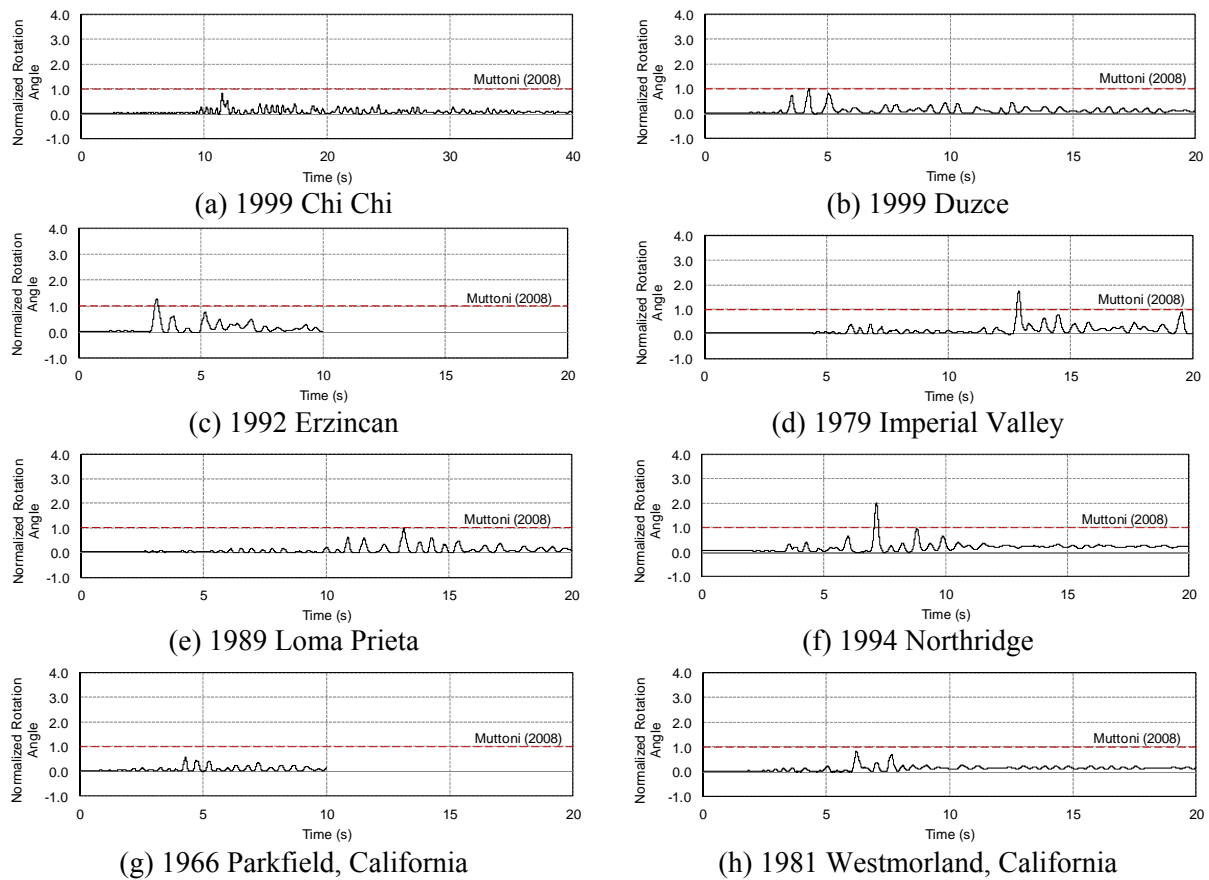


Figure 4-14 Normalized slab rotation due to ground motion applied in x-direction

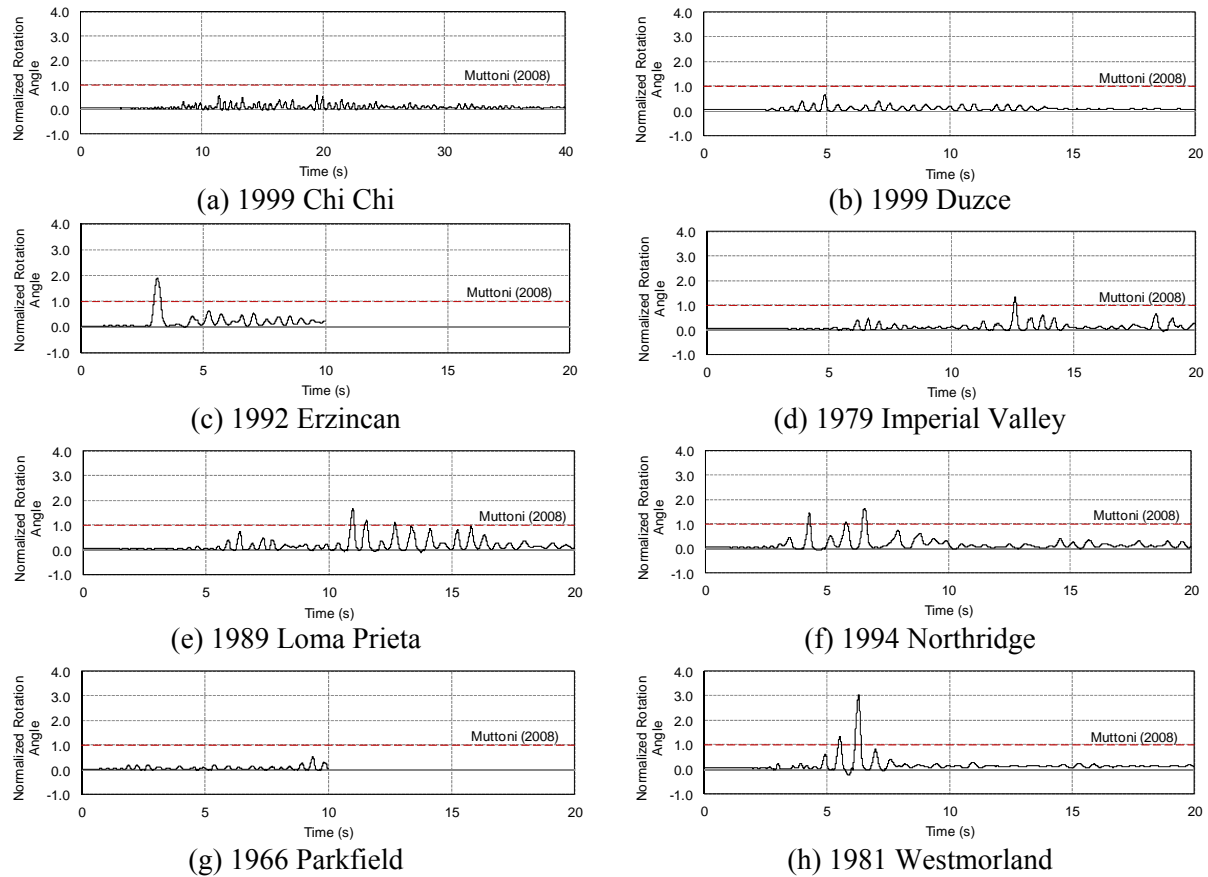


Figure 4-15 Normalized slab rotation due to ground motion applied in y-direction

Table 4-4 Maximum normalized slab rotation angle per seismic record

Seismic Record	Normalized slab rotation angle				% Change between 2 and 3-directional motion
	x	y	2-directional	3-directional	
Chi Chi	0.83	0.59	1.17	2.35	67.1
Duzce	1.01	0.65	1.34	1.78	28.2
Erzincan	1.29	1.9	2.66	2.84	6.55
Imperial Valley	1.74	1.35	1.97	2.19	10.6
Loma	0.97	1.68	2.1	2.47	16.2
Northridge	2.02	1.63	3.69	4.96	29.4
Parkfield	0.58	0.54	0.36	0.78	73.7
Westmorland	0.83	3.03	3.32	3.76	12.4
Average	1.16	1.42	2.07	2.64	30.5

4.5.2 Using Slab Rotation Capacity for Bi-directional Ground Motion

Figure 4-16 demonstrates that seismic ground motion applied in two horizontal directions simultaneously produced a rotational demand greater than the capacity for all seismic records except the 1966 Parkfield ground motion, which logs a normalized slab rotation of 0.36. The 1994 Northridge ground motion records the largest normalized slab rotation of 3.69 with Westmorland trailing close behind at 3.32. With the exception of the 1966 Parkfield motion, all seismic records were at least 17% overstressed.

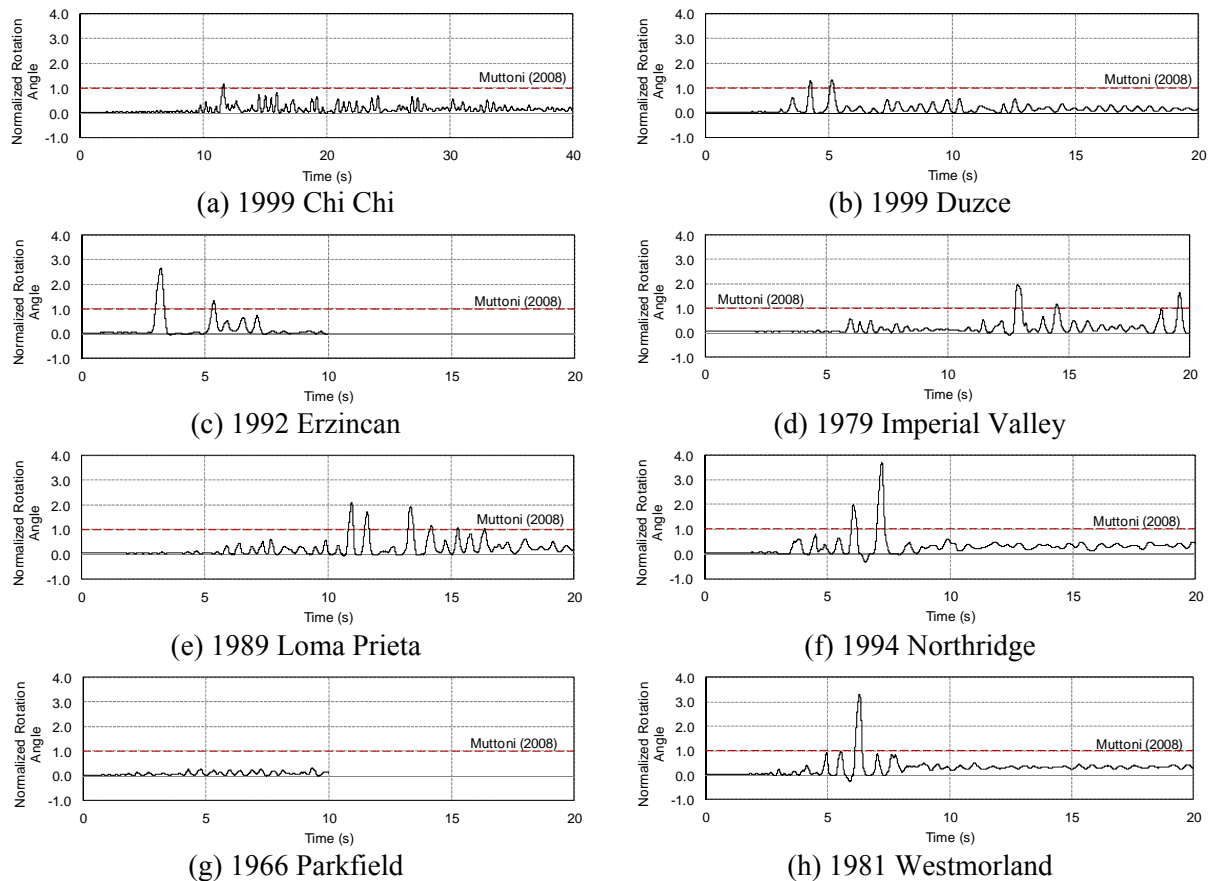


Figure 4-16 Normalized slab rotation due to 2-directional ground motion

As shown in Table 4-4, the average peak normalized slab rotation is significantly greater than uni-axial loading condition. Such a result is consistent with the observations obtained from the experiments conducted by Pan and Moehle (1992) on isolated slab-column specimens: bi-axial loading causes both reduced slab-column connection stiffness and reduced deformation capacity of slab-column connections.

4.5.3 Using Slab Rotation Capacity for Tri-directional Ground Motion

Ground motion is applied in three directions simultaneously: two horizontal directions and one vertical direction. Figure 4-17 shows the normalized rotation angle for each seismic record. Tri-directional ground motion produces a rotational demand nearly two times larger than the capacity in every seismic record with the exception of the 1966 Parkfield ground motion, which records a maximum rotation angle at 78% of capacity. The 1994 Northridge ground motion logs the largest peak rotational response with a normalized value of 4.96.

For all seismic records a significant increase in normalized slab rotation corresponding to increased risk of punching failure, when the vertical ground motion is included, is found as shown in Table 4-4. Compared with the case of bi-directional loading, an average change of 30.5% is made, with the 1966 Parkfield ground motion producing the largest percent change of 73.68%, even though this ground motion may not lead to the values of normalized slab rotation greater than unity or a distress of punching failure. The 1992 Erzincan ground motion gives the smallest percent change of 6.55% and is the only record to have an increase of normalized slab rotation less than 10%.

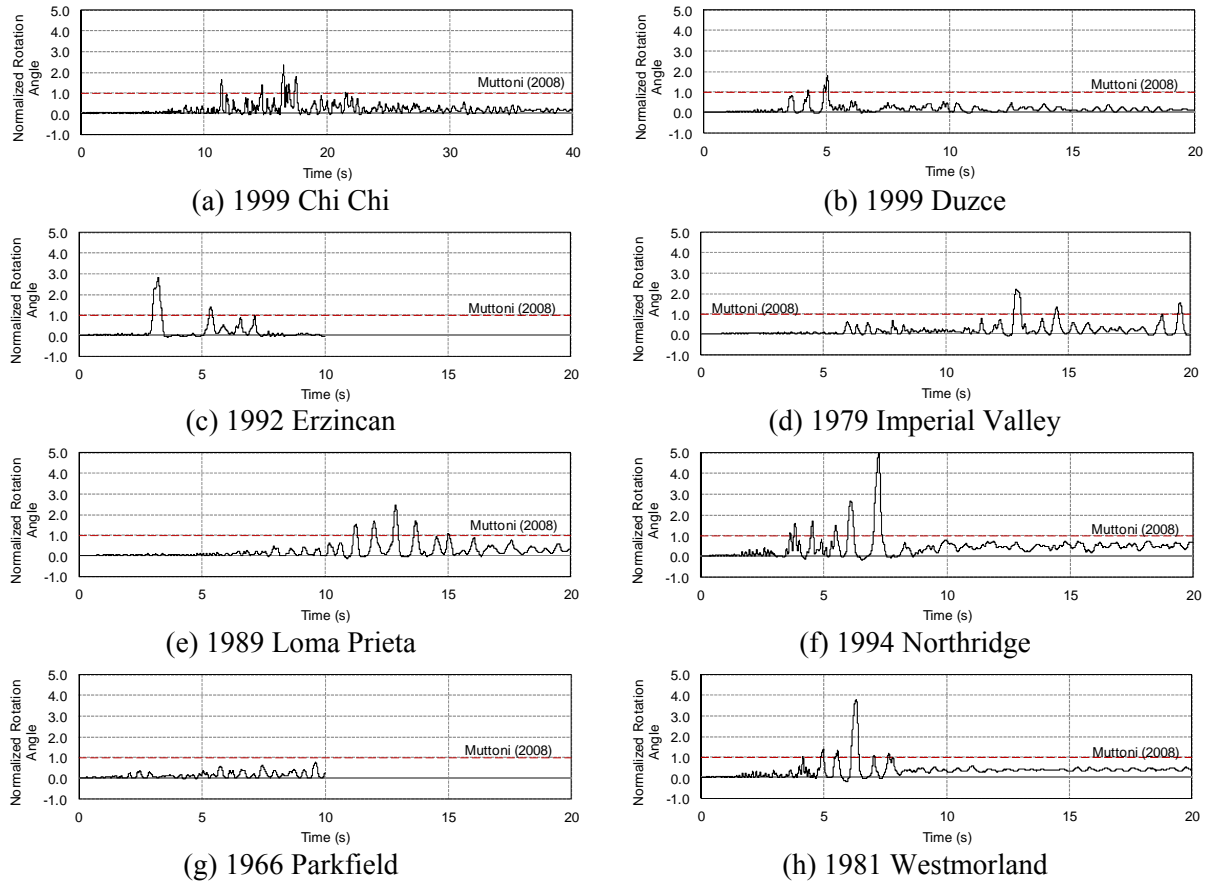


Figure 4-17 Normalized slab rotation due to 3-directional ground motion

4.6 SUMMARY OF PUNCHING FAILURE RISK USING DIFFERENT CRITERIA

An overview of the application of each type of punching failure criterion to the prototype building is shown in Figure 4-18. X, Y, XY, and ALL correspond to the results for ground motion applied in x-direction only, y-direction only, both x- and y-directions, and all three directions. The average normalized demand for the eight ground motion records is also shown in this figure and is the basis of the following discussions.

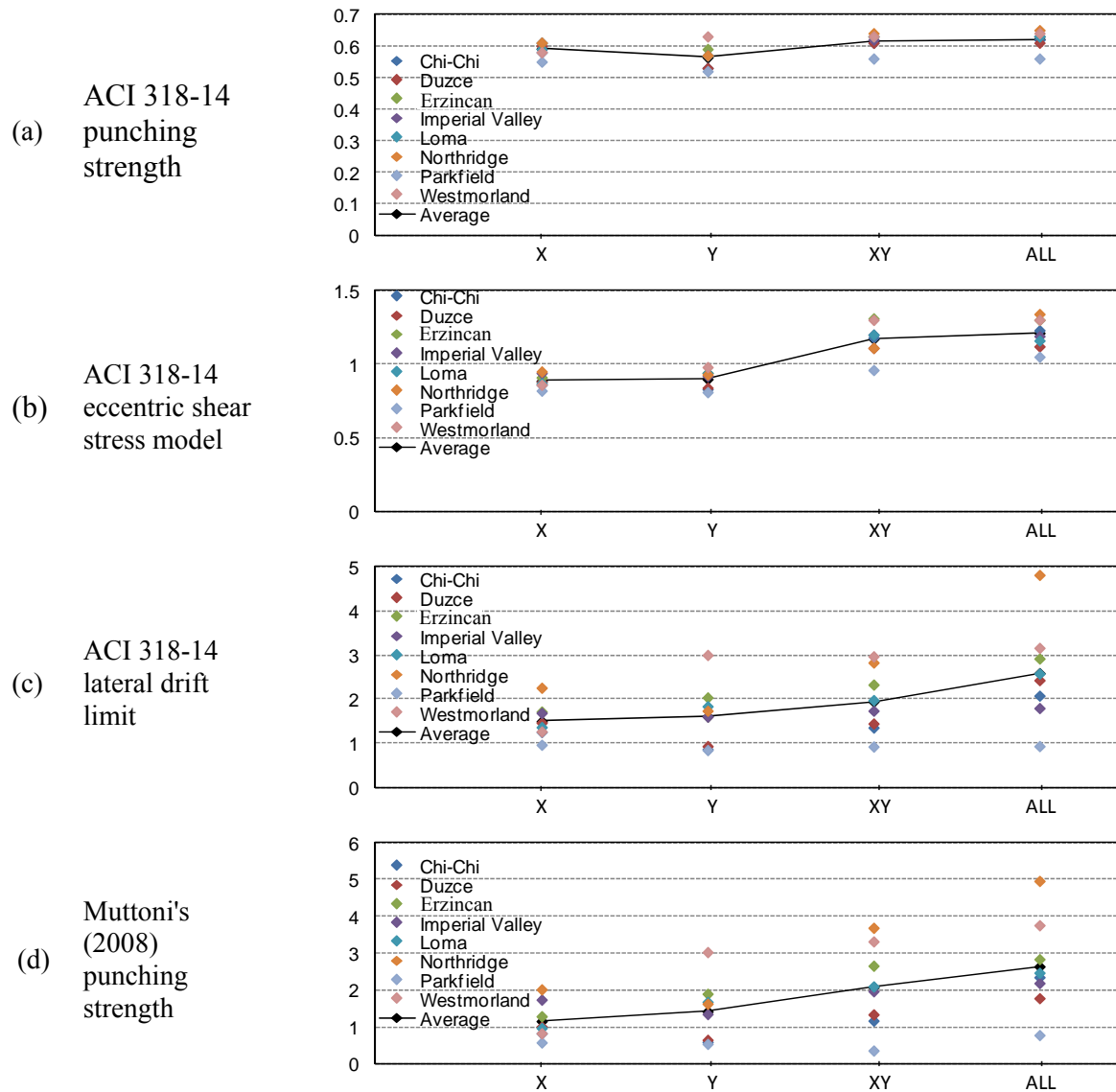


Figure 4-18 Summary of results of punching failure prediction

Using the shear stress predicted by the grid beam model and the shear strength defined by ACI 318, punching failure of slab-column connections cannot occur (Figure 4-18(a)). This is because, due to the relatively low slab reinforcement ratio and thus the low flexural strength, the shear stress in slab can never reach the code-defined two-way shear strength. This is highly unrealistic for an average slab rotational demand up to 0.05 rad. for ground motion in three directions as shown previously in Table 4-2. Given that punching failure will eventually occur at

large deformation regardless of the level of shear stress, such an approach apparently shall not be used to predict the punching failure potential of flat-plate structures.

As seen in Figure 4-18(b), the use of eccentric shear stress model predicts no punching failure under uniaxial loading condition. Even though this approach indeed indicates the likelihood of punching failure under bi-axial and tri-axial loading, it shows little effects of vertical ground motion on punching failure potential. This is because, as described in Section 3.3.3, lateral displacement demands are similar between bi-directional and tri-directional ground motions; thus, the model predicts similar punching failure risk. However, it is clear from the previous discussions that the addition of vertical ground motion creates both significant additional vertical shear transfer and slab local deformation demand, leading to a greater likelihood of failure.

It is interesting to note that the ACI 318 drift limit approach and the Muttoni's punching failure criterion predict very similar risk of punching failure for all four types of loading conditions. Each approach indicates that punching failure may occur in the uniaxial loading condition with greater risk under loading in y-direction alone. Moreover, each one predicts the trend of greater risk of punching failure due to the incorporation of vertical ground motion. More importantly, the two approaches predict almost identical value of failure index when the ground motions are applied bi-directionally and tri-directionally. Even though the ACI drift limit approach correlates punching failure with global deformation rather than slab local deformation that causes a failure, this approach was developed empirically based on experimental data.

CHAPTER 5

EFFECTS OF SOIL-STRUCTURE INTERACTION

5.1 INTRODUCTION

During an earthquake, seismic waves are transferred from the surrounding soil to the foundation and then into the structure. The dynamic behavior of the structural system can be affected by the soil and foundation properties. The induced motion of the structure in-turn generates inertial forces which are transferred back to the foundation and into the surrounding soil. The dynamic interrelationship where response of soil, foundation and structure to a specified ground motion is evaluated is referred to as soil-structure interaction (SSI) analysis. Common practice of analysis and design of buildings is to assume the base of building to be conventionally fixed, whereas in reality supporting soil influences the structural response by allowing movement due to its inherent ability to deform. The goal of modeling the soil-structure interaction for this study is to examine the effects of SSI on the response of plat-plate building especially when considering vertical ground motion. For this purpose, the foundation of the prototype building is designed, SSI is modeled, and time-history analyses incorporating SSI are conducted.

5.2 FOOTING DESIGN OF PROTOTYPE BUILDING

For the prototype building with assumed site condition, a sandy soil is considered with soil properties outlined by Madani et al. (2015) and a shear wave velocity (V_s) of 656 ft/s comprising a soil type of D per IBC (2015). The soil is assumed to be homogenous with an allowable bearing pressure of 2000 psf used for footing design per IBC (2015) for sand type soils. Additional soil properties are given in Table 5-1.

Table 5-1 Soil properties used to design column footings

Allowable Bearing Pressure	2000 psf
Soil Unit Weight (γ)	120 pcf
Friction Angle (ϕ)	35°
Coefficient of Base Friction	0.462
Shear Wave Velocity (V_s)	656 ft/s
Shear Modulus ($G = \frac{\gamma V_s^2}{g}$) where g = gravity	11.15 psi
Poisson's Ratio (ν)	0.4

A spread footing at shallow embedment depth was designed for each column of the prototype building. Three types of column exist for the prototype structure: corner column, interior column and perimeter column. Spread footings are checked for bearing pressure, shear capacity, overturning, and sliding per ACI 318-14 (2014). Loading conditions determined from various load combinations for each column result in similar footing size. Therefore uniform dimensions for all three types of column are chosen for simplicity in modeling. The design results are summarized in Table 5-2.

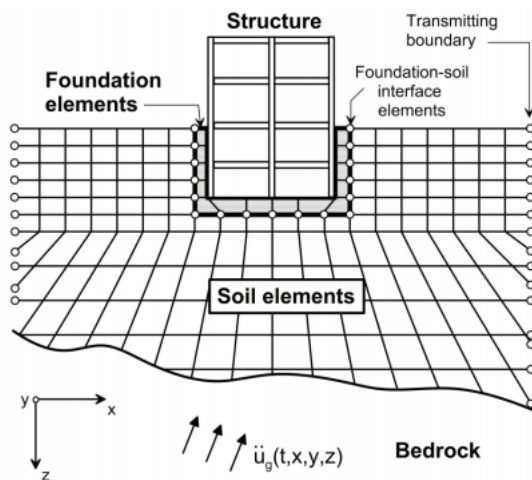
Table 5-2 Spread footing sections of prototype building

Column Condition	Width x Length x Depth (ft)	Steel Reinforcement	
Corner	10 x 10 x 3	Top: Bottom:	11- #3 ea. way 11- #8 ea. way
Interior	10 x 10 x 3	Top: Bottom:	11- #3 ea. way 11- #6 ea. way
Perimeter	10 x 10 x 3	Top: Bottom:	11- #3 ea. way 11- #6 ea. way

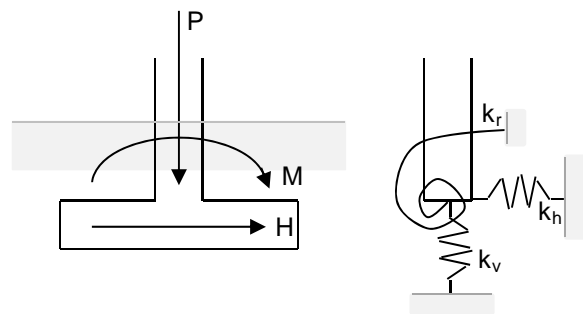
5.3 MODELING SOIL-STRUCTURE INTERACTION

5.3.1 Overall Modeling Considerations

SSI is commonly evaluated by either a direct method (Figure 5-1a) or substructure method (Figure 5-1b). The direct method allows the soil, structure, and foundation to be represented as a continuum model. The components are modeled together using finite element and the ground motion is specified as the free field motion applied at all boundaries. The direct method can give in-depth analysis, but computational costs are high for complex systems. The substructure method models the stiffness at the soil foundation interface by use of springs which represent the soil material properties. Sub-structure method is computationally more efficient than the direct method. Many substructure models have been proposed for simple representation of SSI such as the cone model (Wolf and Meek, 1994) and many variations of the Winkler model (Winkler, 1867). Due to the large degree of freedom of the prototype structure, the substructure modeling approach by Gazetas (1991) is employed in this study.



(a) Direct continuum model (NIST, 2012)



(b) Substructure model (Adhikary et al., 2008)

Figure 5-1 SSI modeling

Foundation movement is considered for each degree of freedom including the two perpendicular horizontal directions, vertical direction, and the rotation about the three directions. The nonlinear finite element model for the prototype building described previous is modified by adding translational springs along three directions and rotational springs about the lateral axes below each column to simulate the soil-structure interaction as shown in Figure 5-2. Each spring is assigned with elastic behavior.

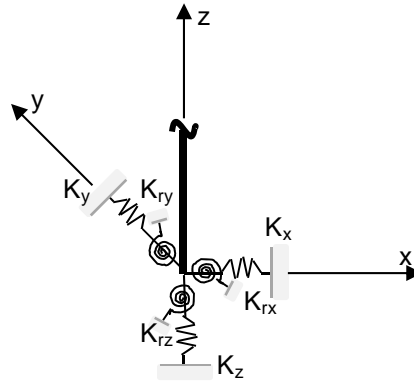


Figure 5-2 Translation and rotational springs for soil-interaction

One approach for modeling soil springs is considering a dynamic stiffness, which is defined as a function of input ground motion frequency even though soil properties are frequency independent (Gazetas, 1991). The dynamic spring stiffness can reflect both the stiffness and the inertia of the soil supporting a structure. For this purpose, a dynamic stiffness coefficient (k) is used to modify the spring stiffness (K), as shown in the Equation 5-1.

$$\bar{K} = K \times k(a_0) \quad \text{Equation 5-1}$$

$$a_0 = \frac{\omega B}{V_s} \quad \text{Equation 5-2}$$

The dynamic stiffness coefficient (k) depends upon a dimensionless frequency factor (a_0) per Equation 5-2 where ω is the frequency of the forcing function, V_s is the shear wave velocity, and B represents half the lateral dimension of the footing as shown in Figure 5-4 where $B \leq L$. The use of the frequency factor is demonstrated in Figure 5-3 for translational stiffness in the horizontal and vertical direction.

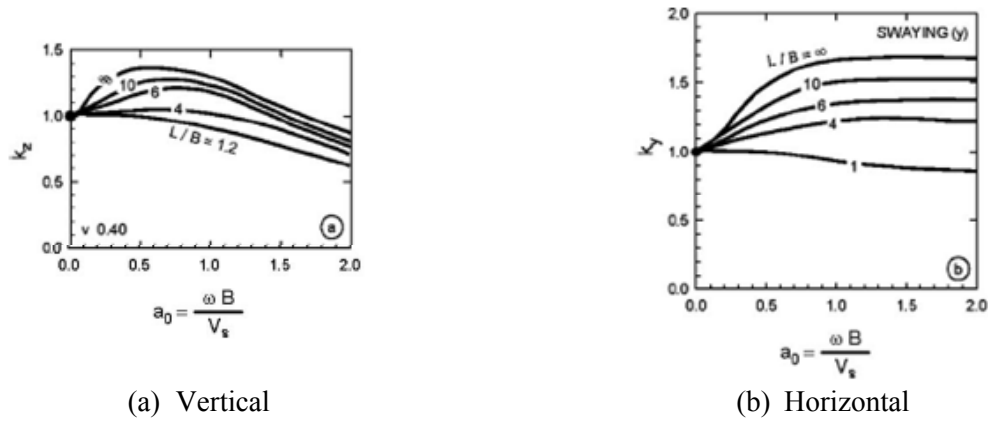


Figure 5-3 Frequency factor for translational spring stiffness

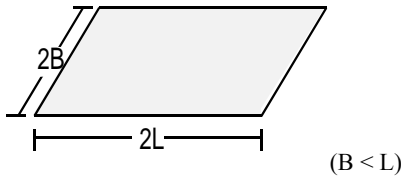


Figure 5-4 Foundational footing dimensions

Ghannad and Jahankhah (2007) found that for ordinary building types the practical range for a_0 is between zero for fixed-base structures and three for cases with predominant SSI effects. It should be noted that a value of zero for a_0 results in a dynamic stiffness coefficient of 1.0 for translational and rotational stiffness. Furthermore, unless the dynamic time-history analysis is carried out in the frequency domain, it can be difficult to consider any frequency dependent

multiplier because a seismic motion involves a wide range of participating frequencies. Some literature (Parmelee et al., 1969, Prakash and Puri, 1988) has recommended against the use of such multiplication factor perceivably for this reason. Therefore, the dynamic stiffness coefficient is not considered in this study.

A factor that accounts for foundations that are fully or partially embedded in a deep and homogenous soil deposit may be applied to define soil spring stiffness. Embedded foundations are inclined to be stiffer due to soil compaction around the footing. However, horizontal forces at large embedment depths induce rotational oscillations at the footing base creating horizontal rocking impedance. The rocking impedance is negligibly small for surface and shallow foundations (Gazetas, 1991). Therefore, the effect of embedment on the prototype building designed with a shallow embedment depth is not considered.

Another parameter affecting SSI is the damping property of soil. Estimating the total damping of a system is often difficult due to complex radiation damping generated by waves propagating away from the vibrating foundation in translation and rotation and material damping due to energy dissipated in the soil by hysteretic action. Gazetas (1991) considers a simple method for estimating damping by considering damping to be frequency dependent by use of a dimensionless frequency factor. However, simple methods typically used to estimate structural damping from the dynamic response of the structure often fail to yield realistic system damping (Ostadan, 2004). Therefore, soil damping is neglected in this study.

5.3.2 Modeling Spring Stiffness for SSI

The stiffness of the springs is defined using Gazetas's model (1991), which takes into account foundation shape, footing embedment, and significant modes of vibration. The soil

profile for this model is assumed as homogenous half-space continuum. Half-space continuum allows soil medium to be mathematically idealized by assuming soil is a flat surface and its properties extend to infinity in the horizontal direction and in depth (McGuire et al., 1994).

The model considers rectangular footing having a length of $2L$ and a width of $2B$ where $L > B$ as shown in Figure 5-4. The stiffness of the springs associated with the six degrees of freedom is defined using Equations 5-3 through 5-8, where SI units shall be used. The direction with large dimension is termed hereafter as longitudinal (x) direction and another horizontal direction is termed as transverse (y) direction.

$$K_z = \left[\frac{2GB}{1-\nu} \right] (0.73 + 1.5(A_b 4L^2)^{0.75}) \quad \text{Equation 5-3}$$

$$K_y = \left[\frac{2GB}{2-\nu} \right] (2 + 2.5(A_b 4L^2)^{0.85}) \quad \text{Equation 5-4}$$

$$K_x = \left[\frac{2GB}{2-\nu} \right] (2 + 2.5(A_b 4L^2)^{0.85}) - \left[\frac{0.2}{0.75-\nu} \right] GL \left[1 - \frac{B}{L} \right] \quad \text{Equation 5-5}$$

$$K_{rx} = \left[\frac{G}{1-\nu} \right] I_{bx}^{0.75} (B/L)^{0.25} [2.4 + 0.5(B/L)] \quad \text{Equation 5-6}$$

$$K_{ry} = \left[\frac{3G}{1-\nu} \right] I_{by}^{0.75} (B/L)^{0.15} \quad \text{Equation 5-7}$$

$$K_t = 3.5GI_{bz}^{0.75} (B/L)^{0.4} (I_{bz}/B^4)^{0.2} \quad \text{Equation 5-8}$$

where K_z , K_y , and K_x are the stiffness of springs oriented in the vertical, transverse, and longitudinal directions, respectively; K_{rx} , K_{ry} , and K_t are the stiffness of springs providing rotational stiffness about longitudinal direction, rotational stiffness about transverse direction, and torsional stiffness; B and L ($L \geq B$) represent the half width and half length of the footing respectively as shown in Figure 5-4; A_b is footing area; G is soil shear modulus, ν is soil Poisson's ratio; I_{bx} , I_{by} , and I_{bz} are the area moments of inertia of the x-, y- and z- axes of the actual soil-foundation contact surface. Because square footings are used in the prototype

building, the spring stiffness representing soil-structure interaction is simplified per Equations 5-9 through 5-12, which use SI units. Table 5-3 gives the soil spring stiffness defined for the prototype building. It is noted that because stiffness depends upon the foundation area, identical springs with different horizontal, vertical, and rotational stiffness are used at each column.

$$K_z = \frac{4.54GB}{1 - \nu} \quad \text{Equation 5-9}$$

$$K_x = K_y = \frac{9GB}{2 - \nu} \quad \text{Equation 5-10}$$

$$K_{rx} = K_{ry} = \frac{0.45GB^3}{1 - \nu} \quad \text{Equation 5-11}$$

$$K_t = 8.3GB^3 \quad \text{Equation 5-12}$$

Table 5-3 Soil spring stiffness for translational directions

Spring	Stiffness
K_x, K_y	3762 (kip/in)
K_z	5061 (kip/in)
K_{rx}, K_{ry}	1805934 (kip-in/rad)
K_{rz}	19985670 (kip-in/rad)

To model the translational soil springs in OpenSees, a fixed node was placed one unit length away from the bottom end of every column in the x-, y- and z-direction (Figure 5-5). To model the translational soil stiffness, soil springs spanning between the fixed node and the column bottom end are modeled by truss elements which allow the user to specify cross sectional area and material properties so that the spring stiffness can be equivalently defined.

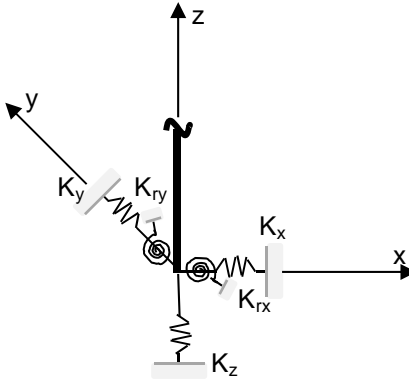


Figure 5-5 Soil spring model at end of column

Rotational soil springs are modeled for the x- and y-axes by the use of zero-length elements defined by two nodes at the same location (bottom of the column) with one end fixed and the other at column bottom (Figure 5-5). Rotational spring about at the z-axis is neglected for the prototype building due to the structure's regular symmetry and its high torsional stiffness per Table 5-3. Therefore, boundary conditions are specified to allow rotation about the horizontal x- and y-axis for the column end, but are restrained from torsional rotation about the z-axis.

Additionally, the translational movements of column bottom end are permitted in all the three directions. Constraints are also imposed for the rotational springs so that they would not be functional in the degrees of freedom that are not being investigated, i.e. springs for rotation about x-axis would not resist translations in the x-, y-, or z-axis nor would it restrain rotation about the y- or z-axis. Finally, the material and material direction of the zero-length elements are specified so that the spring stiffness can be consistently defined in the desired direction.

The material properties of the translational and rotational springs are specified as elastic by the force-deformation relationship shown in Figure 5-6. Stiffness of the truss element is not specified directly, but instead is calculated by the use of the cross sectional area (A), length (L), and Young's modulus (E). By setting the length and Young's modulus of the truss element to

one, the area equals the stiffness per Equation 5-13. The stiffness of the zero-length rotational springs (K_r) is able to be input directly by the moment (M)-rotation (θ) relationship given in Equation 5-14 and shown in Figure 5-6.

$$\text{Stiffness } (K) = \frac{AE}{L} \quad \text{Equation 5-13}$$

$$\text{Stiffness } (K_r) = \frac{M}{\theta} \quad \text{Equation 5-14}$$

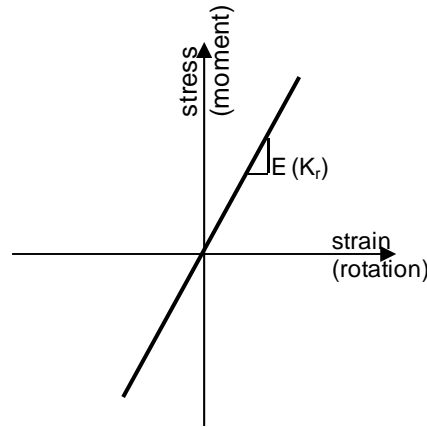


Figure 5-6 OpenSees elastic material definition

5.4 SOIL-STRUCTURE INTERACTION RESULTS

The prototype structure is subjected to the eight scaled seismic ground motions that have been employed previously and the effects of soil are incorporated by use of soil springs described previously. Ground motion accelerations are applied at the nodes, from which translational and rotational soil springs are connected to column bottom ends, and are applied tri-directionally. The analysis results, in terms of the responses of lateral drift, axial force in the interior columns, and slab local rotation, are compared with those obtained without considering any SSI.

5.4.1 Lateral Displacement Response Considering SSI

Figure 5-7 shows the roof lateral displacement response for seismic ground motions applied simultaneously in the x-, y-, and z-directions to the prototype structure with SSI (labeled as soil) and without SSI (labeled as original). Due to the high in-plane rigidity of slab and beams, the columns displace similarly. Thus, the displacement time-history is given at the top of the center column (at node 5012 per Figure 3-1). The lateral displacement is the resultant displacement obtained from the two orthogonal horizontal components. Table 5-4 summarizes the peak dynamic displacement response for the two type of dynamic analysis (with and without SSI) as well as the percent change in the resultant lateral displacement.

The lateral displacement response due to triaxial loading for SSI shows a nearly identical trend to the results where SSI is not incorporated. Overall an average percent change of 2.68% is evidenced for the eight scaled seismic ground motions including SSI versus the results where SSI is excluded. The largest displacement response of 7.44 in. is recorded by scaled 1994 Northridge seismic record, corresponding to a 3.42% change from its counterpart that does not include SSI. The lowest lateral displacement of 2.0 in. is created by the scaled 1966 Parkfield ground motion, resulting in just over 4% change from the outcome of triaxial loading without SSI. The scaled 1999 Chi Chi seismic record causes the least percent change of 0.66% while the 1999 Duzce produces the highest percent change at 5.93%. The resulting average drift ratio is 3.87%, only slightly higher than the drift ratio where soil effects are not considered.

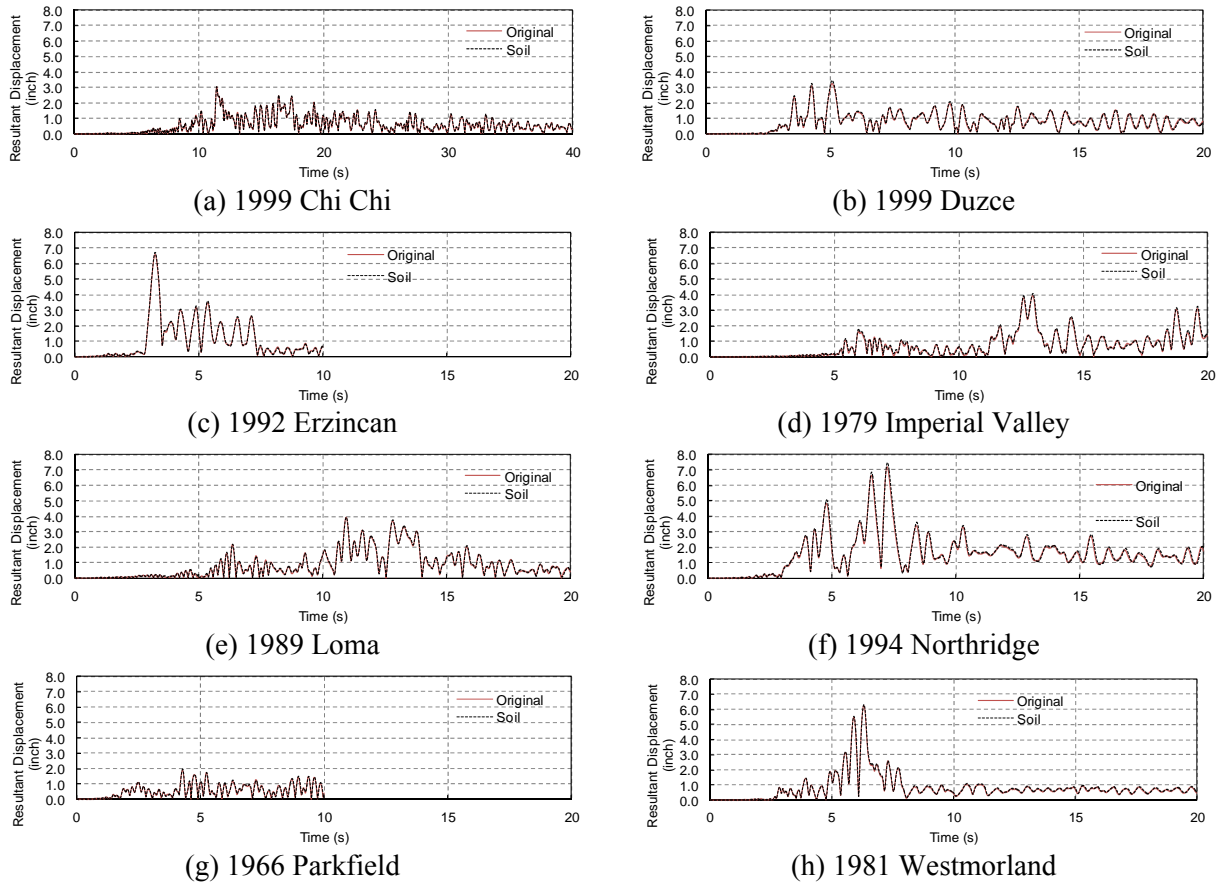


Figure 5-7 Lateral displacement due to ground motions applied tri-directionally for SSI

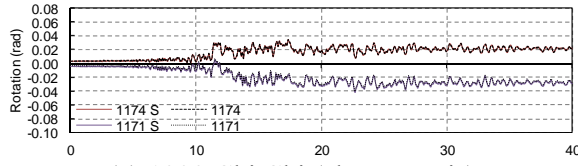
Table 5-4 Maximum displacement response due to tri-directional ground motion with and without considering soil-structure interaction

Seismic Record	Peak displacement (in.)						% Change
	considering SSI			without SSI			
	x	y	Resultant	x	y	Resultant	
Chi Chi	2.48	1.94	3.03	2.46	2.01	3.05	0.66
Duzce	3.26	1.28	3.27	3.46	1.30	3.47	5.93
Erzincan	4.85	4.68	6.62	4.96	4.76	6.75	1.94
Imperial Valley	3.35	3.23	3.96	3.37	3.44	4.07	2.74
Loma	3.65	3.46	3.92	3.75	3.53	3.97	1.27
Northridge	5.60	4.76	7.19	5.69	5.05	7.44	3.42
Parkfield	1.90	1.44	1.92	1.96	1.45	2.00	4.08
Westmorland	3.60	5.46	6.27	3.67	5.57	6.36	1.43
Average	3.59	3.28	4.52	3.67	3.39	4.64	2.68
Ave. Drift Ratio %	2.99	2.73	3.77	3.05	2.82	3.87	

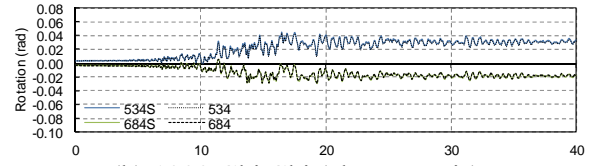
It is seen from Section 3.3 that vertical seismic ground motion has little effect on the lateral drift response since the overall lateral deformation of the structural system is controlled by the perimeter moment frame, which may not be affected much by the vertical ground motion. Similarly, the vertical soil interaction will most likely have an insignificant effect on the lateral drift of the system. It follows that only the horizontal SSI may allow significant foundation movement in the lateral direction with the varying soil stiffness. However, the results obtained from this study suggest that SSI does not much affect the lateral deformation response of the structure. This is due to the relatively high soil stiffness in the lateral direction. As shown in Figure 3-3, at a lateral displacement of 0.2 in. the lateral force is 156 kips, which gives a lateral stiffness of 780 kip/in., indicating that the horizontal soil stiffness as shown in Table 5-3 is much greater than the lateral stiffness of the upper structure. Thus, the small difference in drift response is primarily caused by the rocking of footing, which is restrained by soil rotational stiffness.

5.4.2 Dynamic Response of Slab Rotation considering SSI

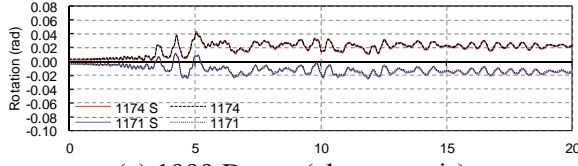
Slab rotation relative to the column for the prototype model incorporating the effects of SSI is recorded about the x- and y-axes at the face of the column as detailed in Section 3.4 for ground motion applied tri-directionally for the eight scaled seismic records. The slab relative rotation time-history with SSI is shown in Figure 5-8, denoted with the letter 'S', and compared with the simulation results without considering SSI. The slab rotations about x- and y-axes are recorded at nodes 5007 and 4012, respectively. The maximum slab relative rotation about the x- and y-directions for each seismic record with and without SSI as well as the percent difference is given in Table 5-5.



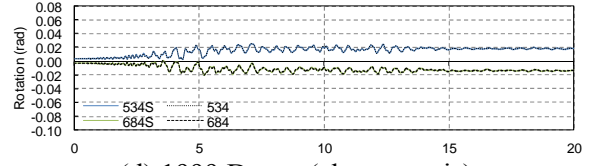
(a) 1999 Chi Chi (about y-axis)



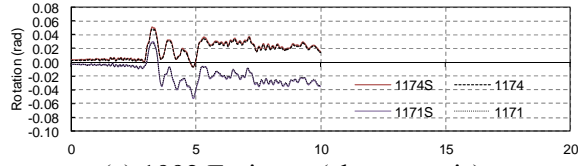
(b) 1999 Chi Chi (about x-axis)



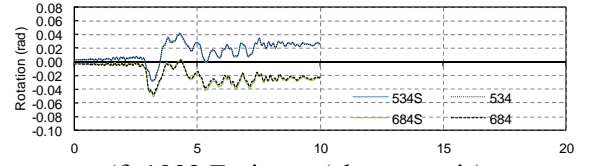
(c) 1999 Duzce (about y-axis)



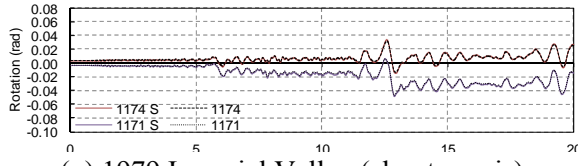
(d) 1999 Duzce (about x-axis)



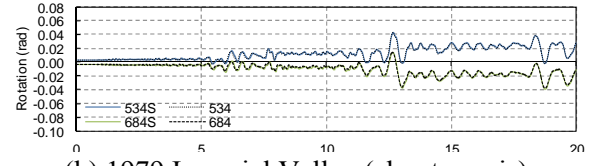
(e) 1992 Erzincan (about y-axis)



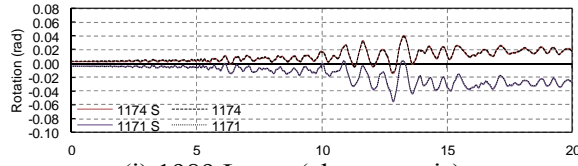
(f) 1992 Erzincan (about x-axis)



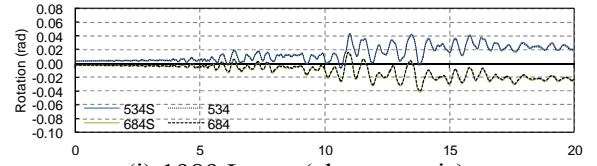
(g) 1979 Imperial Valley (about y-axis)



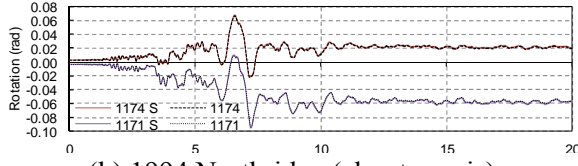
(h) 1979 Imperial Valley (about x-axis)



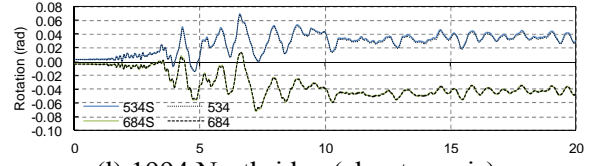
(i) 1989 Loma (about y-axis)



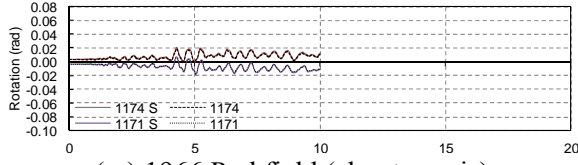
(j) 1989 Loma (about x-axis)



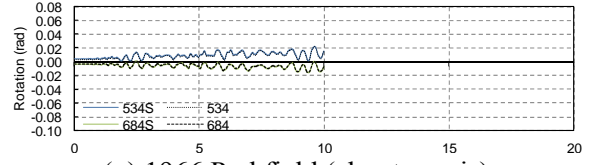
(k) 1994 Northridge (about y-axis)



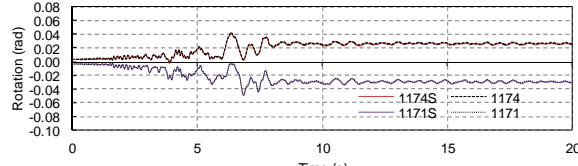
(l) 1994 Northridge (about x-axis)



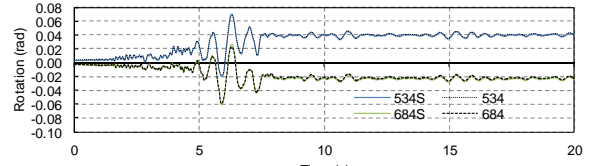
(m) 1966 Parkfield (about y-axis)



(n) 1966 Parkfield (about x-axis)



(o) 1981 Westmorland (about y-axis)



(p) 1981 Westmorland (about x-axis)

Figure 5-8 Slab rotation about the x- and y-axes for tri-directional ground motion with SSI

On average a percent difference in slab rotation about the x- and y-axis of 2.70% and 3.27% is found respectively indicating that similar to lateral deformation, slab relative rotation experiences little change after incorporating SSI in the prototype structure modeling. The largest change in slab rotation about the x- and y-axis (5.83% and 5.94%) is provided by the scaled 1992 Erzincan seismic record. No change about either axis due to the incorporation of SSI is recorded by the scaled 1966 Parkfield ground motion, which also has the lowest peak relative rotation of 0.02 rad. and 0.022 rad. about the x- and y-axis respectively. The largest slab relative rotation under SSI effects is caused by the scaled 1994 Northridge seismic record with 0.095 rad. and 0.073 rad about the x- and y-axis, respectively. On average the peak relative rotation reaches 0.051 rad. about the x-axis and 0.047 rad. about the y-axis. Further results are summarized in Table 5-5.

Table 5-5 Maximum Rotation per Seismic Record

Seismic Record	Rotation (rad)				% change in θ_x	% change in θ_y
	considering SSI		without SSI			
	θ_x	θ_y	θ_x	θ_y		
Chi Chi	0.040	0.044	0.041	0.045	2.47	2.25
Duzce	0.042	0.025	0.043	0.026	2.35	3.92
Erzincan	0.050	0.049	0.053	0.052	5.83	5.94
Imperial Valley	0.048	0.042	0.049	0.044	2.06	4.65
Loma	0.054	0.043	0.056	0.044	3.64	2.30
Northridge	0.094	0.071	0.095	0.073	1.06	2.78
Parkfield	0.020	0.022	0.020	0.022	-	-
Westmorland	0.047	0.068	0.049	0.071	4.17	4.32
Average	0.050	0.042	0.051	0.047	2.70	3.27

Comparing the results of slab relative rotation under triaxial seismic loading with and without the effects of SSI demonstrates negligible effects SSI, an observation similar to that for

lateral displacement response. Furthermore, the degree of changes in peak relative rotation about each axis is comparable to those in lateral deformation in the x- and y-direction, which increases by nearly 2% and 3% respectively. It has been noted previously that the peak slab rotation response coincides with that of the peak lateral deformation response, indicating a strong association between slab rotation relative to column and lateral drift. Therefore, the slight change in relative rotation is most likely the cause of small changes in lateral deformation due to the soil stiffness in the horizontal directions.

5.4.1 Dynamic Response of Axial Force in Interior Columns Considering SSI

Shear force transfer between the surrounding slab and the column is recorded via axial force time-history for the prototype structure with and without SSI effects. It can be assumed due to symmetry and identical footing parameters that the axial force in all interior columns will fluctuate similarly; therefore, the results are shown in Figure 5-9 using only the center interior column where ‘S’ denotes the result for SSI effects. Table 5-6 reports the absolute value of peak axial force in the center column with and without considering the effects of SSI.

Table 5-6 Maximum compressive axial force per seismic record

Seismic Record	Axial Force (kip)		% Change
	considering SSI	without SSI	
Chi Chi	135.1	135.1	-
Duzce	111.5	116.3	-4.21
Erzincan	110.1	110.3	-0.18
Imperial Valley	114.3	112.1	1.94
Loma	104.4	103.3	1.06
Northridge	126.5	123.9	2.08
Parkfield	99.9	99.8	0.10
Westmorland	130.0	129.2	0.62
Average	116.5	116.3	1.27

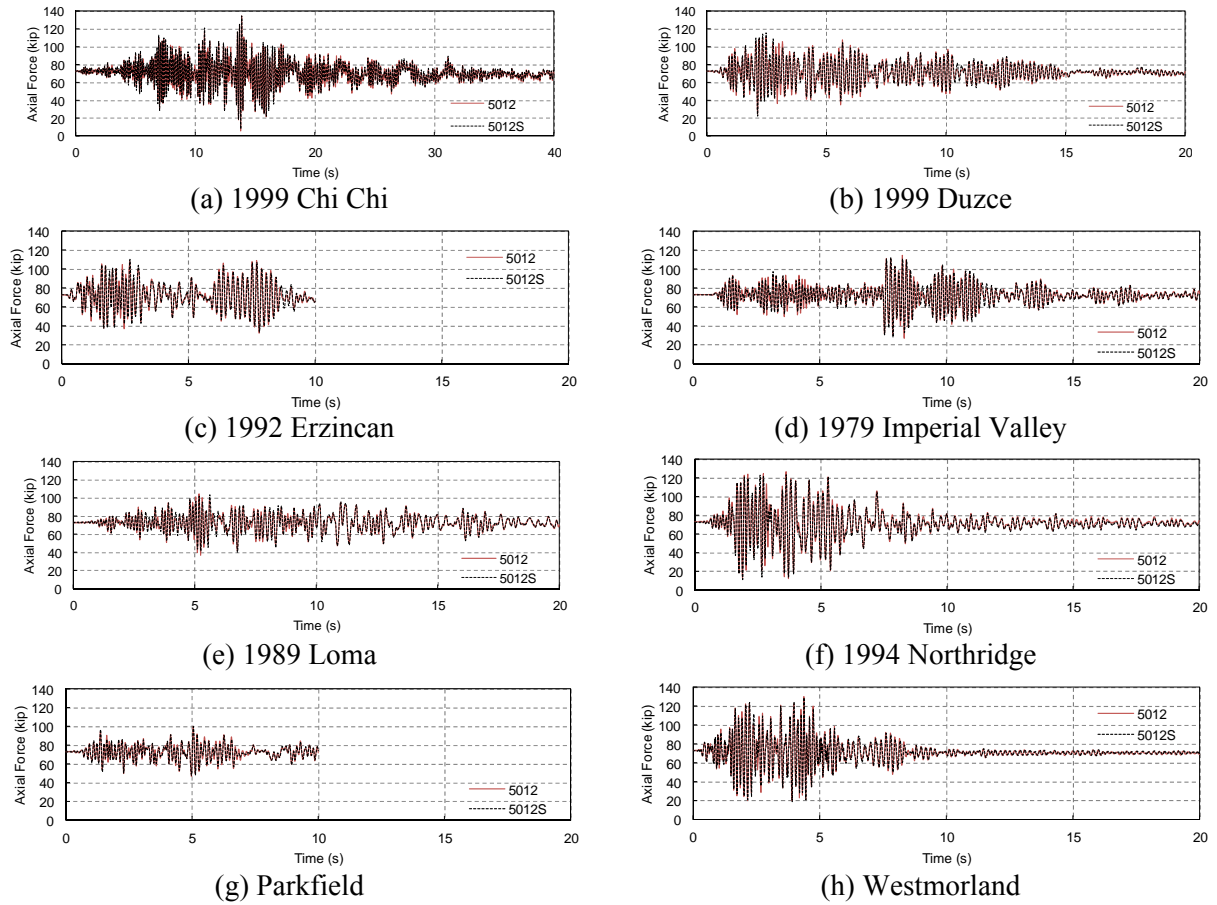


Figure 5-9 Column axial force due to tri-directional ground motion with SSI

The effects of SSI on shear transfer between the column and surrounding slab is found to be minimal. This is not surprising given the similar results for lateral deformation and slab relative rotation. An average percent change of 1.27% is calculated for the eight scaled seismic ground motions with five of the seismic ground motions, 1979 Imperial Valley, 1989 Loma, 1994 Northridge, 1966 Parkfield, and 1981 Westmorland, producing a negative change when SSI is included in the model. The largest axial force of 135.1 kips is caused by scaled 1999 Chi Chi ground motion; it also produces no change between the prototype model with and without SSI. Of the eight seismic records, six causes a percent change less than 2% while the scaled 1994

Northridge and 1999 Duzce create the largest with 2.08% and 4.21% respectively. Additional results for axial force can be located in Table 5-6.

The shear transfer recorded by axial force at the interior columns reveals that the effects of soil on the structure cause little change. In some cases the axial force is reduced when soil effects are included. This may be the result of soil that reduces the vertical inertia force through SSI in the vertical direction. However, the difference between the models with and without SSI is too small to distinguish this trend in the prototype structure.

CHAPTER 6

SUMMARY AND CONCLUSIONS

6.1 RESEARCH SUMMARY

To date very little attention has been given to the role of vertical component of a seismic ground motion; however several near-source seismic events, in which vertical ground motions were prevalent, have produced a high level of seismic damage. The objective of this research is to study the effects of vertical ground motion on reinforced concrete (RC) flat-plate buildings, in particular their vulnerability to punching failure, through nonlinear finite element simulations. Due to the much higher stiffness and strength of RC columns verse those of the slabs, it is expected that for a multi-story flat-plate framing, only the column bottom will experience flexural yielding while the column of slab-column connections will remain elastic. Therefore a one-story flat-plate building is taken as a prototype structure and analyzed. In the numerical model, the slab is simulated using a grid beam model that allows mass to be distributed over the slab and permits better simulations of the nonlinear actions at slab-column connection; perimeter moment frames are utilized in the prototype building as the lateral system and simulated using fiber sections assigned with nonlinear material properties for concrete and reinforcing steel.

Eight near-source seismic ground motions recorded at sites with the same class as that for the prototype building (stiff soil) are chosen as ground excitations. These ground motions vary in the frequency characteristic, V/H ratio, peak vertical and horizontal accelerations, and interval of peak acceleration arrival time. Each ground motion record is then scaled per current code standards and design recommendations. A series of dynamic analyses considering uni-axial, bi-axial, and tri-axial seismic loading are conducted on the prototype structure. Dynamic demands in terms of lateral drift, slab rotation and deflection, and slab-column shear transfer are

determined and compiled. From the analysis results, the effects of vertical ground motion are examined. The effectiveness of the current design approach for considering vertical seismic motion is studied, as well as the punching failure potential of the flat-plate structure due to vertical seismic ground motion. Punching failure is evaluated based on four criteria, which consider either shear stress, or lateral drift, or localized slab rotation at the slab-column connections. Finally, the soil-structure interaction is considered for the tri-axial dynamic analyses of the prototype structure by inclusion of soil springs representing translational and rotational soil stiffness. The dynamic demand for lateral drift, slab rotation, and shear transfer at the slab-column connection are presented.

6.2 CONCLUSIONS

The following conclusions are reached from the time-history analyses of the prototype flat-plate building:

- A flat-plate structure, although designed only as a gravity load-carrying system, possesses some lateral strength and stiffness. From the static pushover analysis it is found that even though the slab-column framing is inherently weaker than the moment frames, it can still provide about 20% extra strength and stiffness to the lateral force resisting system. This is mainly caused by the larger number of slab-column connections.
- Lateral drift is shown to be largely unaffected by the vertical seismic ground motion. This is expected since the lateral deformation is governed by the perimeter moment frames that are potentially unaltered by the vertical ground acceleration.
- Vertical ground motion is shown to significantly magnify slab rotation relative to the supporting column. This is most likely the result of accumulating slab damage from loading reversals combined with the inertia force produced by vertical motion. However,

clear correlations between slab local deformation demand and V/H-ratio or vertical PGA, that are the major vertical ground motion properties are unable to be established.

- The addition of vertical ground motion leads to considerable axial force increase at the column due to the shear force transfer from the surround slab. This increase can have a profound effect on the potential punching failure of the slab-column connections. Large fluctuations in axial force are also observed for the column which may have an exaggerated effect on higher stories in a multistory flat-plate building.
- Peak lateral drift and peak relative slab rotation are shown to occur nearly simultaneously. Only 3 ground motion records cause a time difference of more than 1 sec. and the average time interval is about 1.5 seconds. It is therefore concluded that a strong correlation exists between the relative rotation of the slab and the global behavior indexed by lateral story drift.
- The current design approach specified by ASCE/SEI 7-10, which incorporates a dead load scale factor of $0.2S_{DS}$, is shown to be sufficient to incorporate the effects of vertical ground motion in the design of flat plates. However, no obvious trend can be identified to determine the use of a higher or lower scale factor based on vertical PGA, epicentral source distance, V/H-ratio, vertical response spectrum, time interval between peak vertical and horizontal accelerations, or time interval between peak vertical acceleration and peak slab relative rotation. It is recommended that the parameter of $0.2S_{DS}$ be used in the design of slab-column framing to account for the vertical ground motions.
- The ACI 318 two-way shear design approach does not account for relatively low slab reinforcement ratios and inherently overestimates punching resistance. This study shows that even at large slab rotation demands (greater than 0.05 rad.), punching failure cannot

be identified by the code formulation. The eccentric shear stress model given by ACI 318 is shown to predict very little difference in the punching failure potential of a flat-plate system when vertical ground motion is included. Therefore, it is concluded that these two code-specified approaches may not be able to adequately predict the potential of punching failure when vertical ground motion is considered.

- The ACI 318 drift limit approach and Muttoni's punching failure criterion model predict similar risk of punching failure for uni-axial, bi-axial, and tri-axial loading. Furthermore, both models predict a greater possibility of punching failure when vertical ground motion is incorporated. It is concluded that these two formulations effectively forecast punching failure
- Incorporating soil-structure interaction produces little change in the dynamic response of the prototype building under tri-axial loading. It is concluded that, if the soil is stiff, the performance of a flat-plate structure will not be significantly altered by soil-structure interactions.

6.3 RECOMMENDATIONS FOR FUTURE WORK

This study is limited to flat plates where the design is governed by gravity loads, perimeter moment frames are utilized as the lateral force-resisting system, and slabs are supported on square columns without using any shear reinforcement. Furthermore, eight seismic records with diverse parameters are chosen to analyze the dynamic demands on the structure. It is recommended that future work of flat-plate structures under vertical seismic loading address the following issues:

- (1) The slab dynamic response identified from finite element simulations can be greatly affected by the nonlinear grid beam model adopted in this study. To reduce the uncertainty

involved in this macro-modeling approach, it shall be further validated or improved by more experimental data of slab-column connections subjected to seismic loading.

- (2) Experimental research, such as shake stable testing, shall be conducted to investigate the vertical ground motion effects on flat-plate structures and to examine the effectiveness of numerical models.
- (3) The dynamic performance of flat-slabs with varied design limitations including shear walls as the lateral force resisting system, asymmetrical plan layout, varied column sizes and higher reinforcement ratios can be investigated.
- (4) Simulations of flat-slabs under seismic ground motions with comparable characteristics such as similar V/H ratios, peak vertical and horizontal time intervals, frequency, or source distance can be conducted to individually study the effects of these parameters.
- (5) Analyses that incorporate soil-structure interaction using more detailed modeling approach can be performed on flat-plate structures situated on softer soils, where more pronounced effects of soil-structure interaction are anticipated.

REFERENCES

2009 NEHRP recommended seismic provisions: Design examples (FEMA P-751) (2012).

(2012th ed.). Washington, DC, US: Prepared by Building Seismic Safety Council (BSSC) for the Federal Emergency Management Agency (FEMA) National Earthquake Hazards Reduction Program (NEHRP).

2009 NEHRP recommended seismic provisions: Training and instruction materials (FEMA P-752) (2013). (2013th ed.). Washington, DC, US: Prepared by Building Seismic Safety Council (BSSC) for the Federal Emergency Management Agency (FEMA) National Earthquake Hazards Reduction Program (NEHRP).

262 code for concrete structures (2003). . Zurich, Switzerland: SIA, Swiss Society of Engineers and Architects.

AASHTO. (2010). *LRFD bridge design specifications*. Washington, D.C.: American Association of State Highway and Transportation Officials.

ACI Committee 318, American Concrete Institute, & International Organization for Standardization. (2005). Building code requirements for structural concrete (ACI 318-05) and commentary (318R-05). *Building Code Requirements for Structural Concrete (ACI 318-05) and Commentary (318R-05)*, 430.

ACI Committee 318, American Concrete Institute, & International Organization for Standardization. (2008). ACI building code requirements for reinforced concrete, ACI 318-08.

- ACI Committee 318, American Concrete Institute, & International Organization for Standardization. (2014). *Building code requirements for structural concrete (ACI 318-14) and commentary*. Farmington Hills, Mich.: American Concrete Institute.
- Adhikary, S., Singh, Y., & Paul, D. (2008). Modeling of soil-foundation-structure system. *Department of Earthquake Engineering, IIT Roorkee.*, 01, 7
- Agbabian, M. S., Higazy, E. M., Abdel-Ghaffar, A. M., & Elnashai, A. S. (1994). Experimental observations on the seismic shear performance of RC beam-to-column connections subjected to varying axial column force. *Earthquake Engineering & Structural Dynamics*, 23(8), 859-876.
- Akiyama, H., & Hawkins, N. M. (1984). Response of flat plate concrete structures to seismic and wind forces. *Structures and Mechanics Rep*, , 320.
- ASCE/SEI 41-13 seismic evaluation and retrofit of existing buildings. (2006).
- ASCE/SEI 43-05 seismic design criteria for structures, systems, and components in nuclear facilities (2005). . Reston, VA: American Society of Civil Engineers.
- ASCE/SEI 7-05 minimum design loads for buildings and other structures (2005). . Reston, VA: American Society of Civil Engineers. Retrieved from <http://www.library.unlv.edu/help/remote.html>; <http://site.ebrary.com/lib/unlv/Doc?id=10435298>;
- ASCE/SEI 7-10 minimum design loads for buildings and other structures (2010). Reston, VA: American Society of Civil Engineers. Retrieved

from <http://www.library.unlv.edu/help/remote.html>; <http://site.ebrary.com/lib/unlv/Doc?id=10435298>

- Bozorgnia, Y., & Niazi, M. (1993). Distance scaling of vertical and horizontal response spectra of the loma prieta earthquake. *Earthquake Engineering and Structural Dynamics*, 22(8), 695-707.
- Bradley, B. A., & Cubrinovski, M. (2011). Near-source strong ground motions observed in the 22 february 2011 christchurch earthquake. *Seismological Research Letters*, 82(6), 853-865.
- Button, M. R., Cronin, C. J., & Mayes, R. L. (2002). Effect of vertical motions on seismic response of highway bridges. *Journal of Structural Engineering*, 128(12), 1551-1564.
- Chopra, A. K. (2007). Elastic response spectrum: A historical note. *Earthquake Engineering & Structural Dynamics*, 36(1), 3-12.
- Collier, C. J., & Elnashai, A. S. (2001). A procedure for combining vertical and horizontal seismic action effects. *Journal of Earthquake Engineering*, 5(4), 521-539.
- Cope, R. J. (1986). Nonlinear analysis of reinforced concrete slabs. *Computer Modelling of RC Structures*, , 3-43.
- Coronelli, D. (2010). Grid model for flat-slab structures. *ACI Structural Journal*, 107(6), 645-653.

- Damjanic, F., & Owen, D. R. J. (1984). Practical considerations for modeling of post-cracking concrete behavior for finite element analysis of reinforced concrete structures. Paper presented at the 693-706.
- Delray Engineering Inc. (2015). 48 unit apartment buildings. Retrieved from <http://www.delrayengineering.ca/>
- Di Sarno, L., Elnashai, A. S., & Manfredi, G. (2011). Assessment of RC columns subjected to horizontal and vertical ground motions recorded during the 2009 L'aquila (italy) earthquake. *Engineering Structures*, 33(5), 1514-1535.
- EERI. (2015). Earthquake engineering research institute. Retrieved from www.eeri.org
- Elnashai, A. S., & Papazoglou, A. J. (1997). Procedure and spectra for analysis of RC structures subjected to strong vertical earthquake loads. *Journal of Earthquake Engineering*, 1(1), 121-155.
- Elstner, R. C., & Hognestad, E. (1956). Shearing strength of reinforced concrete slabs. *ACI Journal*, 53(1), 29-58.
- Elwood, K. J., & Moehle, J. P. (2003). Shake table tests and analytical studies on the gravity load collapse of reinforced concrete frames. *Shake Table Tests and Analytical Studies on the Gravity Load Collapse of Reinforced Concrete Frames*,
- FEMA. (2005). In Fema 65 (Ed.), *Federal guidelines for dam safety: Earthquake analyses and design of dams*. Washington, D.C.: Interagency Committee on Dam Safety for FEMA.

- FERC. (2007). *Draft seismic design guidelines and data submittal requirements for LNG facilities*. Washington, D.C.: Federal Energy Regulatory Commission Office of Energy Projects.
- Gazetas, G. (1983). Analysis of machine foundation vibrations: State of the art. *International Journal of Soil Dynamics and Earthquake Engineering*, 2(1), 2-42.
- Gazetas, G. (1991). Formulas and charts for impedances of surface and embedded foundations. *Journal of Geotechnical Engineering*, 117(9), 1363-1381.
- Ghannad, M. A., & Jahankhah, H. (2007). Site-dependent strength reduction factors for soil-structure systems. *Soil Dynamics and Earthquake Engineering*, 27(2), 99-110.
doi:10.1016/j.soildyn.2006.06.002
- Gilbert, R. I., & Warner, R. F. (1978). Tension stiffening in reinforced concrete slabs. *ASCE J Struct Div*, 104(12), 1885-1900.
- Guandalini, S., Burdet, O. L., & Muttoni, A. (2009). Punching tests of slabs with low reinforcement ratios. *ACI Structural Journal*, 106(1), 87-95.
- Guo, Z., & Zhang, X. (1987). Investigation of complete stress-deformation curves for concrete in tension. *ACI Materials Journal*, 84(4), 278-285.
- Hillerborg, A., Modeer, M., & Petersson, P. E. (1976).
Analysis of crack formation and crack growth in concrete by means of fracture mechanics and finite elements
Cement and Concrete Research, 6, 773-782.

- Hsu, T. T. C. (1968). Torsion of structural concrete-interaction surface for combined torsion, shear and bending in beams without stirrups. *ACI Journal, Proceedings*, 65(1), 51-60.
- International building code (IBC)* (2015). . Country Club Hill, Illinois, US: International Code Council (ICC).
- Kadid, A., Yahiaoui, D., & Chebili, R. (2010). Behaviour of reinforced concrete buildings under simultaneous horizontal and vertical ground motions. *Asian Journal of Civil Engineering*, 11(4), 463-476.
- Kam, W. Y., Pampanin, S., & Elwood, K. (2011). Seismic performance of reinforced concrete buildings in the 22 february christchurch (lyttleton) earthquake.
- Kang, T. H., Wallace, J. W., & Elwood, K. J. (2009). Nonlinear modeling of flat-plate systems. *Journal of Structural Engineering*, 135(2), 147-158. doi:10.1061/(ASCE)0733-9445(2009)135:2(147)
- Kanoh, Y., & Yoshizaki, S. (1979). Strength of slab-column connections transferring shear and moment. *J Am Concr Inst*, 76(3), 461-478.
- Karsan, I. D., & Jirsa, J. O. (1969). Behavior of concrete under compressive loading. *Journal of Structural Division ASCE*, 95(12), 2543.
- Kent, D. C., & Park, R. (1971). Inelastic behavior of reinforced concrete members with cyclic loading. *Bulletin of the New Zealand Society for Earthquake Engineering*, 4(1), 108-125.

- Kim, S. J. (2008). *Seismic assessment of RC structures considering vertical ground motion* (Ph.D.). Available from ProQuest Dissertations & Theses Full Text. (304603439). Retrieved from <http://search.proquest.com.ezproxy.library.unlv.edu/docview/304603439?accountid=3611>
- Koukleri, S. N. (1992). The effect of vertical ground excitation on the response of R.C. Structures. *The Effect of Vertical Ground Excitation on the Response of R.C. Structures*,
- Kunnath, S., Erduran, E., Chai, Y., & Yashinsky, M. (2008). Effect of near-fault vertical ground motions on seismic response of highway overcrossings. *Journal of Bridge Engineering*, 13(3), 282-290. doi:10.1061/(ASCE)1084-0702(2008)13:3(282)
- Lips, S., Ruiz, M. F., & Muttoni, A. (2012). Experimental investigation on punching strength and deformation capacity of shear-reinforced slabs. *ACI Structural Journal*, 109(6), 889-900.
- Liu, J., Tian, Y., Orton, S. L., & Said, A. M. (2015). Resistance of flat-plate buildings against progressive collapse. I: Modeling of slab-column connections. *Journal of Structural Engineering (United States)*, 141(12) doi:10.1061/(ASCE)ST.1943-541X.0001294
- Luo, Y. H., Durrani, A. J., & Conte, J. P. (1995). Equivalent frame analysis of flat plate buildings for seismic loading. *J.Struct.Eng.*, , 2137-2155.
- Madani, B., Behnamfar, F., & Tajmir Riahi, H. (2015). Dynamic response of structures subjected to pounding and structure-soil-structure interaction. *Soil Dynamics and Earthquake Engineering*, 78, 46-60. doi:10.1016/j.soildyn.2015.07.002

- Mander, J. B., Priestley, M. J. N., & Park, R. (1988). Theoretical stress-strain model for confined concrete. *Journal of Structural Engineering New York, N.Y.*, 114(8), 1804-1826.
- MC2010. (2010). *Fib model code for concrete structures 2010* Ernst & Sohn publishing house.
- McGuire, J. W., Cofer, W. F., Marsh, M. L., & McLean, D. I. (1994). Analytical modeling of spread footing foundations for seismic analysis of bridges. *Transportation Research Record*, (1447), 80-92.
- Megally, S., & Ghali, A. (2000). Punching shear design of earthquake-resistant slab-column connections. *ACI Structural Journal*, 97(5), 720-730.
- Morrison, D. G., Hirasawa, I., & Sozen, M. A. (1983). Lateral-load tests of r/c slab-column connections. *Journal of Structural Engineering*, 109(11), 2698-2714.
- Muttoni, A. (2008). Punching shear strength of reinforced concrete slabs without transverse reinforcement. *ACI Structural Journal*, 105(4), 440-450.
- Mwafy, A. M., & Elnashai, A. S. (2006). Vulnerability of code-compliant RC buildings under multi-axial earthquake loading", *4th International Conference on Earthquake Engineering*, Taipei, Taiwan. , *Paper No. 115*
- Mylonakis, G., Nikolaou, S., & Gazetas, G. (2006). Footings under seismic loading: Analysis and design issues with emphasis on bridge foundations. *Soil Dynamics and Earthquake Engineering*, 26(9), 824-853. doi:10.1016/j.soildyn.2005.12.005

NEHRP recommended seismic provisions for new buildings and other structures (FEMA P-750) (2009). (2009th ed.). Washington, DC, US: Prepared by Building Seismic Safety Council (BSSC) for the Federal Emergency Management Agency (FEMA) National Earthquake Hazards Reduction Program (NEHRP).

NEHRP recommended seismic provisions for new buildings and other structures (FEMA publication 273) (2009). . Washington, DC, US: Prepared by Applied Technology Council (ATC) for the Building Seismic Safety Council (BSSC).

Newmark, N. M., & Hall, W. J. (1982). Earthquake spectra and design. *Earth System Dynamics, 1*

Newmark, N. M., Blume, J. A., & Kapur, K. K. (1973). Seismic design spectra for nuclear power plants. *ASCE J Power Div*, 99(PO2), 287-303.

NIST GCR 12-917-21 soil-structure interaction for building structures. (2012). (NEHRP Publication).NEHRP Consultants Joint Venture.

NIST GCR 11-917-15 Selecting and scaling earthquake ground motions for performing response-history analyses. (2011). (NEHRP Publication).NEHRP Consultants Joint Venture.

Open system for earthquake engineering simulation. (2011).

Ostadan, F. (2004). Seismic soil pressure for building walls-an updated approach, 11th ICSDEE and 3rd ICEGE. *University of California, Berkeley*,

- Pan, A. D., & Moehle, J. P. (1992). An experimental study of slab-column connections. *ACI Structural Journal*, 89, 626-626.
- Papazoglou, A. J., & Elnashai, A. S. (1996). Analytical and field evidence of the damaging effect of vertical earthquake ground motion. *Earthquake Engineering and Structural Dynamics*, 25(10), 1109-1137.
- Park, R., & Gamble, W. L. (2000). *Reinforced concrete slabs* (2nd ed.). New York: Wiley.
- Parmelee R.A., Perelman D.S., & Lee S.L. (1969). Seismic response of multiple-story structures on flexible foundations. *Bulletin of the Seismological Society of America*, 59(3), 1061-1070.
- Paulay, T., & Priestley, M. J. N. (1992). Seismic design of reinforced concrete and masonry buildings., 744.
- Prakash, S., & Puri, V. K. (1988). Foundations for machines: Analysis and design.
- PTC.Mathcad 15.0 (2007th ed.). St. Petersburg: BKhV- Peterburg:
- Robertson, I., & Johnson, G. (2006). Cyclic lateral loading of nonductile slab-column connections. *ACI Structural Journal*, 103(3), 356-364.
- Robertson, I. N. (1997). Analysis of flat slab structures subjected to combined lateral and gravity loads. *ACI Structural Journal*, 94(6), 723-729.
- Robertson, I. N., & Durrani, A. J. (1992). Gravity load effect on seismic behavior of interior slab-column connections. *ACI Structural Journal*, 89(1), 37-45.

- Saadeghvaziri, M. A., & Foutch, D. A. (1991). Dynamic behaviour of R/C highway bridges under the combined effect of vertical and horizontal earthquake motions. *Earthquake Engineering and Structural Dynamics*, 20(6), 535-549.
- Scott, B. D., Park, R., & Priestley, M. J. N. (1980). Stress-strain relationships for confined concrete: Rectangular sections. *Res.Rep.no.80-6*,
- Seismic performance assessment of buildings (FEMA P-58)* (2012). (2012th ed.). Washington, DC, US: Prepared by Building Seismic Safety Council (BSSC) for the Federal Emergency Management Agency (FEMA) National Earthquake Hazards Reduction Program (NEHRP).
- Sherif, A. G., & Dilger, W. H. (1996). Critical review of the CSA A23.3-94 punching shear strength provisions for interior columns. *Canadian Journal of Civil Engineering*, 23(5), 998-1011.
- Spacone, E., Filippou, F., & Taucer, F. (1996). Fibre beam-column model for non-linear analysis of R/C frames: Part II. applications. *Earthquake Engineering and Structural Dynamics*, 25(7), 727-742.
- Swanson, D. (2011). Reid our blog. Retrieved from <https://reidmiddleton.wordpress.com/2011/03/14/5/>
- Tian, Y., Chen, J., Said, A., & Zhao, J. (2012). Nonlinear modeling of flat-plate structures using grid beam elements. *Computers and Concrete*, 10(5), 489-505.
- Tian, Y., Jirsa, J. O., & Bayrak, O. (2008). Strength evaluation of interior slab-column connections. *ACI Structural Journal*, 105(6), 692-700.

- Tian, Y., Jirsa, J. O., & Bayrak, O. (2009). Nonlinear modeling of slab-column connections under cyclic loading. *ACI Structural Journal*, 106(1), 30-38.
- U.S. Army Corps of Engineers. (2009). *Selection of design earthquakes and associated ground motions* EC 1110-2-6000.
- UBC. (1991). Uniform building code standards. Paper presented at the *International Conference of Building Officials, Whittier, CA*,
- United Facilities Criteria 3-310-04. (2004). In Department of Defense (Ed.), *Seismic design for buildings*
- Winkler, E. (1867). Theory of elasticity and strength. *Dominicus Prague, Czechoslovakia*,
- Wolf, J. P., & Meek, J. W. (1994). Dynamic stiffness of foundation on layered soil half-space using cone frustums. *Earthquake Engineering and Structural Dynamics*, 23(10), 1079-1095.
- Xia, Z. (2008, October). Efficient floor framing systems preliminary sizing of post-tensioned floors. *Structural Engineer*, , 42-47.
- Yettram, A. L., & Husain, H. M. (1965). Grid framework method for plates in flexure. *Proc. of ASCE*, 91(EM3), 53-64.
- Zhao, J., & Sritharan, S. (2007). Modeling of strain penetration effects in fiber-based analysis of reinforced concrete structures. *ACI Structural Journal*, 104(2), 133-141.

CURRICULUM VITAE

Graduate College
University of Nevada, Las Vegas

Sara George

Education:

Bachelor of Science in Architectural Engineering, Structural Emphasis, 2007
University of Wyoming

Master of Science in Civil Engineering, Structural Emphasis, 2012
University of Nevada, Las Vegas

Employment:

Consulting Engineer	Summer 2014
Barker Drott Associates	Las Vegas, Nevada
Summer Intern	Summer 2010
ARUP	Houston, Texas
Project Engineer	May 2007- June 2009
Barker Drott Associates	Las Vegas, Nevada
Summer Intern	Summer 2006
Structural Engineers, P.C.	Marshalltown, Iowa

Thesis Title:

Structural performance of reinforced concrete flat plate buildings subjected to fire (2012)

Dissertation Title:

Effects of Vertical Ground Motion on Seismic Performance of Reinforced Concrete Flat-Plate Buildings

Dissertation Examination Committee:

Chairperson, Dr. Ying Tian, Ph.D., P.E.
Committee Member, Dr. Samaan Ladkany, Ph.D., P.E.
Committee Member, Dr. Moses Karakouzian, Ph.D., P.E.
Committee Member, Dr. Sarah Orton Ph.D., P.E.
Graduate Faculty Representative, Dr. Brendan O'Toole, Ph.D.

Publication:

George, S. J. and Tian, Y. (2012). "Structural Performance of Reinforced Concrete Flat Plate Buildings Subjected to Fire," *International Journal of Concrete Structures and Materials*, 6(2), 111-121.